ABSTRACT

ALBERTA HAILSTORMS: A RADAR STUDY AND MODEL

by

A.J. Chisholm, M.Sc.

Radar case studies are presented for four Alberta hailstorms. Weak echo regions (not detected by radar), cloud base updrafts and environmental winds are used to arrive at airflow models for these hailstorms. A loaded moist adiabatic updraft model is utilized to compute estimates of cloud temperatures, liquid water contents and vertical velocities within the hailstorm updraft core. The updraft model results and a cloud droplet model describe the precipitation growth environment within the updraft core of specific hailstorms. A graupel growth model, using drag coefficients, collection efficiencies and heat transfer efficiencies appropriate to smooth spheres, is used to compute the growth of graupel particles (with variable ice accretion density) as small as 100 μ diameter. The resulting computed Z values in the updraft core agree with observed weak echo regions and further indicate that graupel particles grow to hailstone size external to, but close to the weak echo region.

Department of Meteorology
McGill University

Montreal
May, 1970

ALBERTA HAILSTORMS:

A RADAR STUDY AND MODEL

by

A.J. Chisholm, M.Sc.

ALBERTA HAILSTORMS:

A RADAR STUDY AND MODEL

by

A.J. Chisholm, M.Sc.

A thesis submitted to the Faculty of Graduate Studies and Research of McGill University in partial fulfillment of the requirements for the Degree of Doctor of Philosophy

Department of Meteorology
McGill University

Montreal
May, 1970

DEDICATION

To my loving wife Ann, and my son Douglas,
whose patience, understanding and encouragement
have made this thesis possible

ABSTRACT

ALBERTA HAILSTORMS: A RADAR STUDY AND MODEL

Radar case studies are presented for four Alberta hailstorms. Weak echo regions (not detected by radar), cloud base updrafts and environmental winds are used to arrive at airflow models for these hailstorms. A loaded moist adiabatic updraft model is utilized to compute estimates of cloud temperatures, liquid water contents and vertical velocities within the hailstorm updraft core. The updraft model results and a cloud droplet model describe the precipitation growth environment within the updraft core of specific hailstorms. A graupel growth model, using drag coefficients, collection efficiencies and heat transfer efficiencies appropriate to smooth spheres, is used to compute the growth of graupel particles (with variable ice accretion density) as small as 100 μ diameter. The resulting computed Z values in the updraft core agree with observed weak echo regions and further indicate that graupel particles grow to hailstone size external to, but close to the weak echo region.

ACKNOWLEDGEMENTS

The author wishes to acknowledge with sincere appreciation the assistance of his supervisor, Prof. R.H. Douglas whose knowledge, guidance and encouragement helped immeasurably during the course of this study.

In addition, this study has benefited from numerous discussions with staff and students associated with the Alberta Hail Studies Project and the Stormy Weather Group. Particularly appreciated are the many hours of interesting and provocative discussion with J.D. Marwitz and Dr. G. Vali.

This study has been made possible by the Alberta Hail Studies Project which is supported both technically and financially by the Research Council of Alberta, the National Research Council, the Meteorological Service of Canada and McGill University. The task of collecting field data was supervised by the author during the summers of 1967 and 1968. Dr. P.W. Summers (Field Director), his assistant, J.H. Renick, and a substantial summer technical staff are gratefully acknowledged for the very important role they played in gathering the many data required for this study.

Miss M. Candlish is due sincere thanks for her assistance in writing, testing and running the many computer programs which were utilized. Drafting was done by Mr. Cheng-Wong Chang, Miss M. Candlish and the author. The author wishes to express his appreciation to his wife for typing the manuscript, and to Mr. R.W. Ross and Mr. F.C.C. Andrews for editing and proofreading the manuscript.

PREFACE

After completing a radar study of two Alberta hailstorms using the ALHAS 10 cm radar with a broad vertical beam antenna, a unique opportunity arose for the author to further such studies using the ALHAS radar equipped with a 1.15 deg beamwidth antenna. Excellent horizontal and vertical resolution, coupled with a rapid scan cycle (3 min), made possible studies of hailstorms in three dimensions - an exciting prospect indeed. This thesis is the result of what followed.

From data gathered with the narrow beam ALHAS radar during the summer of 1967, it became evident that structures like the vaults found in severe storms by Browning in England and Donaldson in Oklahoma existed, as well, in Alberta hailstorms. During the summer of 1968, cloud base updraft measurements, obtained by the University of Wyoming meteorologically instrumented aircraft, made possible a first verification of Browning's proposal that vaults are due to updrafts containing small scattering particles not detectable by radar. This concept was field tested successfully on a number of storms during 1968 and 1969; four of these storm structures (on two separate days) have been analyzed by the author and are presented in Chaps. II and III. This co-operative effort, with the staff of the University of Wyoming supplying aircraft measurements, is considered a significant, original contribution to the field of severe storm studies. With the insight gained studying these four storm structures, the radar analyses, presented in Chaps. IV and V for two storms in 1967, take on much more significance.

Radar information is invaluable in studying severe storms because it can be used to locate and track the storm, measure its height, areal extent and, in addition, supply an estimate of the precipitation size and/or intensity. However, radar cannot tell one directly how a particular storm functions. It is necessary to formulate qualitative conceptual models, which are able to account for the storm data collected by radar, aircraft and observers on the ground.

The basic feature common to all such models is the storm airflow. Based on the hypothesis that vaults (designated weak echo region in this thesis) consist primarily of micron-size cloud droplets in the core of an updraft, and accompanied by other evidence, airflow models for each of the six storm structures studied in Chaps. II - V have been deduced in Chap. VI. One of these models is similar in many aspects to the Browning SR model. However, the others are different, constituting three basic storm airflow models. The storms studied and airflow models postulated herein were selected from data for more than 30 hailstorm days during the summers of 1967 and 1968 - consequently they are considered to represent the major modes of Alberta hailstorm operation. These models are considered to be a significant, original contribution to the study of severe storms in Alberta.

The airflow models presented in Chap. VI provide a qualitative framework within which an updraft exists and precipitation particles form and grow. However, in providing answers to some questions, the airflow models also give rise to many others. What conditions exist within the updraft core - ie. temperature, water content, vertical velocity? What are the precipitation processes, and can they supply particles sufficiently large to be detected by radar? A search for answers to such questions resulted in the formation of several numerical models. Basic to the storm airflow models of Chap. VI is a strong, persistent updraft of sufficient width to preclude the effect of entrainment within the updraft core. On this simplifying assumption, a loaded moist adiabatic (LMA) updraft model was formulated to obtain estimates of cloud temperature, liquid water content and vertical velocity within the updraft core. This model has been verified successfully by comparing computed storm tops with radar-observed storm tops for 29 major hailstorms during 1967 and 1968. Although the concept is not new, the author believes that this is the first time it has been programmed and used to compute cloud parameters. A far more significant contribution lies in the fact that this model has been used in a consistent manner to compute estimates of cloud temperatures, liquid water content and vertical velocity for 29 major hailstorms during 1967 and 1968. The importance of these data lies in the fact that they are numerical values which can be used to quantify storms and compare them one with another. It is indeed promising that a definite pattern has emerged - the higher the maximum storm energy, the stronger the computed updraft, the higher the observed storm top and the larger the maximum size hail observed at the ground.

Armed with estimates of conditions within the updraft core, it became possible to attack the question of precipitation formation and growth. On the basis of recent experimental and theoretical work on cloud droplet coalescence, it became evident that, within a strong updraft, the major growth must be due to condensation. As a consequence, a monodisperse cloud droplet model was formulated, basing the droplet number concentrations on data obtained from representative cloud base updrafts and average cloud condensation nuclei spectra for Alberta. The combination of the LMA model results and the cloud droplet model constitute a description of the precipitation growth environment within the updraft core - an original contribution to the fields of cloud physics and severe storm studies.

It is argued that the only physically reasonable means of achieving significant precipitation growth in the updraft core is for giant cloud droplets to freeze and grow by an accretion process. This has resulted in the formulation of a graupel growth model which is used to compute growth by accretion and sublimation, using drag coefficients, collection efficiencies and heat transfer coefficients appropriate to smooth spheres. Both wet and dry growth modes are accounted for and the density of accreted ice is also calculated. This model was designed specifically for calculations of the growth of graupel particles from 100 μ to ≈ 1 cm diameter. As such, it is a significant, original contribution to the field of cloud physics. The results of case studies with this model reveal that graupel particles can grow from 100 μ to ≈ 2-4 mm diameter while ascending through the updraft core. Using estimated particle concentrations, it is evident that this growth can occur and yet the scattering particles would still escape detection by radar - giving rise to a weak echo region. These results agree very well with the observed radar structures of the storms studied. Additionally, the results suggest that in storms having strong updrafts, the graupel particles grow to hailstone size during descent external to (but in close proximity with) the weak echo region. Conversely, weak updrafts permit graupel particles to grow while descending back through the updraft core, resulting in the destruction of the weak echo region. This predicted behaviour was indeed observed in the appropriate storms studied herein, resulting in further verification of the weak echo region hypothesis as well as providing substantial support for the airflow models, updraft model and graupel model.

The individual parts of this thesis are like pieces of a jigsaw puzzle - belonging to something larger - yet still important contributions in their own right. However, it is the fitting together of all these individual pieces into a coherent picture of the Alberta hailstorm which permits each element to be viewed in proper perspective and in relation to the others. It is this aspect which constitutes the major contribution of this study.

LIST OF FIGURES

Page

Page

Page

Page

TABLE OF CONTENTS

CHAPTER I

INTRODUCTION AND REVIEW OF THUNDERSTORM AND SEVERE STORM MODELS

1.1 Introduction

This study is concerned with Alberta hailstorms which result from intense thunderstorms[1] (severe storms[2] or severe local storms). Each summer such storms cause millions of dollars of damage to agricultural crops in the farming regions of central Alberta. The task of studying severe storms is a difficult one. Unable to create severe storms at will, or model them in a laboratory, investigators must observe severe storms in the field in order to gain insight into their operation. This places the investigator at the mercy of nature to provide the desired storms at a convenient time and location. The dimensions, velocity and duration of the severe storm determine the spacing and frequency of observations which are needed to delineate and study them. Characteristically, the severe storm is about 10 x 10 x 10 km, moves at 10 m sec^{-1}, and is in an intense mature stage for 100 min. It would be desirable to have comprehensive observations within the severe storm at 1 km intervals (total of 1000 grid points) each minute in order to delineate and study the storm in question. Such a mammoth program has not yet been undertaken. Instead, the severe storm is treated much like a "black box" with pertinent observations being taken and used to formulate or test hypotheses about the physical processes which occur within it. This study deals with radar case studies of four selected Alberta hailstorms and

[1] A thunderstorm is a local storm produced by a cumulonimbus cloud and accompanied by lightning, strong gusts of wind and heavy rain.

[2] A severe storm or severe local storm is an intense thunderstorm characterized by very strong surface winds, heavy rain, hail and/or tornadoes.

with estimates of the processes which transpire in the core of the updraft region in these severe storms.

1.1.1 The Alberta Hail Studies Project (ALHAS)

The Alberta Hail Studies Project is a co-operative project supported jointly by the Research Council of Alberta, the National Research Council, the Meteorological Service of Canada and McGill University. Begun in 1956, the object of the ALHAS project is to study the behaviour and mechanisms of hailstorms in order to determine what might be done about them. Toward this end, ALHAS operates a field observation program in central Alberta. The field project area (approximately 300 km N-S by 210 km E-W), shown in Fig. 1.1.1, is bounded on the west by the pine and spruce forested foothills of the Rocky Mountains. East of the foothills, the geography changes rapidly to slightly rolling farmland (approximately 1 km MSL) with mixed farming and cereal crops predominating. Since a great variety of field observations from the summers of 1967 and 1968 have been used in this study, a brief outline of the ALHAS field observation program during 1967 and 1968 follows:

(i) Co-operative hailfall observations: The co-operation of farmers within the area is solicited by requesting that they complete a hail report postcard when hail falls on their land. Additional surface hail observations are obtained from farmers by conducting telephone hail surveys along major storm tracks.

(ii) Surface weather observations: Meteorological Branch weather stations located at Edmonton, Penhold, Rocky Mountain House and Calgary (see Fig. 1.1.1) supply hourly weather reports by teletype.

(iii) Radiosonde observations: Radiosonde soundings are taken at Edmonton

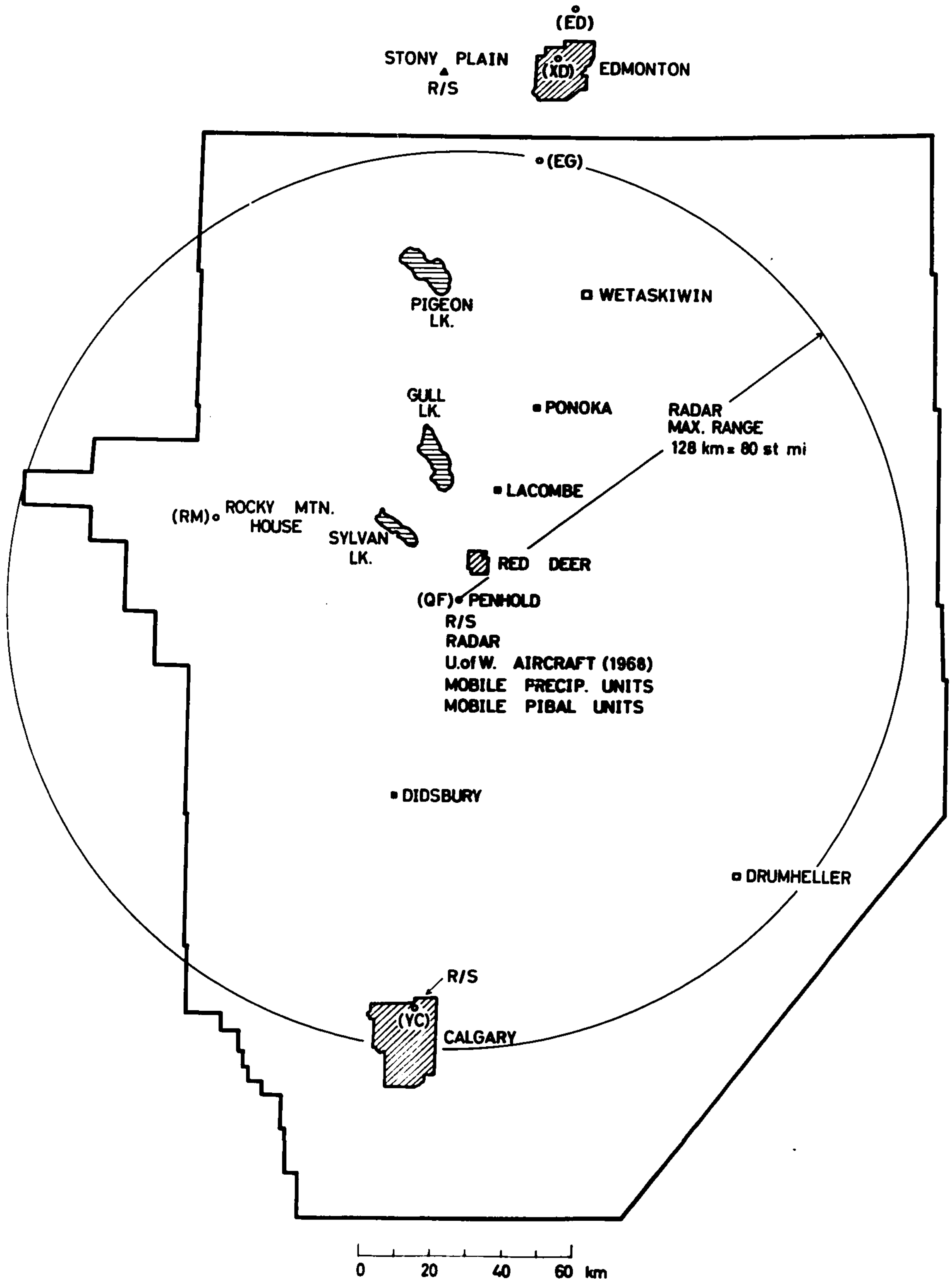

Fig. 1.1.1 Map of Alberta Hail Studies (ALHAS) Project Area. The ALHAS project area boundary is indicated by the heavy solid line. Meteorological Service weather reporting stations are shown by small circles and radiosonde stations are marked (R/S). Observing equipment located or based at project headquarters is also indicated.

(Stony Plain) and Calgary twice daily at 0415 and 1615 MST. A METOX radiosonde unit located at Penhold is also used for routine soundings at 1615 MST as well as additional radiosonde ascents at approximate 2 hr intervals during severe storms.

(iv) ALHAS 10 cm radar observations: A modified AN/FPS-502 radar is operated at ALHAS project headquarters.

Its characteristics are given below:

P_t	- transmitted power	-	250 kw
G	- gain	-	43.25 db
θ	- horizontal half-power beamwidth	-	1.15 deg
ϕ	- vertical half-power beamwidth	-	1.15 deg
h	- pulse length	-	1.75 μsec
PRF	- pulse repetition frequency	-	480 sec^{-1}
MDS	- minimum detectable signal	-	-100 dbm (nominal)
λ	- wavelength	-	10.4 cm
f	- frequency	-	2880 MHz
ω	- antenna rotation rate	-	8 rpm
D	- antenna diameter	-	6.8 m

The antenna operates in a fixed spiral scan (0-20 deg), elevating 1 deg per revolution to complete a scan cycle in 3 min. A five-level grey shade PPI display is photographed with 35 mm film (Kodak 4-X, Type 5224) for later study.

(v) Stereo cloud photo observations: Two 16 mm movie cameras, operated at sites approximately 4.5 km apart (taking single frame photographs at 3 sec intervals), are used to study visual cloud and precipitation motions when photographic conditions are suitable.

(vi) Pilot balloon observations: To delineate the wind structure in the sub-cloud layer near a severe storm, a mobile crew, equipped with four optical theodolites, is directed into the vicinity of a severe storm to visually track pilot balloons. These theodolites can be used independently at any location or as double theodolite couples at pre-surveyed sites.

(vii) Mobile precipitation observations: Two radio-equipped panel trucks with high-speed tipping-bucket rain gauges, hail recording gauge and hail and rain sampling equipment were also directed into the vicinity of hailstorms. They gather rain and hail samples for SO_2 and ice nuclei studies as well as collecting data on rain and hailfall rates.

(viii) Aircraft observations: During the summer of 1968, an instrumented C-45H twin Beechcraft was operated from Penhold by the University of Wyoming. This aircraft obtained cloud base observations of vertical velocity, updraft area, temperature and ice nucleus counts (NCAR counter). Air samples were taken for later analysis of cloud condensation nuclei and a shotgun-type cloud droplet sampler was also available for use during cloud penetration.

1.2 A Review of Thunderstorm and Severe Storm Models

A complete review of all thunderstorm and severe storm models is beyond the scope of this study. Ludlam (1963) has provided a comprehensive review of the literature to that date. The pertinent features of these models will be outlined and more recent models relevant to this study will be reviewed briefly.

1.2.1 Visual Models

Thunderstorm and severe storm models presented prior to World War II were based largely on exterior visual observations as indirect and direct sensing techniques were not available to examine the storm interior. The major features (as summarized from Ludlam; 1963) of these visual models are:

(i) An <u>updraft</u> system which enters the storm along the leading and/or trailing edge and proceeds upward through the storm to its top.

(ii) A spreading anvil cloud which indicates a region of high-level divergence above the major updraft.

(iii) A low-level downdraft with an accompanying meso-scale cold front maintained by the weight of the falling precipitation and/or by the melting and evaporation of precipitation elements.

(iv) A low dark cloud (the storm collar) whose fringes mark the entrance into the storm of an oppositely directed flow at the foot of the updraft.

(v) The presence of mammatus cloud formations which are often observed below the thicker portions of the anvil.

1.2.2 The Byers-Braham Thunderstorm Model

During and after World War II, the advent of radar and aircraft capable of penetrating storms renewed the exploration of the thunderstorm in depth. The Thunderstorm Project, undertaken by the U.S. Weather Bureau during 1946-47 in Florida and Ohio, added significantly to knowledge of the thunderstorm. The project report (Byers and Braham; 1949) did not substantially modify previous storm concepts but did add considerable support with measurements of vertical velocity, temperature and precipitation. The thunderstorm was found to be a complex consisting of smaller units or cells. These cells were found to evolve through three major stages (as illustrated in Fig. 1.2.1):

(i) The Cumulus Stage: This initial stage is characterized by an updraft throughout the depth of the cloud. Precipitation

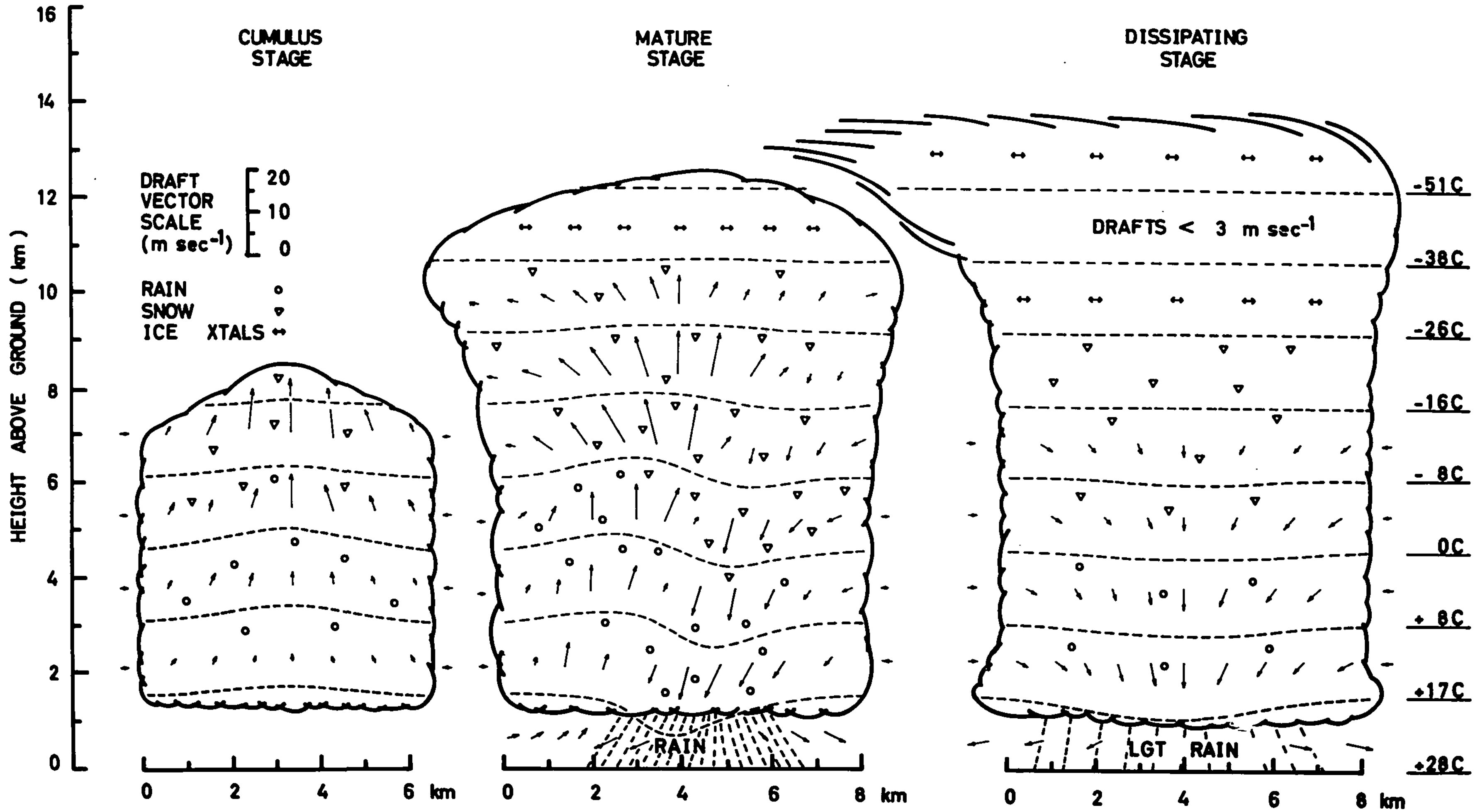

Fig. 1.2.1 Schematic Diagram Illustrating the Three Stages of the Byers-Braham Thunderstorm Model. The Cumulus, Mature and Dissipating Stages of the Byers-Braham Thunderstorm Model are illustrated with draft vectors and characteristic precipitation elements indicated. In the Cumulus stage the cloud is characterized by an updraft throughout its entire depth. The Mature stage is marked by the onset of a rain-induced downdraft on the upwind side of the storm. This downdraft spreads to occupy the entire storm in the Dissipating stage.

forms abruptly at mid-levels.

(ii) The Mature Stage: The updraft continues to exist throughout the cloud depth, but a rain-induced downdraft begins on the upshear side with rain extending through to the ground.

(iii) The Dissipating Stage: As the cold downdraft spreads out beneath the storm, the updraft weakens. Shortly, the updraft disappears and downdraft occupies the whole cell. Eventually the downdraft weakens and dissipates.

It must be noted that the observations of the Thunderstorm Project are typical of thunderstorms in Florida and not necessarily representative of severe storms. Consequently, the Byers-Braham model applies to the short lived cellular storm which does not produce hail of sufficient size to reach the ground. That both types of storm exist is an established fact. Although they differ in size, duration and intensity, the energy sources and precipitation mechanisms must be similar in each type of storm.

1.2.3 Severe Storm Models

A comprehensive study of a severe storm, which occurred near Wokingham, England on 9 July 1959, by Browning and Ludlam (1960, 1962) is one of the most complete single storm analyses made to this date. Utilizing data from five radars, serial radiosonde ascents, a research aircraft and dense surface weather and precipitation observations, it was possible for Browning and Ludlam to postulate an airflow and hailstone growth model for the Wokingham storm. On 4 May 1961, a storm similar in structure to the Wokingham storm was observed near Geary, Oklahoma. Donaldson (1962) published a preliminary analysis of this storm which was furthered by Browning and Donaldson (1963) to include a qualitative airflow model for this storm. A voluminous study of a storm family which occurred in Oklahoma on 26 May 1963 has also been reported by Browning (1965).

Although each severe storm studied and reported by Browning has had its individual characteristics, there are essential similarities which are embodied in the Browning SR (Severe Right) model. The essential characteristics of Browning's observations and qualitative airflow and precipitation model are outlined below.

A. Observed SR Storm Characteristics

(i) Wind structure and direction of storm travel: The wind structure characteristically veers and increases with height (as shown in Fig. 1.2.2) such that low-level winds have a component toward the storm, mid-level winds are from the RH flank and high-level winds have a component away from the storm in the downwind direction (see Fig. 1.2.2). In relation to the low and mid-level winds, the severe storms studied by Browning have been found to travel to the right of the winds (see Fig. 1.2.2).

(ii) Storm reflectivity structure: Three related reflectivity features characterize the SR storm; an overhang, an echo-free vault (or vault) and a hook echo (see Fig. 1.2.3). The overhang is an extensive overhanging echo on the storm's right flank which slopes downward to the ground toward its left flank. A region of low reflectivity at low levels, which extends from the right flank into the heart of the storm and penetrates upward for some distance beneath the storm's highest top, is known as the echo-free vault or vault. The hook echo (referred to in the Wokingham storm as a wall) is a hook-shaped appendage, which surrounds the vault at low levels on the storm's right rear flank.

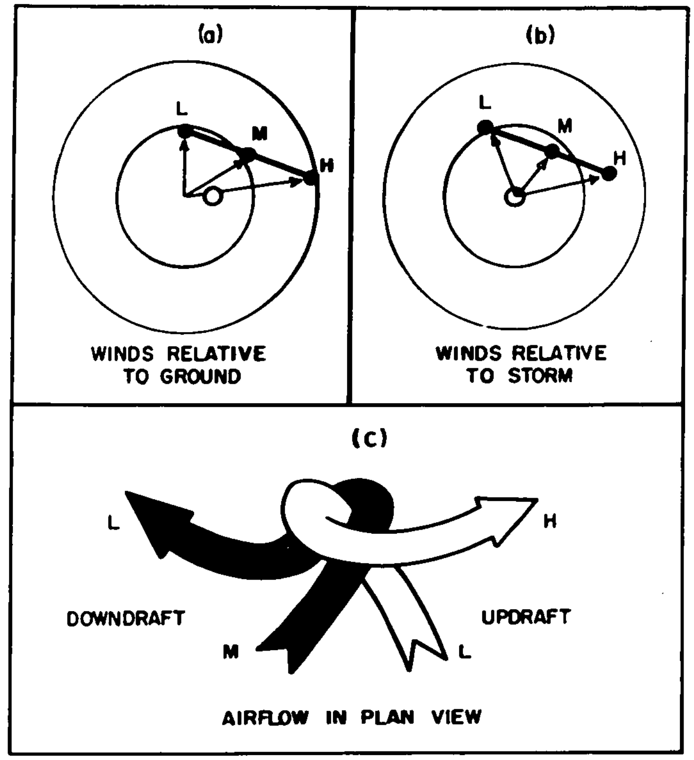

Fig. 1.2.2 Wind Hodographs and Airflow in an SR Storm (after Browning). L, M and H represent wind velocity vectors in the low, middle and high levels. The storm velocity is denoted by an open circle.

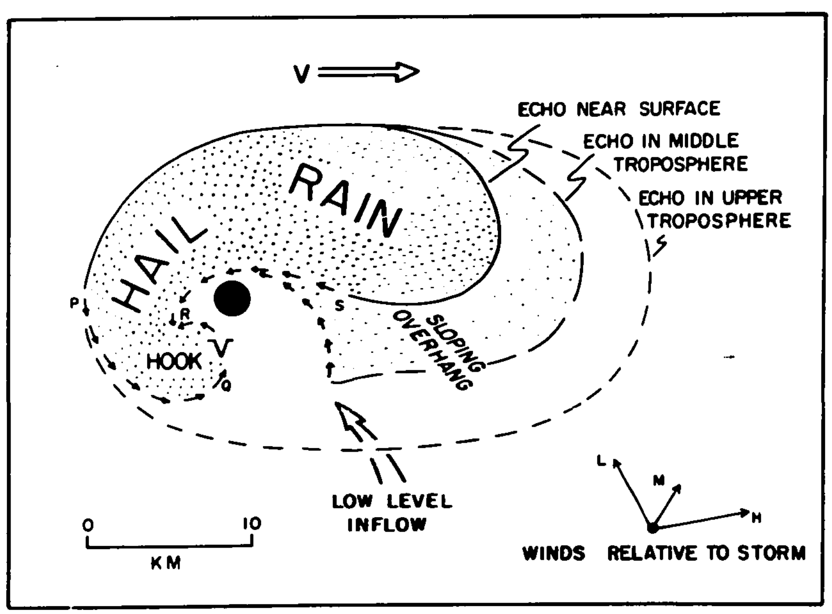

Fig. 1.2.3 Schematic Diagram Showing Horizontal Sections Through an SR Storm Supercell (after Browning). The heavy black spot marks the position of the highest echo top and the vault at lower levels. When a tornado occurs, it is situated near the leading edge of the hook echo. Hail falls from the echo surrounding the vault, and occasionally from below the hook.

(iii) Steady-state structure: Observations of the storm top indicate rather minor fluctuations in the maximum storm top over periods of 45 min to 2 hr. Echo-free vaults are found beneath the maximum storm top during this time, indicating that the airflow tends toward a steady-state circulation.

B. Airflow Characteristics in the Browning SR Storm Model

(i) Inflow: As depicted in Fig. 1.2.4, warm air at low levels approaches the storm from the right forward quadrant, while converging, to enter the storm updraft system.

(ii) Updraft: The updraft system (see Fig. 1.2.4) is inclined toward the rear of the storm at low levels, becomes more vertical in the central section and is rapidly sheared in the downwind direction at the storm top. Browning postulates that the air in the updraft turns counterclockwise through 270 deg as it ascends through the updraft system, leaving the storm in the direction of the high-level winds.

(iii) Outflow: The air at the summit of the updraft diverges in all directions before being carried downshear by the high-level winds.

(iv) Downdraft: Dry air at mid-levels approaches the SR storm from the right flank (see Fig. 1.2.2). Small precipitation particles from the overhang evaporate into this air making it negatively buoyant to induce a downdraft on the downshear side of the updraft. This downdraft air must leave the storm predominantly toward the left rear flank diverging in all directions.

C. Precipitation Trajectories in the Browning SR Storm Model

Figure 1.2.4 illustrates the trajectories of precipitation particles (of millimetric size) which are released near the summit of the updraft above

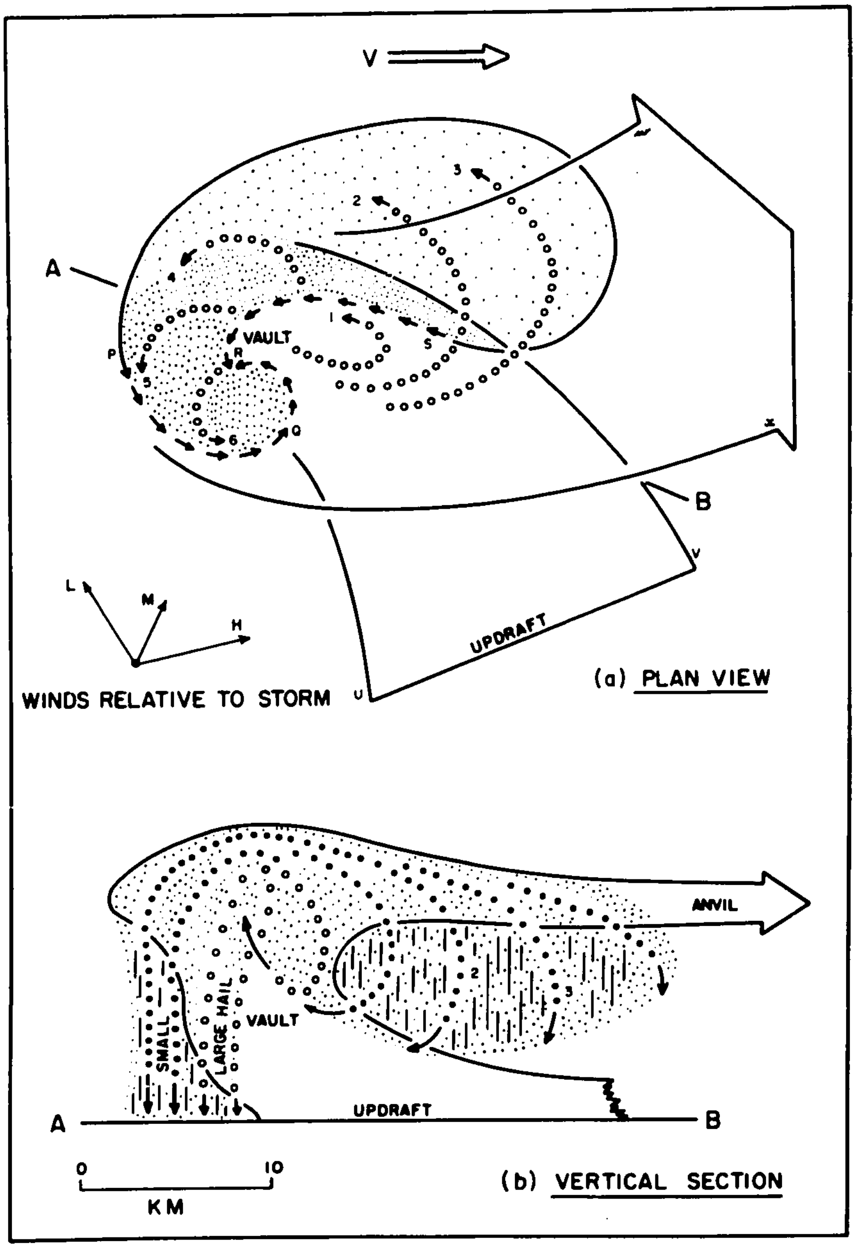

Fig. 1.2.4 Schematic Horizontal and Vertical Sections Illustrating Precipitation Trajectories in an SR Storm (after Browning). The extent of the updraft is represented by solid curves; precipitation trajectories are denoted by dotted curves. In (a), the extent of rain and hail close to the surface is shown by light and heavy shading respectively, and the arrows around PQRS indicate the direction of motion of protuberances on the edge of the low-level radar echo. AB is oriented in the direction of the mean wind shear, into which the updraft is inclined at low and medium levels. In (b), the presence of downdrafts with strong normal components of motion is indicated by vertical hatching. On the downshear side of the updraft (right side of page) these components are directed into the page; beneath the updraft on its upshear side they are directed out of the page.

the vault. Trajectories 1, 4, 5 and 6 are for hailstones just large enough to descend through the edges of the updraft where the updraft is comparatively weak. Larger hailstones follow similar trajectories descending closer to the vault through regions of stronger updraft. With a tilted updraft, the possibility of hailstones re-entering the updraft and growing while ascending (re-cycling) exists. The larger the hailstone, the higher must be its re-entry point in the updraft. Such hailstones grow to the largest sizes to descend to the ground close to the vault.

In addition to Browning's work there are numerous other studies of significance. A hailstorm near Cheyenne, Wyoming, photographed from a C-130 aircraft by Cunningham (1959), prompted a hailstorm model based on photogrammetric analysis by Fujita and Byers (1962). This storm was similar to the severe storms studied by Browning, existing in a highly sheared environment and exhibiting a storm top with only minor fluctuations. On the basis of volumetric analysis, the average storm updraft was computed to be 20 m sec^{-1}.

Studies by Fankhauser (1967) and Haglund (1969) also document severe storms which are similar to Browning's SR model. As Browning has indicated, however, the SR storm model applies to only one class of severe storms. In a study of echo motions on 27 July 1956, Hitschfeld (1959) found evidence of a splitting echo with the two fragments moving at an angle as large as 50 deg. Hammond (1967), in a study of a left-moving storm, proposed an airflow model which is, essentially, a mirror image of the Browning SR model. Fujita and Grandoso (1968) have postulated a different explanation of the left-moving thunderstorm based on the gradient, coriolis, drag and lift forces acting on a rotating (solid body) thunderstorm. Since no obvious left-moving storms were observed within the ALHAS project area during 1967 and 1968, they have not been considered in this study.

1.3 An Outline of Extended Severe Storm Studies in This Thesis

The study which follows is essentially a study of severe storms; in this respect it is inevitable that it be both inspired and influenced by Browning's prominent work on severe storms. But, it also extends the study of severe storms into areas not previously examined, and establishes more firmly a number of concepts which have been utilized in severe storm studies by Browning and others.

As radar and other meteorological observations are of unequivocal importance in the study of severe storms, they have been utilized extensively in this thesis to diagnose the structure, character and motions of four severe storms. But, in addition to this observational study, the cloud physical processes which transpire within the core of a severe storm updraft have also been modelled. Particular emphasis has been put on the effects which these cloud physical processes have on radar observable features. This parallel study has been accomplished by treating specific storms. The feedback which results has influenced both the assumptions and estimates used for the cloud physical models and the interpretation of the radar observations. This technique has resulted in a relatively complete and consistent examination of a series of Alberta severe storms in a manner not previously accomplished.

The thesis is logically divided into four distinct parts. Chapters II - V constitute the first part, dealing with the observed characteristics of four severe storms in Alberta. In a study such as this one faces a dilemma; whether to present on the one hand specific cases, or on the other hand averages for a large group. The solution arrived at here has been to present radar case studies of four specific storms, these storms being chosen (from a total of 29 major storm days in 1967 and 1968 for which radar data were available) as represntative of a larger class of severe storms.

The second part (Chapter VI) utilizes aircraft observations, radar observations and the weak echo region (or echo-free region) hypothesis to deduce a simple qualitative airflow model for each of the storms studied in Chapters II - V. In spite of the elegance and simplicity of the Browning SR model, it is clear that there are other important modes of storm operation in Alberta which differ substantially from the SR model.

Having established the existence of a broad, strong, persistent updraft extending from cloud base upward through the severe storm, the third part of this study (Chapter VII) uses a loaded moist adiabatic vertical velocity model to compute estimates of the temperature, liquid water content and vertical velocity in the core of a severe storm updraft. Close agreement between computed storm tops and observed radar storm tops for 29 severe storms lends considerable support to the validity of these estimates.

The fourth and final part (Chapters VIII and IX) treats the growth of precipitation elements within the core of a severe storm updraft. The precipitation growth environment (based on estimates from Chapter VII) and the precipitation growth mechanism for cloud droplets within the updraft core are examined and a simple cloud droplet model deduced. Various possibilities for precipitation growth are considered; the growth of graupel from giant droplets being examined in detail by utilizing a graupel growth model. The resulting radar reflectivity factors are compared with observed values resulting in a verification of the weak echo (or echo-free) region hypothesis.

CHAPTER II

A RADAR CASE STUDY OF THE STORM OF 25 JULY 1968

2.1 Introduction

This chapter and the three chapters which follow consist of radar observational case studies of four Alberta Hailstorms. As will become evident, these storms had both similarities and differences. Two of these storms bore some resemblance to Browning's SR storm model, but even they differed in detail.

Due largely to the fact that differences in the radar observed features were found between the Browning SR storms and the Alberta severe storms studied here, a number of new terms have been introduced to describe these features. These terms are related to the echo-free vaults which Browning found in the severe storms he studied.

First it is necessary to consider the composition of the echo-free vault structure. It is proposed that Browning's echo-free vaults and similar structures found in Alberta severe storms are scattering volumes which consist of freshly-formed cloud droplets ($D \simeq 5 - 30\ \mu$) in adiabatic water concentrations. In addition, it is proposed that these echo-free vaults are coincident with the updraft core of a severe storm, and are the result of the high vertical velocities (and therefore brief residence times) which air parcels and the accompanying cloud droplets experience in the updraft core. The brief residence times (less than 10 min) do not permit the growth of cloud droplets to sizes detectable by conventional weather radars (3 - 10 cm wavelength). This proposal will be referred to as the Weak Echo Region Hypothesis and will be examined in detail in Chapters VIII and IX.

Although an echo-free vault consisting of micron-size droplets may be free of echo as seen by a conventional weather radar, it is not free of all radar echo. Calculations indicate that equivalent radar reflectivity factor (Z_e) values of the order of 10^{-3} - 10^{-1} mm^6 m^{-3} would be found in the updraft core of a severe storm. Echo regions with Z_e values of this order could be detected by short wavelength radar, and at close range might also be detected by 3 cm radars and by high power, high sensitivity 10 cm radars. Consequently, since the very existence of an echo-free region is largely a function of the sensitivity of the radar used, such regions will instead be referred to in this study as <u>weak echo regions</u>.

The term "echo-free vault" used by Browning is indeed descriptive of the storms which he studied. However, a definite structure is implied by the word "vault" (see Section 1.2.3). Several of the Alberta severe storms studied here exhibit weak echo regions which are open on one or more sides and therefore do not qualify as vaults. A weak echo region is normally recognized (in plan view) by the existence of a radar echo boundary around a portion (or all) of the weak echo region. In the case where this boundary exists (in plan view) in completion around the weak echo region, the weak echo region will be referred to as a bounded weak echo region (abbreviated BWER). Conversely, cases where the weak echo region is not bounded by a radar echo or only partially bounded (in plan view) by echo will be referred to specifically as unbounded weak echo regions (abbreviated UWER). The term weak echo region (abbreviated WER) will be used as a general term when referring collectively to both bounded and unbounded weak echo regions. In this system of terminology, Browning's echo-free vault becomes a bounded weak echo region (BWER).

In the following chapters numerous figures are used depicting radar data. These data were derived from returned power (P_r) measurements obtained from the radar PPI grey-scale display using the Probert-Jones (1962) meteorological radar equation. The derived equivalent radar reflectivity factor (Z_e) values are normally expressed as Z_e ($mm^6\ m^{-3}$) or as $10 \log_{10} Z_e$. Since the measured values of Z_e range from 10^0 to 10^6 $mm^6\ m^{-3}$, they are more conveniently expressed on a dB scale. Such a scale is to be introduced in a forthcoming textbook by P. Smith. As Smith (1970) has indicated, the logical basis for such a scale is 1 $mm^6\ m^{-3}$. Therefore:

$$Z_e\ (\mathrm{dBz}) \equiv 10 \log_{10} \left[Z_e (mm^6\ m^{-3}) \ / \ (1\ mm^6\ m^{-3}) \right] \qquad \text{Defn. 2.1.1}$$

A comparable definition also applies to the radar reflectivity factor (Z). A Z_e value of 10^4 $mm^6\ m^{-3}$ now becomes 40 dBz, and 2×10^2 $mm^6\ m^{-3}$ may be expressed as 23 dBz.

2.2 Airmass and Wind Structure in the Vertical

A radiosonde sounding taken at the radar site at 1615 MST (illustrated by the tephigram in Fig. 2.2.1) exhibits a moderately warm maritime Polar airmass with a minor subsidence inversion at 550 mb. This sounding, representative of the airmass in which the severe storms of 25 July 1968 occurred, illustrates that the airmass was indeed unstable. Using representative cloud base conditions, a moist adiabatic parcel trajectory (taking account also of adiabatic liquid water loading) shown in Fig. 2.2.1 indicates that maximum cloud tops of approximately 10.3 km would be possible. The "positive area" (area between parcel trajectory and environment curve) exhibited by this tephigram is relatively small. As a consequence, the buoyant forces would not be expected to produce an updraft of high velocity. It will be shown in Chapter VII that this was indeed a storm of relatively low energy, a

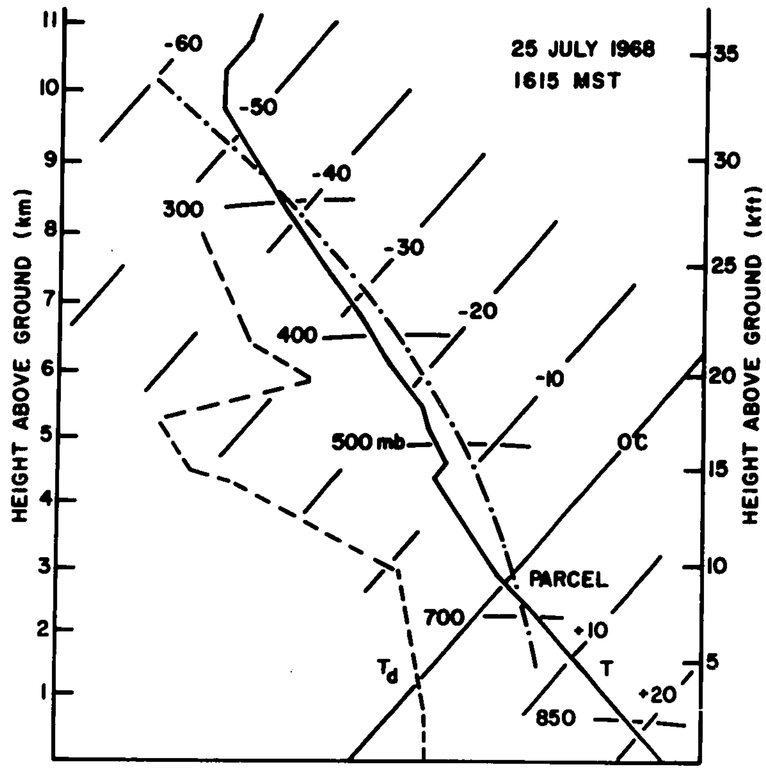

Fig. 2.2.1 Radiosonde Sounding 1615 MST - 25 July 1968. Dot-dash line indicates a moist adiabatic parcel trajectory using representative cloud base conditions. A minor subsidence inversion appears at 550 mb. Note the relatively small "positive area".

maximum vertical velocity of only 19.1 m sec^{-1} being computed for its updraft core.

The wind structure in the vertical at 1615 MST is shown by the hodograph in Fig. 2.2.2. It is immediately obvious that this storm did not exist in a highly sheared environment. However, it is interesting that the winds in the sub-cloud layer are from the northeast and north, continuing to back with height up to 11 km. The resulting wind hodograph is almost a direct opposite to the pattern described by Browning for an SR storm (see Fig. 1.2.2). This environmental wind structure and its effect on the storm airflow will be discussed in detail in Chapter VI.

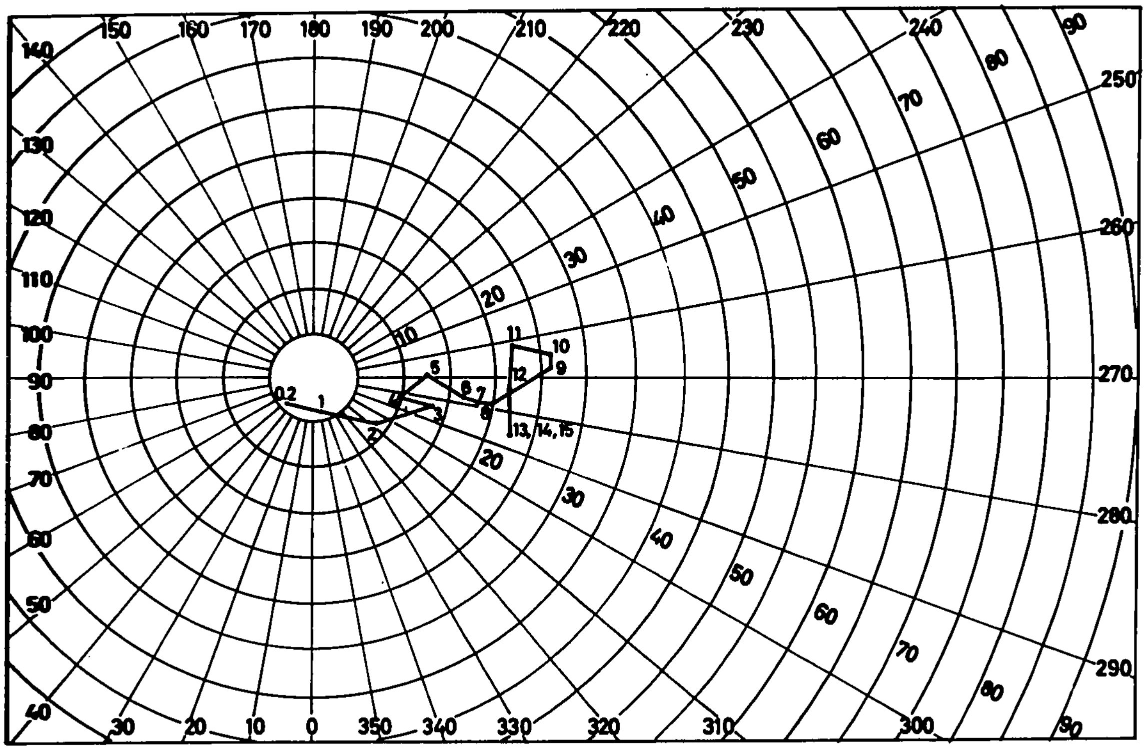

Fig. 2.2.2 Wind Hodograph 1615 MST - 25 July 1968. Wind speeds are plotted in m sec^{-1} and heights are indicated in km AGL. Note north and northeasterly winds near the surface and backing of the winds with height.

2.3 The History of the Storm of 25 July 1968

The storm of 25 July 1968 was first detected by radar at maximum range at 1720 MST, 128 km NW of the radar site. It was evident that the storm was in an advanced stage of development, and had probably begun in the foothills NW of Penhold, out of radar range. By 1820 MST, it was apparent that the storm was a squall line consisting of a series of cells which extended northward out of radar range. The squall line moved eastsoutheastward, developing new cells on its south end or RH flank[1] to pass over the radar site at

[1]In referring to directions with respect to a severe storm, the convention is adopted that one is at the center of a coordinate system fixed to the storm, facing in the direction of storm motion. Thus, for an eastward moving storm, the south side or flank becomes the RH side or RH flank and the north side or flank is referred to as the LH side or LH flank of the storm. The east side of an eastward moving storm is commonly referred to as the downwind side or downshear side of the storm and the west side is the upwind or upshear side.

approximately 2010 MST. Preceding the arrival of precipitation was a gust front which reached the radar site at approximately 1945 MST. By 1952 MST, the wind was sufficiently strong so as to curtail radar operation until after 2030 MST. Upon resuming radar operation, it was clear that the storm was not as intense as it had been prior to 1952 MST; and by 2050 MST the storm had begun to dissipate east of the radar site, spreading into a widespread area of light precipitation. Very light rain from the storm fell at the radar site until approximately 2230 MST, some 2 1/4 hr after the storm cell had passed over the radar site. A bright band phenomenon was observed in this light precipitation echo, indicating that the light rain which followed the storm resulted from ice crystals falling from the extensive anvil system associated with this storm. By 2250 MST, only small patches of echo were evident south and east of the radar site indicating the end of the severe storm of 25 July 1968.

In addition to radar observations, the University of Wyoming C-45H aircraft obtained vertical velocity measurements at cloud base in the inflow-updraft region of this storm. Aircraft-measured cloud base vertical velocities are available for the period 1840 - 2004 MST, and radar observations are available up to 1952 MST. Consequently, it will be the period 1840 - 1952 MST which will be considered in detail in this study. Although this period does not represent the complete storm duration, fortuitously it was during this period that the storm was at close radar range and also in its most intense phase.

Figure 2.3.1 illustrates the maximum Z_e envelope for the period 1846 - 1952 MST. It depicts (at any given location) the maximum Z_e value (dBz) which passed over that location at 0 deg elevation during the period 1846 - 1952 MST. As this is a time-integrated representation of the storm, it is useful in delineating the paths of the intense storm cells.

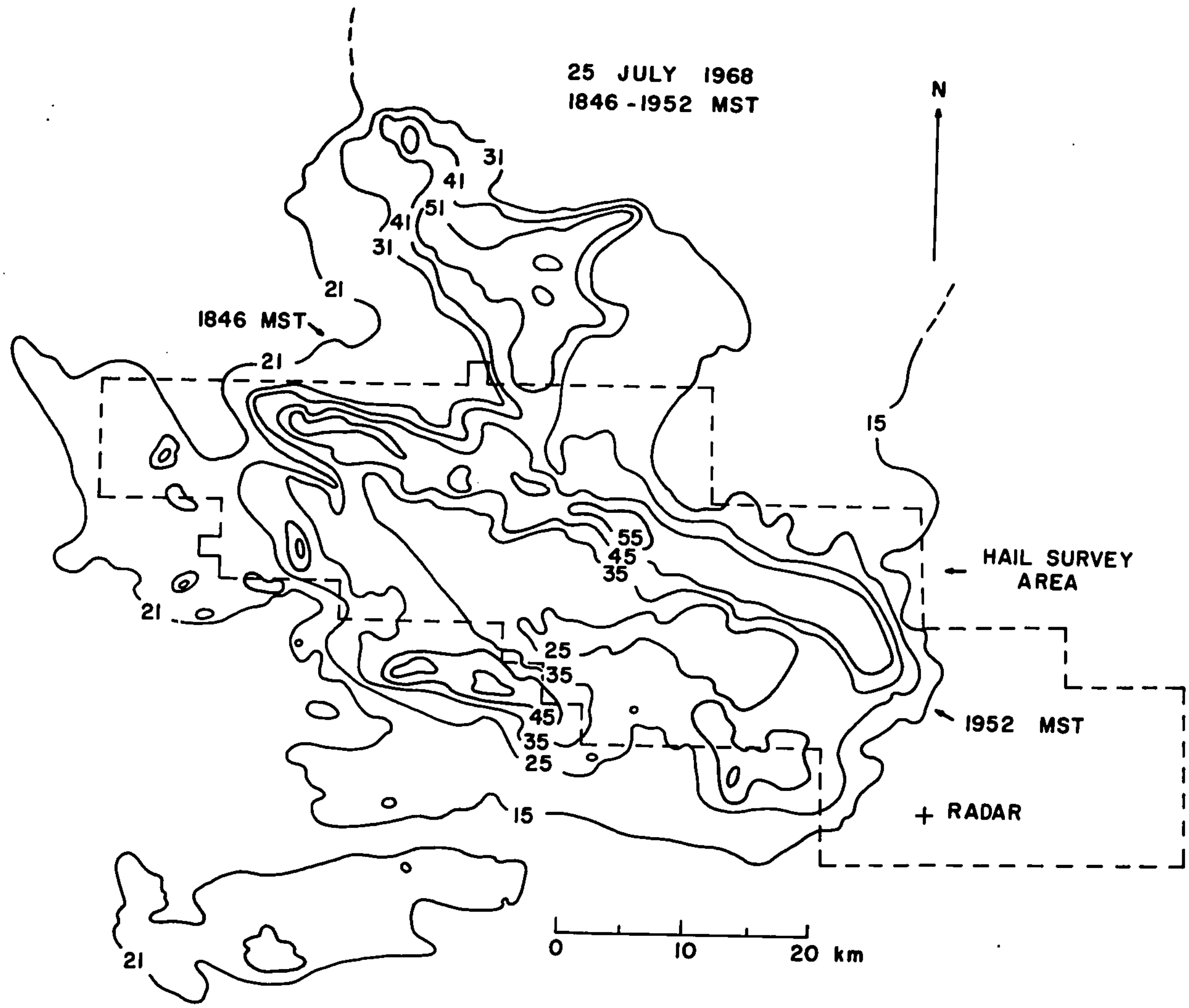

Fig. 2.3.1 Maximum Z_e Envelope 1846 - 1952 MST - 25 July 1968. The envelope of maximum Z_e values (dBz) at 0 deg elevation is shown for the period 1846 - 1952 MST. A telephone hail survey was conducted within the area inside the dashed outline.

It is evident from Fig. 2.3.1 that, even in the restricted southern segment of this squall line, there were several major storm cells. The largest and most intense of these cells was in an advanced stage of development at 1846 MST and persisted beyond 1952 MST. It travelled eastsoutheastward to pass approximately 10 km north of the radar site. Maximum Z_e values along the axis of this storm cell exceeded 50 dBz. However, since the radar was operated at maximum sensitivity (after 1923 MST) the 40 dB range of the five grey-scale levels was unable to depict the complete range of received radar

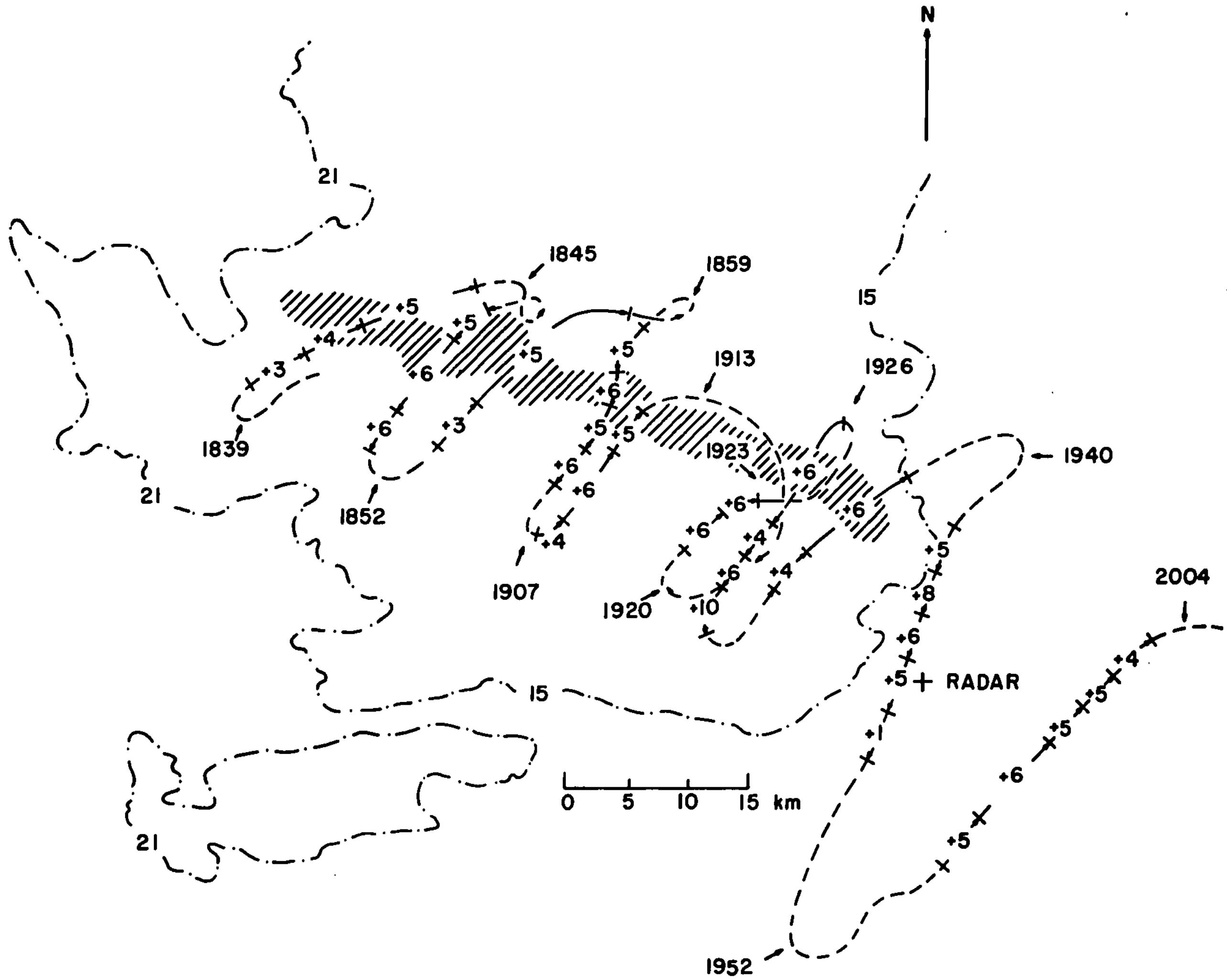

Fig. 2.3.2 Aircraft Track and Vertical Velocity Measurements at Cloud Base 1839 - 2004 MST - 25 July 1968. The dot-dash outline delineates the outer Z_e maximum contour as in Fig. 2.3.1 with contours labelled in dBz. Regions where Z_e values (at 0 deg) exceeded 40 - 45 dBz are indicated by diagonal hatching. The aircraft track during the period 1839 - 2004 MST is shown and vertical velocity measurements at cloud base are indicated in m sec^{-1}. Note the relation between the updraft zone and the maximum Z_e values.

echo. Consequently, it is possible that maximum Z_e values attained levels considerably higher than 50 dBz.

The flight path of the University of Wyoming aircraft (with respect to the ground) between 1839 and 2004 MST is shown in Fig. 2.3.2. A continuous, uniform, laminar updraft approximately 6 km wide (E-W) and 18 km long (N-S) was found to persist close to the downwind side of the storm precipitation.

Flight procedure was such that the aircraft was flown in the inflow-updraft area ahead of the precipitation and normal to the direction of storm motion. When the updraft weakened to less than the threshold of detectability, the aircraft executed a 180 deg turn and returned along a parallel path. Thus the extent of the aircraft track in Fig. 2.3.2 also depicts the breadth of the updraft zone.

The vertical velocities in the updraft were measured using a technique outlined by Auer and Sand (1966) and are considered accurate within ± 1 m sec^{-1}. It is clear from an examination of Fig. 2.3.2, that the updraft zone measured by the aircraft was associated with the most intense storm cell. A continuous updraft associated with this storm cell was evident from 1839 MST until after 2004 MST. Vertical velocities during this time were typically 4 - 6 m sec^{-1}, with a maximum vertical velocity of 10 m sec^{-1} at 1930 MST. Evidence that this broad, continuous updraft originated near the surface was supplied by the fact that smoke plumes from piles of burning brush were observed to rise and move into the updraft region along the downwind side of the storm. In addition, the smell of the wood smoke was detected by observers on board the aircraft at flight level just below cloud base. A vertical profile of the updraft was obtained after 2000 MST between cloud base ($\approx$ 1.5 km AGL) and a point 0.6 km above ground. At cloud base the vertical velocity was 5 m sec^{-1}, decreasing in magnitude downward from cloud base to decay into isolated updraft "fingers" with a vertical velocity of 3 m sec^{-1} at 0.6 km above ground. The location of the updraft zone with respect to the radar echo at a given time will be considered in the following section.

2.4 The Storm Reflectivity Structure in Three Dimensions

A close examination of the storm features responsible for the major Z_e maximum swath, depicted in Figs. 2.3.1 and 2.3.2, reveals not one but two

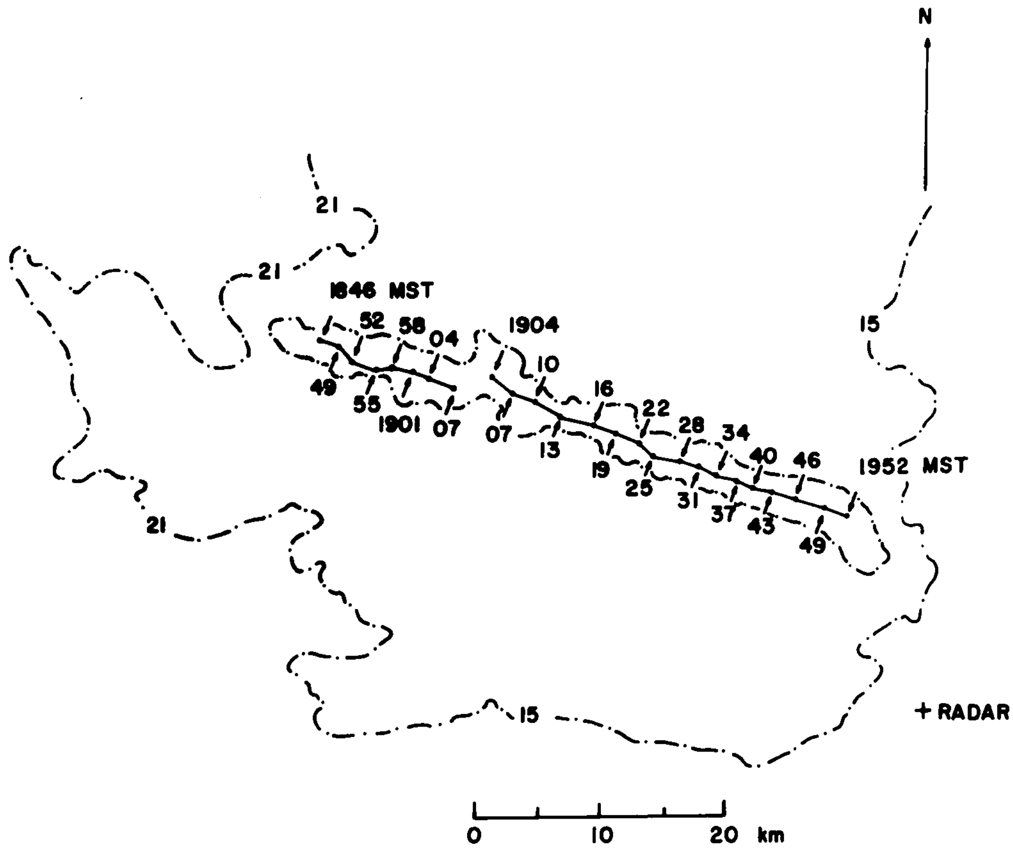

Fig. 2.4.1 Z_e Maximum Cell Tracks 1846 - 1952 MST. Cell tracks of two Z_e maxima are shown within the Z_e maximum outline. Contours are labelled in dBz and times in MST. Note the appearance of the new cell at 1904 MST.

cellular segments. The tracks of these two Z_e maxima, depicted in Fig. 2.4.1, show that the first Z_e maximum was in existence at 1846 MST and persisted as a recognizable feature until 1907 MST; the second Z_e maximum appeared at 1904 MST and was still visible when radar operations were curtailed at 1952 MST. During this 45 min period, the second Z_e maximum had an average horizontal velocity of 10.8 m sec^{-1}.

It will become evident in the following portions of this section that such Z_e maxima are the surface manifestations of cell-like, columnar structures which exist throughout the depth of the storm. The top of one of these cells is normally the highest detectable point in the storm. Consequently, it is possible to relate the history of the highest radar storm top to the

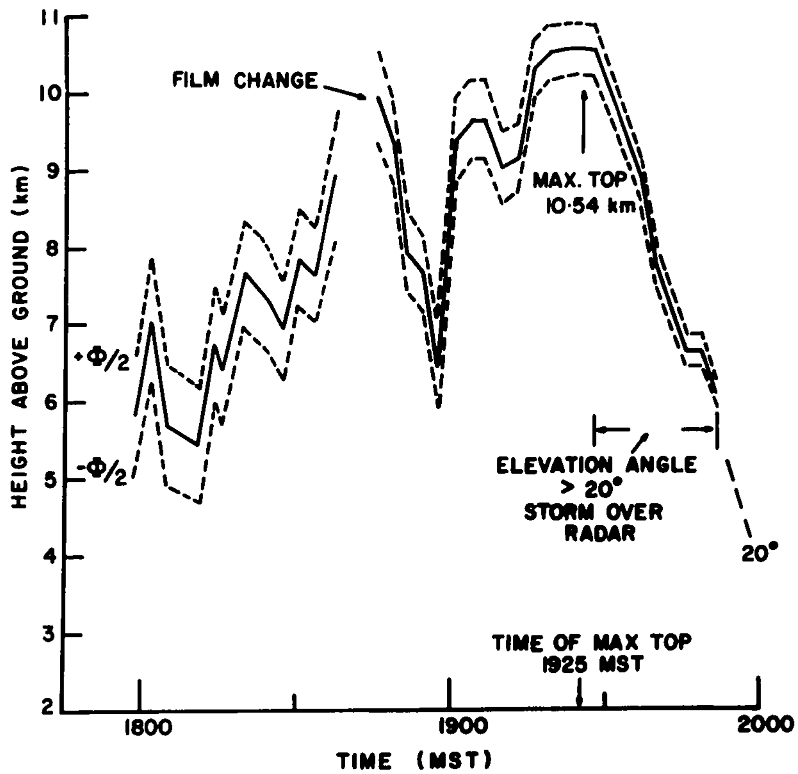

Fig. 2.4.2 Height of Maximum Radar Storm Top vs. Time - 25 July 1968. The height of the radar beam axis at 3 min intervals is indicated by the solid line. Upper and lower half-power beam points (Ø/2, -Ø/2) are delineated by dashed lines. Note maximum at 1846 MST and rapid decrease thereafter to be replaced by second storm top maximum by 1916 MST.

motion and behaviour of the Z_e maximum at the surface. As displayed in Fig. 2.4.2, the radar storm top (associated with the first Z_e maximum) reached maximum height at 1845 MST after which time it subsided indicating the dissipation of the storm cell. Following 1858 MST, a new radar storm top (associated with the new Z_e maximum) appeared as the highest radar storm top. It reached a maximum of 10.54 km at 1925 MST, the top remaining relatively steady. As the storm approached the radar site, the elevation angle of the storm top exceeded 20 deg, precluding a determination of the height of the storm top after 1928 MST. Nonetheless, it is evident that one storm cell did exist continuously from 1904 until after 1952 MST. In order to exhibit the three dimensional structure of this cell and its accompanying features, selected PPI sections and vertical cross-sections (in the direction of storm motion and normal to the direction of motion) will be displayed for 1905, 1925 and 1949 MST.

Figure 2.4.3 consists of a series of selected PPI (Plan Position Indicator) sections at 1905 MST which illustrate the major features of the storm structure. The contours represent constant values of returned power (P_r), labelled with the corresponding Z_e value in dBz. Strictly speaking, these Z_e values are correct only at the range given. However the change in corresponding Z_e value across a storm for a given P_r contour is only a few dBz except at very close ranges. Since this study is concerned largely with relative values of reflectivity this effect is of little consequence.

In order that storm dimensions may be compared from storm to storm, the PPI section in this Chapter and the following three Chapters are presented in the same scale. Due to the large horizontal dimensions of the storm of 25 July 1968, it has been necessary to divide the PPI sections for this storm into two figures.

There are four basic features of the storm structure exhibited in Fig. 2.4.3 and the vertical cross-sections (Figs. 2.4.4 and 2.4.5) accompanying it. The first is the $\underline{Z_e}$ __maximum__ which appears at 0 deg several kilometers NW of the intersection of lines AB and CD. It is possible to follow this Z_e maximum almost vertically from 0 deg to its top at 11 deg. Associated with the Z_e maximum is the second feature, a shelf-like structure or __overhang__ which extends downwind from the Z_e maximum above 3 deg, reaching its greatest horizontal extent at 7 deg. This overhang occurs directly above the __updraft__ measured at cloud base by the University of Wyoming aircraft. Between cloud base and the base of the overhang exists an updraft region which appears to be composed of freshly-formed cloud droplets, and is not detected by radar. It is bounded (in plan view) on one side only by the sharp reflectivity gradient

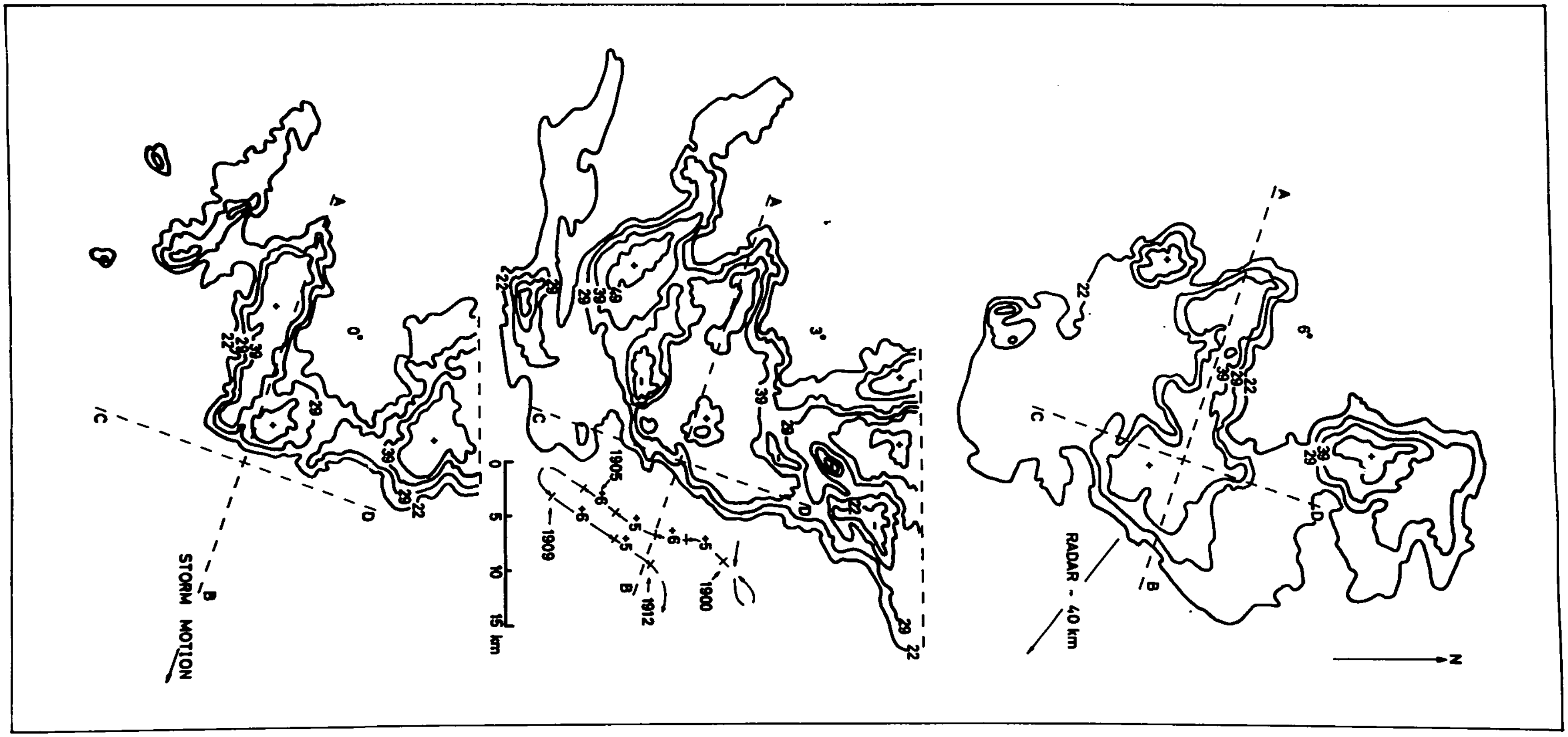

Fig. 2.4.3 Selected PPI Sections at 1905 MST - 25 July 1968. Contours of Z_e are labelled in dBz, and elevation angles indicated in deg. At 3 deg (approximately the same altitude as aircraft) the track of the aircraft is shown with measurements of the vertical velocity in m sec^{-1} indicated. Note the overhang at 6 deg which extends out over the updraft zone.

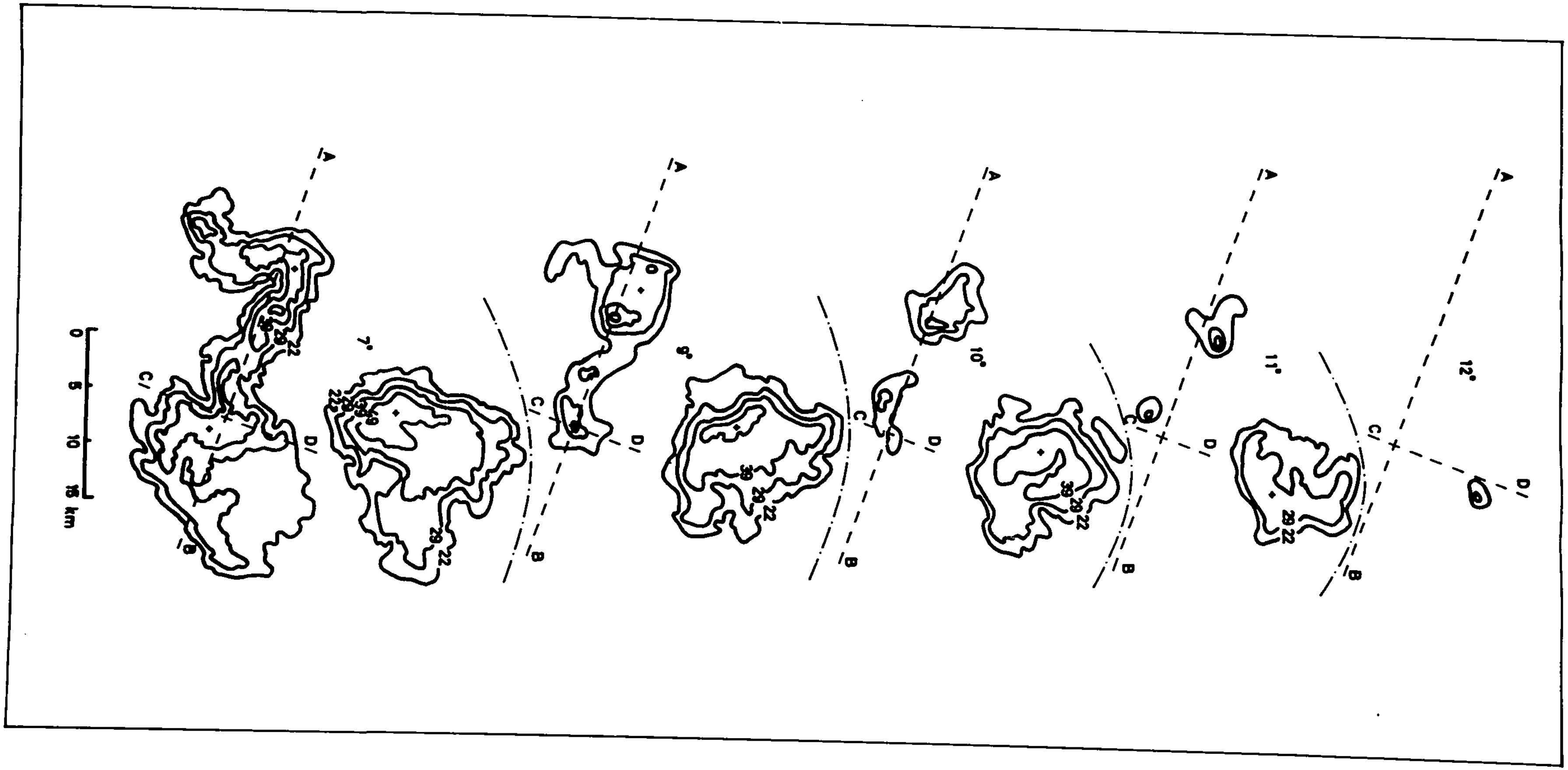

Fig. 2.4.3 (Continued) Selected PPI Sections at 1905 MST - 25 July 1968. Contours of Z_e are labelled in dBz, and elevation angles indicated in deg.

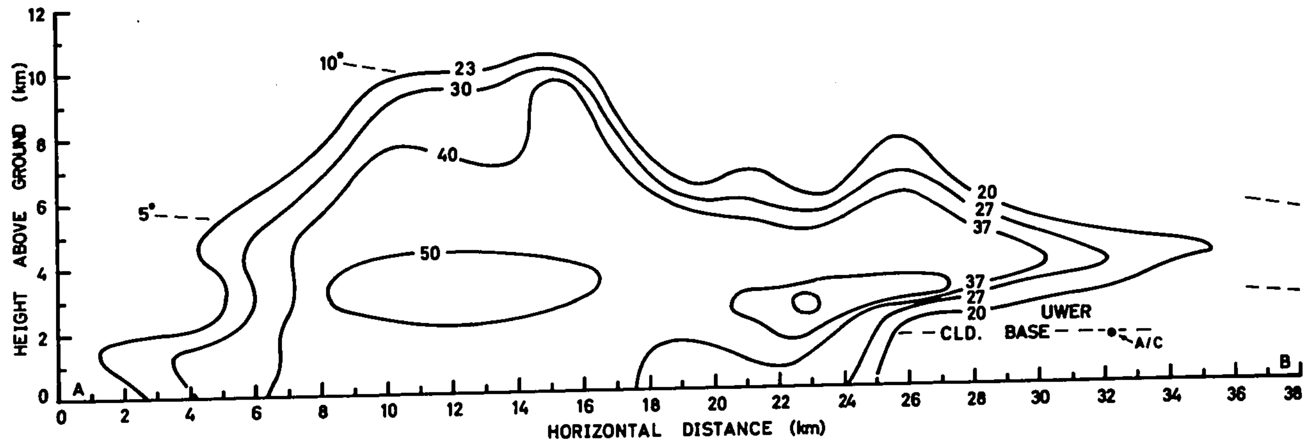

Fig. 2.4.4 Vertical Cross-Section in the Direction of Motion at 1905 MST - 25 July 1968. Contours of Z_e are labelled in dBz. Note the two cellular Z_e maxima and the overhang extending out over the UWER and the updraft at cloud base.

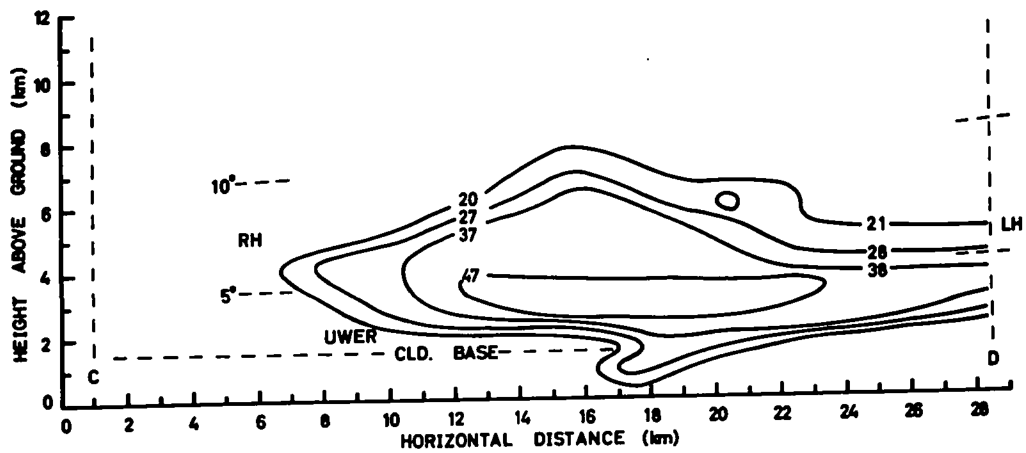

Fig. 2.4.5 Vertical Cross-Section Normal to the Direction of Motion (along CD) at 1905 MST - 25 July 1968. This figure views the storm along line CD (looking upstream) and depicts a portion of the overhang. Contours of Z_e are labelled in dBz.

associated with the Z_e maximum. Consequently, this feature will be referred to as the unbounded weak echo region (UWER).

Vertical velocity measurements obtained just beneath cloud base by the University of Wyoming aircraft are shown in Fig. 2.4.3 at 3 deg elevation (approximately the altitude of the aircraft). The vertical velocity at this time averaged approximately 5 m sec^{-1} over an area of 93 km^2 (5.6 x 16.7 km).

The Z_e maximum, overhang, updraft and UWER are particularly well exhibited in Fig. 2.4.4, a vertical cross-section taken along line AB (in the direction of storm motion) in Fig. 2.4.3. Both Z_e maxima are exhibited in depth in Fig. 2.4.4, although this study is concerned with the Z_e maximum in the downstream position. The overhang extends approximately 10 km downwind from the Z_e maximum and the UWER is found above the aircraft-measured updraft at cloud base.

Figure 2.4.5 is a vertical cross-section along line CD (see Fig. 2.4.3) normal to the direction of storm motion. This figure views the storm in the upstream direction (ie. looking WNW) and the right hand and left hand flanks are labelled RH and LH respectively. What is seen is a cross-section through the broad (22 km wide) shelf-like overhang above the UWER.

It is interesting to point out in Fig. 2.4.3 that a new Z_e maximum has, at this time, begun to form at the southern end of the squall line. The development of this cell will also be outlined briefly at 1925 and 1949 MST.

Twenty minutes later at 1925 MST, a structure similar to that found at 1905 MST is seen in a more advanced stage of development. At this time, the radar storm top has reached its maximum height, and as can be seen in Fig. 2.4.6, the Z_e maximum is also larger in horizontal extent. As before, an overhang

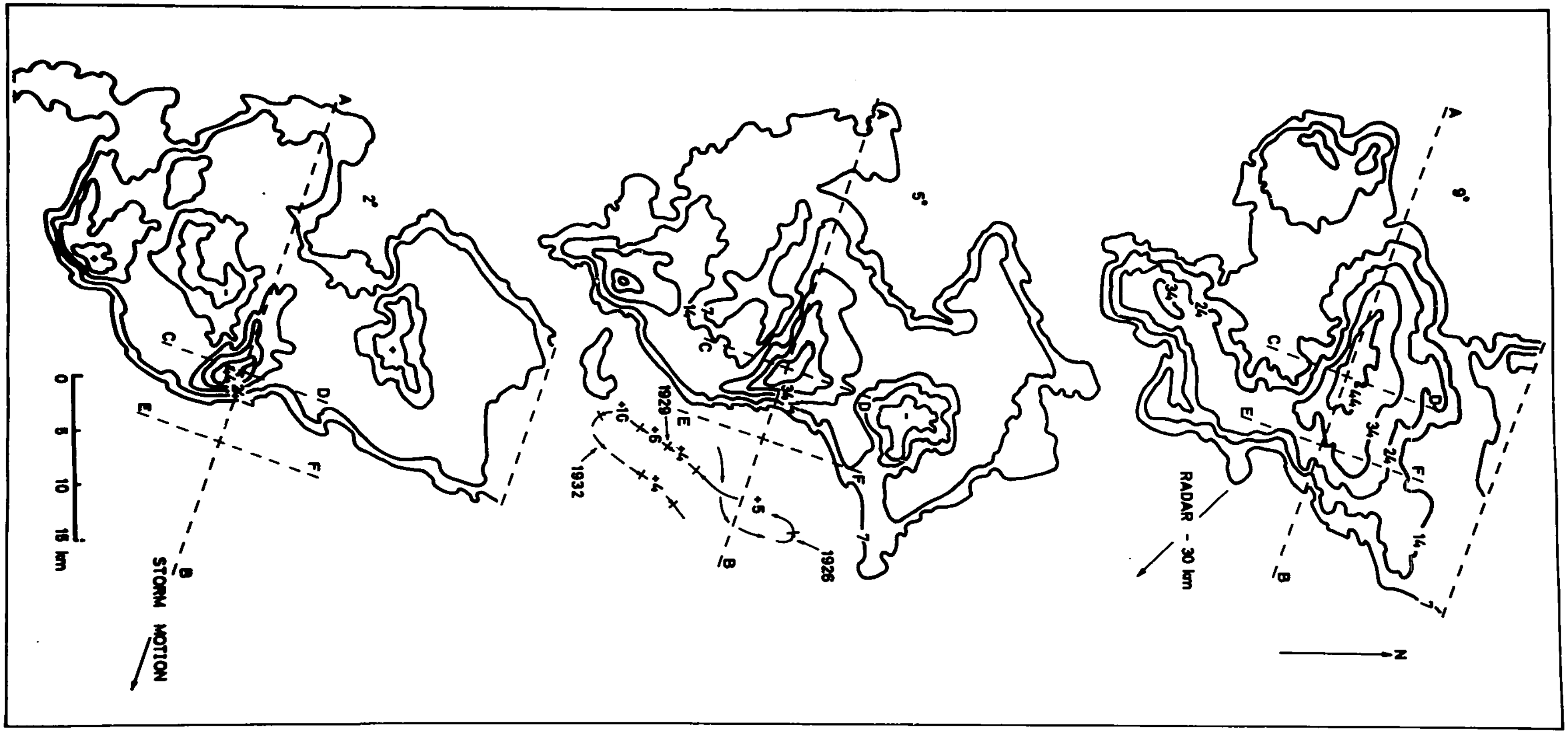

Fig. 2.4.6 Selected PPI Sections at 1925 MST - 25 July 1968. Contours of Z_e are labelled in dBz, and elevation angles indicated in deg. The aircraft track is shown at 5 deg (approximately the same altitude as the aircraft) with measurements of the vertical velocity in m sec^{-1} indicated. Note the well-developed Z_e maximum plus the overhang which extends out over the aircraft measured updraft zone.

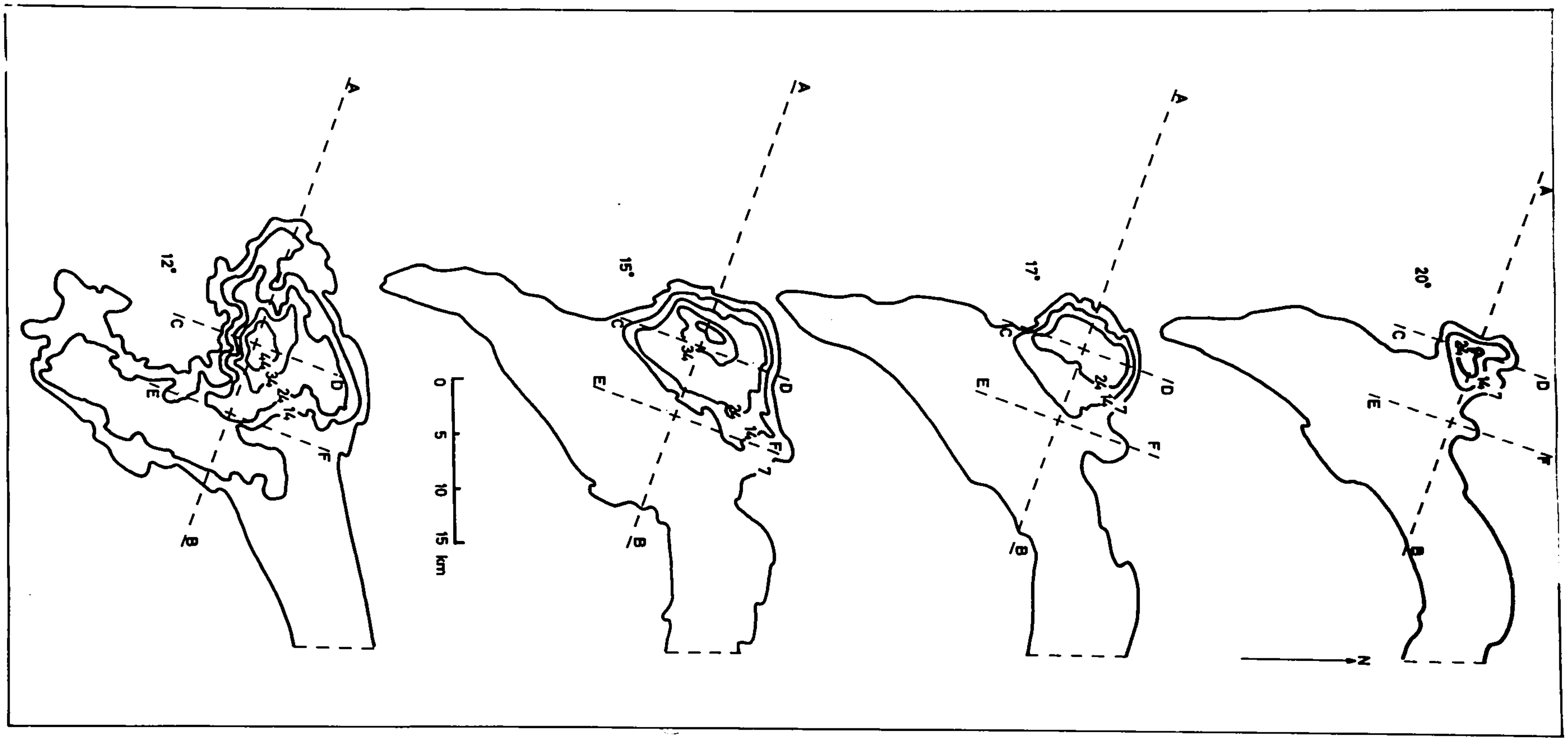

Fig. 2.4.6 (Continued) Selected PPI Sections at 1925 MST - 25 July 1968. Contours of Z_e are labelled in dBz and elevation angles indicated in deg. Note the well-developed Z_e maximum.

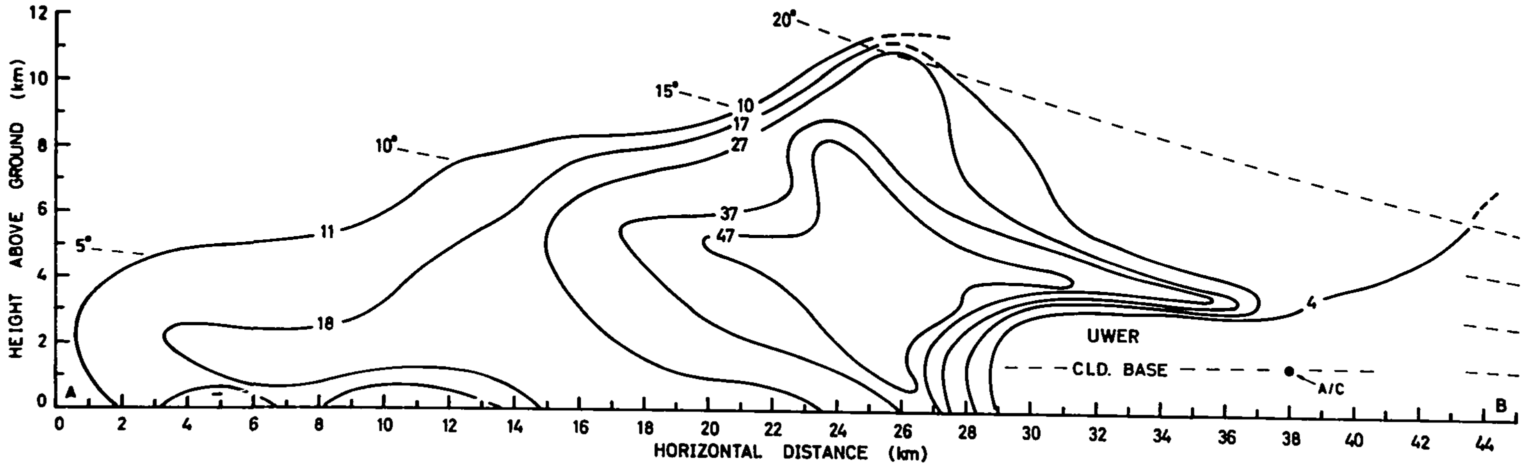

Fig. 2.4.7 Vertical Cross-Section in the Direction of Motion at 1925 MST - 25 July 1968. Contours of Z_e are labelled in dBz. Note the well-developed Z_e maximum and the overhang which extends over the UWER and the cloud base updraft.

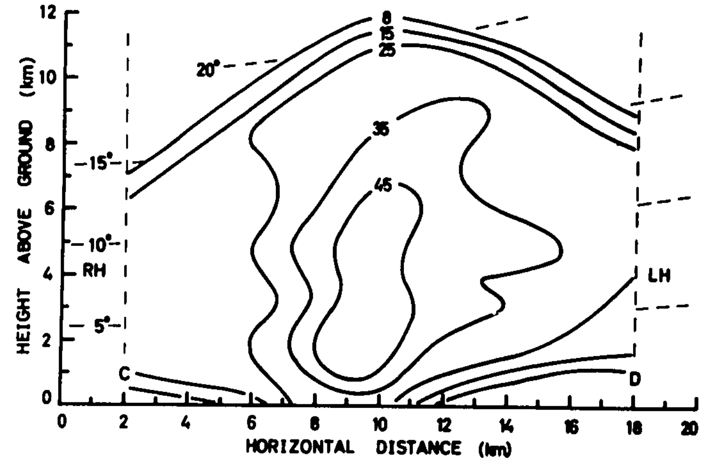

Fig. 2.4.8 Vertical Cross-Section Normal to the Direction of Motion (along CD) at 1925 MST - 25 July 1968. This figure views the storm along line CD (looking upstream). Contours of Z_e are labelled in dBz. Note the vertically oriented Z_e maximum.

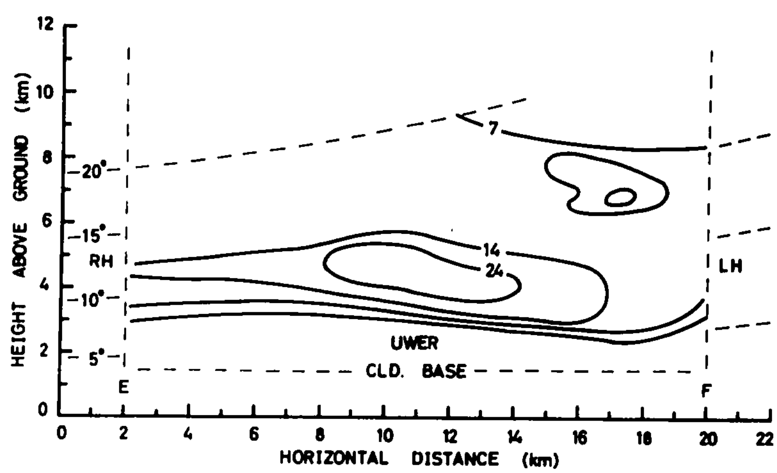

Fig. 2.4.9 Vertical Cross-Section Normal to the Direction of Motion (along EF) at 1925 MST - 25 July 1968. This figure views the storm along line EF (looking upstream). Contours are labelled in dBz. Note the broad, shelf-like overhang above the UWER.

extends out over the UWER and updraft region above 8 deg.

Vertical velocities measured just below cloud base at this time averaged 6 m sec^{-1} over an area of 104 km^2 (5.6 x 18.5 km). Toward the southern end of the aircraft flight path a maximum vertical velocity of 10 m sec^{-1} was experienced. It is possible this was in association with the rapidly developing new cell on the southern end of the squall line.

The vertical cross-section along line AB (see Fig. 2.4.6) in the direction of storm motion shown in Fig. 2.4.7 illustrates clearly the major Z_e maximum with an extensive overhang reaching downwind out over the UWER and cloud base updraft. It is evident from this figure that the highest radar storm top is displaced to the rear of the cloud base updraft and is almost directly above the surface position of the Z_e maximum. This vertical structure of the Z_e maximum is also exhibited in the plane of CD shown in the vertical cross-section in Fig. 2.4.8. Moving downwind, the shelf-like overhang is again seen in Fig. 2.4.9, viewed in the upstream direction along line EF.

At 1949 MST, the cellular structure exhibited at 1905 and 1925 MST was still in existence and showing no signs of weakening. The selected PPI sections shown in Fig. 2.4.10 illustrate the same basic features; a well developed Z_e maximum accompanied by its overhang, UWER and cloud base updraft. These features are also exhibited in Fig. 2.4.11, the vertical cross-section in the direction of storm motion along line AB (see Fig. 2.4.10). A portion of the overhang is exhibited in Fig. 2.4.12, the vertical cross-section normal to the direction of motion along line CD. As the storm was close to the radar site at this time, it is not possible to view the storm in depth. Nevertheless, it is significant that at this close range the radar was capable of detecting Z_e values as low as 0 dBz, and yet still a UWER is found to exist as high as 2 km above cloud base.

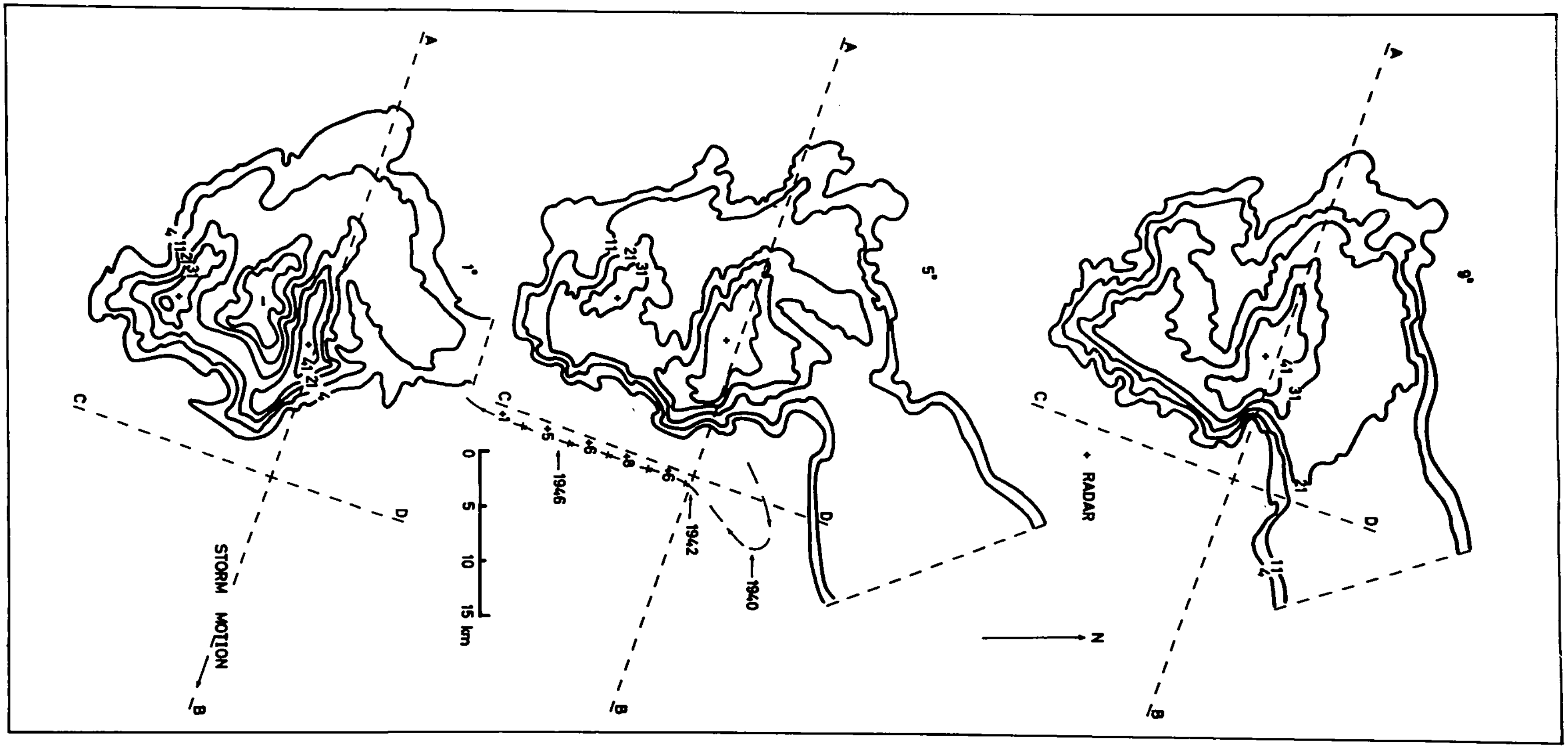

Fig. 2.4.10 Selected PPI Sections at 1949 MST - 25 July 1968. Contours of Z_e are labelled in dBz, and elevation angles indicated in deg. Aircraft-measured vertical velocities are given in m sec^{-1}. Note the development of the new cell on the southern boundary of the squall line.

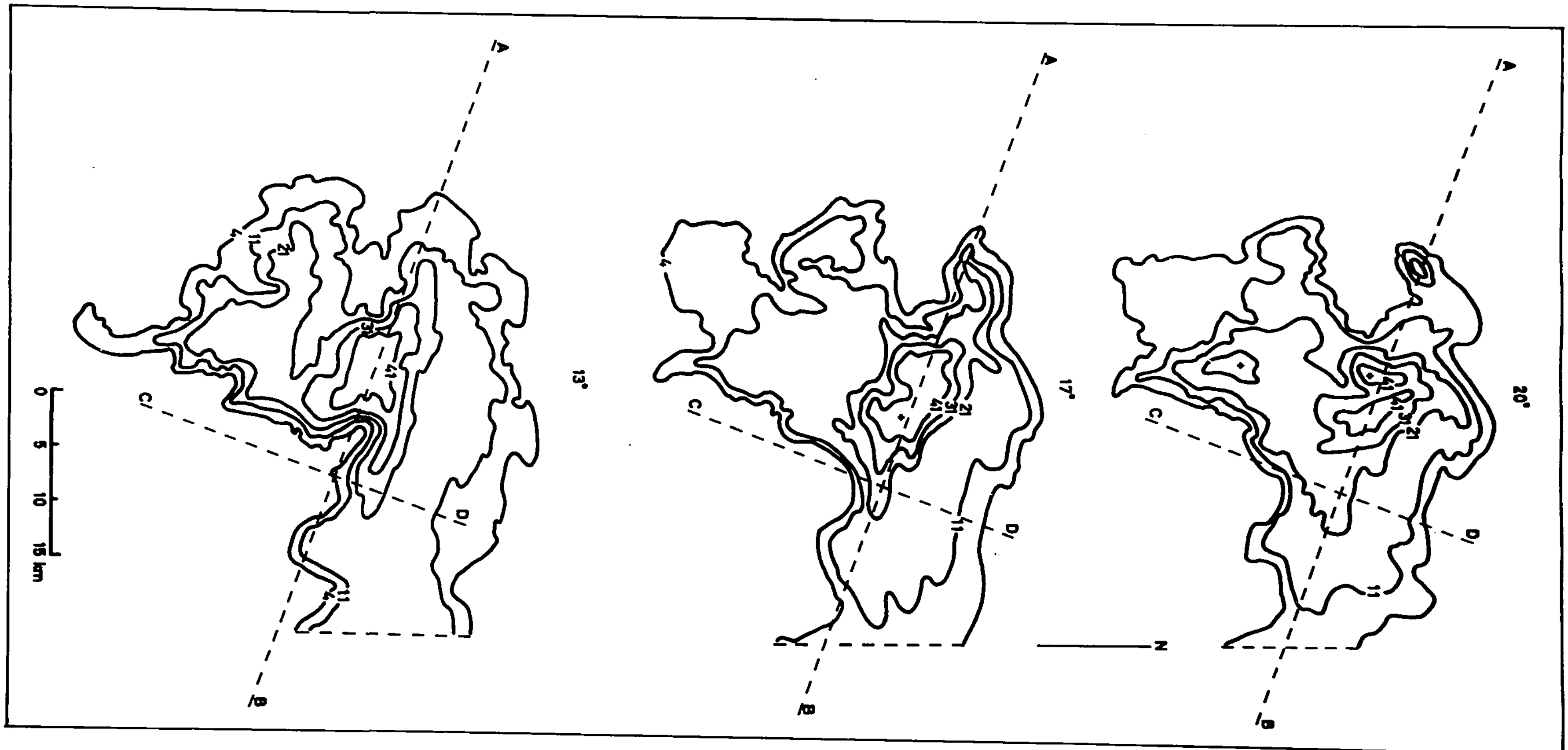

Fig. 2.4.10 (Continued) Selected PPI Sections at 1949 MST - 25 July 1968. Contours of Z_e are labelled in dBz, and elevation angles indicated in deg.

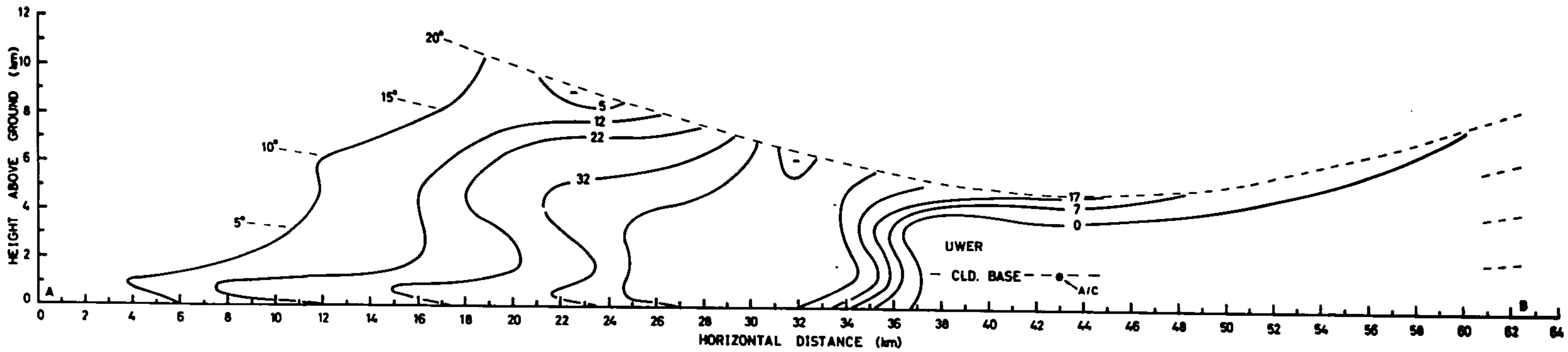

Fig. 2.4.11 Vertical Cross-Section in the Direction of Motion at 1949 MST - 25 July 1968. Contours of Z_e are labelled in dBz. Note the Z_e maximum, and the overhang which extends out over the UWER and the updraft region at cloud base.

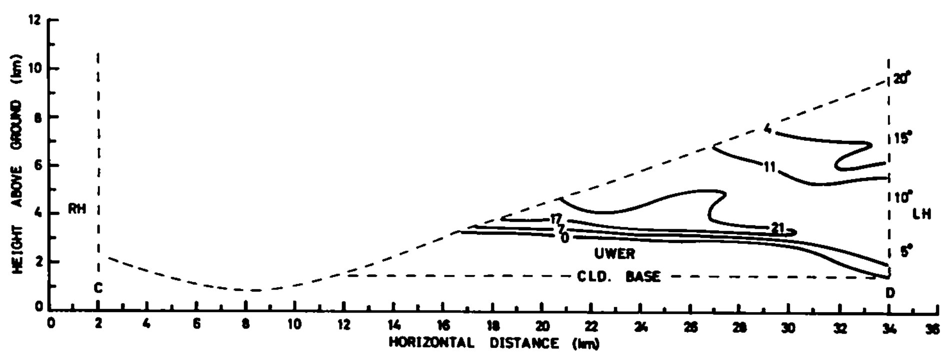

Fig. 2.4.12 Vertical Cross-Section Normal to the Direction of Motion (along CD) at 1949 MST - 25 July 1968. This figure views the storm along CD (looking upstream), and depicts a portion of the overhang.

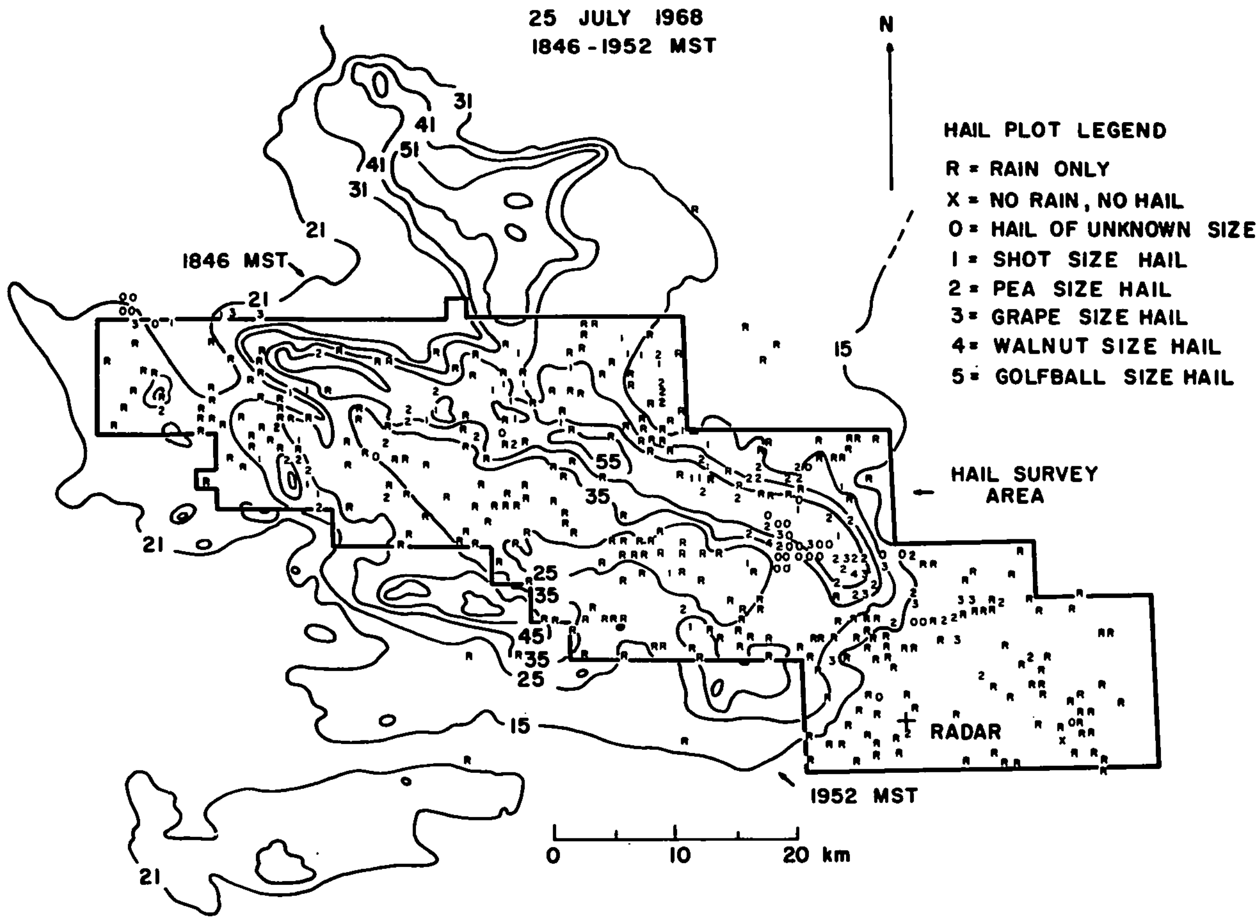

Fig. 2.4.13 Maximum Z_e Envelope and Hail Survey Data - 25 July 1968. Hail and rain reports are shown in relation to the Z_e maximum value which occurred at 0 deg elevation. Note the correspondence between areas of high Z_e and largest hail.

Vertical velocities measured at cloud base at this time by the University of Wyoming aircraft averaged 6 m sec^{-1} over an area of 93 km^2 (5.6 x 16.7 km). It is interesting that the aircraft flight path in Fig. 2.4.10 (at 5 deg) extends south to include an updraft ahead of the new cell developing on the southern end of the squall line.

The resulting precipitation which occurred at the surface in conjunction with this storm is illustrated in Fig. 2.4.13. The hail reported at the surface is the largest hail observed at that point. It is obvious that the majority of hail fell along the axis of travel of the Z_e maximum studied; shot and pea size hail reports being most common with grape and walnut size hail occurring at the surface after 1925 MST - the time of maximum storm height.

One segment of a large squall line has been examined here. It is certain that this major cell lasted in excess of 48 min (more likely 70 min or more) and during this time it reached a quasi-steady state. A continuous, broad, laminar updraft exhibiting vertical velocities of 4 - 6 m sec^{-1} over an area of 100 km^2 was found (by aircraft measurements) in advance of the major Z_e maximum and the accompanying precipitation zone for the duration of this period. The Z_e maximum was found upwind of the updraft region with its top almost directly above the position of the surface Z_e maximum. Extending downwind, the shelf-like canopy or overhang capped the unbounded weak echo region directly above the cloud base updraft. The persistence of these features over a 40 min time interval also implies a quasi-steady state in the airflow character of this storm. Hail fell from the Z_e maximum and was found to be largest after maximum vertical development of the storm. The airflow structure of this storm will be treated in depth in Chapter VI.

CHAPTER III

A RADAR CASE STUDY OF THE STORM OF 28 JULY 1968[1]

3.1 Airmass and Wind Structure in the Vertical

The airmass which produced severe storms on 28 July 1968 was a very warm, moist maritime Polar airmass, as illustrated by the radiosonde sounding for 1610 MST depicted in Fig. 3.1.1. Surface temperatures were near 30C (86F) with surface dewpoints of approximately 16C (60F). Such warm, moist, airmasses occur infrequently in central Alberta. A parcel trajectory shown in Fig. 3.1.1, using representative cloud base conditions and taking account of liquid water loading, reveals a very unstable airmass with a large "positive area". Parcel temperatures are found as much as 12 deg C warmer than the surrounding environment. As a consequence, high vertical velocities and a high storm top (14 km AGL) would be expected. As will be indicated in Chapter VII, this storm was the deepest, most energetic storm to occur within the ALHAS project area during the summers of 1967 and 1968.

At 1610 MST, the wind structure at the radar site (see hodograph in Fig. 3.1.2) exhibited only a weak shear in the vertical, with a maximum velocity of 29 m sec^{-1} from 270 deg at 13 km. This wind sounding is probably representative of the environment around the storm above 3 km, but it is unlikely that it is typical of the wind structure in the sub-cloud layers since the storm developed after 1700 MST in the foothills approximately 140 km WNW of the radar site. Figure 3.1.3 illustrates the wind structure in the vertical

[1]A preliminary analysis of this storm was presented by Marwitz, Chisholm and Auer (1969) at the Sixth Conference on Severe Local Storms.

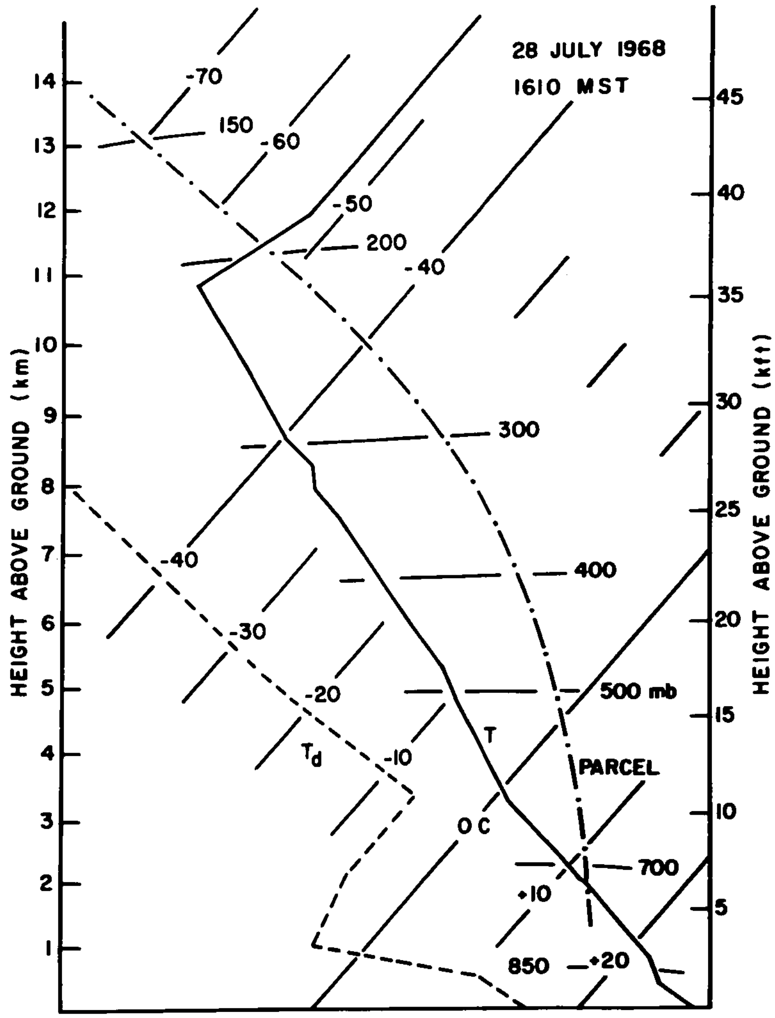

Fig. 3.1.1 Radiosonde Sounding 1610 MST - 28 July 1968. Dot-dash line indicates a moist adiabatic parcel trajectory using representative cloud base conditions. Note the large "positive area" and the penetration of the tropopause by the parcel curve at 11 km (200 mb).

at the radar site at 2022 MST, when the storm was approximately 60 km NW of the radar site. The winds above 6 km have decreased slightly and veered about 15 deg. Winds in the lower levels have remained southerly, but have increased in magnitude since 1610 MST.

3.2 The History of the Storm of 28 July 1968

There are numerous data available to treat the history of a storm; for example, the motions, reflectivity structure, cloud base updrafts, hail and rain reports, and storm top heights, each considered as a function of time. These data will be utilized to outline briefly the storm history. The

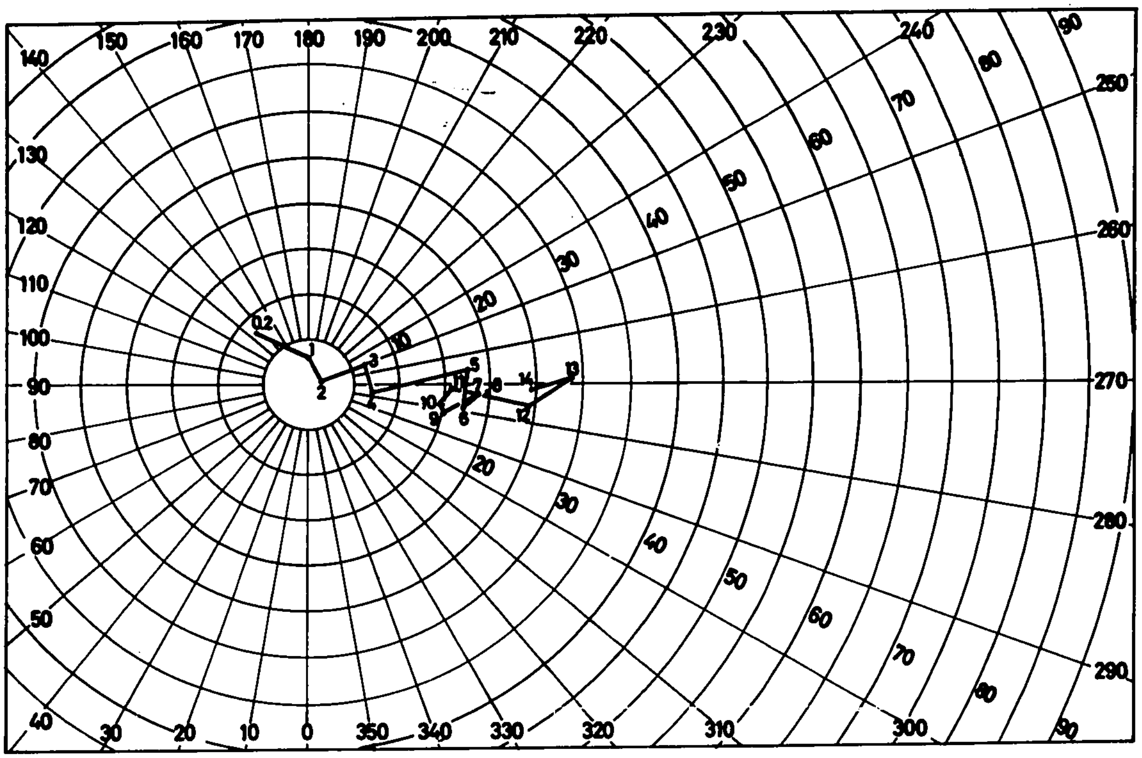

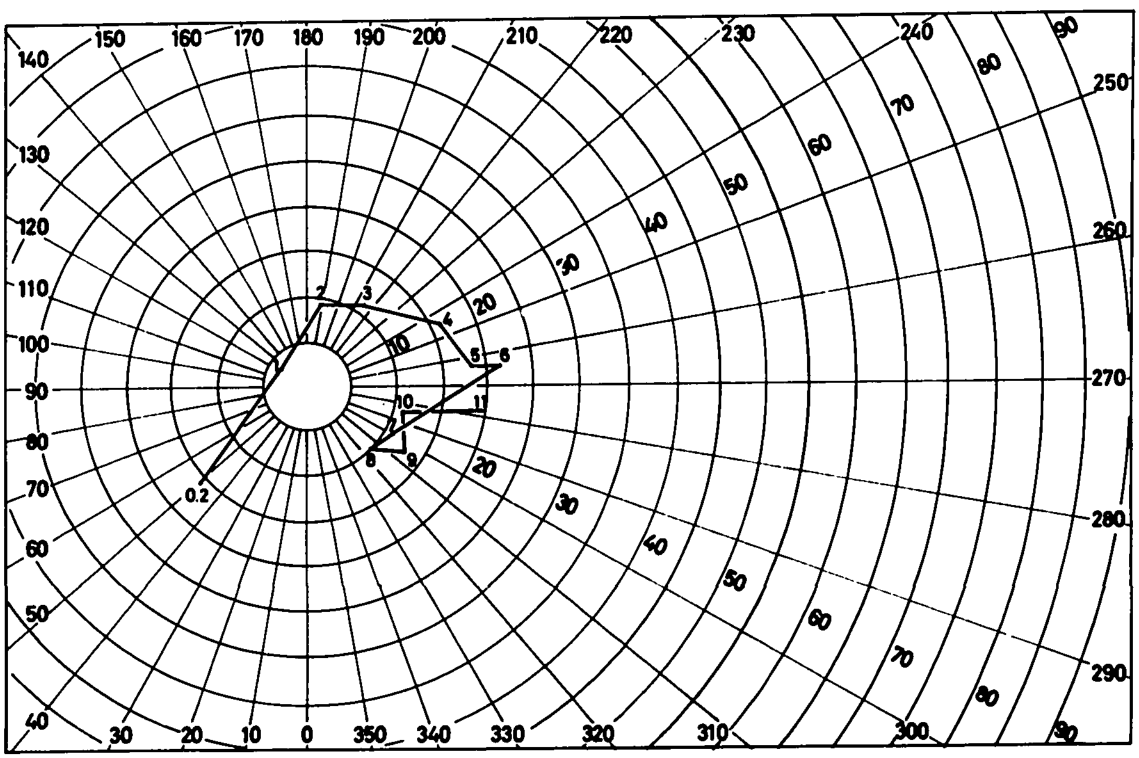

Fig. 3.1.2 Wind Hodograph 1610 MST - 28 July 1968 (Top figure).
Fig. 3.1.3 Wind Hodograph 2022 MST - 28 July 1968 (Bottom figure).
Wind speeds are plotted in m sec^{-1} and heights indicated in km AGL. At 1610 MST note wind from S and SE in sub-cloud region and veering winds above. However, at 2022 MST, winds in sub-cloud region have increased in magnitude while winds above 6 km have veered and decreased.

storm of 28 July 1968 differed from the other storms considered in this study in that it had three distinct phases, each with its own characteristics. Consequently, the above data will also be used to characterize this storm in each of its separate phases.

The storm first appeared on radar at 1736 MST WNW of the radar site at a range of 133 km. It was evident that the storm was in an advanced stage of development; Z_e values exceeded 40 dBz and radar echo appeared at all elevations from 0 - 4 deg. At this time the storm was situated over the lee side of the easternmost range of the Rocky Mountain foothills. Between 1741 and 1802 MST, the center of the storm Z_e maximum appeared almost motionless over the eastern slope of the foothills, moving less than 1 km during that 21 min period (horizontal speed < 0.8 m sec^{-1}). However, during that same period, the downwind edge of the storm echo moved some 11.2 km (horizontal speed ≃ 8.9 m sec^{-1}). After 1805 MST, the center of the storm Z_e maximum (at 0 deg) began to move and progressed eastward from the foothills between 1805 and 1844 MST with a horizontal speed of 8.6 m sec^{-1}. This phase of the storm of 28 July 1968, which will be referred to as Phase I, is illustrated in Fig. 3.2.1 at 1814 MST. A UWER is seen on the upwind side of the storm with a sharp reflectivity gradient bounding it on its downwind side. The reflectivity structure of this phase in three dimensions will be considered in Section 3.3. The essentially stationary behaviour of the storm Z_e maximum is considered to be a result of the influence which the foothills exerted on the storm airflow. This aspect will be treated in Chapter VI.

By 1841 MST, the Z_e maximum associated with Phase I was dissipating, being replaced by two new Z_e maxima. The tracks of these two Z_e maxima are evident in the maximum Z_e envelope displayed in Fig. 3.2.2. Phase II was a transitory stage, the two storms seen in Fig. 3.2.1 reaching a peak in their development by 1859 MST. During Phase II, the storm differed substantially

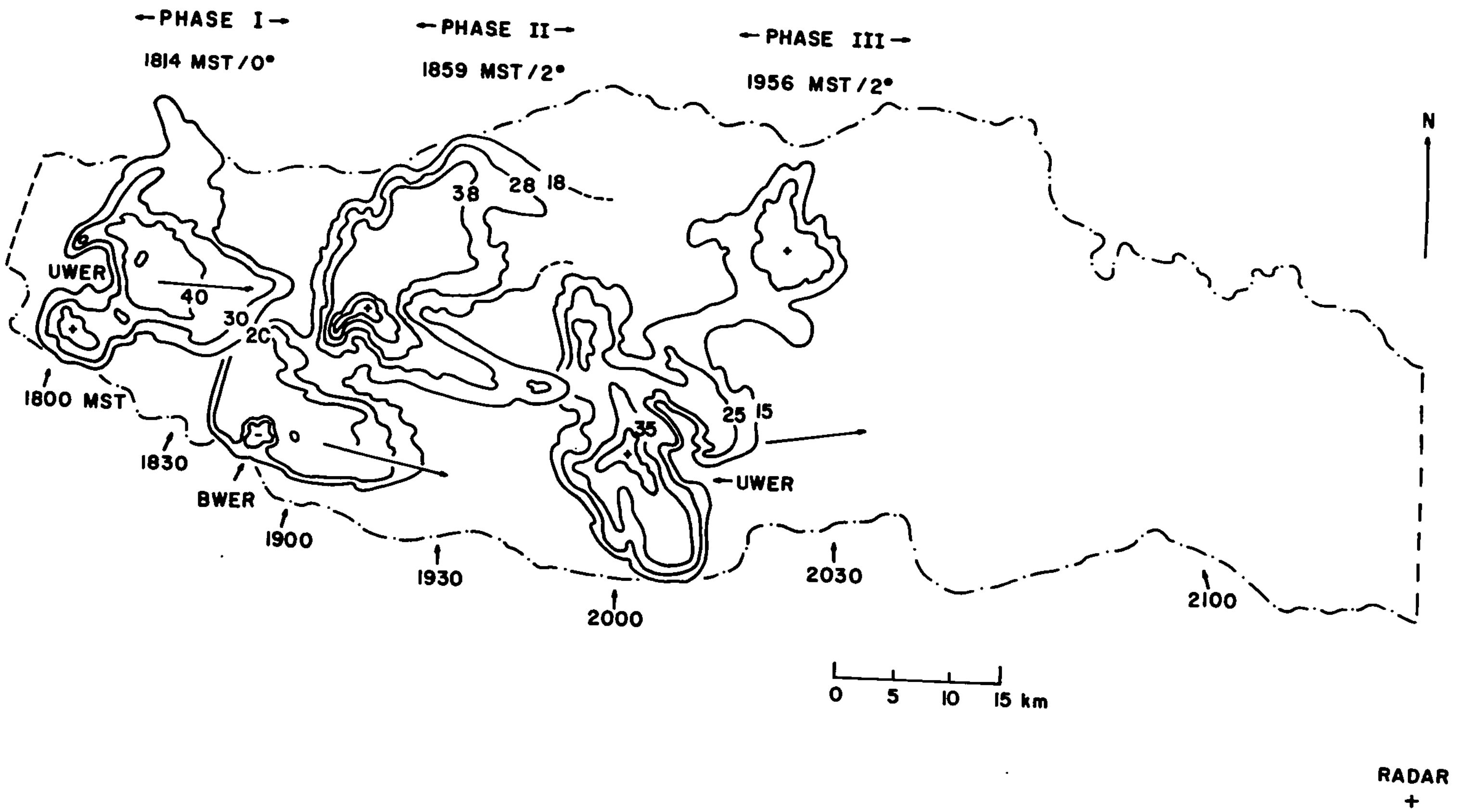

Fig. 3.2.1 Storm Phases and Maximum Z_e Envelope - 28 July 1968. Selected PPI sections for 1814, 1859 and 1956 MST are depicted (within the Maximum Z_e envelope - see Fig. 3.2.2) to display the three phases of this storm. Note the UWER on the upwind side of the storm at 1814 MST, the BWER on the RH flank at 1859 MST and the UWER on the downwind side of the storm at 1956 MST. The direction of storm motion for each phase is indicated.

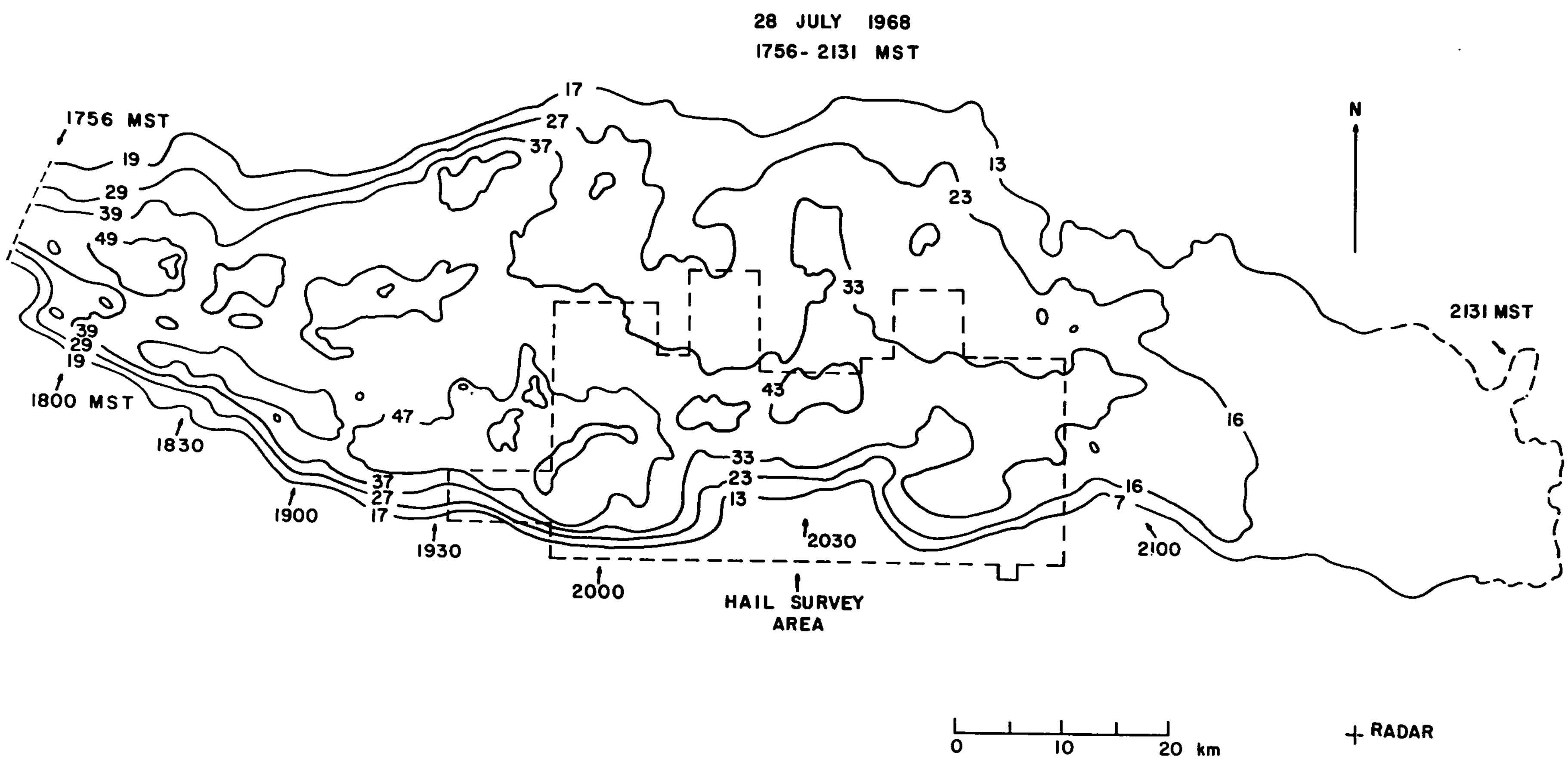

Fig. 3.2.2 Maximum Z_e Envelope 1756 - 2131 MST - 28 July 1968. The envelope of maximum Z_e values (dBz) at 0 deg elevation is shown for the period 1756 - 2131 MST. A telephone hail survey was conducted within the area inside the dashed outline. Note the tendency for high gradients of reflectivity on the southern edge of the storm envelope.

from Phase I, exhibiting characteristics not unlike the Browning SR storm model. Of note is the BWER on the RH flank of the southernmost storm, surrounded by a tight reflectivity gradient. The reflectivity structure in three dimensions for Phase II will be considered in detail in Section 3.3.

The two storm cells seen in Phase II amalgamated by 1930 MST and were transformed into a structure similar to that of a squall line. This third phase resembled the storm of 25 July 1968 analyzed in Chapter II. As seen in Fig. 3.2.1, it is characterized at 1956 MST by a long, narrow, UWER along the downwind side of the storm. Phase III was the final phase of the storm of 28 July 1968. It continued until after 2100 MST, showing slow dissipation throughout this period. Shortly after 2030 MST maximum Z_e values (see Fig. 3.2.2) dropped to less than 40 dBz and after 2100 MST, the maximum Z_e values had decreased to less than 30 dBz with "rain only" being reported at the surface. By 2200 MST, the storm had broken into numerous small weak echoes NE of the radar site and at 2300 MST only a small echo fragment remained, heralding the end of the storm of 28 July 1968.

The University of Wyoming aircraft measured vertical velocities at cloud base between 1751 and 2108 MST. Figure 3.2.3 illustrates the aircraft flight path with respect to the maximum Z_e envelope (from Fig. 3.2.2) and vertical velocities at cloud base are indicated in m sec^{-1}. During Phase I, the aircraft flew a tight, short, N-S path measuring vertical velocities at cloud base of 3 - 6 m sec^{-1} near the center and RH flank of the storm track. Vertical velocities of 4 - 5 m sec^{-1} were observed along the southern edges of the two storms constituting Phase II. During Phase III, the flight path changed to a regular N-S pattern with updrafts of 6 - 8 m sec^{-1} (maxima as high as 13 m sec^{-1}) being found along a track 15 - 20 km long, downwind from the radar echo.

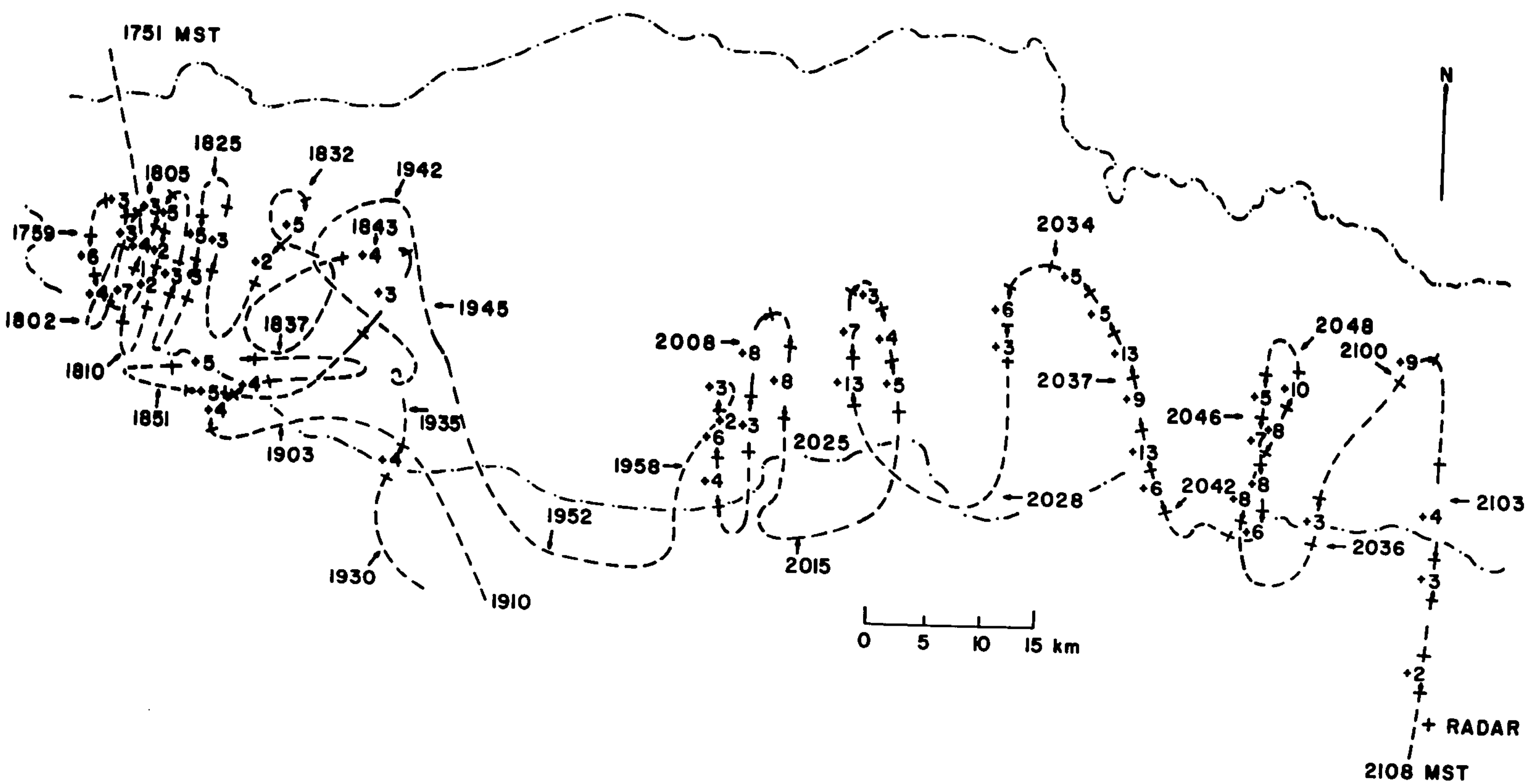

Fig. 3.2.3 Aircraft Track and Vertical Velocity Measurements at Cloud Base 1751 - 2108 MST - 28 July 1968. The dot-dash line delineates the outer maximum Z_e contour as in Fig. 3.2.2. The aircraft track during the period 1751 - 2108 is shown and vertical velocities at cloud base are indicated in m sec^{-1}.

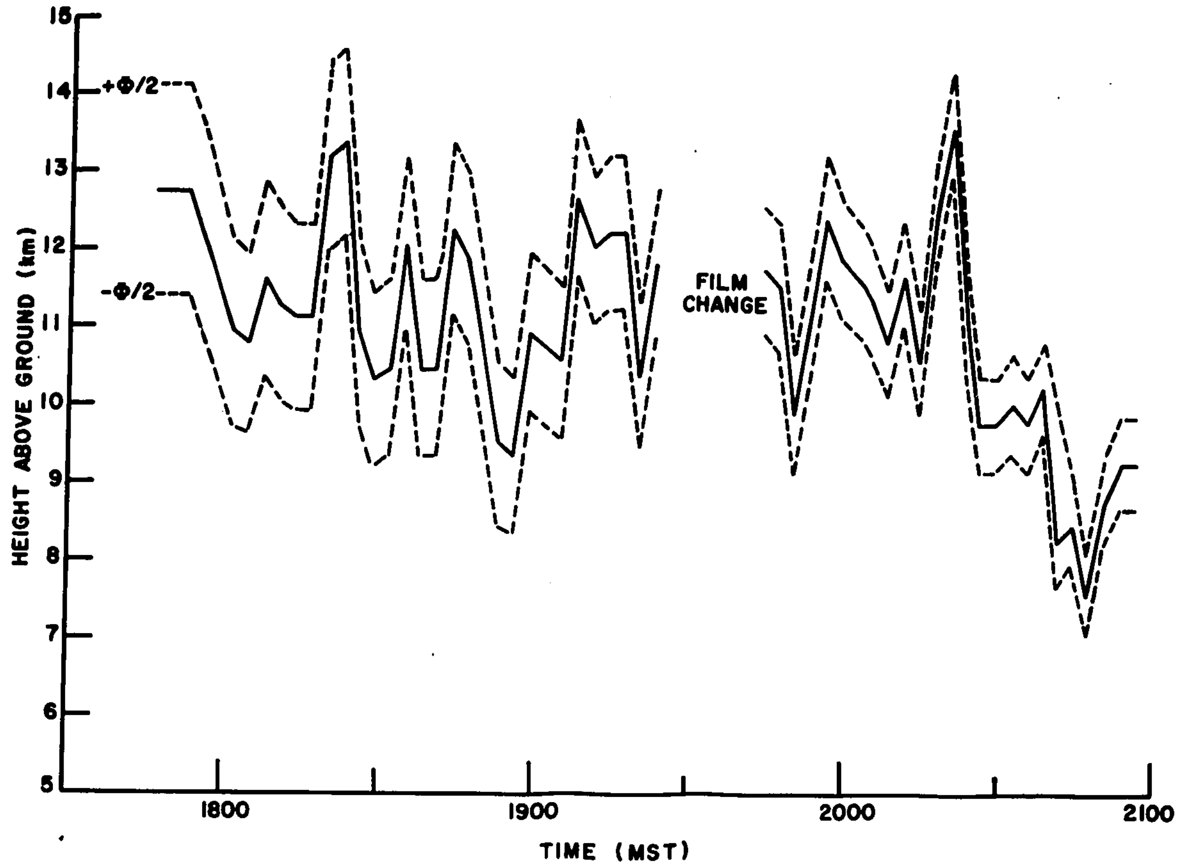

Fig. 3.2.4 Height of Maximum Radar Storm Top vs Time - 28 July 1968. The height of the radar beam axis at 3 min intervals is indicated by the solid line. Upper and lower half-power beam points (Ø/2, -Ø/2) are delineated by dashed lines. Note the consistently high storm tops (above 11 km AGL) between 1745 and 2015 MST, with tops reaching as high as 13.5 km for brief periods.

Figure 3.2.4 depicts the history of the highest radar storm top. Between 1800 and 2000 MST, the storm top is consistently higher than 11 km AGL, with two brief maxima exceeding 13 km in height. It appears that the storm was characterized by a high, relatively steady storm top, upon which are superimposed brief excursions to greater heights due to individual cell activity. After 2015 MST, dissipation sets in rapidly.

Surface reports of rain and hail are shown in Fig. 3.2.5. A telephone hail survey was conducted within the area delineated by the solid line, and additional reports were obtained by mobile precipitation units. Since a

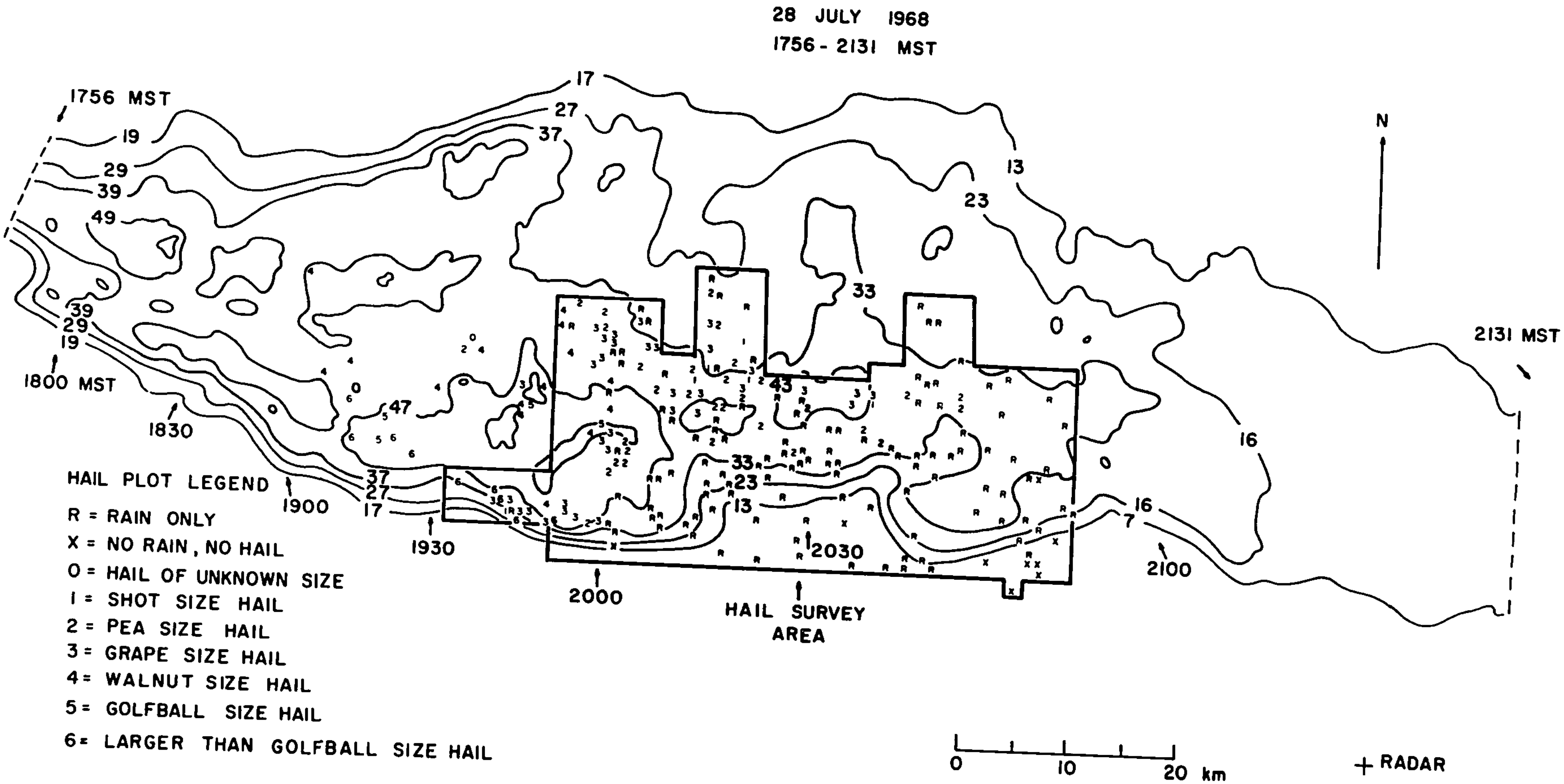

Fig. 3.2.5 Maximum Z_e Envelope and Hail Survey Data - 28 July 1968. Maximum size hail reports and rain reports are shown in relation to the maximum Z_e value which occurred at a given location at 0 deg elevation. A telephone hail survey was conducted within the area bounded by the solid line.

substantial portion of the storm (approximately 1736 - 1946 MST) occurred over uninhabited forest regions, complete precipitation report coverage for the western extent of the storm is unavailable. Hail larger than golfball size was observed, by mobile precipitation sampling units, between 1915 and 1945 MST with hailstones as large as 7 cm diameter being reported (largest hail reported in the ALHAS project area in 1968). This hail fell during the latter portion of Phase II. There was a slow decrease in maximum observed hail size during Phase III. After 2000 MST, no hail larger than grape size was reported, and "rain only" was reported following 2045 MST.

3.3 The Storm Reflectivity Structure in Three Dimensions

As was outlined in the previous section, this storm presented itself in the form of three distinct phases. PPI sections and vertical cross-sections for each of these phases will be presented to depict the characteristic three-dimensional structure of this storm.

Figure 3.3.1 displays PPI sections at 1814 MST depicting the storm in Phase I, shortly after it began to move east of the lee side of the foothills. This figure exhibits a well-developed UWER on the upwind side of the storm. This UWER diverges with height, and is bounded on its downwind side by a sharp reflectivity gradient; a feature found in conjunction with the boundary of an updraft region in Chapter II.

In addition, Fig. 3.3.1 depicts vertical velocities measured at cloud base by the University of Wyoming aircraft. Vertical velocities of 3 - 6 m sec^{-1} were observed beneath cloud base in precipitation areas downwind from the UWER. At this time, the aircraft encountered soft hail of 1.0 - 1.5 cm diameter in association with regions where Z_e values exceeded 45 - 50 dBz. Navigation in this region was difficult due to poor visibility, and

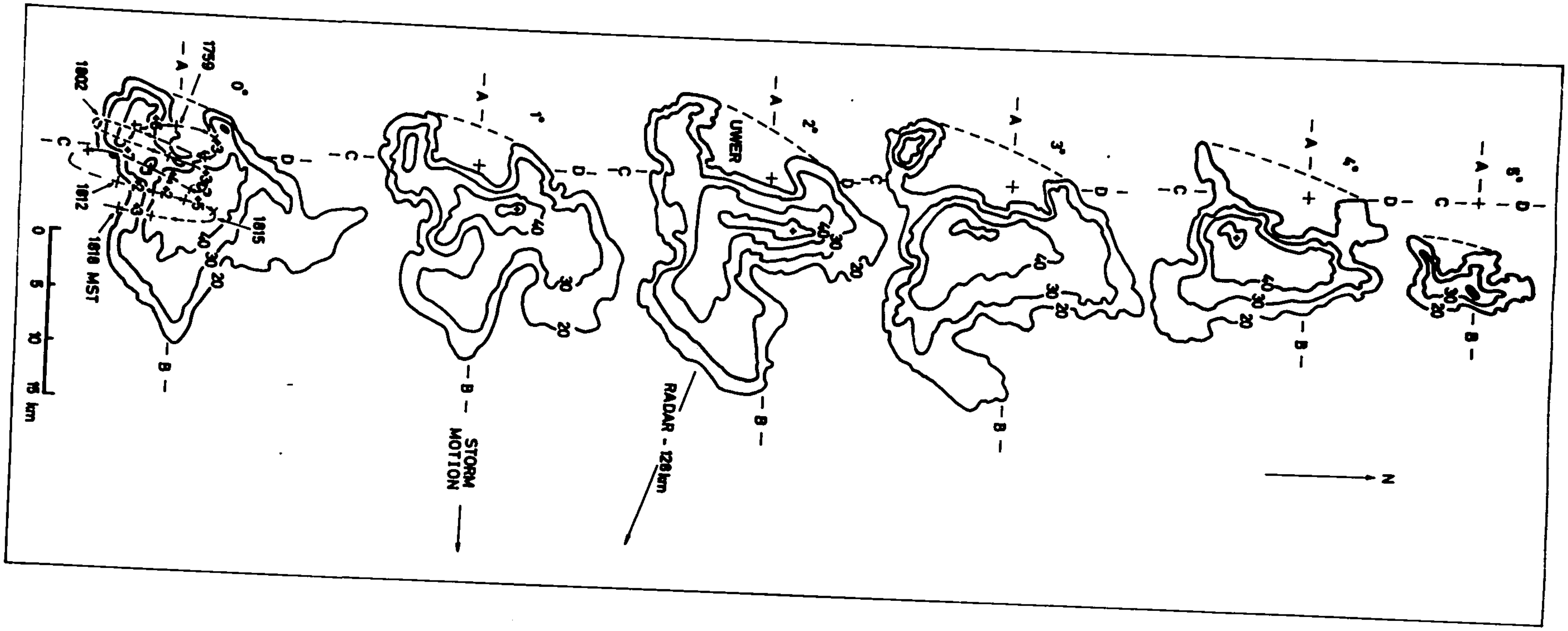

Fig. 3.3.1 PPI Sections at 1814 MST - 28 July 1968. Contours of Z_e are labelled in dBz, and elevation angles are indicated in deg. The aircraft flight path is shown (at 0 deg) with cloud base measurements of vertical velocity indicated in m sec^{-1}. Note the UWER on the upwind side of the storm extending from 0 - 5 deg. The dashed line has been added to indicate the approximate extent of the UWER.

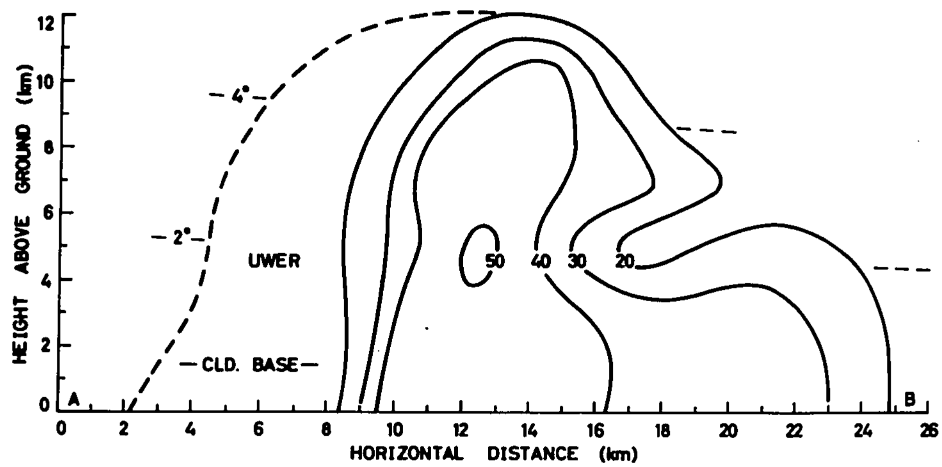

Fig. 3.3.2 Vertical Cross-Section in the Direction of Motion at 1814 MST - 28 July 1968. Contours of Z_e are labelled in dBz. The approximate extent of the UWER on the upwind side is delineated by dashed lines (see Fig. 3.3.1). Note that the UWER tilts downwind particularly near the storm top. Downwind from the UWER is found an almost vertical Z_e maximum and a sharp gradient bounding the downwind side of the UWER.

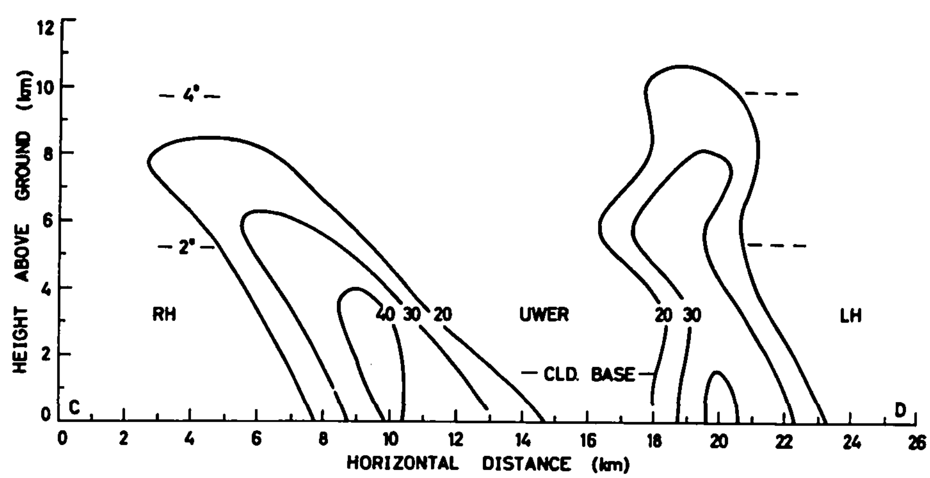

Fig. 3.3.3 Vertical Cross-Section Normal to the Direction of Motion (along CD) at 1814 MST - 28 July 1968. The vertical section along line CD is shown viewed in the upstream direction. The RH and LH flanks are indicated and contours of Z_e are labelled in dBz. Note the divergence of the UWER with height.

the updraft regions found were disorganized and small in areal extent. Thus, there is not conclusive evidence that there was an organized updraft at cloud base under the UWER at this time since the aircraft did not specifically fly beneath the UWER. Conversely, there is no evidence that there was not an updraft at cloud base beneath the UWER. The existence of the UWER and the sharp reflectivity gradient downwind are, however, highly indicative of an updraft associated with the UWER.

A vertical cross-section taken along line AB (see Fig. 3.3.1) in the direction of storm motion is shown in Fig. 3.3.2. The extent of the UWER on the upwind side of the storm is depicted by the dashed line (from Fig. 3.3.1). The steep reflectivity gradient, and nearly vertical Z_e maximum are found directly downwind. Figure 3.3.3 illustrates a vertical cross-section along line CD normal to the direction of motion directly through the UWER. The diagram depicts the diverging character of the UWER with height.

Phase I deteriorated rapidly after moving east of the foothills, and was replaced by Phase II. By 1847 MST, evidence of a BWER formation on the RH flank of the southernmost storm was found. This BWER developed, reaching maximum definition at 1859 MST, the period displayed by the selected PPI views in Fig. 3.3.4. After 1911 MST, the BWER formation was no longer in evidence. A study of the radar records at 3 min intervals over this 24 min period reveals a progressive development and decay of this BWER formation. It is reminiscent of the Browning SR storm model with its vault, wall and overhang. The storm to the NE exhibited similar features - without a BWER. These two storms, with a narrow band of echo (Z_e > 18 dBz) connecting the two at low levels, is strikingly similar to a series of severe storms in Oklahoma, analyzed by Browning (1963). Browning was able to establish that a precipitation curtain from the southern storm was swept into the vault

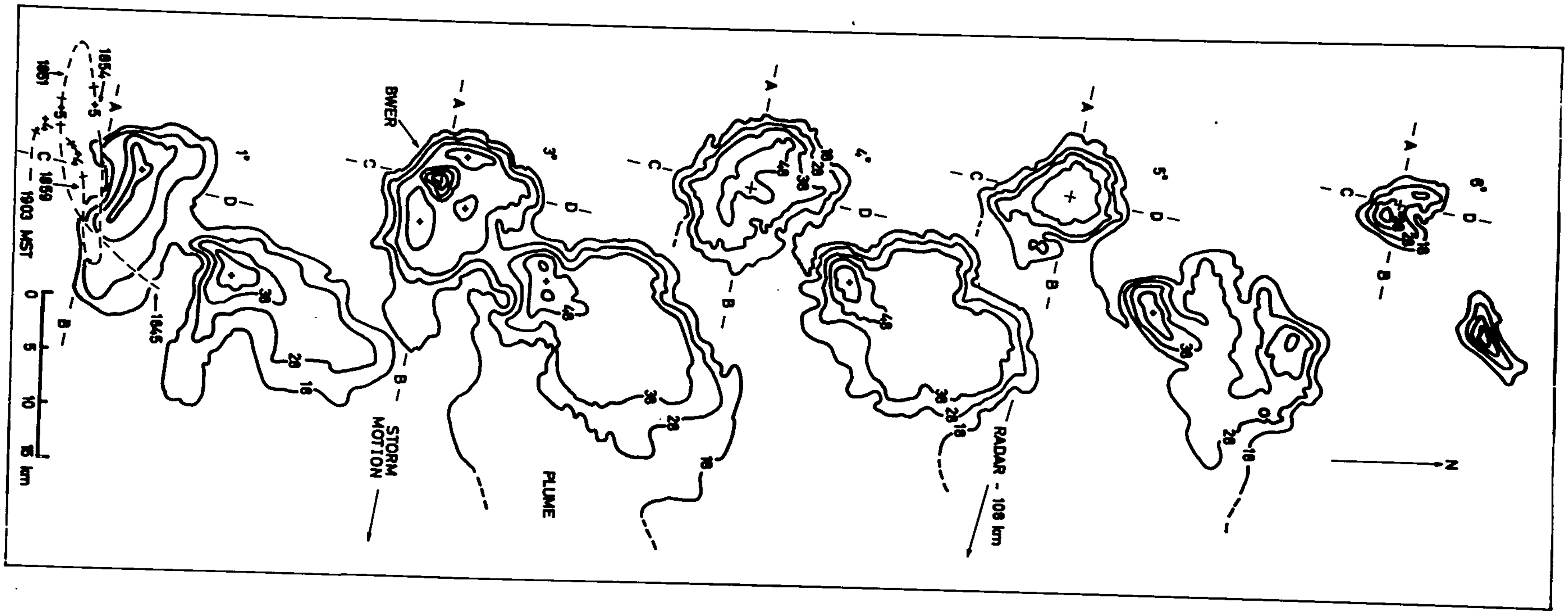

Fig. 3.3.4 Selected PPI Sections at 1859 MST - 28 July 1968. Contours of Z_e are labelled in dBz, and elevation angles are indicated in deg. The aircraft flight path is shown (at 0 deg) with cloud base measurements of vertical velocity indicated in m sec^{-1}. Note the BWER at 3 deg elevation which occurs above the cloud base updraft region.

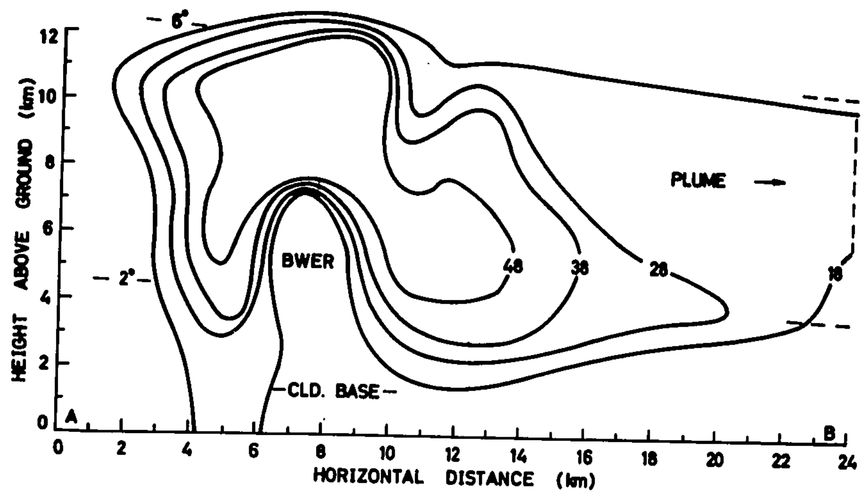

Fig. 3.3.5 Vertical Cross-Section in the Direction of Motion at 1859 MST - 28 July 1968. Contours of Z_e are labelled in dBz. The BWER enters the storm from the downwind side and ascends (with a slight lean to the upwind side) to 7 km. A Z_e maximum caps the BWER, diverging at high levels with an extensive overhang and plume system appearing downwind of the BWER. Note the similarity of this cross-section to the Browning SR storm vertical section in Fig. 1.2.4.

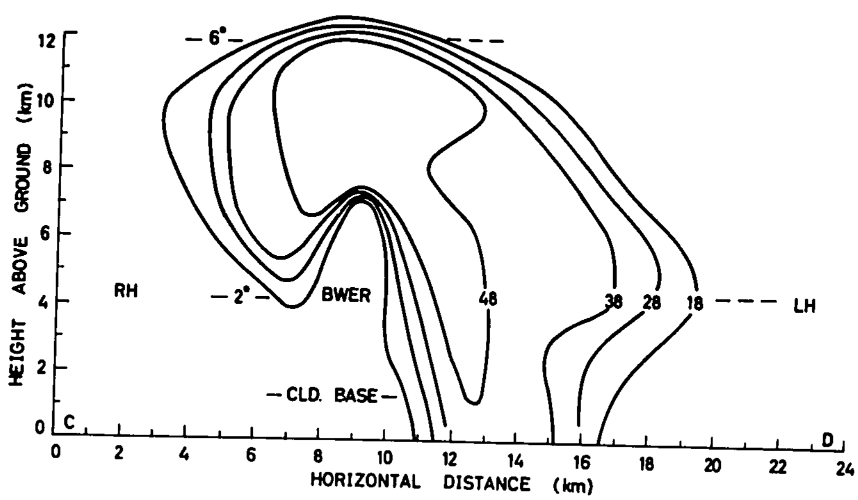

Fig. 3.3.6 Vertical Cross-Section Normal to the Direction of Motion (along CD) at 1859 MST - 28 July 1968. The vertical cross-section along CD is shown viewed in the upstream direction. The RH and LH flanks are indicated and contours of Z_e are labelled in dBz. Entering the storm from the RH flank, the BWER reaches 7 km before being capped by the Z_e maximum. This Z_e maximum extends toward the surface on the LH flank of the BWER. Note the sharp reflectivity gradients along the wall of the BWER.

region of the northern storm by an updraft associated with the vault at low levels. This might also be the case for the storm of 28 July 1968, to the extent that the intruding precipitation curtain completely masked the BWER in the northern storm.

As shown in Fig. 3.3.4, the aircraft measured updrafts of 4 - 5 m sec^{-1} at cloud base on the RH flank of the storm, beneath the BWER, and also to the south of the storm echo. Referring to Fig. 3.2.3, it is seen that updrafts of 3 - 5 m sec^{-1} were measured between 1832 and 1842 MST. These updrafts were observed on the RH flank of the northern storm. It is clear that both these storms had an updraft at cloud base beneath the BWER (on the RH flank).

Having established the existence of a cloud base updraft beneath the BWER, it is interesting to consider the storm structure in the vertical line along AB, in the direction of storm motion. Figure 3.3.5 shows the BWER penetrating almost vertically to a height of 7 km AGL, above which sits a reflectivity maximum capping the BWER. The shape of this reflectivity structure suggests a divergence of the precipitation particles aloft and also depicts the existence of a substantial overhang and plume system downwind of the BWER. Figure 3.3.6 displays a vertical cross-section along line CD (see Fig. 3.3.4) normal to the direction of motion. The BWER enters the storm from the RH flank, penetrating upward. The reflectivity cap structure is found to join with a column-like structure on the LH flank of the BWER.

Phase II has been found to differ substantially from Phase I, and Phase III is yet an even different structure. Phase III is illustrated in plan view by the PPI section in Fig. 3.3.7 at 1956 MST. The almost rectangular echo is suggestive of a squall line, sirilar to the case analyzed in Chapter II. Here a UWER is found on the downwind side of the storm, above

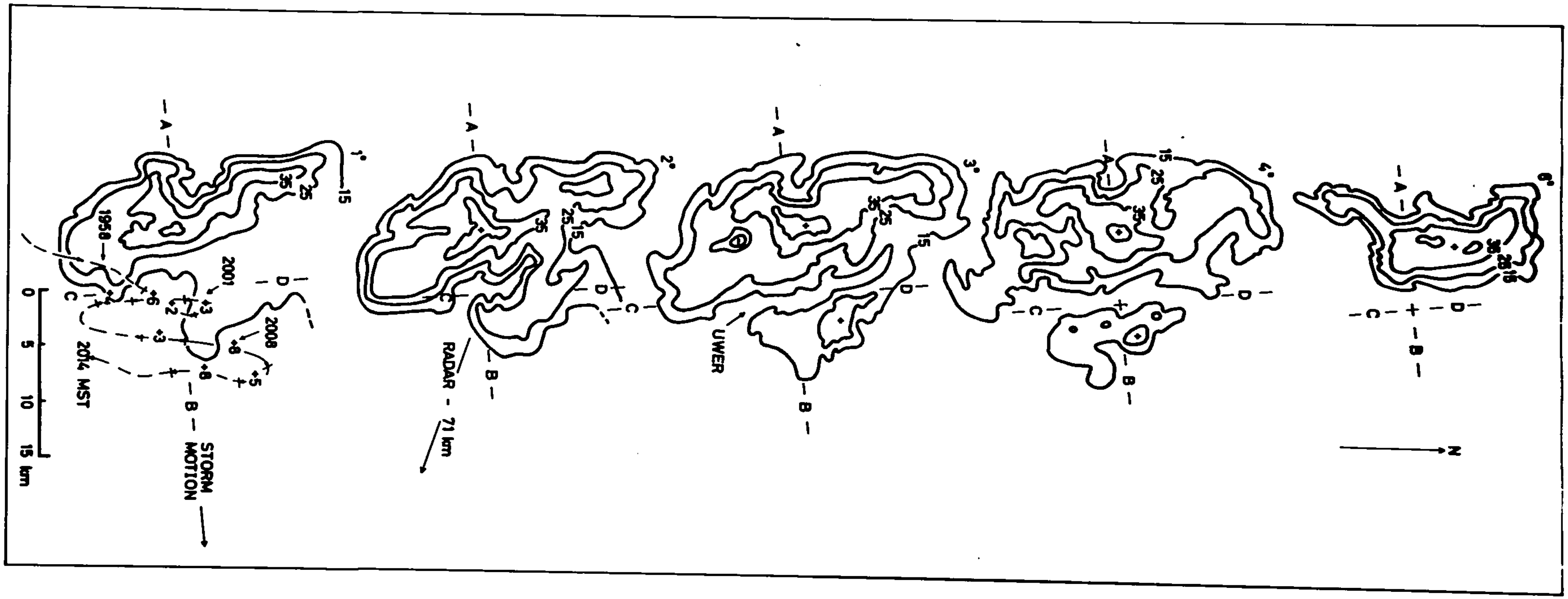

Fig. 3.3.7 Selected PPI Sections at 1956 MST - 28 July 1968. Contours of Z_e are labelled in dBz, and elevation angles are indicated in deg. The aircraft flight path is shown (at 0 deg) with cloud base measurements of vertical velocity indicated in m sec^{-1}. Note the UWER which appears on the downwind side of the storm above the cloud base updraft region.

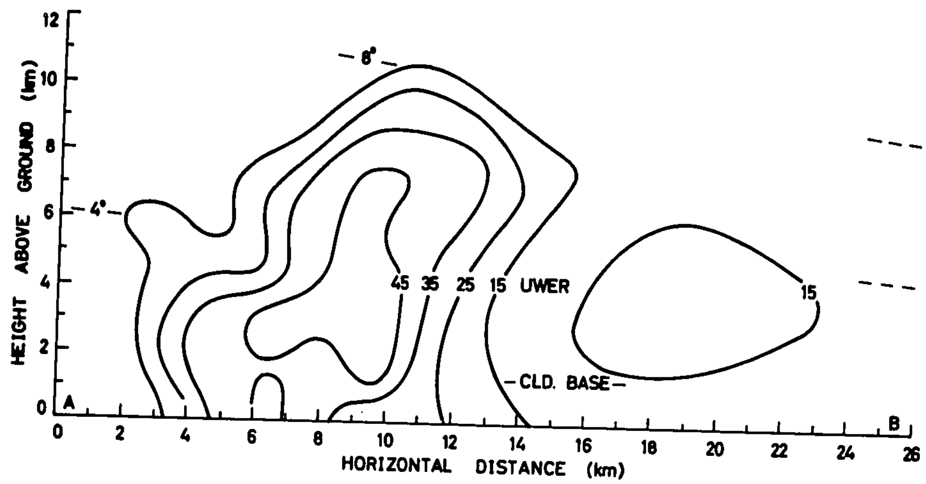

Fig. 3.3.8 Vertical Cross-Section in the Direction of Motion at 1956 MST - 28 July 1968. Contours of Z_e are labelled in dBz. The UWER enters the storm from the downwind side ascending toward the upwind side, then reversing to lean in the downwind direction.

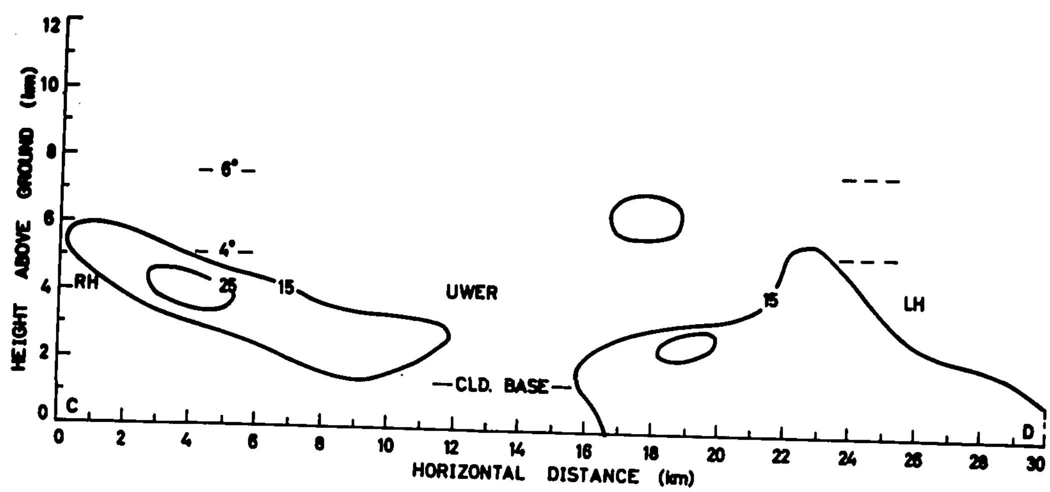

Fig. 3.3.9 Vertical Cross-Section Normal to the Direction of Motion (along CD) at 1956 MST - 28 July 1968. The vertical cross-section along CD is shown viewed in the upstream direction. The RH and LH flanks are indicated and contours of Z_e are labelled in dBz.

an aircraft measured updraft region with vertical velocities at cloud base of 4 - 8 m sec^{-1}. Figure 3.3.8 is a vertical cross-section taken along line AB in the direction of storm motion. It shows the UWER ascending toward the upwind side of the storm to reverse and tilt downwind. An extensive Z_e maximum is found upwind of the BWER, with the radar storm top occurring at the top of this Z_e maximum. Figure 3.3.9 shows the vertical cross-section along line CD through the central portion of the UWER normal to the direction of storm motion. With the exception of a few small protruding irregularities, it is clear from this figure that the UWER was a sheet-like structure penetrating upward through the storm.

As was the case for the storm of 25 July 1968, a vertical velocity profile was measured by the aircraft from cloud base (approximately 1.4 km AGL) downward in advance of the squall line formation. The observed vertical velocity was 7 - 8 m sec^{-1} at cloud base and decreased to a vertical velocity of 3 - 4 m sec^{-1} at 0.5 km AGL. Smoke plumes emanating from the ground were observed to rise in this updraft region.

Summarizing, the storm of 28 July 1968 was found to last more than 4 hr, while proceeding through three separate and distinct phases. The reflectivity structure of each phase has been examined in three dimensions and related to aircraft-measured cloud base updrafts. Conclusive evidence has been shown that an updraft existed at cloud base beneath the BWER in Phase II and the UWER in Phase III. The UWER and sharp reflectivity gradient along the downwind side of the UWER in Phase I are highly indicative of an associated updraft in this case also. A detailed analysis of the airflow structures of the three phases of this storm will follow in Chapter VI.

CHAPTER IV

A RADAR CASE STUDY OF THE STORM OF 29 JUNE 1967[1]

4.1 Synoptic Conditions and the Airmass and Wind Structure in the Vertical

During the evening of 28 June 1967, a cold maritime Arctic airmass began moving into Alberta from the Pacific coast. By 0500 MST on 29 June 1967, this cool airmass covered the entire ALHAS project area with the associated Maritime front lying in a NE-SW line from northern Saskatchewan across the southeastern corner of Alberta and through to southern Oregon. At 1700 MST, the Maritime front had pushed eastward to extend from northwestern Ontario to Oregon as shown in Fig. 4.1.1.

Accompanying this frontal system was an intense jet stream which had a profound influence on the severe storms which occurred in the ALHAS project area on 29 June 1967. A zonal flow was exhibited at 500 mb with winds averaging 18 - 28 m sec^{-1} throughout the central and southern portions of British Columbia and Alberta. On the 0500 MST 300 mb chart, the jet stream maximum was just west of the continental divide. As shown in Fig. 4.1.2, the jet stream maximum of 72 m sec^{-1} (140 kt) had advanced into central Alberta by 1700 MST on 29 June 1967.

The wind structure throughout the depth of the troposphere on 29 June 1967 is illustrated by the wind hodograph in Fig. 4.1.3. This wind sounding (taken at the radar site) is considered representative of the

[1]A preliminary analysis of this storm was presented by Chisholm (1968) at the 13th Radar Meteorology Conference.

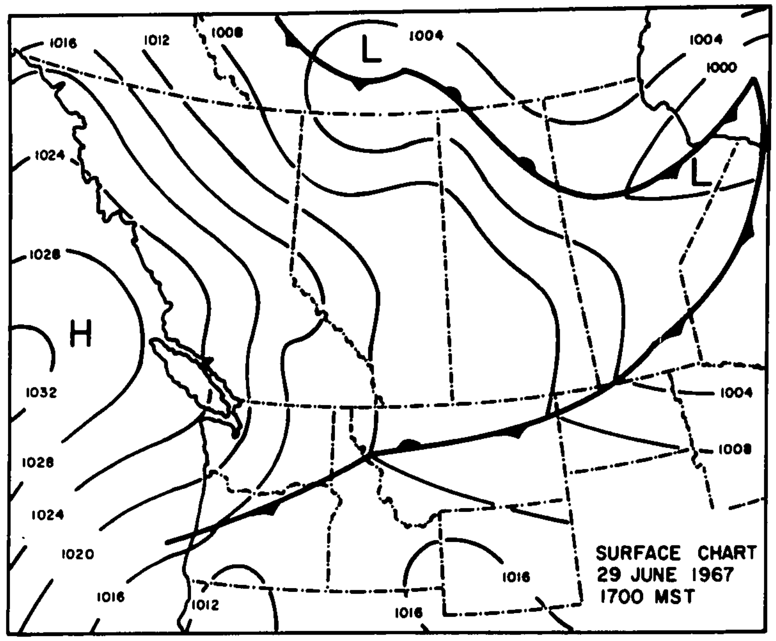

Fig. 4.1.1 Surface Chart 1700 MST - 29 June 1967. Solid lines are isobars at 4 mb intervals. Heavy lines delineate fronts. Note the Maritime front south of the Canada-USA border.

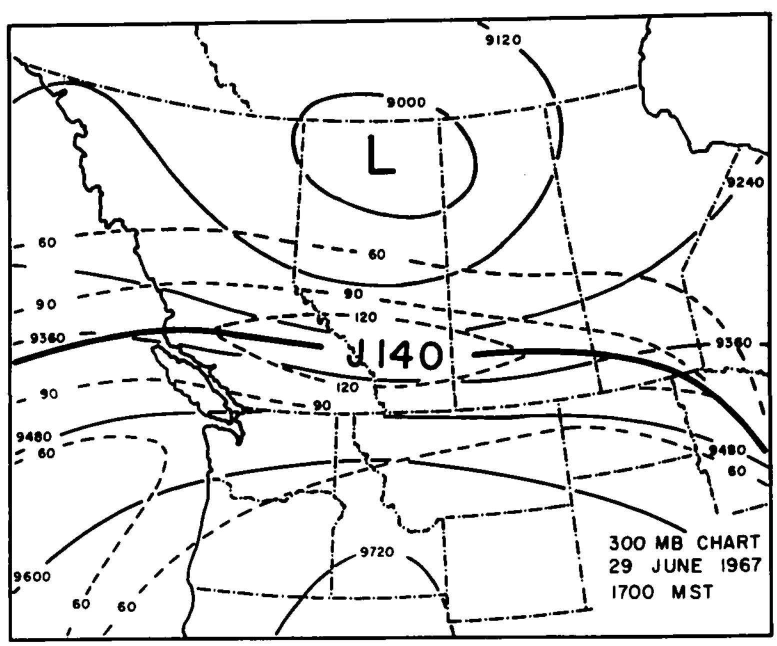

Fig. 4.1.2 300 MB Chart 1700 MST - 29 June 1967. Thin solid lines depict geopotential heights (m) and dashed lines indicate isotachs in kt. The jet stream axis is delineated by the heavy solid line. Note the 140 kt (72 m sec^{-1}) jet stream maximum over the ALHAS project area.

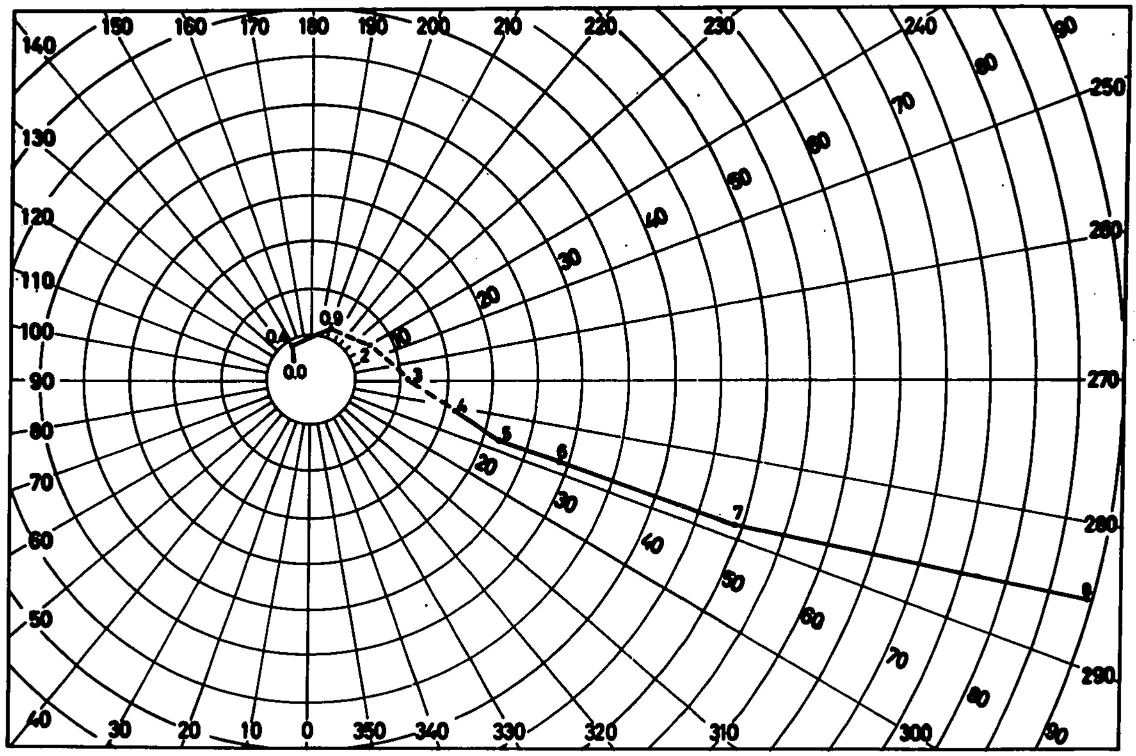

Fig. 4.1.3 Wind Hodograph 1219 MST - 29 June 1967. Wind speeds are plotted in m sec^{-1} and heights are indicated in km AGL. Values at 2 and 3 km are interpolated. Note veering winds in lowest 2 km and small directional shear above 4 km.

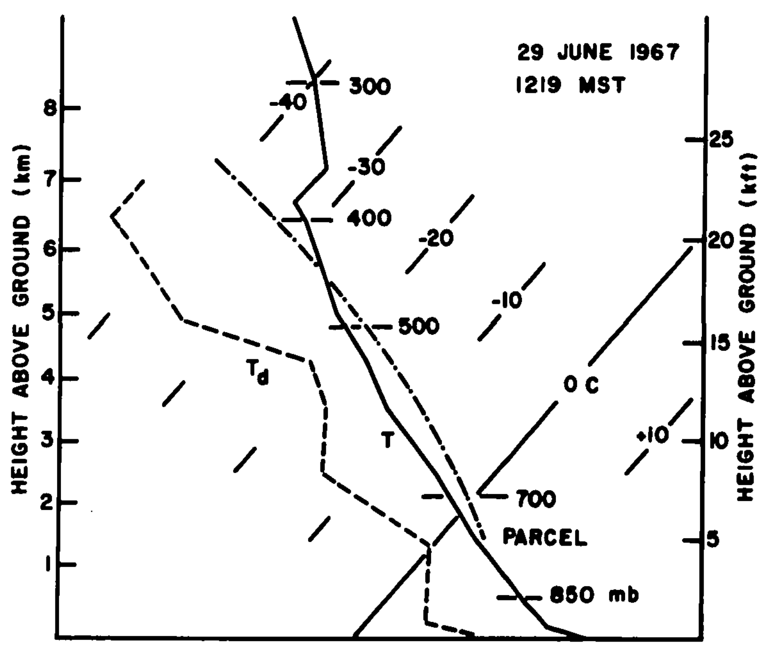

Fig. 4.1.4 Radiosonde Sounding 1219 MST - 29 June 1967. Dot-dash line indicates a moist adiabatic parcel trajectory using representative cloud base conditions. Note warm inversion at 380 mb.

environment in which severe storms existed on 29 June 1967. As is frequently the case with severe storms in Alberta, the low-level winds (in the sub-cloud layer) were light and south to southeasterly. Above 1 km, the wind veered rapidly to 280 - 290 deg and a very high wind shear value was found above 5 km. The consequences of this wind structure on the storm configuration will be discussed in Chapter VI.

A radiosonde sounding (see Fig. 4.1.4), taken prior to the approach of the series of severe storms, illustrates the airmass in which the storms occurred. This sounding is typical of a cold maritime Arctic airmass. It had a freezing level at 680 mb (1.8 km AGL) and a 500 mb temperature of -21C.

Using representative cloud base conditions, a moist adiabatic parcel trajectory (taking account of adiabatic liquid water loading) has been added to the tephigram in Fig. 4.1.4, illustrating that the maximum height of convection would be approximately 7.2 km AGL. A frontal inversion based at 380 mb was able to act on convective motion as an artificial tropopause. The tephigram in Fig. 4.1.4 illustrates a relatively small "positive area". As will be shown in Chapter VII, the buoyant forces were only capable of producing a maximum vertical velocity of 23.1 m sec^{-1} in the updraft core.

A radiosonde sounding taken at 1618 MST indicates that there were no frontal passages associated with the severe storms on 29 June 1967. Temperature differences, between the 1219 and 1618 MST soundings, at a given pressure level, were generally less than 0.5 deg C with a maximum temperature difference of 1.5 deg C. Thus, there is little doubt that the severe storms of 29 June 1967 were of the airmass variety.

It should be pointed out that the temperature and moisture conditions on 29 June 1967 were not typical of summer airmasses in Alberta; on the contrary they were more typical of mid-spring conditions. In fact, the maximum surface temperature did not exceed 18C (65F) and the dewpoint was not higher than 7C (45F). Nevertheless, the combination of a cool, unstable airmass and intense surface heating produced vigorous convection.

4.2 The History of the Storm of 29 June 1967

By 1130 MST, radar echoes were detected in the foothills region 110 km WNW of the radar site. Although numerous storms developed and persisted in this airmass, it is interesting that these storms remained isolated and did not form a squall line. Quite similar characteristics and behaviour were exhibited by the individual members of this series of storms, but only the largest, most intense storm will be treated in this study.

The storm of interest, which was first observed at 1130 MST, tracked ESE across the radar site (at 1430 MST) to dissipate after 5 hr of activity at 1638 MST. Figure 4.2.1 illustrates the envelope of maximum Z_e values at 0 deg elevation between 1130 and 1638 MST. Z_e values as high as 50 dBz were found at the time of initial storm detection (1130 MST), indicating that the storm was already in an advanced stage of development and probably yielding hail and/or heavy rain. During the 3 hr period prior to the storm passing over the radar site, Z_e values in excess of 60 dBz were frequently found along the axis of the storm swath with occasional maxima along the right hand edge. It was during this time that the storm was in its most intense stage, and surface observations indicate that the storm commonly yielded hail of grape and walnut size with occasional reports of hail as large as golfball size. After passing east of the radar site, the storm ceased to yield hail and maximum Z_e values dropped below 50 dBz after 1530 MST, some 4 hr after first detecting the storm. The storm continued to dissipate rapidly, being last seen at 1638 MST. The dashed line in Fig. 4.2.1 delineates the area which was

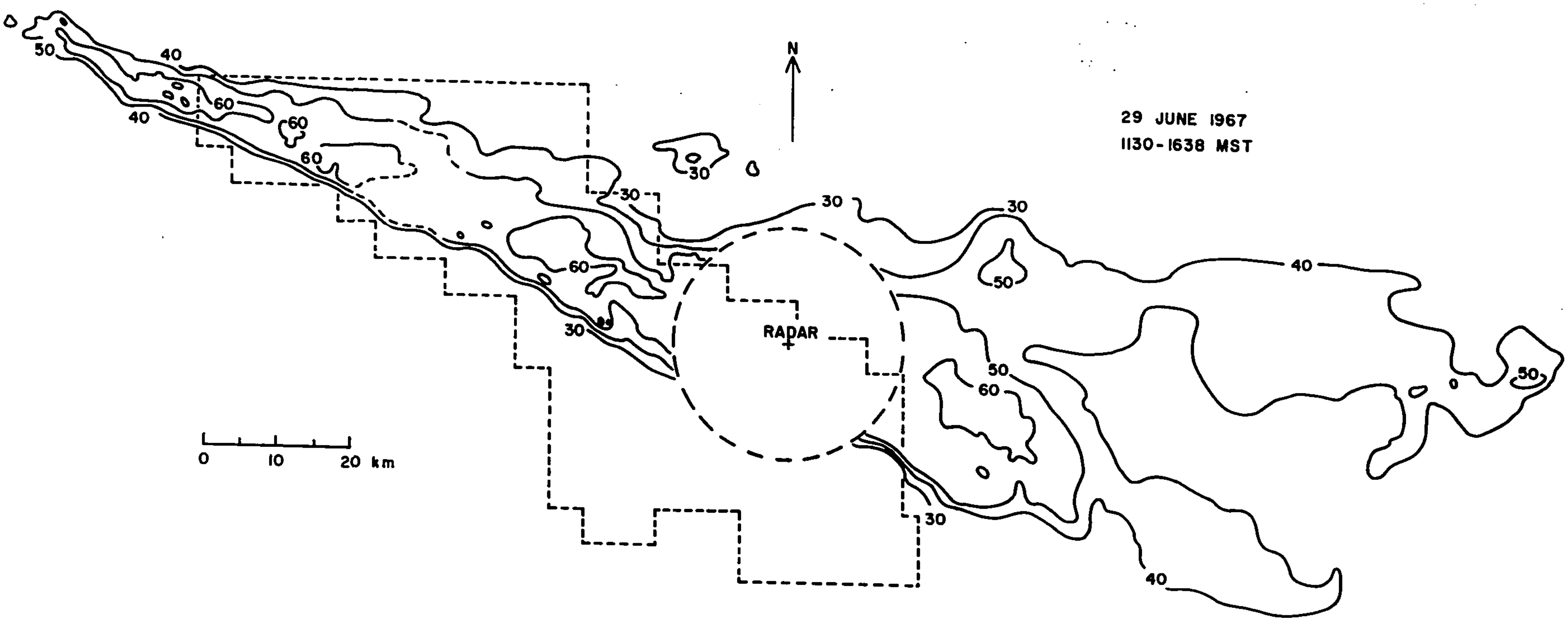

Fig. 4.2.1 Maximum Z_e Envelope - 29 June 1967. The envelope of maximum Z_e values (dBz) at 0 deg elevation is shown for the period 1130 - 1638 MST. An intensive hail survey (see Fig. 4.4.11) was conducted within the dashed outline. Dashed Z_e contours indicate a data gap due to film cahnge. Radar data within 16 km range has not been included due to confusion with ground clutter.

subjected to an intensive telephone hail survey (detailed hail survey map shown in Fig. 4.4.11). Because surface rain and hail reports were less dense outside this area and the storm dissipated rapidly as it passed southeastward over the radar site, the analysis of this storm will concentrate on the intense, mature stage northwest of the radar site.

During the approach of the storm, its radar appearance retained a high degree of continuity and did not exhibit particularly rapid changes in form or structure. A number of features showed this relatively continuous structure. UWER's, taking the form of notches in the right flank of the storm, were initially found at 1145 MST. These WER's became more organized, and one BWER existed continuously from 1248 to 1423 MST. The history and structure of this BWER will be considered in detail in Section 4.3.

Another feature which exhibited almost continuous behaviour was the storm top. Rapidly fluctuating turrets were not found; instead the storm top appeared to ascend slowly during the intense, mature stage between 1130 and 1430 MST. Figure 4.2.2 depicts this behaviour. It should be pointed out that by converting the time scale in Fig. 4.2.2 into a distance scale, using the storm velocity, it can be shown that there is approximately a nine-fold exaggeration in the vertical. This makes changes in the height of the radar storm top appear rapid, yet the average rate of change of the storm top height was only 0.3 m sec^{-1}. Such a small average rate of change in the maximum storm top is indicative of <u>the existence of a continuous storm updraft, the magnitude of which changes only slowly with time</u>.

As can be seen in Fig. 4.2.2, the storm top penetrated the warm frontal inversion at 1327 MST and reached its highest point at 1344 MST. After 1344 MST, the radar storm top decreased in height. Between 1401 and 1452 MST, the storm was directly over the radar site and the elevation angle

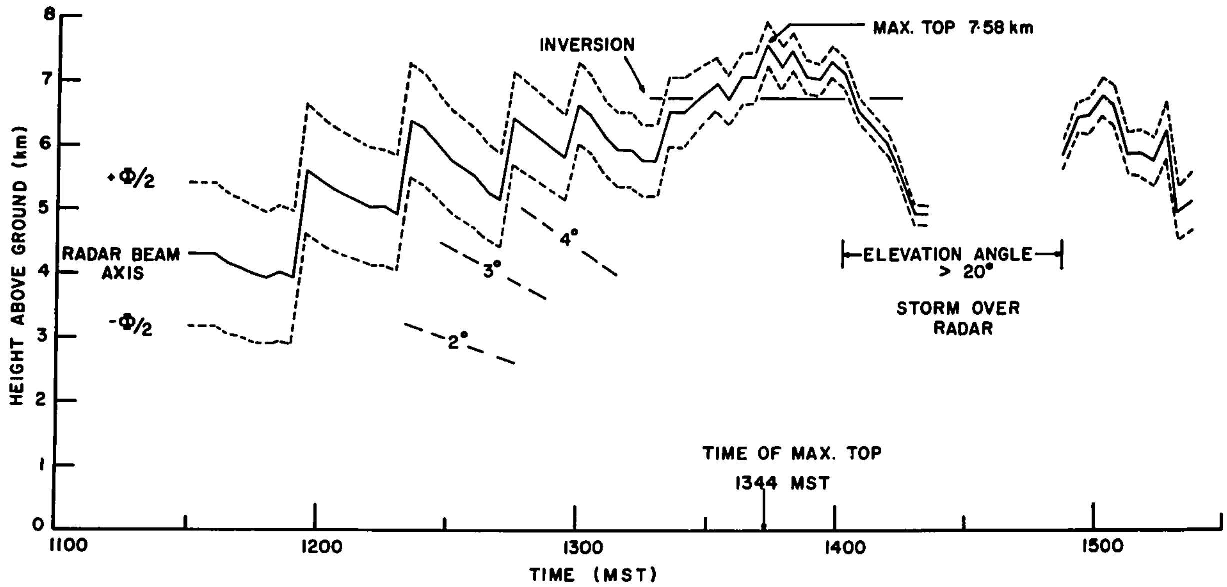

Fig. 4.2.2 Height of Maximum Radar Storm Top vs. Time - 29 June 1967. The height of the radar beam axis at 3 min intervals is indicated by the solid line. Upper and lower half-power beam points (Ø/2, -Ø/2) are delineated by dashed lines. Note penetration of inversion between 1327 and 1405 MST, and the general decrease in the height of the radar storm top after reaching a maximum at 1344 MST. The sawtooth pattern is due to the discrete (1 deg) increases in the radar-observed elevation angle on successive scans.

of the storm top was in excess of 20 deg. Thus, there are no measurements of the maximum storm top available during this period. Nonetheless, it is very unlikely that the storm top exceeded the 7.5 km maximum attained at 1344 MST. Instead, the storm top very likely decreased steadily between 1401 and 1452 MST. After 1452 MST, there is evidence of a brief increase in height until 1501 MST, then dissipation set in rapidly.

4.3 The Motion and Behaviour of the Bounded Weak Echo Region (BWER)

One of the most interesting features of this particular storm was the persistent and well-defined BWER. The first evidence of a WER was the observation of a notch-shaped UWER on the RH flank of the storm at 1145 MST. By 1203 MST, this notch had become more defined and was intermittently bounded

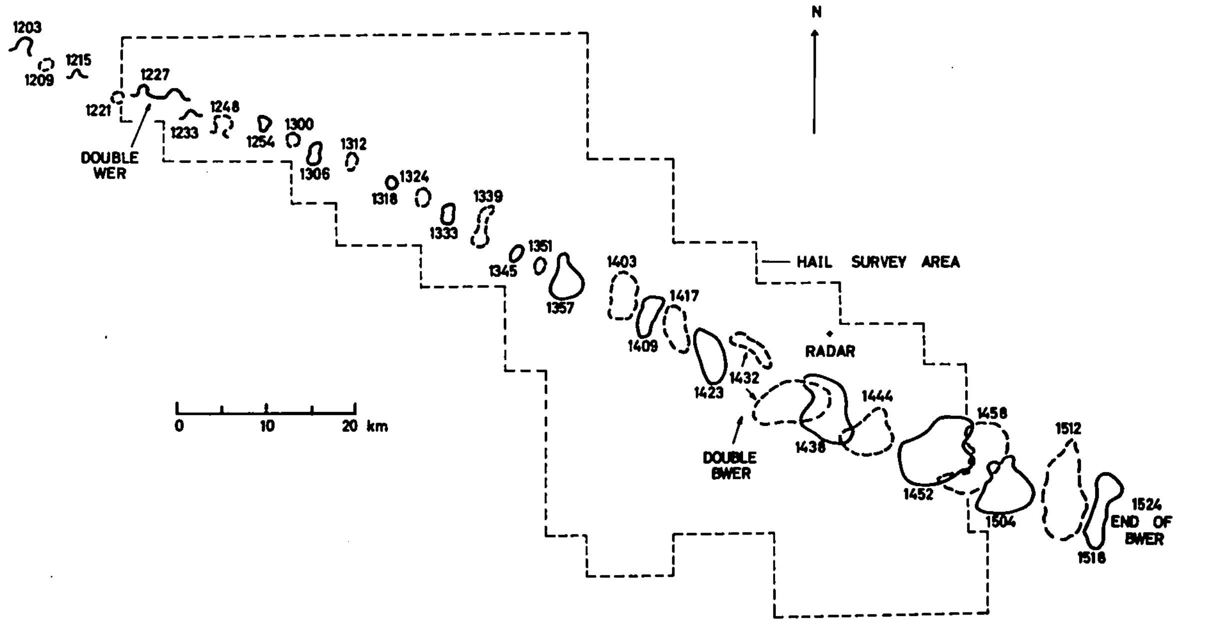

Fig. 4.3.1 History of the Weak Echo Region 1203-1524 MST - 29 June 1967. The location and shape of the UWER or BWER (that is the region without echo) is shown at 6 min intervals. Note the very regular behaviour of the BWER between 1254 and 1423 MST, and the rapid increase in the diameter of the BWER after 1420 MST. Double WER's are found at 1227 and 1432 MST.

between 1203 and 1248 MST, as is shown in the plan view of the WER history in Fig. 4.3.1. After 1248 MST, the UWER became completely bounded and the storm exhibited substantial organization and continuity for approximately 90 min. As illustrated in Fig. 4.3.1, it is possible to follow the movement of the BWER in an almost straight line between 1254 and 1423 MST. It was during this time that the storm was in its most intense stage.

At 1432 MST another phase began with the appearance of a second BWER downwind from the previous one. This new BWER continued until after 1518 MST when it dissipated rapidly. During this last phase (1432 - 1518 MST) the BWER reached its greatest horizontal dimensions (as large as 6.5 x 10 km), while the maximum storm top decreased and no hail was reported at the surface.

The formation of a new BWER, which appears to be a form of discontinuous propagation, was also found to occur in a similar manner at 1227 MST

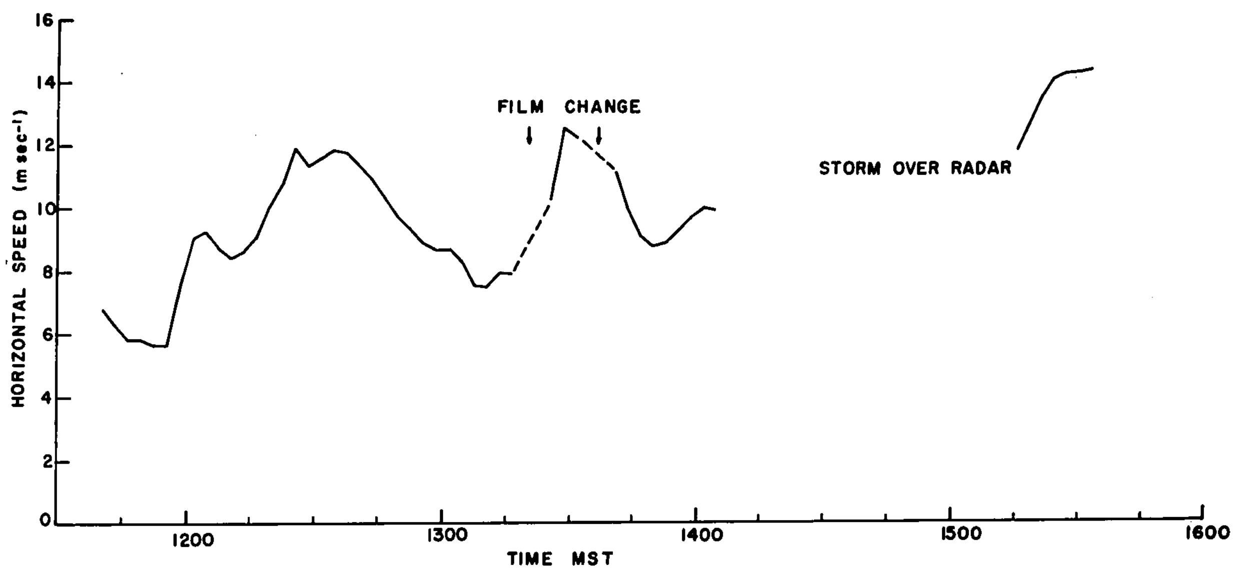

Fig. 4.3.2 Horizontal Storm Speed vs. Time - 29 June 1967. Note high storm speed during periods 1220 - 1235 MST and 1325 - 1340 MST.

(see Fig. 4.3.1). This phenomenon, which has been found to occur in other Alberta severe storms, usually results in the collapse of the original BWER (and its associated Z_e maximum) and the continuation of the recently formed BWER as the new center of activity. In this instance, it has resulted in a downwind shift of the storm center so that one would anticipate an increase in the apparent storm speed. Figure 4.3.2 depicts the horizontal storm speed as a function of time. The horizontal storm speed shown in this figure was obtained in the following fashion. The center of the Z_e maximum (at 0 deg) was located at 3 min intervals. Displacements over 15 min periods were determined for each 3 min interval. Horizontal storm speeds were then calculated using the 15 min displacements, resulting in a series of time-centered speeds (V_t) at 3 min intervals. These speeds were then smoothed using $\overline{V}_t = (V_{t-3} + 2V_t + V_{t+3})/4$; $\overline{V}_t$ being displayed in Fig. 4.3.2.

There is a definite maximum in the storm speed between 1220 and 1235 MST - the time of the first discontinuous UWER propagation. Difficulty in tracking the echo over the radar site (ground clutter and range dependent sensitivity) does not permit a comparison at 1432 MST. With such a substantial shift in the major BWER position, it is certain that there was an increase in the horizontal speed. Another maximum in the storm speed is apparent between 1325 and 1340 MST. This occurred during a film change, but there is evidence from the radar film record, just prior to the film change, which indicates that a new BWER was forming downstream from the current BWER at this time.

The mechanism of propagation is indeed an important one since the frequency and relative location of such events determine, to a large extent, the direction of storm motion and the horizontal speed. In this instance, the propagation took place in the downwind direction resulting in a storm motion almost coincident with the mid and high-level winds. This is not always the case; for example, propagation occurred in the storm of 14 July 1967 predominantly on the RH flank, yielding a storm motion to the right of the high-level winds as in the Browning SR model. In addition, the frequency of propagation for the 29 June 1967 storm was low, three occurrences of discrete propagation resulting in four continuous BWER phases of approximately 50 min length.

4.4 The Storm Reflectivity Structure in Three Dimensions

In order to depict the three-dimensional radar structure of this storm during its most intense stage, PPI sections and vertical cross-sections (in the direction of storm motion and normal to the direction of storm motion) will be illustrated at 1254, 1324 and 1356 MST. The position of the storm at these times, in relation to the radar, the hail survey area and the maximum Z_e envelope is illustrated in Fig. 4.4.1.

The first series of PPI sections, at 1254 MST, is shown in Fig.

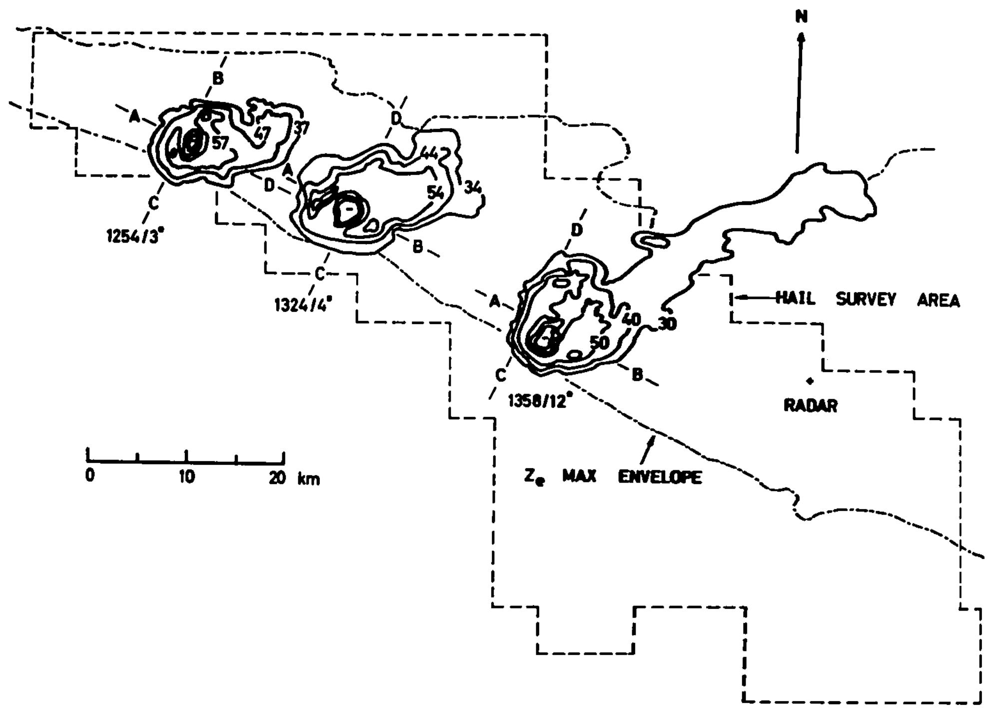

Fig. 4.4.1 Storm Position at 1254, 1324 and 1358 MST - 29 June 1967. Locations of the storm at 1254 MST (4.0 km AGL), 1324 MST (3.8 km AGL) and 1358 MST (5.6 km AGL) are illustrated as well as axes for vertical cross-sections (lines AB and CD) in the direction of storm motion and normal to it.

4.4.2. A UWER appears at 1 deg elevation as a notch-shaped feature on the RH flank of the storm. This notch-shaped UWER gives way to an almost completely bounded WER at 2 deg, and to a BWER at 3 deg. Above the BWER, and displaced slightly downwind, is a Z_e maximum which may be followed downward to a position at the surface downwind and to the LH side of the BWER. The Z_e values in this area exceeded 67 dBz so that hail and heavy rain would be anticipated in this region. A secondary maximum, of lesser areal extent, is also found on the upwind side of the BWER. From the Z_e values, hail would also be anticipated at the surface at this location.

Figures 4.4.3 and 4.4.4 are vertical cross-sections at 1254 MST in the direction of storm motion (along line AB) and normal to the direction of storm motion (along line CD). The cross-section in the direction of storm motion (Fig. 4.4.3) depicts the BWER entering the storm from the downwind

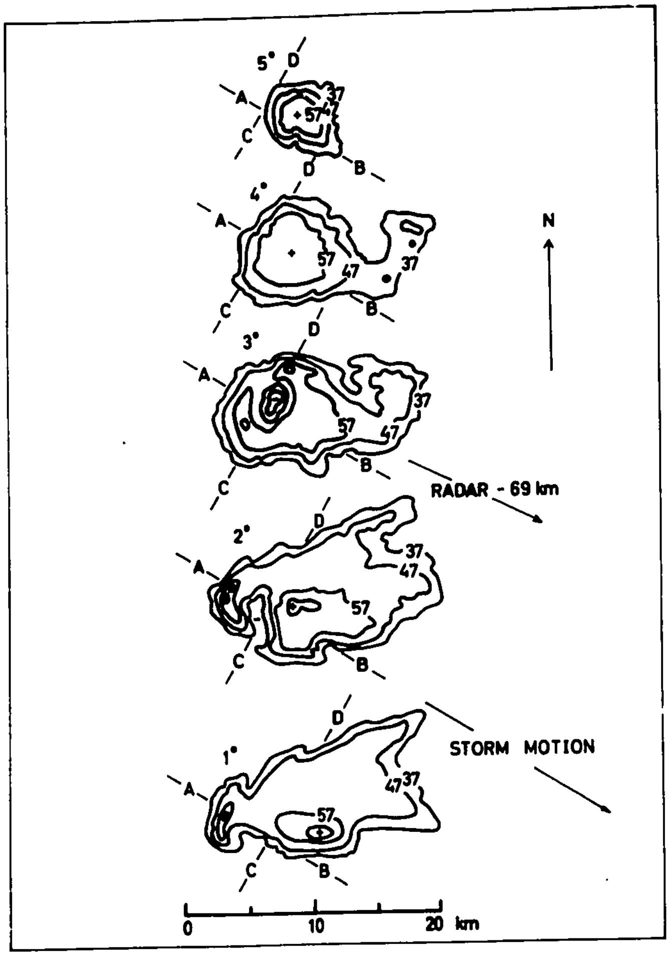

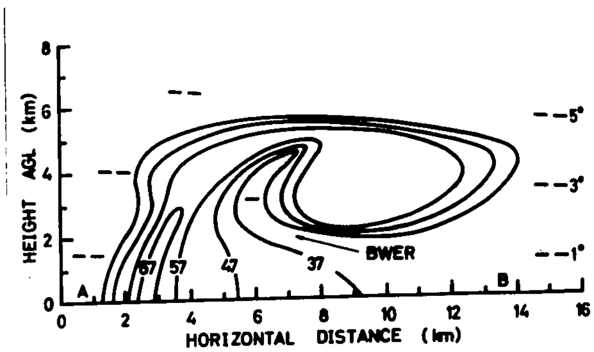

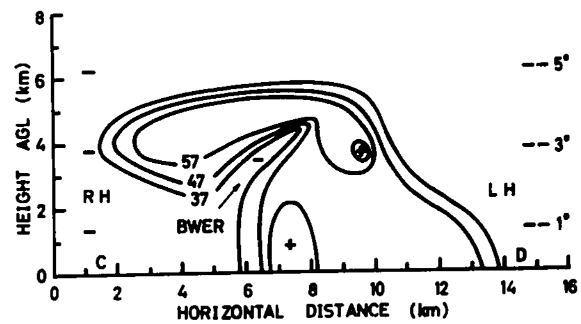

Fig. 4.4.2 (Left) PPI Sections at 1254 MST - 29 June 1967. Contours of Z_e are labelled in dBz and elevation angles indicated in deg. Note the UWER at 1, 2 deg elevation and BWER at 3 deg elevation. Lines AB and CD indicate cross-section axes for Figs. 4.4.3 and 4.4.4.

Fig. 4.4.3 (Top Right) Vertical Cross-Section in the Direction of Motion at 1254 MST - 29 June 1967. Contours of Z_e are labelled in dBz. Note path of BWER toward the upwind side of the storm in lower levels to be sheared downwind near the storm top.

Fig. 4.4.4 (Bottom Right) Vertical Cross-Section Normal to the Direction of Motion at 1254 MST - 29 June 1967. The storm is viewed looking upstream. Note tilt of BWER toward the LH flank (right hand side of the figure) of the storm.

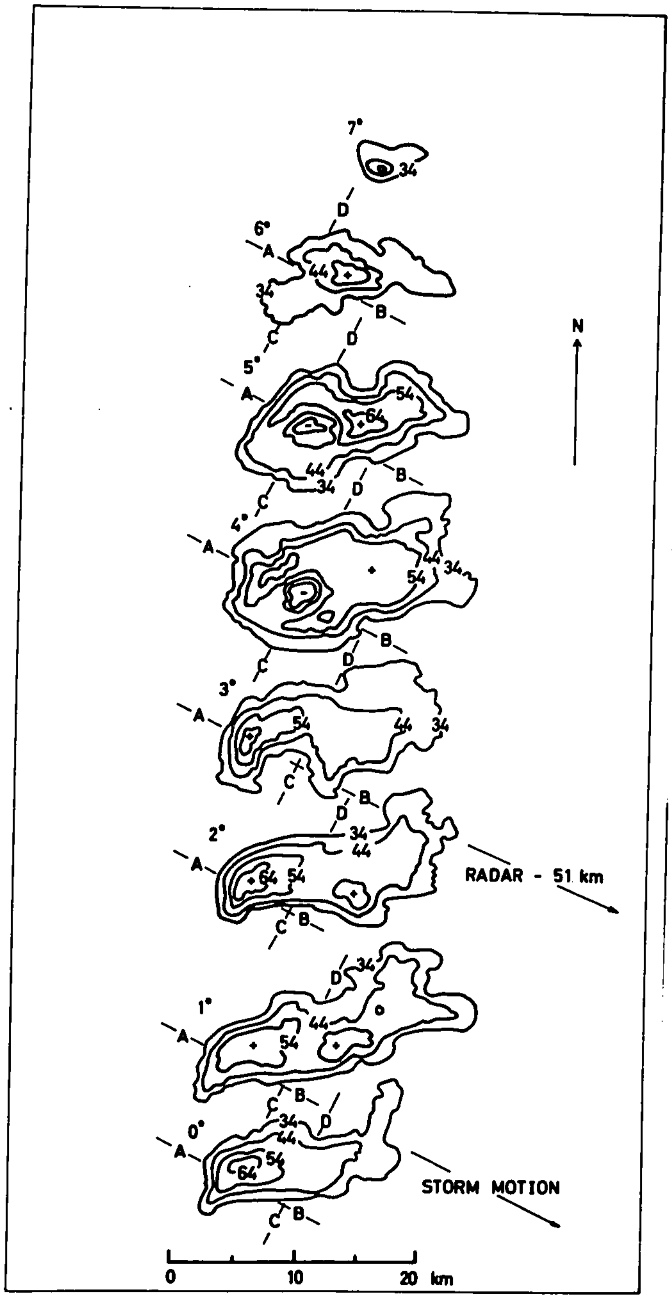

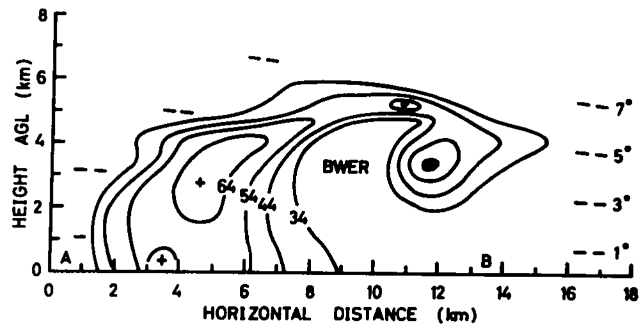

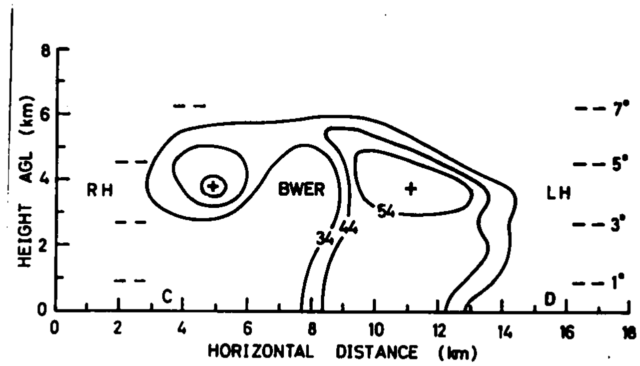

Fig. 4.4.5 (Left) PPI Sections at 1324 MST - 29 June 1967. Contours of Z_e are labelled in dBz and elevation angles are indicated in deg. Note UWER at 3 deg and BWER at 4, 5 deg elevation. Lines AB and CD indicate cross-section axes for Figs. 4.4.6 and 4.4.7.

Fig. 4.4.6 (Top Right) Vertical Cross-Section in the Direction of Motion at 1324 MST - 29 June 1967. Note path of BWER toward the upwind side of the storm at low levels and the downwind tilt near the storm top.

Fig. 4.4.7 (Bottom Right) Vertical Cross-Section Normal to the Direction of Motion at 1324 MST - 29 June 1967. Note tilt of BWER toward the LH flank (right side of the figure) of the storm.

side and ascending toward the upwind side. This trend changes rapidly with height, resulting in a downwind tilt to the BWER near the storm top. Normal to the cross-section along AB, the cross-section along CD (Fig. 4.4.4) reveals that the BWER enters the storm from the RH flank and tilts toward the LH flank. The secondary Z_e maximum is seen in the vertical, upwind of the BWER in Fig. 4.4.3. Figure 4.4.4 shows the major Z_e maximum on the LH side of the BWER.

Half an hour later, a very similar situation is found at 1324 MST. As shown by the PPI sections in Fig. 4.4.5, there is a UWER at 3 deg which becomes a BWER at 4 and 5 deg elevation. A Z_e maximum caps the BWER at 6 and 7 deg. The vertical cross-section in the direction of motion along line AB (see Fig. 4.4.6) shows a BWER entering the storm from the downwind side of the storm, tilting upwind, and then reversing this tilt to the downwind direction. The vertical cross-section normal to the direction of motion, shown in Fig. 4.4.7, illustrates the BWER entering the storm from the RH flank, tilting toward the LH flank with height. Although there are differences in detail between 1254 and 1324 MST, the basic radar configuration is the same.

An hour after the initial cross-section at 1254 MST, and a half hour after the second cross-section at 1324 MST, the basic radar configuration is still essentially the same. In the selected PPI sections, shown at 1356 MST in Fig. 4.4.8, a BWER is found at 7 deg and continues through to 14 deg, being capped by a Z_e maximum. This Z_e maximum may be traced downward to the surface to a position on the LH flank, downwind from the BWER. A secondary Z_e maximum is shown on the upwind side of the BWER, in the form of a hook-shaped appendage on the RH side. The vertical cross-section along line AB in the direction of storm motion in Fig. 4.4.9 shows the BWER entering from the

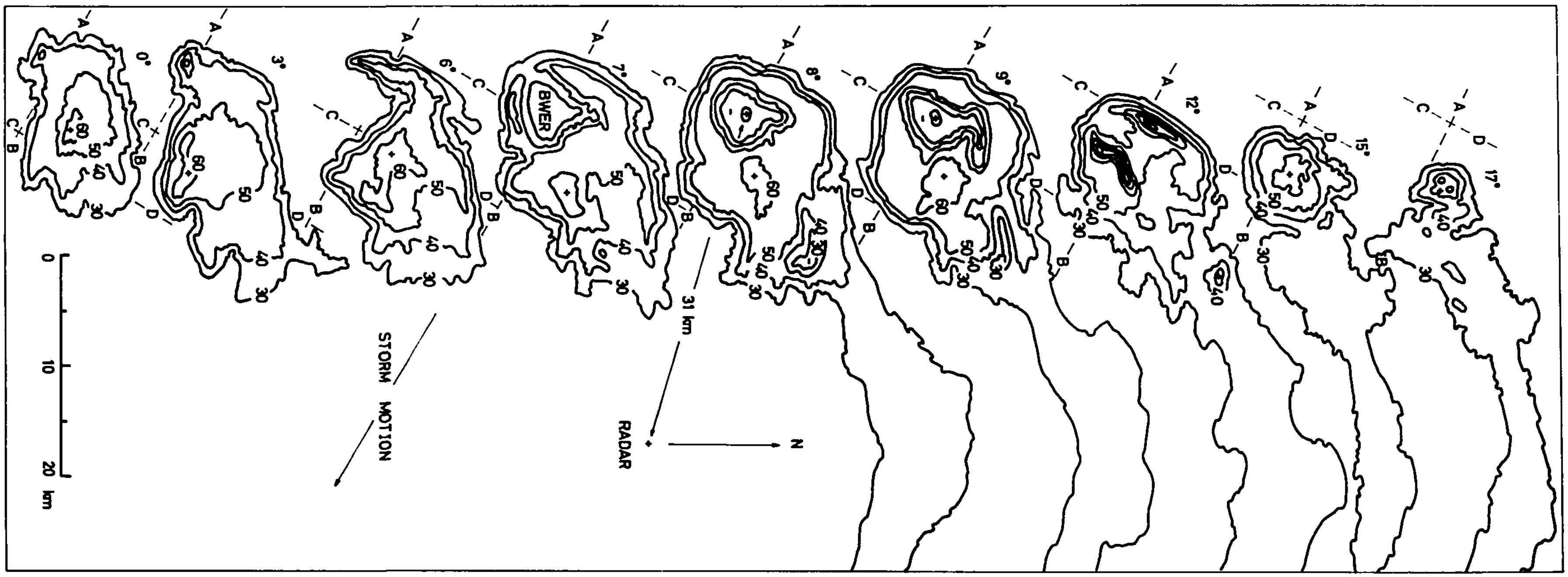

Fig. 4.4.8 Selected PPI Section at 1356 MST - 29 June 1967. Contours of Z_e are labelled in dBz and elevation angles are indicated in deg. Note BWER above 6 deg elevation and the Z_e maximum on the left hand downwind side of the BWER. Lines AB and CD indicate cross-section axes for Figs. 4.4.9 and 4.4.10.

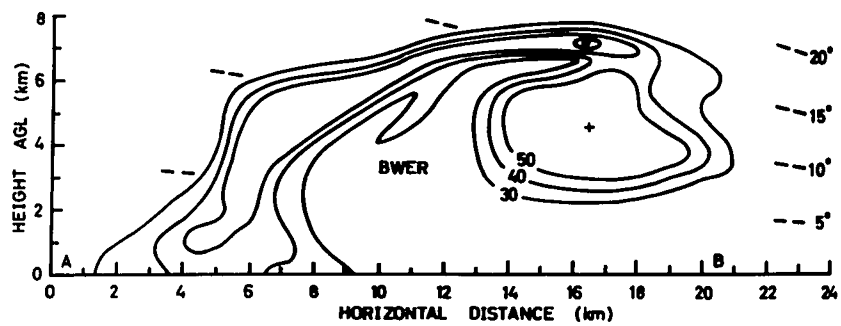

Fig. 4.4.9 Vertical Cross-Section in the Direction of Motion at 1356 MST - 29 June 1967. Contours of Z_e are labelled in dBz and elevation angles are indicated in deg. Note the path of the BWER to a point just beneath the storm top, with a sharp tilt in the downwind direction.

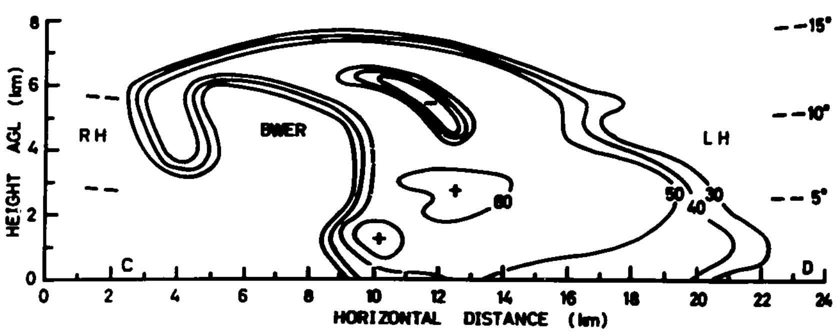

Fig. 4.4.10 Vertical Cross-Section Normal to the Direction of Motion at 1356 MST - 29 June 1967. Contours of Z_e are labelled in dBz and elevation angles are indicated in deg. The storm is viewed in the upstream direction. Note the BWER on the RH flank of the storm and the secondary extension which indicates that the BWER is directed out of the plane of the figure.

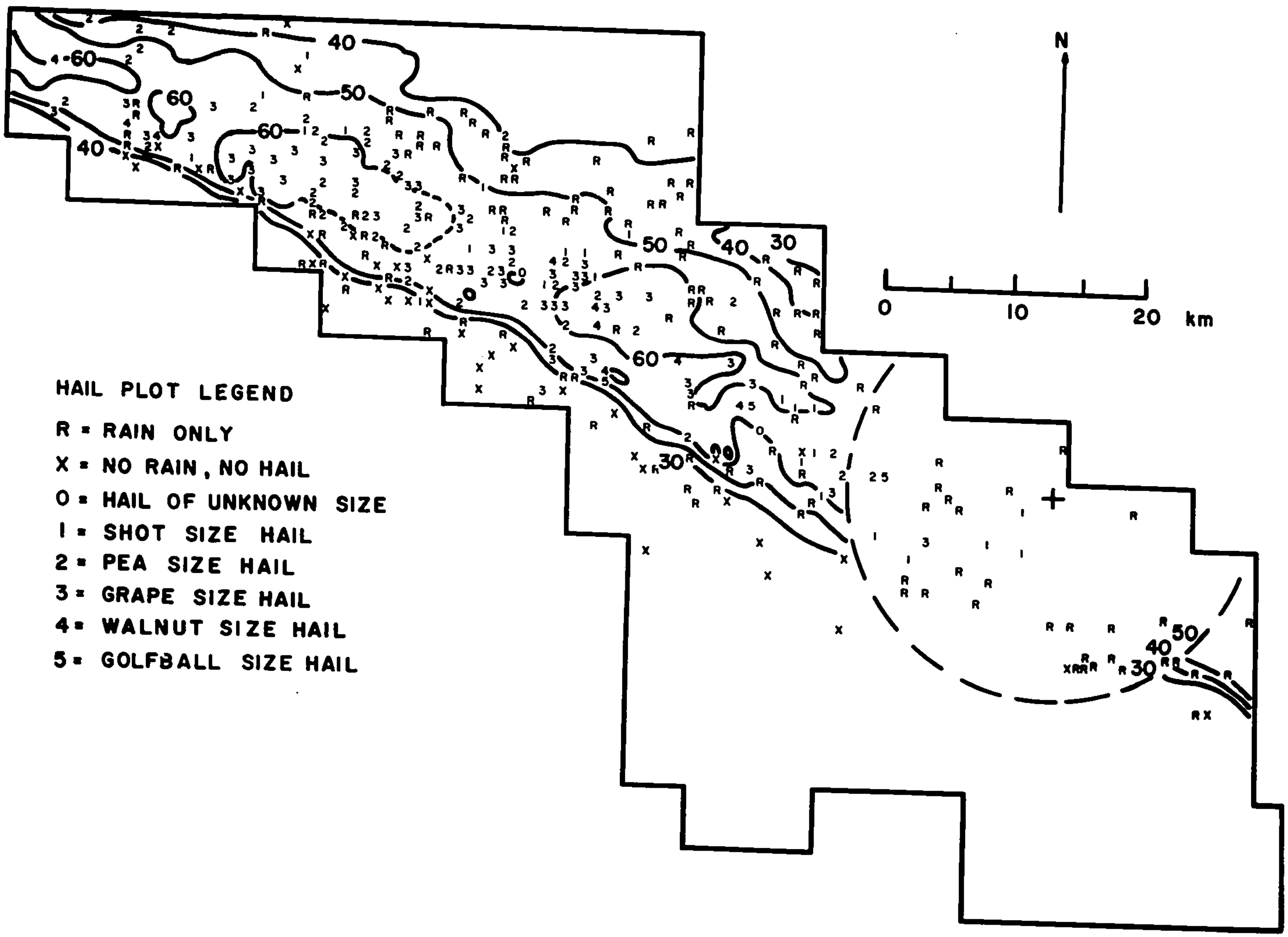

Fig. 4.4.11 Maximum Z_e Envelope and Hail Survey Data. Hail reports are shown in relation to the maximum Z_e which occurred at 0 deg elevation. Note the sharp reflectivity gradient on the RH boundary and the occurrence of large hail in conjunction with this gradient region. The weak gradient of the LH side is associated with a gradual decrease of hail size, eventually yielding to rain-only reports.

downwind side, reversing the upwind tilt rapidly to lean in the downwind direction. The secondary Z_e maximum is also seen in Fig. 4.4.9 on the upwind side of the storm. Normal to the direction of storm motion, the cross-section in Fig. 4.4.9 indicates the BWER entering the storm on the RH flank. Since the BWER tilts substantially in the downwind direction, an extremity of the BWER is seen on the LH side of the major BWER, directed out of the plane of the figure. The Z_e maximum is seen clearly on the LH side of the BWER.

The picture of this storm which emerges during the intense mature stage is of a radar structure dominated by a BWER. This BWER enters the storm from the right hand, downwind quadrant and slopes upwind while penetrating toward the LH flank of the storm. The BWER tilt, in the plane of storm motion, reverses to tilt downwind near the storm top. A major Z_e maximum caps the BWER and can be traced to the surface, paralleling the BWER to lie to the left and downwind of the BWER. The BWER and Z_e maxima lie in close proximity to one another resulting in characteristic strong reflectivity gradients along their common side. The Z_e values, found associated with the Z_e maxima near the surface, are indicative of hail in these regions. Figure 4.4.11 confirms this in that large hail is found to appear abruptly on the RH side of the maximum Z_e envelope. The majority of the hail occurs along the central axis of the maximum Z_e envelope in conjunction with the major storm Z_e maximum. In the weak reflectivity gradients on the LH side of the maximum Z_e envelope in Fig. 4.4.11, successively smaller hail is found, eventually yielding to "rain only" reports.

CHAPTER V

A RADAR CASE STUDY OF THE STORM

OF 27 JUNE 1967

5.1 Airmass and Wind Structure in the Vertical

The storm which will be examined in this chapter differed considerably from the three preceding storms. Of the four storms, it was the smallest, least energetic and did not exhibit a well defined BWER. Nonetheless, it was still capable of yielding pea and grape size hail at the surface. As will be seen in this chapter and chapters to follow, the reason for this anomalous behaviour can be attributed in large measure to the prevailing airmass and wind structure in the vertical.

A radiosonde sounding taken at the radar site at 1617 MST is shown in Fig. 5.1.1. The airmass structure is warmer than the 29 June 1967 case (see Chap. IV) by approximately 5 deg C, and more representative of late spring and early summer airmass conditions in Alberta. No frontal inversions appear on this sounding, and serial soundings taken between 1221 and 1818 MST show only minor changes during this period. It is evident that the storm of 27 June 1967 existed in a consistent airmass and was not influenced by frontal phenomena.

A moist adiabatic parcel trajectory (using representative cloud base temperatures and taking adiabatic liquid water loading into account), also illustrated in Fig. 5.1.1, indicates only minor instability (major contribution between 650 and 500 mb) with a maximum storm top of approximately 7.2 km AGL. The small "positive area" shown in Fig 5.1.1 is indicative of

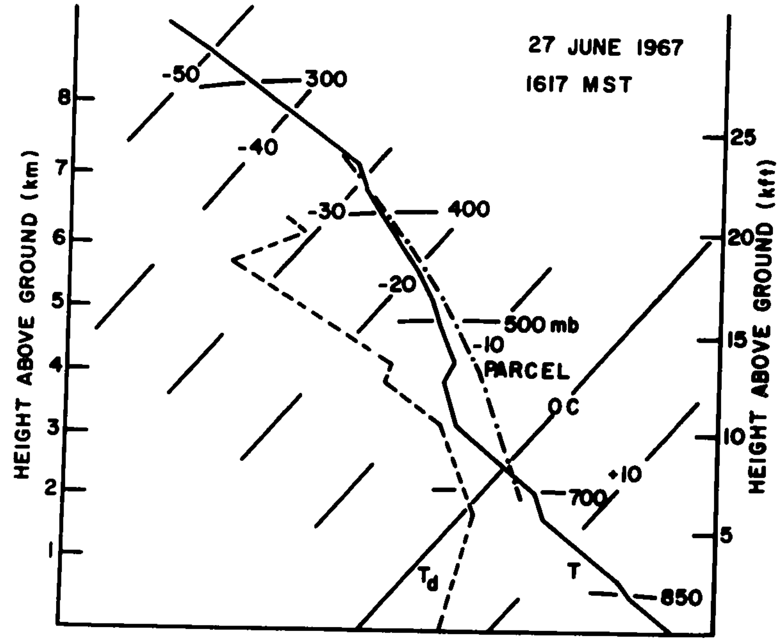

Fig. 5.1.1 Radiosonde Sounding 1617 MST - 27 June 1967. Dot-dash line indicates a moist adiabatic parcel trajectory using representative cloud base conditions. Note major contribution to "positive area" between 650 and 500 mb.

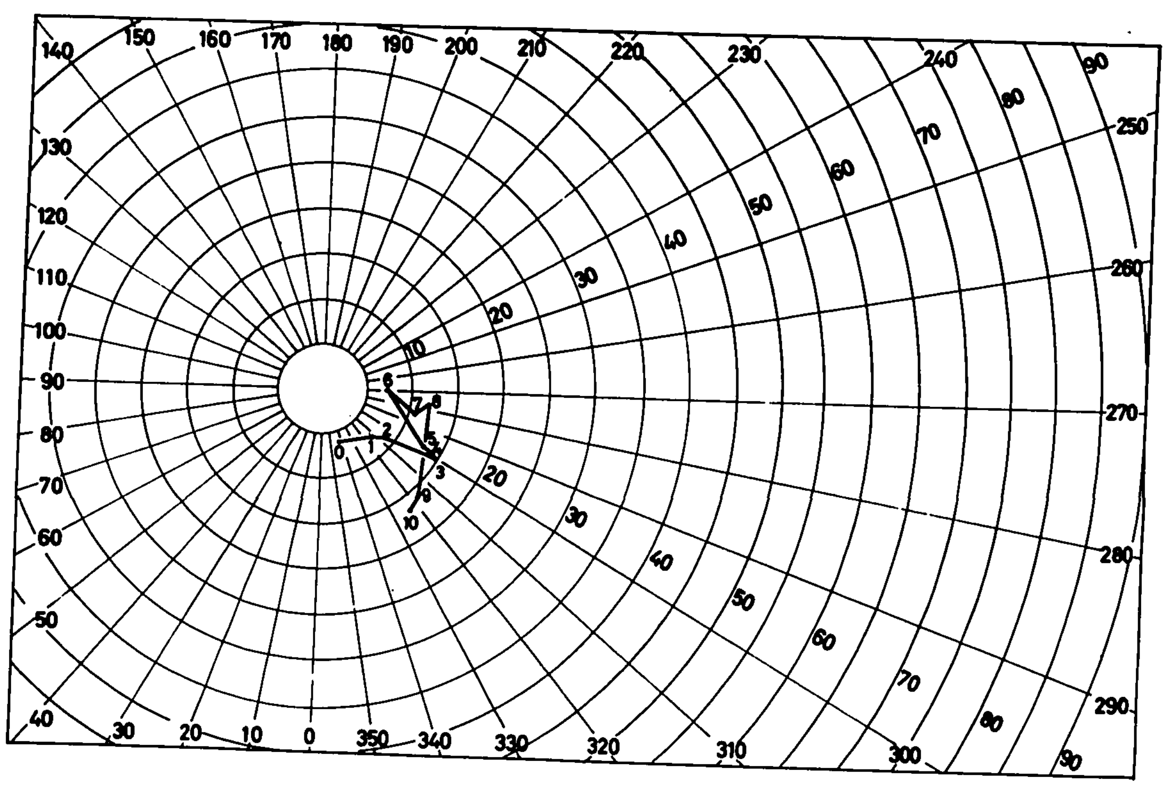

Fig. 5.1.2 Wind Hodograph 1617 MST - 27 June 1967. Wind speeds are plotted in m sec^{-1} and heights are indicated in km AGL. Note wind maximum of 16 m sec^{-1} at 3 km and decreasing wind speeds between 3 and 6 km.

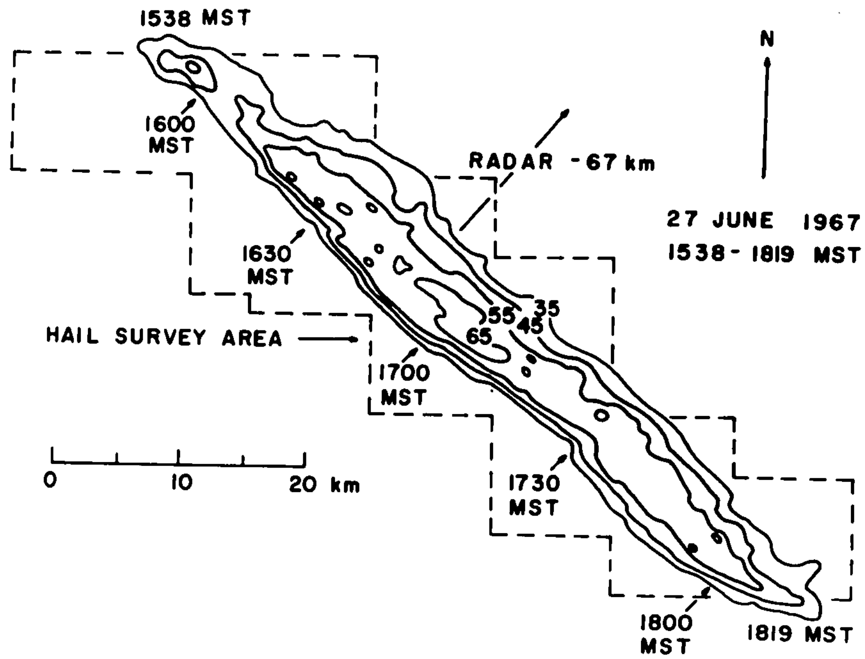

Fig. 5.2.1 Maximum Z_e Envelope 1538 - 1819 MST - 27 June 1967. The envelope of maximum Z_e values (dBz) at 0 deg elevation is shown for the period 1538 - 1819 MST. A telephone hail survey was conducted within the area inside the dashed outline.

a relatively weak storm updraft. Calculations (in Chap. VII) have shown that the maximum vertical velocity in the updraft core of this storm would be 16.4 m sec^{-1}.

The wind structure in the vertical on 27 June 1967 is displayed by the hodograph in Fig. 5.1.2. A maximum wind of 16 m sec^{-1} occurs at 3 km AGL although on the whole the winds below 7 km average about 10 m sec^{-1}. As will be seen in Section 5.3, this weakly-sheared, ill-defined wind structure resulted in an essentially vertical storm which exerted a profound influence on the mode of storm operation.

5.2 The History of the Storm of 27 June 1967

As illustrated in Fig. 5.2.1, the storm of 27 June 1967 was first detected by radar at 1538 MST WSW of the radar site at a range of 72 km. As

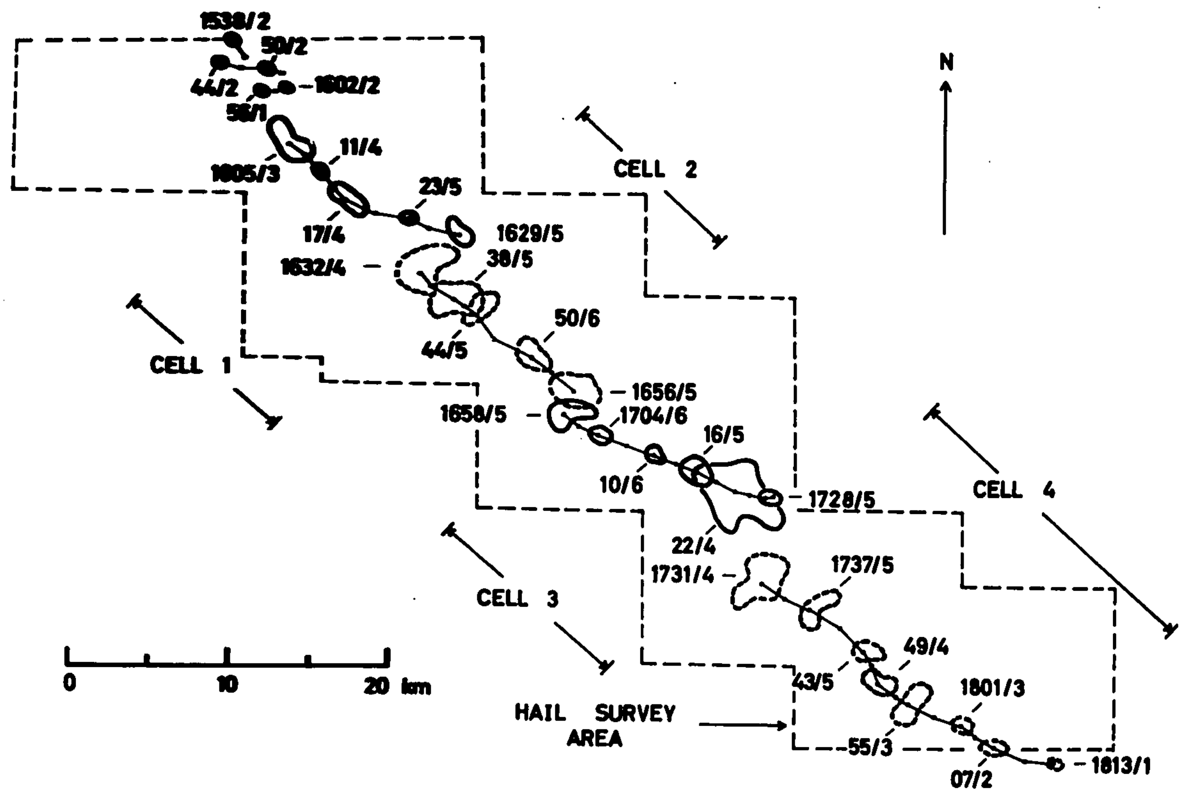

Fig. 5.2.2 **Horizontal Movement** of the Maximum Radar Storm Top - 27 June 1967. **Locations of the** radar storm top are shown at 3 min intervals (with echo **configurations** at 6 min intervals) for the period 1538 - 1813 MST. Times (MST) **and elevation** angles (deg) are indicated (eg. 1538/2 denotes 1538 MST, 2 deg **elevation**). **Note** the formation of a new cell on the RH flank of the dissipating **cell at** 1632, 1658 and 1731 MST.

the storm developed, it travelled southeastward for a period of 2 3/4 hr, eventually dissipating 78 km SSW of the radar site at 1819 MST. Unlike the three storms previously examined, this storm developed, matured and dissipated within radar range and did so at almost constant range.

Examining the maximum Z_e envelope in Fig. 5.2.1, it is evident that prior to about 1615 MST, the Z_e values at the surface exceeded 45 dBz only briefly. However, between 1615 and 1800 MST, maximum Z_e values were greater than 55 dBz and, on occasion, exceeded 65 dBz (particularly at about 1700 MST). With Z_e values of this magnitude between 1615 and 1800 MST, it is not surprising that shot to grape size hail was reported at the surface.

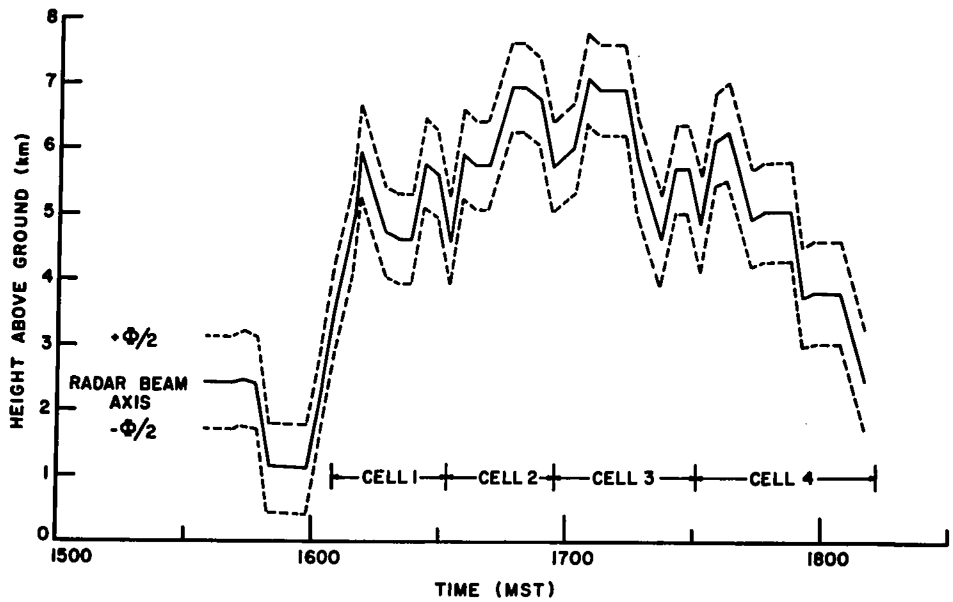

Fig. 5.2.3 Height of the Maximum Radar Storm Top vs. Time - 27 June 1967. The height of the radar beam axis at 3 min intervals is indicated by the solid line. In addition, the upper and lower half-power radar beam points (Ø/2, -Ø/2) are delineated by dashed lines. Note characteristic increase then decrease in storm top in conjunction with Cells 1, 2, 3 and 4.

A study of the radar records reveals that this storm was cellular in structure, each cell progressing through a characteristic cycle of development, maturity and dissipation with a cycle time (as observed by radar) of approximately 25 - 35 min. There are several methods of demonstrating the existence of this cycle mechanism. The first is an examination of the behaviour (in the horizontal) of the maximum radar storm top as shown in Fig. 5.2.2. The motions of the storm top are complex prior to 1605 MST, but a definite pattern emerges thereafter. Tracking the series of storm tops designated as Cell 1 (see Fig. 5.2.2), it is found that this cell begins at 1605 MST and can be tracked until 1629 MST. Following 1629 MST, a new cellular storm top appears abruptly on the RH flank of Cell 1. This new storm top (designated Cell 2) continues on a straight path until it dissipates at 1656 MST, being replaced by Cell 3 on its RH flank at 1658 MST. This discrete formation of a new cell occurs a fourth and final time at 1731 MST, eventually dissipating by 1819 MST.

The second method of demonstrating the discrete cellular nature of this storm is to examine the behaviour of the height of the radar storm top shown in Fig. 5.2.3. In association with each cell, the storm top characteristically ascends to a maximum height, pauses briefly and then descends. It might be pointed out that while radar observations indicate a cycle time of approximately 25 - 35 min, it is only the upper reaches of the cell development which is observed by radar and depicted in Fig. 5.2.3. During the 25 - 35 min cycle, the cell top rises approximately 1.2 - 1.8 km and then descends into the general echo mass, no longer remaining an easily identifiable feature. However, Cell 4, being the last of the series, demonstrates a dissipation stage and lasts a total of 42 min. Making allowances for additional time for development, it is conceivable that each storm cell lasted for approximately 60 min with only the middle 25 - 35 min being detected as a radar-identifiable feature.

The rate of ascent of the radar storm tops during their developing stage is found to be approximately 5 - 7 m sec^{-1}. During this ascent stage, it is most probable that the radar detected precipitation particles with a finite fallspeed. Consequently, the updraft within the cell would be expected to be greater than the apparent 5 - 7 m sec^{-1}. As will be shown in Chap. IX, graupel particles of 1.5 - 3.5 mm diameter (fallspeed 3 - 8 m sec^{-1}) would be expected near the storm top, resulting in a deduced updraft velocity of approximately 8 - 15 m sec^{-1}. On the other hand, the descent rate of the radar storm tops was less (≈2 - 4 m sec^{-1}). This is indicative of continued support of these particles in a strong updraft or the fallspeed of small ice particles from the glaciated storm top. Such fallspeeds (≈ 2 - 4 m sec^{-1}) are similar to those deduced by Hitschfeld (1959) in a study of plumes and anvils associated with thunderstorms.

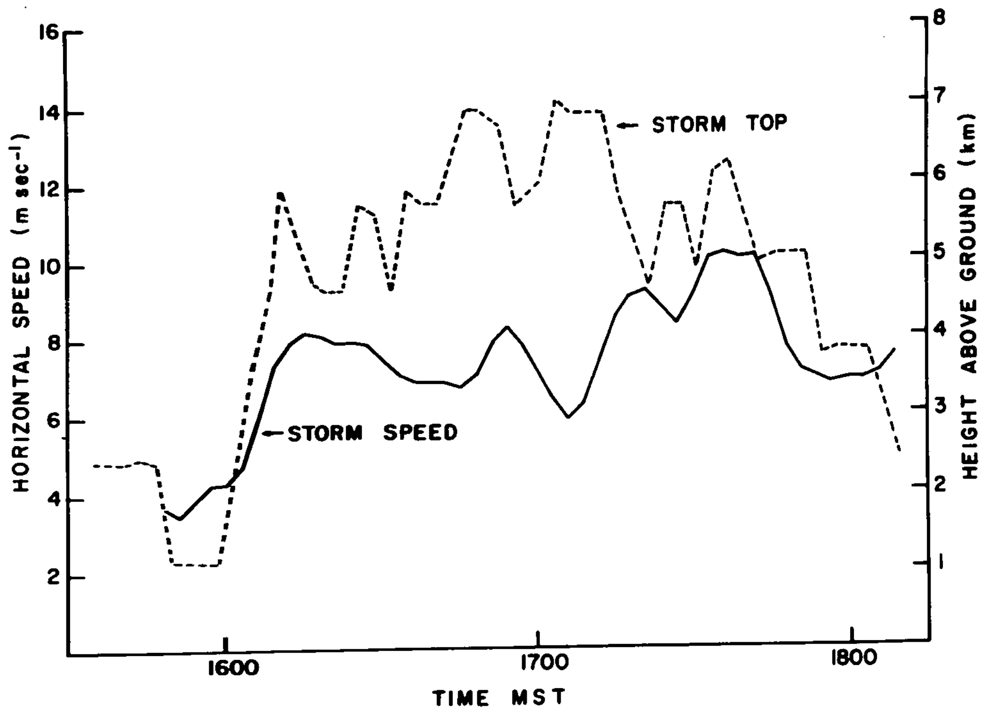

Fig. 5.2.4 Horizontal Storm Speed vs. Time - 27 June 1967. In addition to the horizontal storm speed, the height of the radar storm top is illustrated as well. Note the maxima in storm speed and how they are related to the radar storm top maxima for each cell (see also Fig. 5.2.3).

Effects of the cellular structure of this storm also appear at the surface, although to a lesser degree. Figure 5.2.4 illustrates the horizontal speed of the "center of gravity" of the Z_e maximum at 0 deg elevation. This horizontal speed was obtained in the same manner as described in Chap. IV. In spite of numerous masking effects (shear sorting of precipitation, film registry, etc.,), there are distinct maxima in the horizontal speed which correspond with the times of maximum radar storm tops (also shown in Fig. 5.2.4). There is, however, a slight time lag between the time of maximum storm top and the time of maximum horizontal speed. The higher the storm top, the greater is the time lag. The time lag averaged 6 - 7 min for the cases studied. It is suggested that this lag arises from the time which is required for large precipitation particles associated with a developing storm top to fall to the surface. Using an average storm top of 6 km

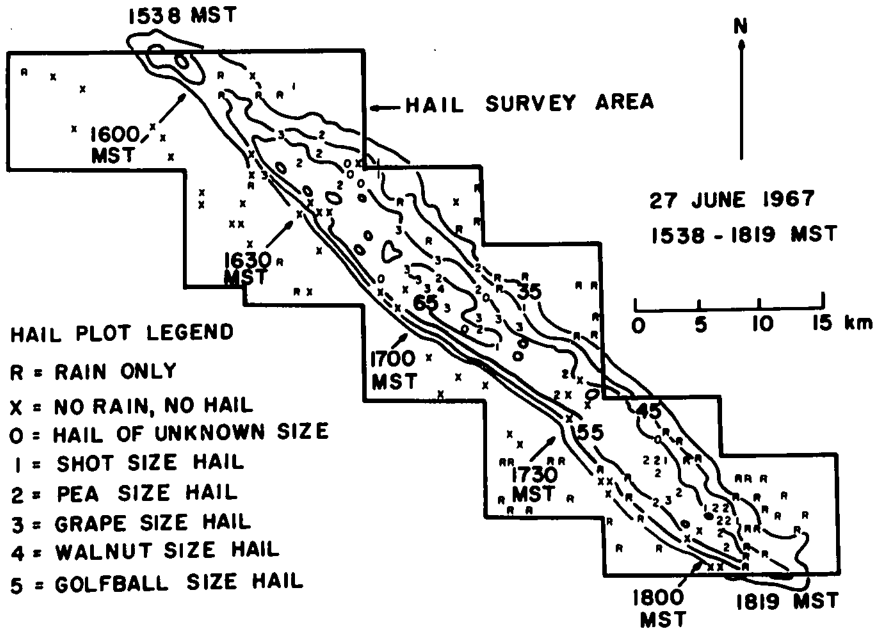

Fig. 5.2.5 Maximum Z_e Envelope and Hail Survey Data - 27 June 1967. The envelope of maximum Z_e at 0 deg elevation for the period 1538 - 1819 MST is shown in conjunction with surface rain and hail reports. Approximate times of storm location are also indicated. Note the correspondence between hail reports and Z_e values in excess of 55 dBz.

and an average fallspeed of 15 m sec^{-1}, the resulting descent time is 6.7 min. The increase observed in horizontal speed of the Z_e maximum is clearly due to the interaction between the ascending - descending storm cell and the environmental wind. It was not the highest penetrating cell which achieved the maximum storm speed. However, referring to Fig. 5.1.2, it is found that the environmental wind reached a maximum at 3 km and decreased between 3 and 6 km. On this basis, the less penetrative storm cells would be expected to have the greatest horizontal speed.

The surface rain and hail reports, shown in Fig. 5.2.5 together with the Z_e maximum envelope, display an interesting pattern. Between 1538 and 1600 MST, when the storm tops are lower than 3 km (and updrafts correspondingly low), there are reports of "rain only" at the surface. The first surface hail reports appear at approximately 1615 - 1620 MST, in conjunction with the maximum development of Cell 1 at 1610 MST. Hail reports continue to be found at the surface until shortly after 1800 MST when the radar storm top descends below 4 km. It is of significance, however, that the largest hail (grape and walnut size) is found at the surface between 1645 and 1715 MST associated with Cells 2 and 3. These cells were the highest of the four cells in this storm. This pattern clearly suggests that the development of the largest precipitation occurred in the highest penetrating storm cells and, in addition, that a critical height and/or updraft was required for the formation of hail large enough to reach the surface.

5.3 The Storm Reflectivity Structure in Three Dimensions

In order to demonstrate the three dimensional reflectivity structure of this storm, PPI sections and vertical cross-sections along and normal to the direction of motion will be illustrated for Cell 3 at 1659, 1708 and 1722 MST. These three times correspond approximately to the developing, mature and dissipating stages of this cell.

Figure 5.3.1 shows a series of PPI sections at 1659 MST. The pattern is somewhat similar to that exhibited by the 29 June 1967 storm in Chap. IV. A notch-shaped UWER appears at 1 and 2 deg elevation and is capped by a reflectivity maximum at 3 and 4 deg. Although this UWER is neither bounded nor well defined (due partly to its small size and the finite radar beamwidth), this was the closest the storm came to achieving a BWER.

There are two Z_e maxima illustrated in the PPI sections in Fig. 5.3.1. At 0, 1 and 2 deg, a Z_e maximum appears on the LH flank displaced toward the downwind side of the storm. This Z_e maximum is due to the remaining precipitation from the dissipating stages of Cell 2. The vertical cross-section along line CD shown in Fig. 5.3.3 also illustrates this remnant of

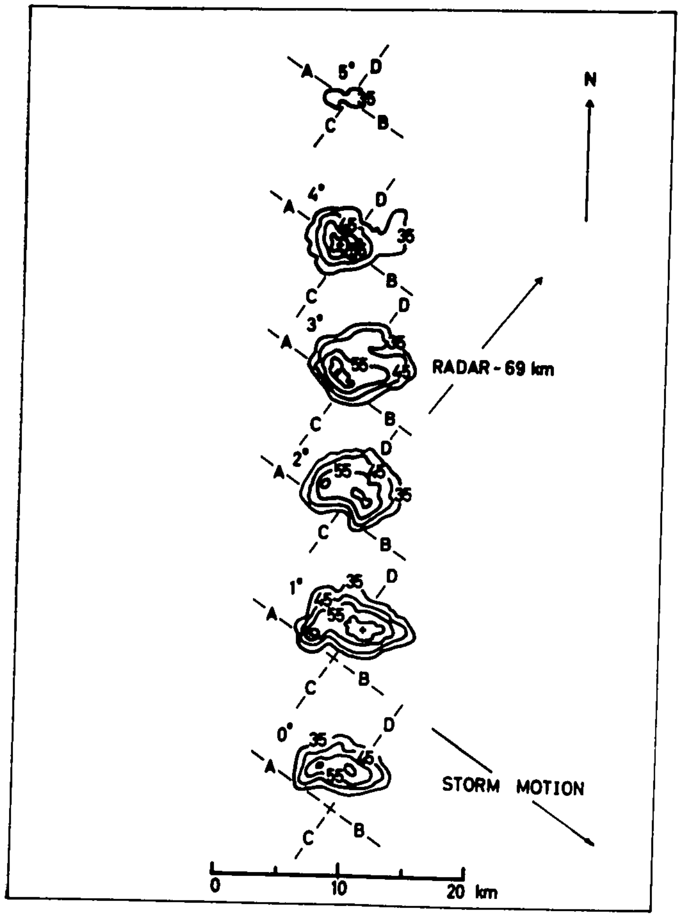

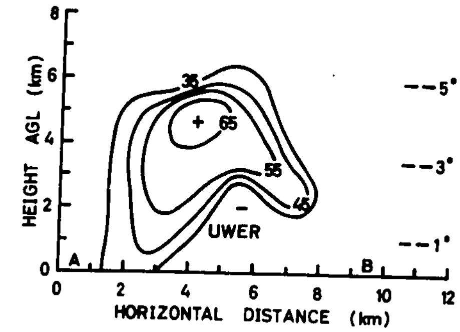

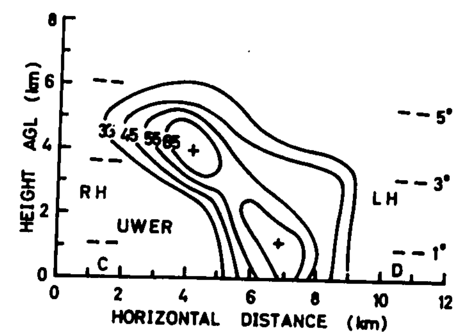

Fig. 5.3.1 (Left) PPI Sections at 1659 MST - 27 June 1967. Contours of Z_e are labelled in dBz. Note notch-shaped WER at 1,2 deg elevation and the existence of two Z_e maxima. Lines AB and CD indicate cross-section axes for Figs. 5.3.2 and 5.3.3.

Fig. 5.3.2 (Top Right) Vertical Cross-Section in the Direction of Motion at 1659 MST - 27 June 1967. Contours of Z_e are labelled in dBz. Note the notch-shaped UWER entering the storm from the downwind side and the highest point in the storm directly above the UWER.

Fig. 5.3.3 (Bottom Right) Vertical Cross-Section Normal to the Direction of Motion at 1659 MST - 27 June 1967. Contours of Z_e are labelled in dBz. Note the UWER which enters the storm from the RH side, and the Z_e maximum which exists above the UWER.

Cell 2 on the LH flank of the storm (right side of Fig. 5.3.3). Figure 5.3.2 and Fig. 5.3.3 show the UWER entering the storm from the downwind side and the RH flank respectively. The highest point in the storm is almost directly above the UWER, and the second Z_e maximum associated with the newly developing Cell 3 is offset slightly upwind and to the LH side of the UWER axis.

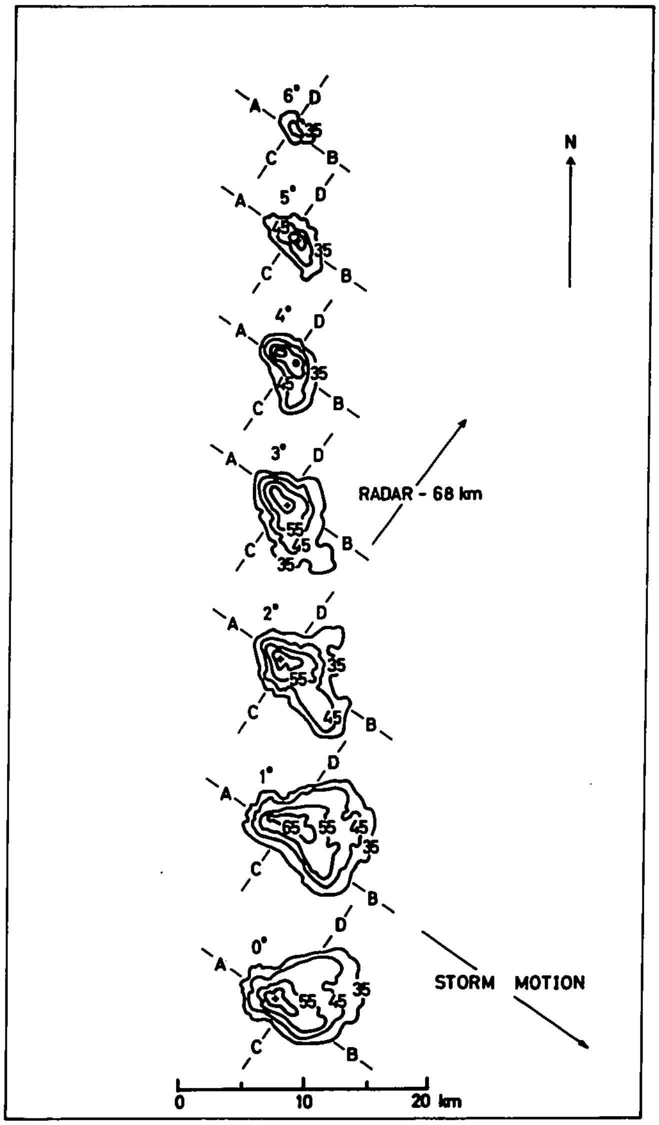

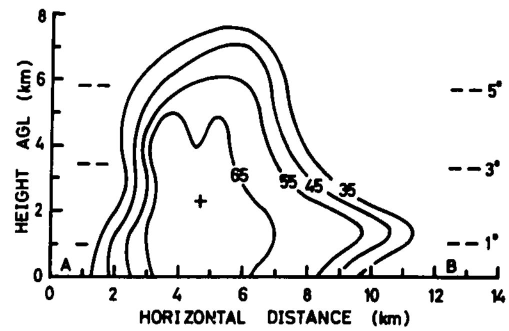

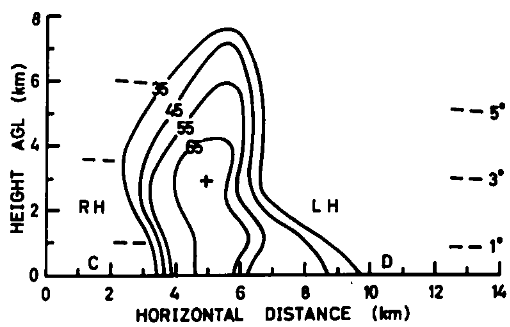

Fig. 5.3.4 (Left) PPI Sections at 1708 MST - 27 June 1967. Contours of Z_e are labelled in dBz. Note the absence of a WER and the existence of one Z_e maximum which extends almost vertically through the storm. Lines AB and CD indicate cross-section axes for Figs. 5.3.5 and 5.3.6.

Fig. 5.3.5 (Top Right) Vertical Cross-Section in the Direction of Motion at 1708 MST - 27 June 1967. Contours of Z_e are labelled in dBz. Note the absence of a WER and the presence of an almost vertical Z_e maximum region (in excess of 65 dBz) from 4.5 km through to the surface.

Fig. 5.3.6 (Bottom Right) Vertical Cross-Section Normal to the Direction of Motion at 1708 MST - 27 June 1967. Note the absence of a WER and the presence of an almost vertical Z_e maximum region (in excess of 65 dBz) from 4 km through to the surface.

Some 9 min later, at 1708 MST, the storm reflectivity structure (see Figs. 5.3.4 - 5.3.6) has changed substantially. The storm has reached its maximum height and the PPI sections at all levels (see Fig. 5.3.4) are dominated by a single Z_e maximum which is almost vertical. There is little evidence of a WER, and the UWER which appeared at 1659 MST is now occupied by precipitation. The Z_e maximum (> 65 dBz), which was found aloft at 1659 MST, has grown in size and extends continuously from 4.5 km through to the surface. It was beneath this Z_e maximum that grape size hail was found at the surface.

By 1722 MST, the dissipation of Cell 3 is well under way. There are few, if any, basic changes in the reflectivity structure since 1708 MST. The PPI sections (see Fig. 5.3.7) show, however, one basic Z_e maximum of smaller area than was found at 1708 MST. Figures 5.3.8 and 5.3.9 illustrate that the storm top has subsided approximately 2 km and the top of the major Z_e maximum (in excess of 65 dBz) has descended to a point 1 km from the surface. An impression is gained of a dissipating cell, yielding its last heavy precipitation and proceeding to decay.

The cycle exhibited here was common to the other cells. It is reminiscent of the Byers-Braham thunderstorm model and does indeed share many common features. However, in addition, this storm displayed a degree of organization and recurring development which is not a feature of the Byers-Braham model. The development of new storm cells was far from a random process, new cells appearing invariably on the RH flank while the current cell was dissipating. Such storms have been found before in Alberta. For example, Chisholm (1966a, 1966b, 1967), using a broad beam vertical radar, was able to track cell motions in two multi-cellular storms, in both of which newly developing cells appeared in succession on the RH flank of the storm.

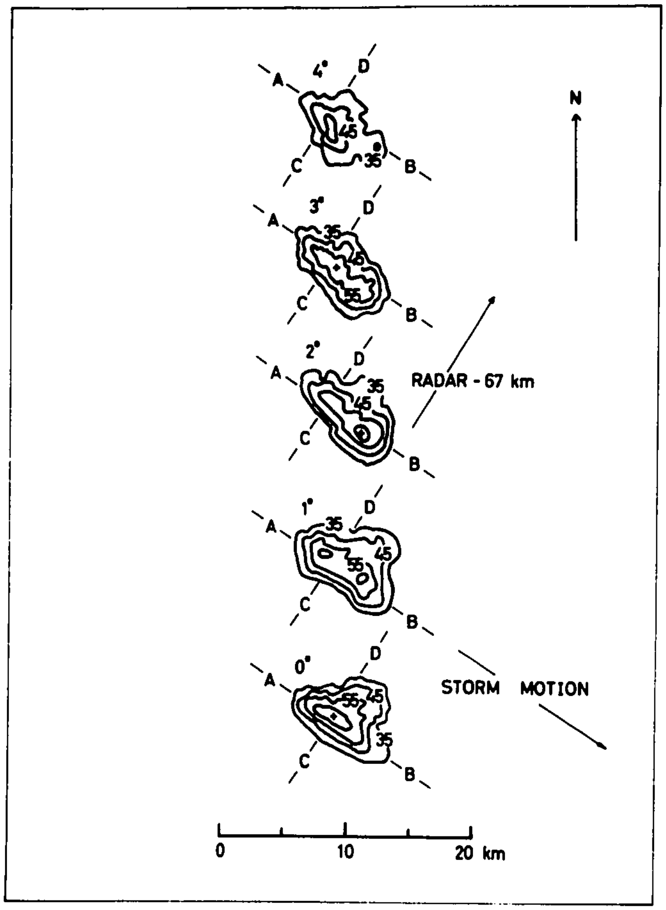

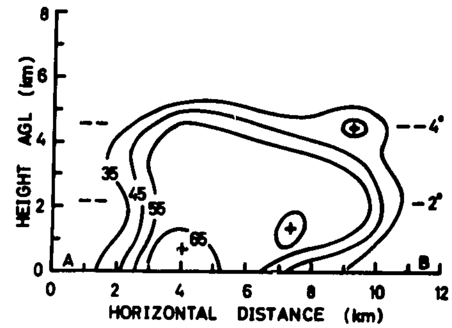

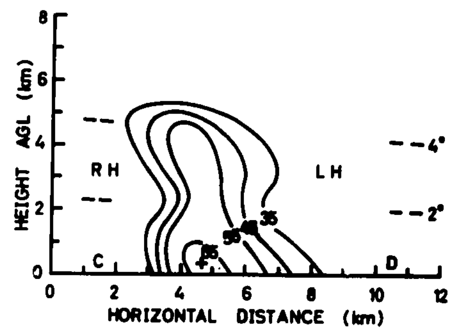

Fig. 5.3.7 (Left) PPI Sections at 1722 MST - 27 June 1967. Contours of Z_e are labelled in dBz. Note the absence of a WER. Lines AB and CD indicate cross-section axes for Figs. 5.3.8 and 5.3.9.

Fig. 5.3.8 (Top Right) Vertical Cross-Section in the Direction of Motion at 1722 MST - 27 June 1967. Contours of Z_e are labelled in dBz. Note the absence of a WER and the location of a small Z_e maximum (in excess of 65 dBz) near the surface.

Fig. 5.3.9 (Bottom Right) Vertical Cross-Section Normal to the Direction of Motion at 1722 MST - 27 June 1967. Note the decrease in storm height and the small Z_e maximum (in excess of 65 dBz) near the surface.

A feature of considerable interest in the three-dimensional structure of the storm of 27 June 1967 was its verticality. The Z_e maximum appeared almost directly above the WER and proceeded to descend, obliterating the WER. This is in contrast to the storm of 29 June 1967 which had a BWER and a deep Z_e maximum zone (precipitation shaft) which appeared side by side. The reason for this difference appears to lie in the wind shear structure. On 29

June 1967, the high wind shear tilted the BWER downshear and toward the LH flank, permitting a precipitation shaft to exist alongside the BWER. In the weak shear situation of 27 June 1967, the storm developed vertically. Large precipitation particles, which began to form in the upper reaches of the storm cell, were forced to fall back through the UWER, bringing about its demise as a radar-identifiable feature.

CHAPTER VI

THE AIRFLOW IN A SEVERE STORM

6.1 Introduction

A problem basic to the study of severe storms is that of determining and understanding the airflow structure which exists in the severe storm. It is within the framework of this airflow that cloud forms and precipitation particles grow, determining the outer cloud boundaries and the radar reflectivity structure of the severe storm. In short, the airflow associated with a particular storm determines how the storm operates, how the storm appears visually and on radar, and from whence the precipitation falls.

In the study of the four storms in Chapters II - V, the airflow was not known. Consequently, the task is to deduce the airflow knowing the radar reflectivity structure, the environmental wind flow and accompanying evidence for a given storm. The observational evidence to be used in deducing the airflow for the storms in Chapters II - V is as follows:

(i) Sub-cloud winds: The wind structure relative to the storm in the sub-cloud layer determines the direction of approach and speed of the air flowing into the storm.

(ii) Cloud base updrafts: Aircraft measurements made at cloud base indicate the size, location and vertical velocity of the cloud base updraft region through which inflow air enters the storm from the sub-cloud layer.

(iii) Weak echo regions: Utilizing the hypothesis that weak echo regions are composed of freshly formed cloud droplets in an updraft, it is frequently possible to determine the location of the updraft core in a severe storm. This concept is invaluable in studying airflow motion.

(iv) Reflectivity structure: The storm reflectivity structure in three dimensions provides numerous clues in deducing the storm airflow. Zones of high Z_e near the surface indicate regions of heavy rain and hail. These may be followed aloft to reveal the approximate trajectories of precipitation particles. Such Z_e maxima are frequently found close to weak echo regions, resulting in a high reflectivity gradient along the boundary between the Z_e maximum and the WER. In addition, the highest point in the storm, as detected by radar, is indicative of the highest point to which precipitation size particles are carried within the updraft. Plume-anvil systems supply additional evidence about the outflow near the storm top.

(v) Mid and high level winds: As shown by Bates and Newton (1965) and Newton (1966), the updraft airflow has exerted upon it forces due to the horizontal wind in the environment. The resulting deflection of the airflow is dependent upon the relative wind and the vertical velocity of the updraft in a complex fashion. Nevertheless, a study of the wind pattern above cloud base will reveal the direction in which the updraft must be tilted. This offers a means of checking the airflow as delineated by the weak echo region.

It is thus clear that there is available a considerable amount of evidence to deduce the airflow through a severe storm. Since the various types of evidence are independent, they provide among themselves a means of cross-checking the deduced airflow. In the sections which follow, airflow patterns for the storms studied in Chapters II - V will be deduced using the

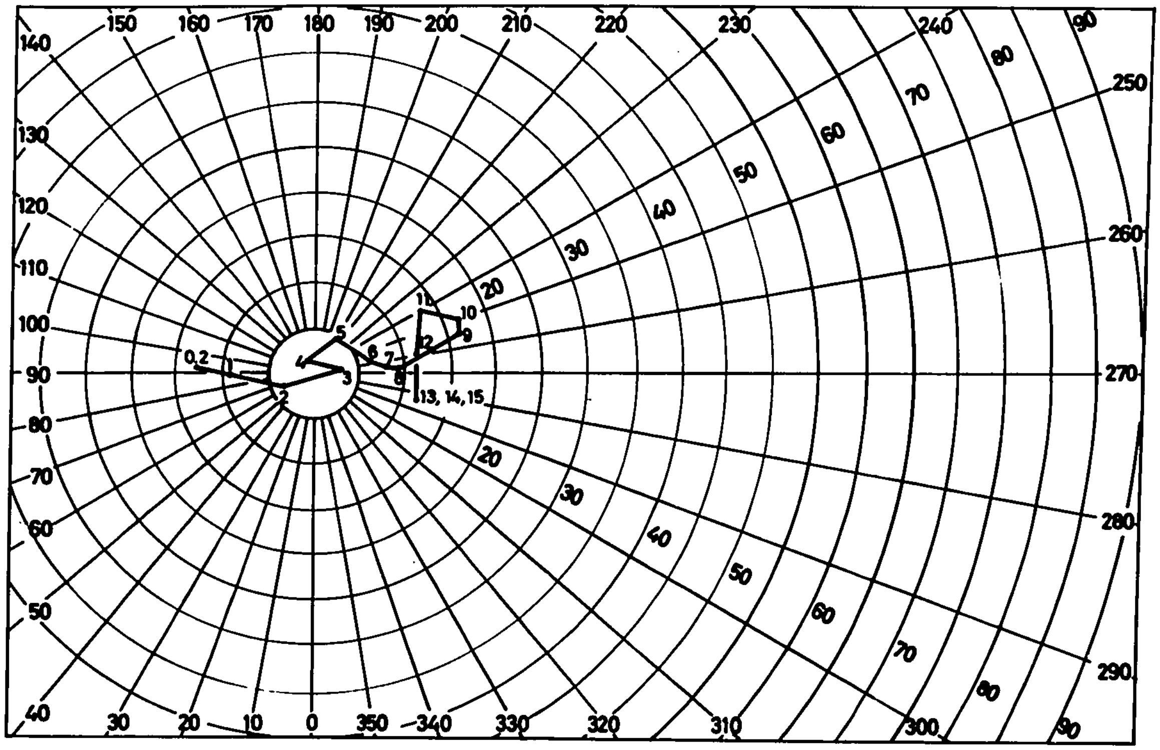

Fig. 6.2.1 Relative Wind Hodograph 1615 MST - 25 July 1968. Wind speeds relative to the storm (storm velocity 289 deg/10.8 m sec^{-1}) are plotted in m sec^{-1} and heights are indicated in km AGL. Note that the wind components relative to the storm lie essentially in an E-W plane.

procedures outlined above. These airflow patterns are qualitative and will be represented in a schematic sense. The purpose of these schematic diagrams is to delineate the general structure of the airflow pattern, not the details.

6.2 The Airflow in the Storm of 25 July 1968

A radar analysis of the squall line storm which occurred on 25 July 1968 has been presented in Chapter II. The three-dimensional reflectivity structure revealed a UWER and overhang above a smooth, persistent cloud base updraft. Upwind from the UWER was an almost vertical Z_e maximum extending in depth throughout the storm. This structure, with a continuous cloud base updraft, persisted for at least 48 min and there is evidence that it persisted for as long as 70 - 80 min. It is clear that the circulation in this storm must have reached a quasi-steady state, exhibiting a continuous flow of air throughout the storm during this period.

Figure 6.2.1 is a wind hodograph which illustrates the environmental winds relative to the storm. This figure is based on a wind sounding shown in Fig. 2.2.2 (page 20) and an average storm velocity of 289 deg/10.8 m sec^{-1}. From this relative wind hodograph, it is clear that winds in the sub-cloud region (below 1.5 km AGL) approached the storm almost directly opposite to the direction of storm motion. This tendency for the inflow air to approach directly from the downwind side was also noted by observers on board the aircraft at cloud base. It is also evident from Fig. 6.2.1 that the environmental winds relative to this storm were essentially in the plane of storm motion at all levels. As a consequence, there would exist only very small forces to divert the storm airflow from an essentially two-dimensional pattern.

Referring to Figs. 2.4.3 (pages 28, 29), 2.4.6 (pages 32, 33) and 2.4.10 (pages 37, 38), it is seen that the updraft area at cloud base was a N-S rectangular region (approximately 7 x 18 km) located on the downwind side of the storm directly beneath the UWER. Thus, the inflow air in Fig. 6.2.2 (based on the vertical cross-section in Fig. 2.4.7, page 34) is illustrated as entering the storm from the downwind side, ascending through the cloud base updraft region into the UWER. The inflow air entering the storm at cloud base has substantial momentum directed toward the upwind side of the storm. For this reason, the updraft would be expected to tilt toward the upwind side of the storm. Above cloud base, the ascending updraft is under the influence of the environmental wind relative to the storm in the plane of storm motion (see Fig. 6.2.2). Only above 5 km is there a component relative to the storm in the downwind direction. This relative wind would exert a force on the up-

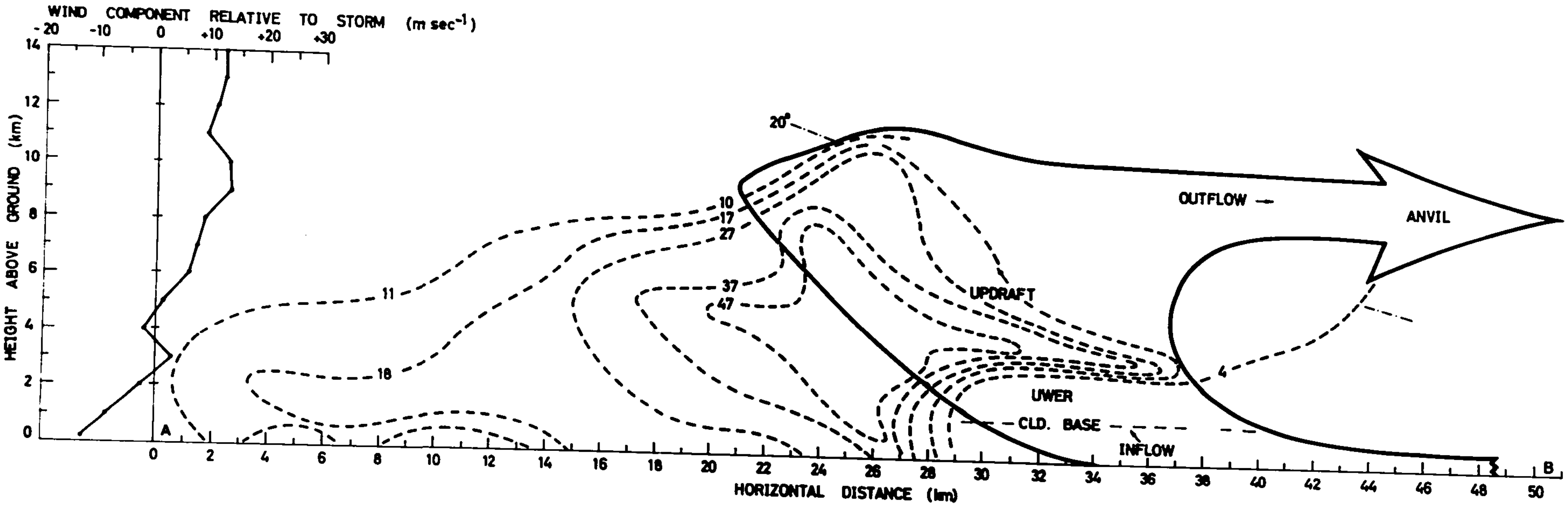

Fig. 6.2.2 Schematic Airflow in the Plane of Storm Motion - 25 July 1968. The airflow in the plane of storm motion is illustrated schematically, superimposed on the vertical cross-section of Fig. 2.4.7. Dashed Z_e contours are labelled in dBz. Wind components relative to the storm (in the plane of storm motion) are shown on the left hand side of this figure. The storm airflow is shown to tilt toward the upwind side of the storm, and the outflow exits in the downwind direction. A Z_e maximum appears on the upwind side of the updraft, a region conducive to the growth of large precipitation particles.

draft column, causing it to reverse its tilt toward the vertical. As the updraft decelerates near the storm top, it would acquire the environmental wind velocity and so the outflow is directed downwind. The vertical cross-section shown in Figs. 2.4.4 (page 30) and 2.4.7 (page 34), and therefore in Fig. 6.2.2, depict the radar storm top upwind from the cloud base updraft. This indicates the highest point in the storm to which radar-detectable particles were carried by the updraft core. On the basis of this evidence and the reasons presented above, the storm top (highest point of updraft core penetration) is shown displaced to the rear of the cloud base updraft position. Since the radar-detectable storm top is due to particles with a finite fallspeed, the boundary of the airflow is extended above the radar storm top.

The Z_e maximum found directly upwind from the cloud base updraft is clearly due to the fallout of rain and hail. A steep reflectivity gradient is found in Fig. 2.4.6 (pages 33, 34) on the side of the Z_e maximum facing the updraft. The growth of precipitation particles can proceed to large size most favorably in an updraft whose vertical velocity is only slightly less than the fallspeed of the particles concerned. It is suggested that the largest precipitation particles in this storm grew while descending through the upwind side of the storm updraft delineated in Fig. 6.2.2, resulting in the Z_e maximum on the upwind side of the storm.

Referring to Fig. 2.4.6 (pages 33, 34), it is found that the Z_e maximum was essentially vertical both in the plane of storm motion and in the normal plane. This is to be expected in view of the fact that the wind components relative to the storm (normal to the direction of storm motion) were very small. The airflow for this storm is thus represented as a two-dimensional pattern.

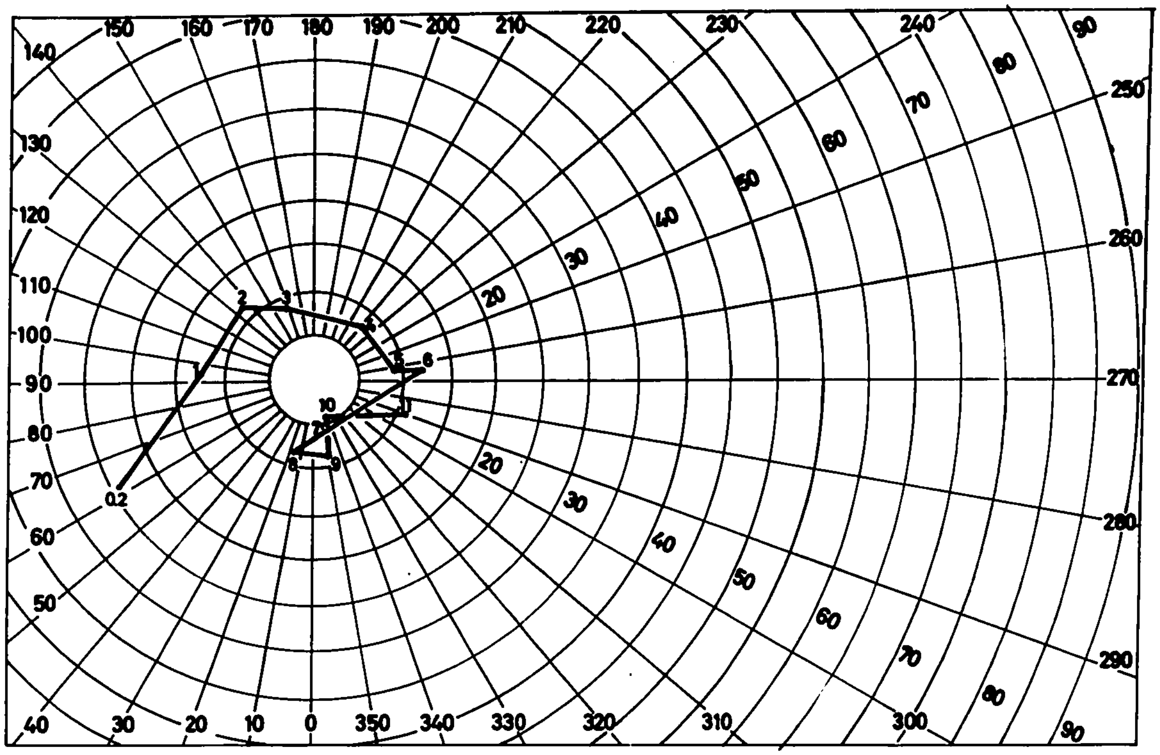

Fig. 6.3.1 Relative Wind Hodograph 2022 MST - 28 July 1968. Wind speeds relative to the storm (storm velocity 261 deg/9.3 m sec^{-1}) are plotted in m sec^{-1} and heights are indicated in km AGL. Note wind component toward the storm below 4 km and away from the storm above 4 km.

The storm configuration and airflow pattern presented here resemble data and computations published by Bates and Newton (1965) and Newton (1966) with the inflow air entering the downwind side of the storm to emerge at the storm top on the upwind side.

6.3 The Airflow in the Storm of 28 July 1968

The storm of 28 July 1968, analyzed in Chapter III, consisted of three distinct phases, each differing in radar structure and airflow. The airflow in Phase III will be considered first due to the similarities between it and the storm of 25 July 1968, which has been considered in the previous section.

6.3.1 The Airflow in Phase III

The PPI sections, illustrated in Fig. 3.3.7 (page 59), show a pattern very similar to those for the storm of 25 July 1968. A long, rectangular, N-S updraft was found at cloud base downwind from the Z_e maximum. Above this updraft, extending into the storm is a UWER. This structure persisted from 2000 MST until after 2100 MST, accompanied throughout this period by a continuous aircraft-measured cloud base updraft.

The wind hodograph, depicted in Fig. 6.3.1, illustrates the environmental winds relative to the storm. It is based on the wind hodograph in Fig. 3.1.3 (page 44) and an average storm velocity for Phase III of 261 deg/9.3 m sec^{-1}. The wind pattern in Fig. 6.3.1 differs from that of Fig. 6.2.1, due mainly to the fact that Fig. 6.3.1 indicates substantial wind components normal to the direction of storm motion. However, the wind component relative to the storm, in the direction of storm motion shown in Fig. 6.3.2, is similar to the corresponding wind component in Fig. 6.2.2. A relative wind of 10 - 20 m sec^{-1} toward the upwind side of the storm is found in the sub-cloud layer. Based on this fact and the location of cloud base updrafts, the inflow in Fig. 6.3.2 is shown entering the storm downwind. Below 4 km AGL, the updraft would be expected to tilt toward the upwind side of the storm due to its initial horizontal momentum. Above 4 km AGL, due to the wind flow relative to the storm, forces exerted on the updraft would cause it to tilt toward the vertical. The UWER, believed due to micron-size water droplets in the updraft core, appears to tilt in the downwind sense near the top of its trajectory. An inspection of Fig. 3.3.7 (page 59) shows this is due partially to the location of the line AB; a cross-section taken slightly further north would exhibit a more vertical stance near the top of the UWER.

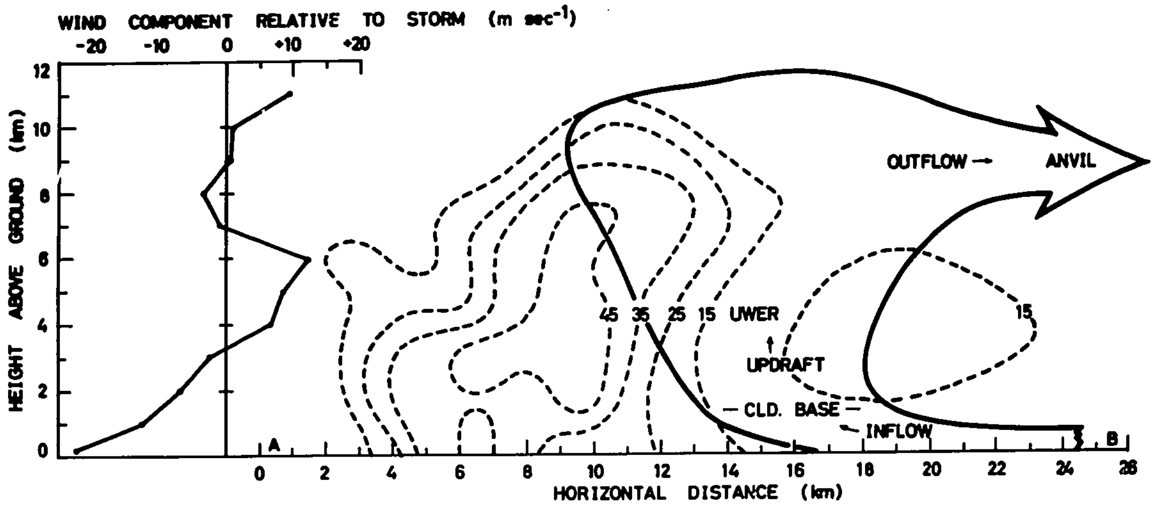

Fig. 6.3.2 Schematic Airflow in the Plane of Storm Motion - Phase III - 28 July 1968. The airflow in the plane of storm motion is illustrated schematically, superimposed on the vertical cross-section of Fig. 3.3.8. Dashed Z_e contours are labelled in dBz. Wind components relative to the storm (in the plane of storm motion) are shown on the left hand side of this figure. The storm airflow enters cloud base tilting upwind, but reverses this trend so that the storm top lies almost directly above the center of the cloud base updraft. As in Fig. 6.2.2, a Z_e maximum appears on the upwind side of the updraft, a region conducive to the growth of large precipitation particles.

As shown by the wind hodograph in Fig. 6.3.1, there was a relative wind component from the RH flank of the storm between 1 and 5 km. It is significant to note that during this phase the aircraft observers noted the inflow from between the downwind and RH sides of the storm. The PPI sections in Fig. 3.3.7 show a UWER which is open on the RH flank, a configuration which could arise from an inclined updraft entering the storm (with a component from the RH flank), precluding precipitation particles from falling through to the surface. Clearly, the airflow in this storm departed from a two-dimensional flow. The evidence suggests that air entered predominantly from the quadrant between the RH and downwind sides, while tilting and ascending through the storm. On the basis of the relative wind pattern at upper levels as indicated by the hodograph, the outflow from the storm would be directed outward toward the quadrant between the RH and downwind sides.

Compared to the storm of 25 July 1968, the airflow in Phase III is illustrated as being tilted to a lesser degree. It is suggested that this is due to a difference in the vertical velocities within the storm updrafts. Computations in Chapter VII reveal that vertical velocities in the case of the storm of 28 July 1968 (Phase III) were substantially greater than those for the storm of 25 July 1968. Indeed, even cloud base updrafts on 28 July 1968 were consistently higher (as high as 13 m sec^{-1}) than those for 25 July 1968. The higher the vertical velocity, the faster the traverse of the air through the updraft and consequently the smaller the reaction of the updraft to the relative wind. Bates and Newton (1965) illustrate this effect clearly, the upshear tilt of the updraft being least when the vertical velocities are strong.

As was the case in the storm of 25 July 1968, an almost vertical Z_e maximum appears upwind from the cloud base updraft. This region, bordering the updraft, is most conducive to the growth of large precipitation particles.

6.3.2 The Airflow in Phase I

Phase I of the storm of 28 July 1968 is almost an exact reverse of Phase III. As shown in Fig. 3.3.1 (page 53), the UWER is located on the upwind side of the storm, bounded on its downwind edge by a sharp reflectivity gradient. During the first portions of Phase I, the Z_e maximum remained essentially stationary over the lee side of a range of foothills. Figure 6.3.3 represents the winds relative to the stationary storm. Since the wind observation was taken approximately 130 km east of the storm, the winds below 3 km AGL are not considered representative of the environment. The foothills terrain would have had a substantial influence on the sub-cloud winds, the

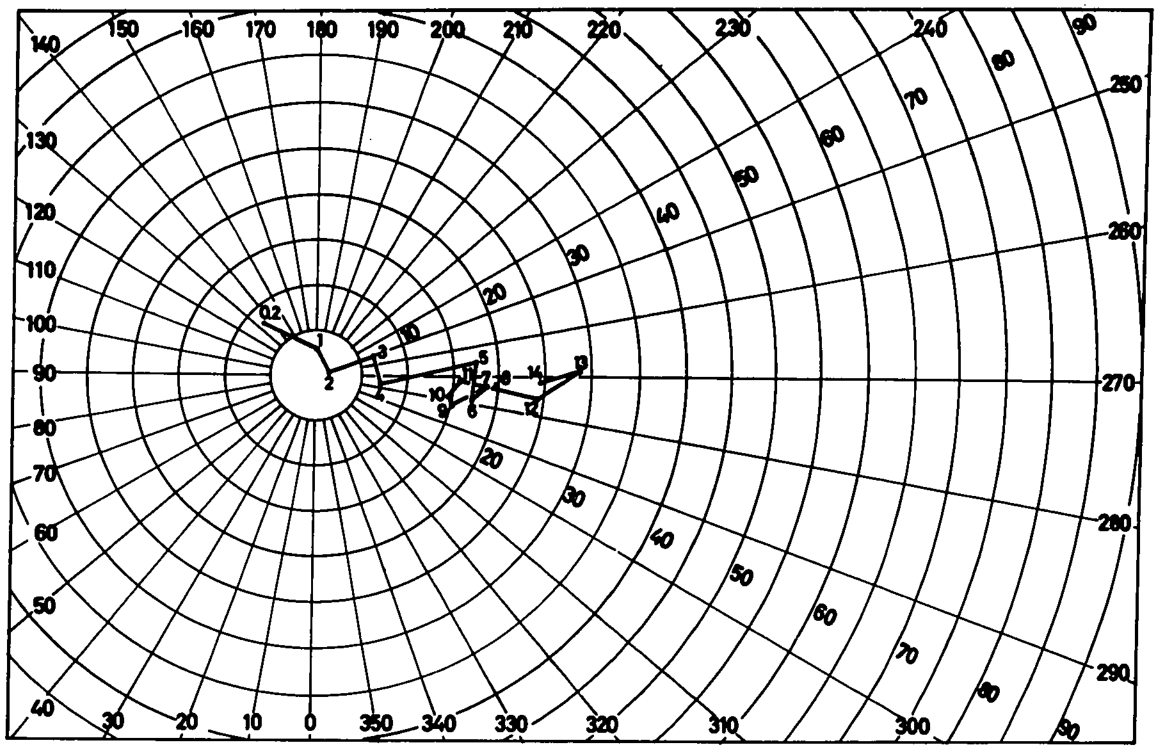

Fig. 6.3.3 Relative Wind Hodograph 1610 MST - 28 July 1968. Wind speeds relative to the stationary storm are plotted in m sec^{-1} and heights are indicated in km AGL. Since this wind sounding was taken 130 km east of the storm, the winds below 3 km are not considered representative of the winds in the environment near the storm.

winds very likely being in an upslope configuration. Such a wind pattern would permit the inflow air to enter the storm from the upwind side as shown in Fig. 6.3.4. Under the influence of the substantial downstream wind component, the updraft would tilt in the downwind sense. Precipitation particles would be expected to fall out of the updraft downwind from the UWER. This suggested airflow pattern could exist as long as the storm remained stationary, "anchored" to the foothills. There is radar evidence which indicates that this was the case. However, upon moving east of the foothills range, it would become extremely difficult for the inflow air to enter the upwind side of the storm. With an eastward storm velocity of approximately 9 m sec^{-1}, a strong westerly wind would be required at sub-cloud levels to maintain a circulation similar to that illustrated in Fig. 6.3.4. It is highly improbable

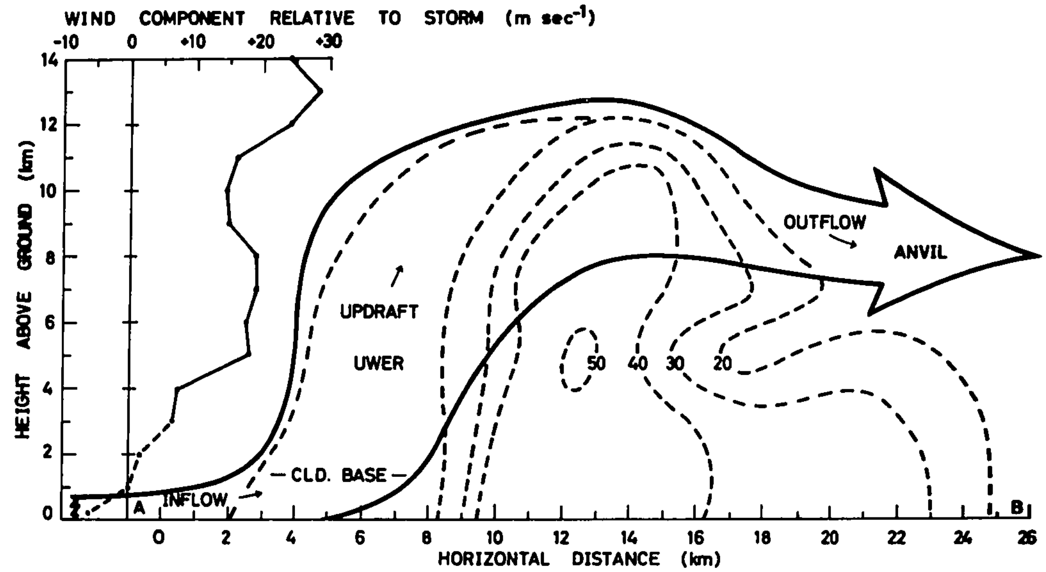

Fig. 6.3.4 Schematic Airflow in the Plane of Storm Motion - Phase I - 28 July 1968. The airflow in the plane of storm motion is illustrated schematically, superimposed on the vertical cross-section of Fig. 3.3.2. Dashed Z_e contours are labelled in dBz. Wind components relative to the storm (in the plane of storm motion) are shown on the left hand side of this figure. The inflow air is shown to enter the storm on the upwind side, ascending upward through the UWER, while tilting downwind. The outflow air exits downstream under the influence of the moderately strong wind component relative to the storm, and precipitation particles would be expected to fall through the Z_e maximum downwind from the updraft.

that such a wind did exist and consequently the airflow configuration was forced to change in order for the storm to continue. As the storm moved east of the foothills, the UWER on the upwind side dissipated and the storm reflectivity structure changed significantly over the course of a half hour to result in Phase II.

6.3.3 The Airflow in Phase II

The reflectivity structure which characterized Phase II is exhibited by the PPI views in Fig. 3.3.4 (page 56). A BWER is found to enter the storm on the RH flank above the cloud base updraft. Figure 6.3.5 illustrates the environmental wind structure relative to the storm for Phase II. It is based on the wind hodograph in Fig. 3.1.3 (page 44) and an average storm velocity

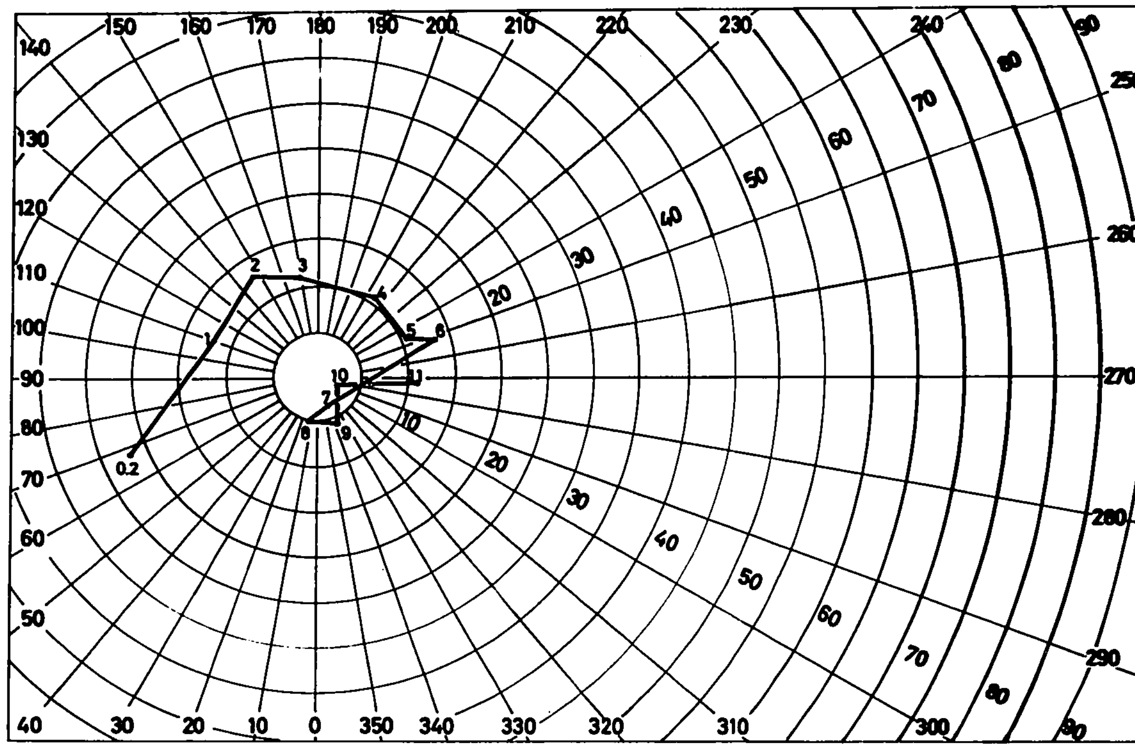

Fig. 6.3.5 Relative Wind Hodograph 2022 MST - 28 July 1968. Wind speeds relative to the storm (storm velocity 283 deg/8.7 m sec^{-1}) are plotted in m sec^{-1} and heights are indicated in km AGL. Note wind component toward the storm in the sub-cloud region.

of 283 deg/8.7 m sec^{-1}. In the sub-cloud layer, the wind has a component from the downwind side of the storm and also from the RH flank (excepting the wind at 0.2 km AGL, which is suspect). The wind component from the downwind side of the storm is shown clearly in Fig. 6.3.6. Based on this sub-cloud wind and the cloud base updraft location, the inflow air in Fig. 6.3.6 is shown to enter the storm from the downwind side, tilting upwind and ascending with the BWER. Winds above 4 km would tend to tilt the updraft toward the downwind side of the storm. This, coupled with a high calculated vertical velocity, would be expected to result in an almost vertical updraft, which indeed appears to be the case. At the storm top, the decelerating air would be sheared downstream, carrying with it small ice particles to form the extensive anvil and plume system illustrated in Fig. 6.3.6. A similar configuration is shown in Fig. 6.3.7, the cross-section normal to the plane

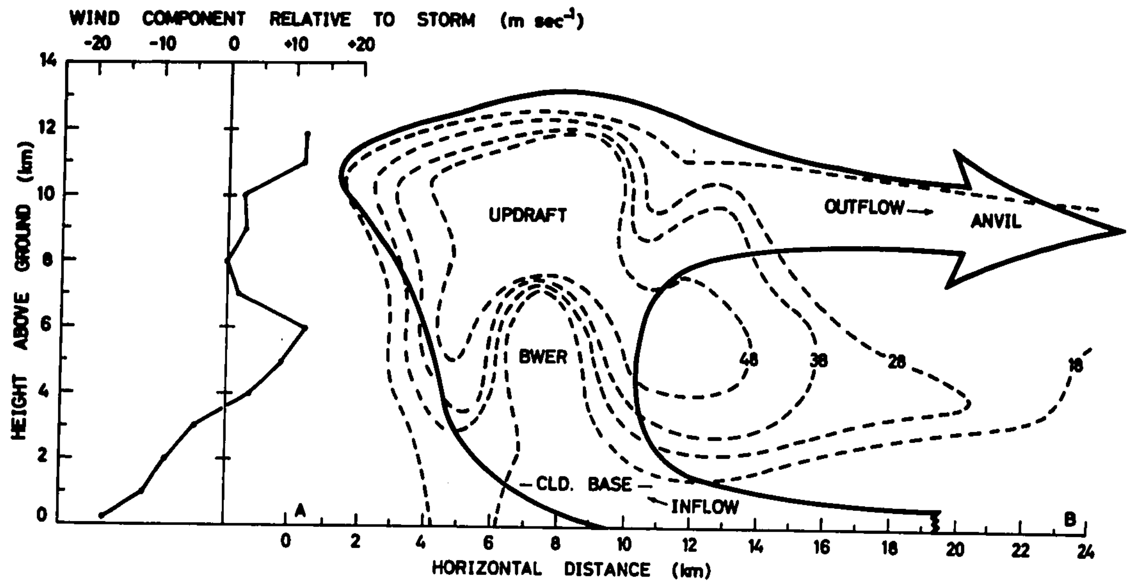

Fig. 6.3.6 Schematic Airflow in the Plane of Storm Motion - Phase II - 28 July 1968. The airflow in the plane of storm motion is illustrated schematically, superimposed on the vertical cross-section of Fig. 3.3.5. Dashed Z_e contours are labelled in dBz.. Wind components relative to the storm (in the plane of storm motion) are shown on the left hand side of the figure. The inflow air is shown to enter the storm on the downwind side, ascending almost vertically through the UWER to exit on the downwind side. Note the similarity to the Browning SR model (see Fig. 1.2.4).

of storm motion. The inflow air is shown to enter the storm from the RH flank, ascending upward through the BWER. The wind component in the plane of the cross-section, in Fig. 6.3.7 at 0.2 km, does not comply with this inflow. However, the wind in the sub-cloud region must be influenced by the convergence associated with the storm itself. It is difficult to justify the existence of a wind component in the inflow region originating from the LH flank of the storm, since it would have to come from a region of heavy precipitation. This is not impossible, but it is not conducive to vigorous convection. Therefore, the wind measured at 0.2 km is not considered to be an accurate representation of the wind near the storm in Phase II. Continuing upward, the updraft diverges and the outflow air exits essentially in the direction of storm motion. This outflow is illustrated as a thick arrow

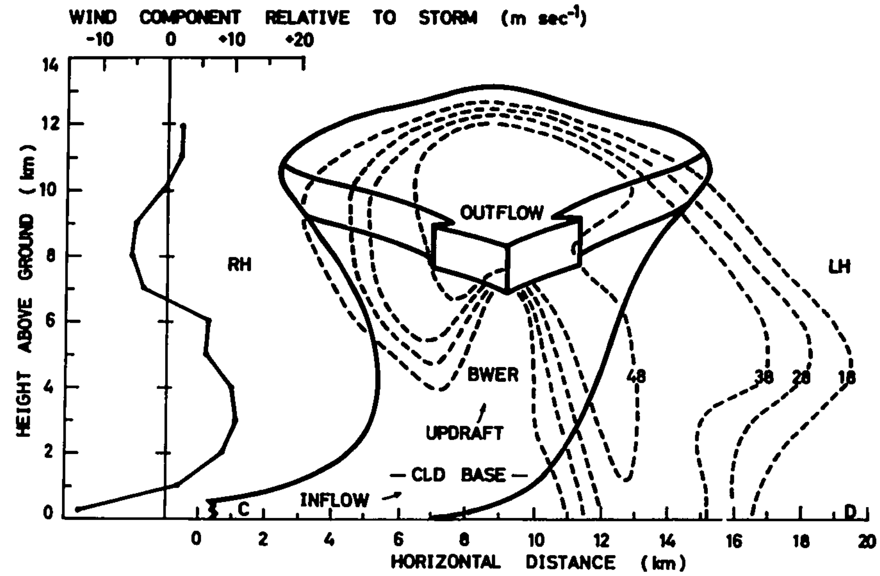

Fig. 6.3.7 Schematic Airflow Normal to the Plane of Storm Motion- Phase II - 28 July 1968. The airflow normal to the plane of storm motion is illustrated schematically, superimposed on the vertical cross-section of Fig. 3.3.6. The storm is viewed looking upstream. Dashed Z_e contours are labelled in dBz. Wind components relative to the storm (normal to the plane of storm motion) are shown on the left hand side of this figure. The inflow air is shown to enter on the RH flank penetrating upward through the BWER almost vertically to the storm top. An outflow arrow depicts the air leaving the storm essentially perpendicular to the plane of the diagram. Note the Z_e maximum extending from the storm top to the surface on the LH flank of the storm.

directed out of the plane of the figure; it is strictly a mechanism to depict the general airflow. The updraft and outflow are not necessarily believed to have rectangular sections.

It is obvious from the vertical cross-sections in Figs. 6.3.6 and 6.3.7 and the PPI sections in Fig. 3.3.4, that the precipitation fallout zone lies on the LH side of the updraft. The steep reflectivity gradient between the BWER and the Z_e maximum indicates that the largest precipitation particles (rain and hail) most probably fell from the updraft region, close to the BWER. As was mentioned in the two previous sections, this portion of the updraft region would be highly conducive to the growth of large hailstones.

As was pointed out in Chapter III, there are striking similarities between the radar appearance of this phase and the SR storm model proposed by Browning. The deduced airflow is also similar, although there is no evidence to advocate a 270 deg turn in the airflow while ascending through the storm as proposed by Browning.

This Phase was of relatively short duration, exhibiting a well-defined BWER for only 24 min. During this period, the BWER was found to propagate upward then collapse. It is suggested that this pattern was due to precipitation loading in an essentially vertical updraft, resulting in the demise of the updraft and descent of precipitation back through this updraft region.

6.4 The Airflow in the Storm of 29 June 1967

There are some basic similarities in the radar reflectivity structure exhibited by the storms of 29 June 1967 and 28 July 1968 (Phase II). Figure 4.4.5 (page 75) and Fig. 3.3.4 (page 56) both show BWER structures and a not dissimilar type of Z_e maximum. There are, however, substantial differences in detail which clearly are related to the differences in wind environment and the vertical velocity within the updraft.

Figure 6.4.1 illustrates the environmental wind structure relative to the storm of 29 June 1967. It is a composite hodograph, winds above 4 km AGL based on the wind sounding at 1219 MST (see Fig. 4.1.3, page 64) and winds below 2.2 km based on a wind sounding (in the inflow region) obtained at 1419 MST. Winds between 2.2 km and 4 km are interpolated values. It is obvious that this storm existed in a highly sheared environment. This is also evident from the relative wind component shown in Fig. 6.4.2. In the plane of storm motion (Fig. 6.4.2), the inflow air is shown to enter the

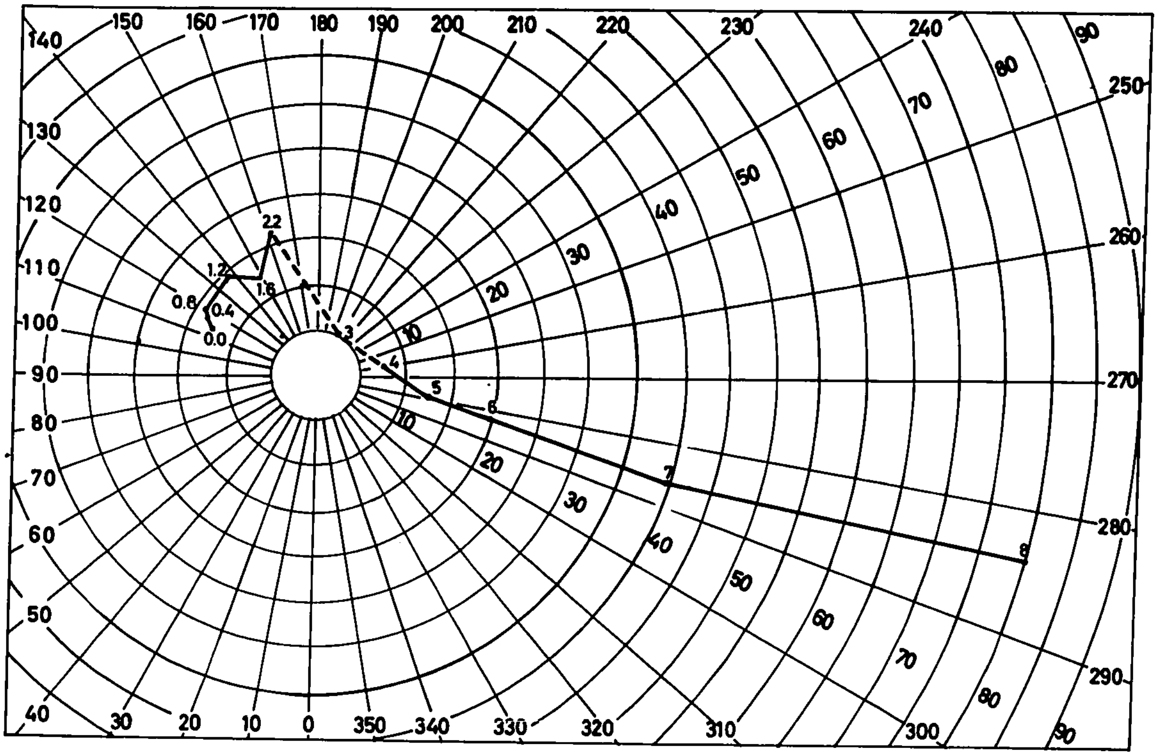

Fig. 6.4.1 Composite Relative Wind Hodograph - 29 June 1967. Wind speeds relative to the storm (storm velocity 297 deg/9.6 m sec^{-1}) are plotted in m sec^{-1} and heights are indicated in km AGL. Winds below 2.2 km were obtained in the storm inflow region at 1416 MST; winds above 4 km were obtained from the 1219 MST sounding. Interpolated values are plotted between 2.2 and 4 km. Note the wind component toward the storm in the sub-cloud region and the very strong wind component away from the storm above 5 km.

storm from the downwind side ascending while tilting toward the upwind side of the storm. There are no aircraft measurements available for this storm. However, cloud stereo photos analyzed and reported by Chisholm and Warner (1968), Warner (1969) and Warner, English, Chisholm and Hitschfeld (1969) show a "plateau" or low, flat, cloud base region without virga or precipitation directly beneath the BWER in this storm. This "plateau" region is suggested to be the region of cloud base updraft in this storm. It is similar in appearance to cloud base updraft regions seen by observers on board the University of Wyoming aircraft in similar storms.

The BWER, hypothesized as micron-size cloud droplets in the core of the updraft, delineates the airflow through the central region of the

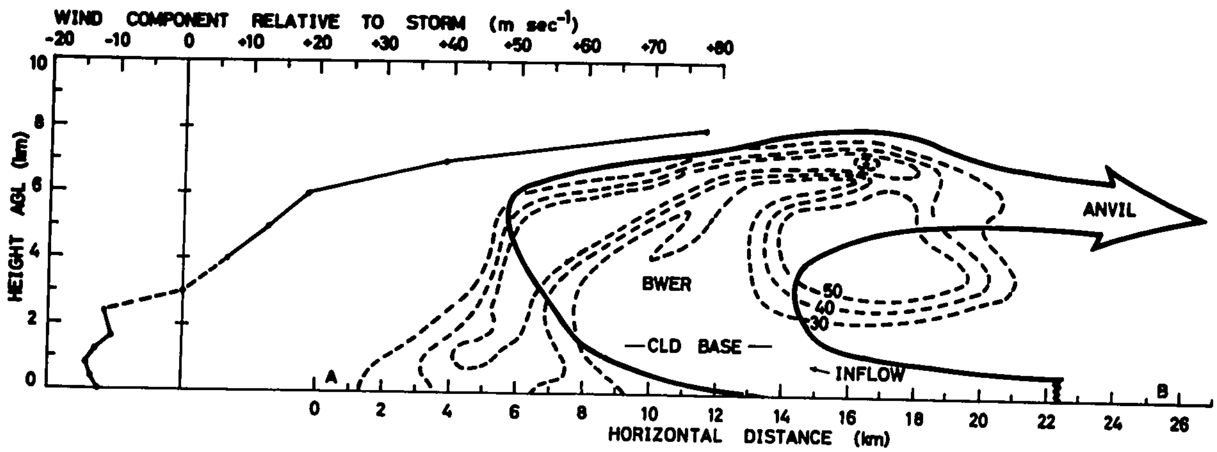

Fig. 6.4.2 Schematic Airflow in the Plane of Storm Motion - 29 June 1967. The airflow in the plane of storm motion is illustrated schematically, superimposed on the vertical cross-section of Fig. 4.4.9. Dashed Z_e contours are labelled in dBz. Wind components relative to the storm (in the plane of storm motion) are shown on the left hand side of this figure. The inflow air enters on the downwind side of the storm, tilting upwind while ascending through the BWER. Under the influence of strong relative winds above 5 km, the updraft tilts rapidly downstream, reaching the storm top downwind from its point of entry. A secondary Z_e maximum is seen on the upwind side of the updraft. Walnut size hail fell in association with this Z_e maximum.

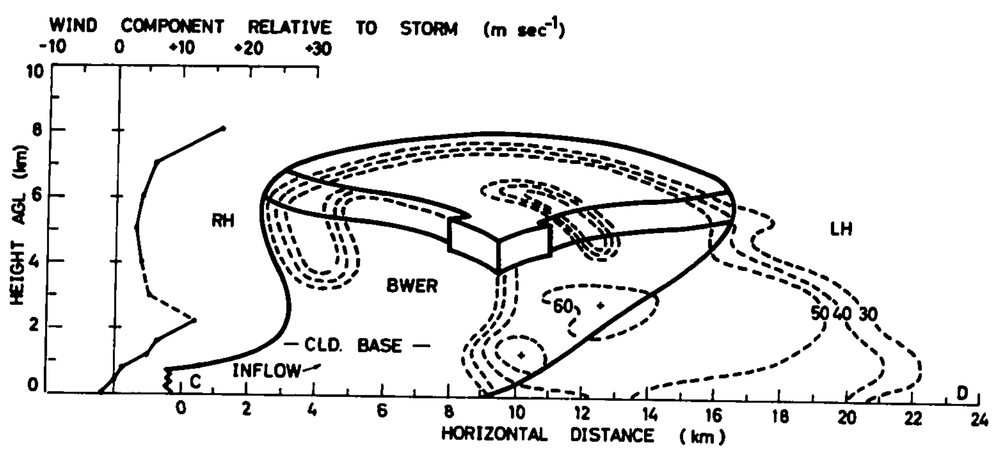

Fig. 6.4.3 Schematic Airflow Normal to the Plane of Storm Motion - 29 June 1967. The airflow normal to the plane of storm motion is illustrated schematically, superimposed on the vertical cross-section of Fig. 4.4.10. The storm is viewed looking upstream. Dashed Z_e contours are labelled in dBz. Wind components relative to the storm (normal to the plane of storm motion) are shown on the left hand side of this figure. The storm airflow enters from the RH flank and ascends almost vertically through the storm exiting (as shown by the airflow arrow) essentially perpendicular to the plane of the figure. Note the Z_e maximum on the LH flank of the storm which descends through the upper portion of the updraft. Walnut and golfball size hail was observed at the surface in association with this Z_e maximum.

storm. In Fig. 6.4.2, the updraft is shown to ascend and diverge while tilting upstream. The updraft is subjected to a downstream component above 3 km, and a very high downstream component above 6 km. Figure 6.4.2 shows the BWER shearing rapidly downstream, and the schematic airflow has been represented to follow this pattern. It is apparent that the updraft core continued to rise, resulting in a storm top displaced downwind from the cloud base updraft. Under the influence of high relative wind velocities, an extensive anvil was found as far as 150 - 200 km downwind from the storm itself.

Figure 6.4.3 shows the airflow in the plane normal to the direction of motion. On the basis of a wind component from the RH flank in the subcloud layer, the inflow is shown entering the storm from the RH flank. Once within the storm, the updraft ascends essentially vertically, to exit from the storm top perpendicular to the plane of the figure. The resulting sinuous three-dimensional path is indeed much more complex than the essentially two-dimensional squall line case treated in Section 6.2.

From the PPI sections in Fig. 4.4.8 and the vertical cross-sections in Figs. 6.4.2 and 6.4.3, it is apparent that the major portion of the large precipitation particles follow a path from near the storm top, descending to a point downwind and to the LH side of the BWER. This results in a precipitation trajectory through a portion of the updraft, a path favorable for the growth of large precipitation particles. A secondary path exists along the upwind side of the storm resulting in a secondary Z_e maximum. From surface hail reports (see Fig. 4.4.11, page 79), it is evident that hail of walnut size was associated with each of these Z_e maxima.

6.5 The Airflow in the Storm of 27 June 1967

The storm of 27 June 1967 was, by comparison with the previous five

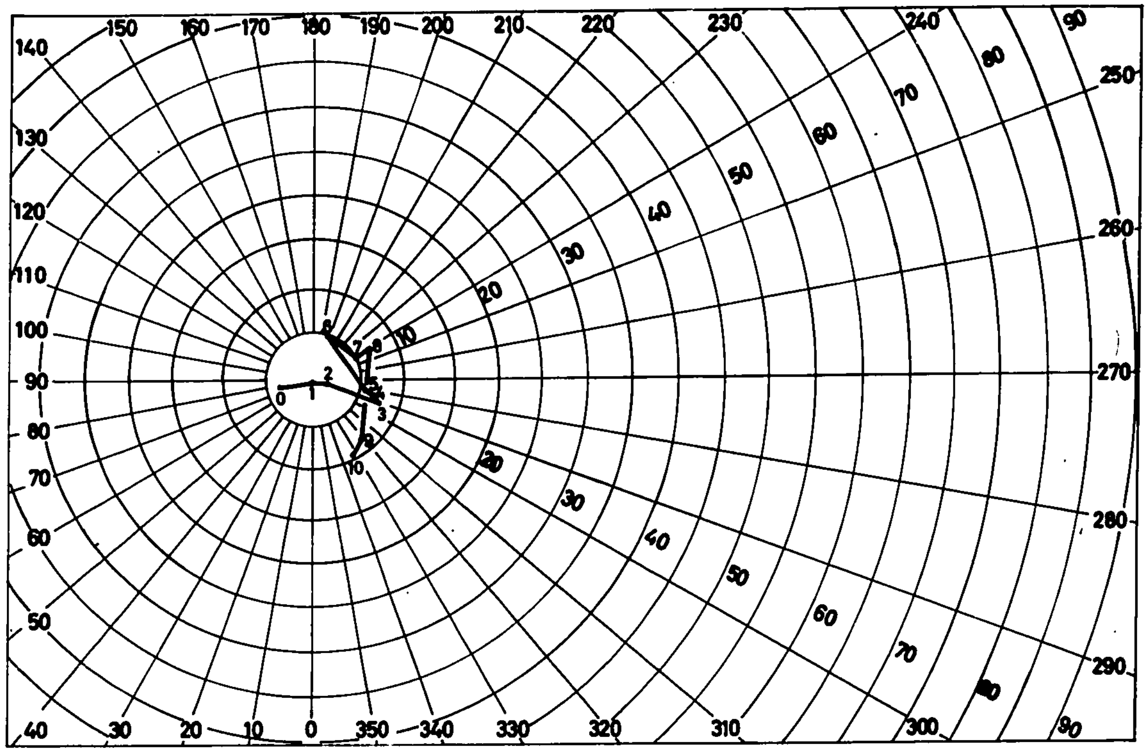

Fig. 6.5.1 Relative Wind Hodograph 1617 MST - 27 June 1967. Wind speeds relative to the storm (storm velocity 311 deg/7.4 m sec^{-1}) are plotted in m sec^{-1} and heights are indicated in km AGL. Note the lack of an organized wind flow relative to the storm.

cases studied, a rather small storm. It was the shallowest, smallest in horizontal extent, and least energetic of the storms examined here. Nevertheless, it resulted in hail as large as grape size, in spite of its small proportions. An examination of the radar structure of this storm in Chapter V has shown that it consisted of a series of recurring cellular elements, which remained as radar-identifiable features for 25 - 35 min.

Figure 6.5.1 shows the environmental winds relative to the storm. It is based on the wind hodograph in Fig. 5.1.2 and an average storm velocity of 311 deg/7.4 m sec^{-1}. As Fig. 6.5.1 shows, there was very little wind relative to the storm. It would be anticipated that convergence in the subcloud region would itself exert a considerable influence on the relative inflow. Figure 6.5.2 shows the airflow into the storm during the latter part

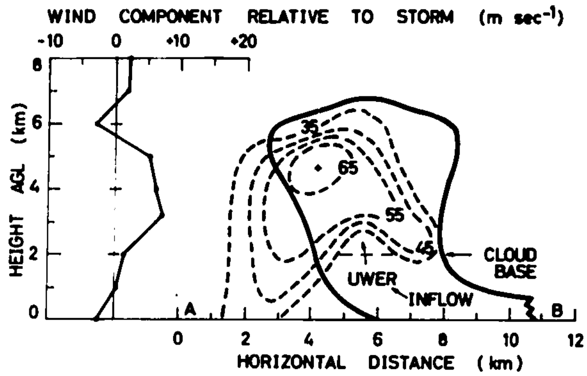

Fig. 6.5.2 Schematic Airflow in the Plane of Storm Motion - 27 June 1967. The airflow in the plane of storm motion is illustrated schematically, superimposed on the vertical cross-section of Fig. 5.3.2. Dashed Z_e contours are labelled in dBz. Wind components relative to the storm (in the plane of storm motion) are shown on the left hand side of this figure. The storm airflow enters on the downwind side of the storm, tilting slightly upwind to the storm top. Since the storm is still in a developing stage with the storm top rising, no outflow has been depicted.

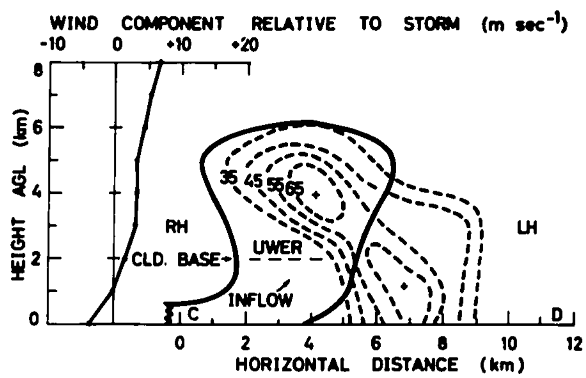

Fig. 6.5.3 Schematic Airflow Normal to the Plane of Storm Motion - 27 June 1967. The airflow normal to the plane of storm motion is illustrated schematically, superimposed on the vertical cross-section of Fig. 5.3.3. The storm is viewed looking upstream. Dashed Z_e contours are labelled in dBz. Wind components relative to the storm (normal to the plane of storm motion) are shown on the left hand side of this figure. The inflow air is shown to enter on the RH flank, ascending almost vertically to the storm top. A Z_e maximum from a dissipating cell is seen on the LH side of the storm. Hail as large as grape size was observed at the surface in association with this Z_e maximum.

of its developing stage. The inflow, on the basis of the relative wind component and the location of the UWER, is shown to enter from the downwind side of the storm. It ascends upward, inclined slightly toward the upwind side to a storm top displaced slightly upwind of the updraft center at cloud base. No outflow is shown since this storm is in a transitory stage, and the storm top is still continuing to rise. Very little relative wind is available to establish an outflow in any direction. Figure 6.5.3 illustrates the airflow in the plane normal to the direction of motion. It would be expected that the local convergence would create an inflow from the RH flank of the storm, in opposition to the weak relative wind shown from the LH flank. Above cloud base, the weak relative wind would permit an almost vertical ascent of the updraft through the storm.

A Z_e maximum, seen in Fig. 6.5.3 on the LH flank, is due to a previously active cell now in its dissipating stage. The developing cell, shown at this time, subsided to yield its precipitation from aloft at a later stage, while yet another cell developed on the RH flank of the storm. It is suggested that this recurring, cellular behaviour is due to the relatively weak updraft associated with this storm and the lack of significant relative wind. In the weak wind shear, the updraft stands almost erect, while precipitation accumulates within the updraft resulting in a load which the weak updraft cannot support. The updraft weakens and dies, permitting the precipitation to fall to the ground.

6.6 A Summary and Comparison with Takeda's Work

The airflow in six different storm structures has been deduced here, based on various arguments and numerous pieces of evidence. In spite of vastly different sets of environmental conditions, there emerges a relatively consistent picture of the airflow through these severe storms. Namely:

(i) An inflow determined by the sub-cloud wind structure,

(ii) An updraft at cloud base with a weak echo region above,

(iii) An updraft airflow whose stance is determined by an interaction between the vertical velocity in the updraft and the environmental wind,

(iv) An outflow into a plume-anvil system determined by the direction and magnitude of the relative wind near the storm top.

These concepts have been applied to a storm not dissimilar to the Browning SR model. However, they have, in addition, accounted for storms whose inflow originated on the upwind and downwind sides respectively, a storm whose BWER tilted over into the downwind flow and also to a cellular propagating storm.

A recent theoretical study of convective storms by Takeda (1970) invites comparisons with the airflow models which have been deduced for the severe storms studied herein. Takeda has simulated large convective storms by integrating numerically the hydrodynamic and thermodynamic equations in a two-dimensional model. Cloud physical processes for rain drops were also modelled, including condensation, evaporation, coagulation, disintegration and the fall of raindrops relative to the air. Sublimation effects and freezing were not considered. The major purpose of Takeda's work was to investigate the effect of the environmental wind shear on convective clouds. Three distinct types of storm evolution resulted - the type of evolution being dependent upon the original wind structure in the vertical. In summary these three storm types were as follows:

Type A - New convective clouds form on either side of the decaying initial cloud.

This type of development occurs in an unstable atmosphere if the vertical shear of the environment were weak. A downdraft develops in the initial cloud due to loading by accumulated water drops and from the cooling which results from their evaporation. The current of cold air which spreads out at the surface as a result of this downdraft pushes potentially warm air in the lower layer upward, to trigger new convection. In the presence of zero vertical wind shear, new convective clouds form symmetrically on both sides of the initial cloud. However, in weak shear, the pattern is asymmetric.

In view of the restrictions imposed by a two-dimensional model, direct comparisons between numerical results of Takeda and the case studies reported here must be made with caution. Nevertheless, it is clear that the Type A development outlined by Takeda is very similar to the operation of the storm of 27 June 1967, which was studied in Chap. V and Section 6.5. The storm existed in a weak wind shear environment, and consisted of a series of essentially vertical cells. Although each cell was short-lived (radar duration 25 - 35 min), the storm lasted for 2½ hrs, due to the recurring development of new cells on the RH flank of the storm.

Type B - The cloud is sharply inclined and short-lived.

This type of development requires a strong wind shear ($\partial U/\partial z$) of constant sign. The cloud is inclined downshear and precipitation falls from the downshear side, developing a downdraft in this region. New updrafts are initiated both downshear and upshear from the precipitation-downdraft region. However, the downshear updraft is rapidly damped out by the vertical wind shear, and the updraft on the upshear side is unable to develop because the upcurrent is required to move faster than the environment - such a movement appears impossible.

This sort of development is indeed quite similar to Phase I of the storm of 28 July 1968, treated in Chap. III and Section 6.3.2. It exhibited a UWER (inclined in the downshear sense) on the upwind side of the storm. A Z_e maximum, indicative of heavy precipitation, was found on the downshear side of the storm. Existing in moderate wind shear of constant sign, it was short-lived and was found not to recur.

Type C - The cloud is almost erect and long lasting.

This type of development occurs with a jet (or extreme wind) within a certain critical range of heights in the lower atmosphere. The jet is characterized by a reversal in the sign of the vertical wind shear, occurring most favorably not far above cloud base. The resulting patterns of rainfall, updraft and downdraft are organized in such a manner that the updraft is on the downshear side and the precipitation and downdraft are on the upshear side of the storm. The convective cloud attains a steady-state and so may be termed long-lasting.

Type C development appears to apply to several of the storms studied here. Perhaps the best comparison exists in the case of the storm of 25 July 1968, studied in Chap. II and Section 6.2. The environmental wind exhibited essentially a two-dimensional pattern with moderate wind shear. This storm was observed to be well organized and long-lived. However, the "jet" which Takeda finds necessary for a long-lived storm is not in evidence. Phase III of the storm of 28 July 1968 (Chap. III and Section 6.3.1) was also of similar structure and, as well, without a "jet". The storm of 29 June 1967 (Chap. IV and Section 6.4) departs substantially from being a two-dimensional storm, but was definitely long-lived and displayed a "jet"-like structure in the plane of storm motion.

In summary, some remarkable similarities exist between the observations and analysis presented in this thesis and Takeda's two-dimensional theoretical model, in spite of the restrictions which exist. These similarities promote confidence both in the conclusions arrived at by observational means and the results of the theoretical model.

CHAPTER VII

THE UPDRAFT IN A SEVERE STORM

7.1 Observational Evidence

Considerable observational evidence has been presented in Chapters II - V establishing that one of the major characteristics of severe storms in Alberta is a broad, strong, persistent, essentially vertical updraft. In summary, some of the evidence is as follows:

(i) Weak echo regions (both bounded and unbounded) of the order of 2 - 10 km diameter are found to exist for periods of 10 - 100 min within radar observable severe storms or on their boundaries. To escape detection, these weak echo regions must have Z_e values < 20 dBz at maximum range (140 km) and < 0 dBz at close range (16 km). Such small Z_e values could be realized by a scattering volume composed primarily of micron size (20 - 30 μ diameter) droplets grown mainly by diffusion during a brief residence time (5 - 8 min) in a strong updraft.

(ii) Aircraft observations at cloud base beneath these weak echo regions demonstrate the presence of a smooth, persistent updraft ($\approx$ 4 - 8 m sec^{-1}) of substantial area (20 - 100 km^2). These updraft regions at cloud base have been found devoid of precipitation size particles.

(iii) The upper extent of weak echo regions are bounded by reflectivity maxima or secondary maxima (typically 40 dBz $< Z_e <$ 60 dBz). These boundary regions are normally the highest points within the radar-detectable storm. Such behaviour appears to be the result of a strong, penetrative updraft carrying precipitation particles into the upper reaches of the storm.

(iv) Weak echo regions have been found to be essentially vertical in structure (particularly at mid-levels) indicating that the updrafts which cause them are also essentially vertical. However, in the case of high wind shear, a tilt in the weak echo region has been found both at the base and at the top. In instances of extreme wind shear near the storm top, narrow weak echo regions have also been detected out into the storm plume.

Substantial evidence to support the concept of a strong updraft in a severe storm has been reported by many workers. Wichmann (1951) reported that sailplanes in Germany experienced cloud base updrafts of 4 - 5 m sec^{-1}; higher penetrations indicated updraft cores as high as 20 - 30 m sec^{-1}. Byers and Braham (1949) found updraft speeds of 5 - 10 m sec^{-1} in short-lived Florida thunderstorms with maxima of 25 m sec^{-1} at 7.6 km MSL. Bibilashvili (Battan; 1963), tracking balloons through thunderstorms with radar, obtained cloud base updrafts of 5 - 7.5 m sec^{-1} and maximum updrafts of 17.5 - 27.5 m sec^{-1}. More recently, measurements made by Hart and Cooper (1968), with balloon transponder systems, have shown maximum updrafts of 15 - 30 m sec^{-1} at 4.5 - 6.0 km MSL in severe storms in Oklahoma. Booker, Hall, Hart and Cooper (1969), using data from a ruptured balloon transponder system, have deduced a maximum updraft speed as high as 45 m sec^{-1} in an Oklahoma severe storm.

Although the configuration and behaviour of the updraft varies considerably from storm to storm, it is quite apparent that <u>a strong updraft is one of the major features of a severe storm</u>. In this chapter, the updraft will be discussed and a simple computational model introduced to examine the updraft structure of Alberta severe storms. The computed storm tops will be compared with radar-observed storm tops for individual severe storms, and characteristic storm updraft structures discussed.

7.2 The Squires-Turner and Weinstein-Davis Models

The observational evidence summarized in Section 7.1 lends considerable support to the concept of a continuous flow updraft of sizeable dimensions and substantial duration. It is clear that a truly steady-state updraft is an impossibility; the development and eventual dissipation of the updraft make time-dependence an essential element. Nevertheless, in many severe storms there exists a period, from approximately 20 min to several hours, during which a quasi-steady state is achieved in the character, depth and magnitude of the severe storm updraft. By utilizing the steady-state assumption, it is possible to model and compute numerically an estimate of the vertical velocity within the updraft.

A number of steady-state models have been proposed; two models of particular relevance to this study will be outlined. Squires and Turner (1962) utilized the results of laboratory experiments on entraining jets as the basis for a steady-state jet model. They assumed a "top hat" (uniform in the horizontal dimension) distribution of all properties across the updraft and envisaged entrainment of environmental air to be proportional to the vertical velocity and inversely proportional to the updraft radius. Provision was made to account for latent heat released by freezing (linear freezing law from -15C to -40C) as well as by condensation. They used an environment with a constant lapse rate to illustrate the characteristics of their model, but no attempt was made to test it against observed storm data. More recently, Marwitz, Middleton, Auer and Veal (1969) have programmed the Squires Turner model and tested it on a selection of 11 hailstorms in Alberta, Nebraska and South Dakota.

Weinstein and Davis (1967) have also used the Squires-Turner entrainment scheme in a similar steady-state updraft model. A different computational technique was used and the latent heat due to freezing was introduced instantaneously at a given temperature (usually -15C). This model has been utilized by the Arizona Weather Modification Research Program on 19 clouds (both seeded and unseeded) in Arizona.

The environmental and cloud base conditions required for the Squires Turner model and the Weinstein-Davis model are essentially the same. A basic requirement is a description of the environment surrounding the cloud:

T_e - environmental temperature
RH_e - environmental relative humidity
P_e - environmental pressure
W_e - environmental vertical velocity (assumed = 0)

These environmental conditions are normally obtained by a radiosonde sounding near the storm. In addition, the following information is required at cloud base:

T_o - initial temperature at cloud base
R_o - initial updraft radius at cloud base
W_o - initial vertical velocity at cloud base
RH_o - initial relative humidity at cloud base (assumed = 100%)
P_o - initial pressure at cloud base (Z_o = height at cloud base may be used instead)

Both Marwitz et al and Weinstein and Davis used aircraft measurements of the temperature (T_o), radius (R_o), and height (Z_o) at cloud base. Marwitz et al also used aircraft measurements of the vertical velocity (W_o) at cloud base, but Weinstein and Davis used instead a constant cloud base vertical velocity ($W_o = 2$ m sec^{-1}). The Squires-Turner model assumes that, at cloud base, the <u>virtual temperature</u> in the cloud and environment are equal (a condition of neutral buoyancy at cloud base). Weinstein and Davis have assumed instead that the <u>temperature</u> in the cloud and environment are equal (a condition of positive buoyancy at cloud base).

The resulting steady-state conditions, as computed by the Squires Turner model and the Weinstein-Davis model, are:

R - cloud radius as a function of height
T - cloud temperature as a function of height
W - cloud vertical velocity as a function of height
LWC - cloud liquid water content as a function of height
H_{max} - maximum cloud height

Observed values of these storm parameters might be compared with the model results to verify or refute the model in question. Measurements of adequate density and sufficient accuracy of the temperature (T), liquid water content (LWC) and vertical velocity (W) within the storm updraft are not yet available. Although cloud radius (R) measurements might be made under favorable photographic conditions, this technique does not constitute a practical, routine method of cloud radius measurement. Radar measurements are not reliable either since the sensitivity of weather radars enables them to detect precipitation particles and not cloud droplets. The only remaining measurement which might be used for verification is the maximum cloud height (H_{max}). This can be measured by aircraft observation, but such data are not commonly available. The observed data normally available are the radar-observed storm tops. Due to the sensitivity problem mentioned, the radar observes precipitation particles with a finite fallspeed (likely 5 - 10 m sec^{-1}). As a consequence, the radar-observed storm top will be consistently lower than the maximum cloud height (H_{max}).

Marwitz et al have used the Squires-Turner model to compute steady state conditions for 11 hailstorms observed in Alberta, Nebraska and South Dakota. A graph depicting the radar-observed storm tops vs. the computed

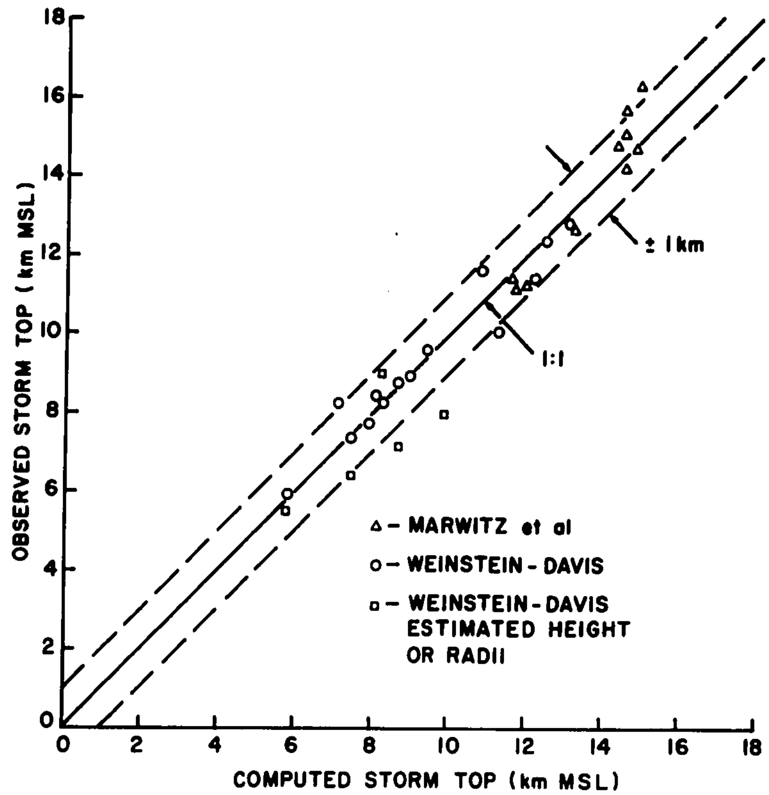

Fig. 7.2.1 Squires-Turner and Weinstein-Davis Model Storm Tops vs. Observed Storm Tops. Squires-Turner model tops (after Marwitz et al) are plotted for 11 hailstorms in Alberta, Nebraska and South Dakota. Weinstein-Davis model tops are indicated for 19 clouds in Arizona.

maximum cloud heights is shown in Fig. 7.2.1. The computed maximum cloud heights and the radar-observed storm tops (taken at 20 min intervals) are found to agree within ±1.4 km. Maximum updrafts were generally found to be 20 - 30 m sec^{-1} with liquid water contents between 4 and 9 gm kg^{-1}(2.0 - 4.5 gm m^{-3}). Weinstein and Davis tested their model on 19 clouds (both seeded and unseeded) in co-operation with the Arizona Weather Modification Research Program. Figure 7.2.1 also illustrates observed storm tops vs. computed maximum cloud heights (the method of observing the storm tops is not stated, it is assumed it was accomplished by radar) for the Weinstein-Davis model results. In most instances, the heights agree within ±1 km and all cases agree within ±2 km.

7.3 A Loaded Moist Adiabatic (LMA) Updraft Model

As both Marwitz et al and Weinstein and Davis have indicated, the "top hat" assumption and the entrainment scheme of Squires and Turner are not physically realistic, particularly when dealing with updrafts having a radius of the order of 2 km or more. The Squires-Turner model requires an instantaneous mixing of entrained air across the entire width of the cloud updraft. Except in cases of extreme vertical wind shear ($\partial V/\partial z$), it is difficult to envisage a turbulent mixing process which could transport the entrained air inwards toward the cloud axis at a rate exceeding the vertical velocity of the updraft. Thus, the penetration of the entrained air, into a cloud updraft, may be depicted as in Fig. 7.3.1 with the result that the inner core may be totally unaffected by entrainment, or in extreme cases affected only near the storm top.

In addition, any mixing process which transports entrained air inwards toward the updraft axis must continually mix partially diluted cloud with cloud which has adiabatic properties. Thus, the effect of entrainment upon the temperature, vertical velocity and liquid water content must be more pronounced at the cloud boundary than at the cloud axis. This would lead to a non-uniform profile of all cloud properties as illustrated schematically in Fig. 7.3.2. The cloud base profile may, indeed, be close to the "top hat" case as has been observed and reported by Auer, Veal and Marwitz (1969). Nevertheless, entrainment and mixing will tend to lead to a centrally peaked cloud property profile which becomes more pronounced with height.

One outcome of this proposed mixing process is that the vertical velocity at the cloud boundary would be significantly less than that computed by the Squires-Turner model and so the entrainment rate would be small.

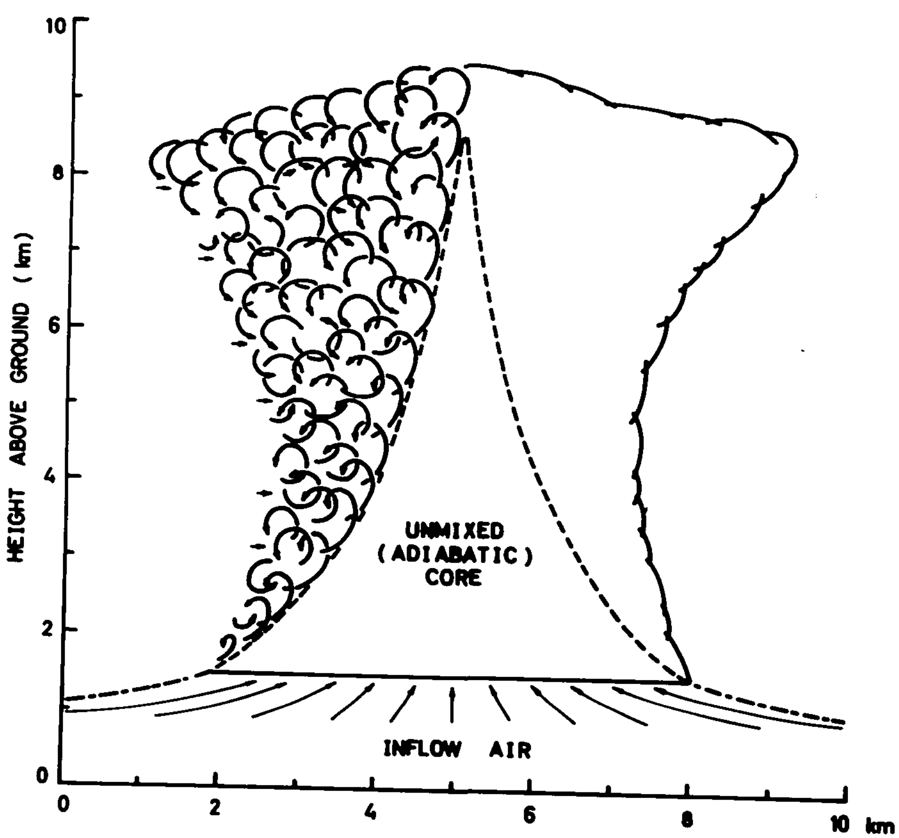

Fig. 7.3.1 Schematic Diagram Illustrating Penetration of Entrained Air into an Updraft by Turbulent Mixing. An updraft (with uniform properties at cloud base) is shown affected by turbulent mixing (circular arrows) from the cloud boundary inward. Note the central core unaffected by environment.

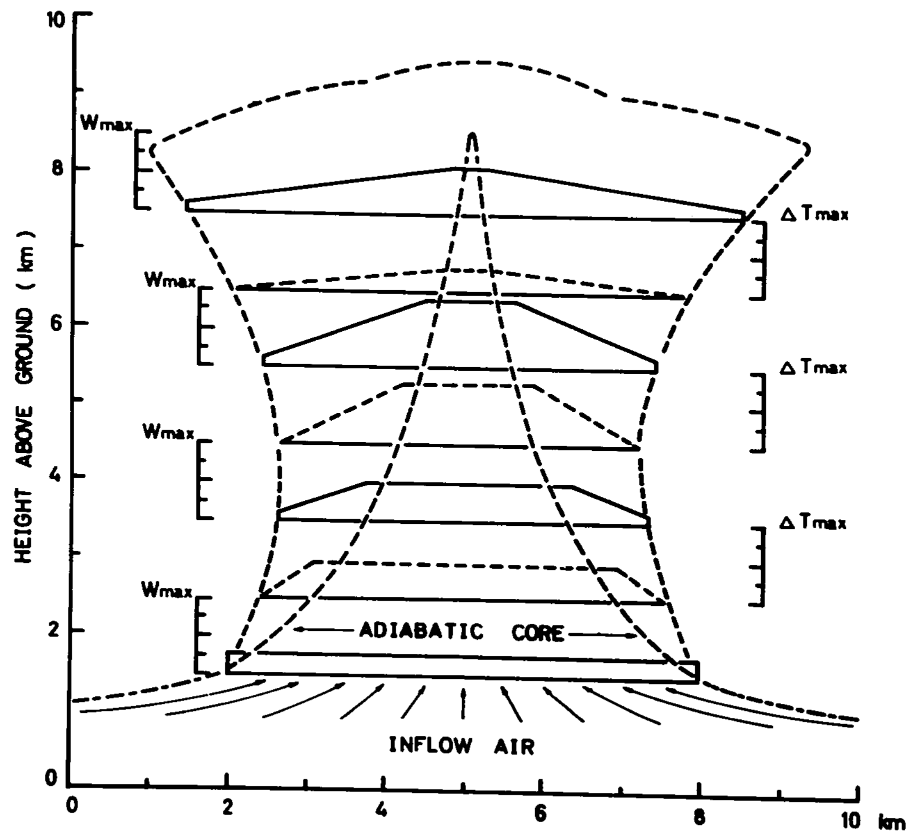

Fig. 7.3.2 Schematic Diagram Illustrating Vertical Velocity and Temperature Excess Distributions Across an Updraft Affected by Turbulent Mixing. Vertical Velocity (W) and temperature excess ($\Delta T = T_c - T_e$) distributions (normalized) typical of the updraft in Fig. 7.3.1 are shown. Note unaffected (adiabatic) core.

Stereo photography cloud measurements, made in Alberta, indicate that elements in the cloud wall ascend (or descend) at vertical velocities of ±1 - 3 m sec^{-1} and not 15 - 25 m sec^{-1} as would be the case for the Squires-Turner or Weinstein-Davis models.

It is considered beyond the scope of this thesis to devise a numerical cloud model which would account for the effects outlined above. Instead, one readily concludes that along the central axis of the updraft cloud conditions must be very close to moist adiabatic conditions. This is, indeed, a very attractive simplification and one which appears to be more realistic in describing cloud conditions along the updraft axis than either the Squires-Turner or Weinstein-Davis model.

With these concepts and simplifications in mind, a loaded moist adiabatic (LMA) updraft model has been devised, programmed and used to obtain estimates of the cloud properties within specific Alberta hailstorms.

7.3.1 Environmental Conditions

The basic information, used to describe the environment around a given storm, was obtained from radiosonde data taken at ALHAS field project headquarters at Penhold. These soundings were generally taken within two hours of the time of maximum storm height and usually less than 50 km (30 st mi) from the particular storm being studied. The temperature (deg C) and relative humidity (%) were extracted from the original adiabatic computation chart at pressure intervals of not more than 30 mb, as well as at all levels of significant temperature change. This was done to minimize error in the radiosonde information due to graphical computation, coding and transmission of the radiosonde data.

These data were first interpolated to yield temperature and relative humidity at 10 mb pressure intervals. Using the following definitions, the mixing ratio, virtual temperature and geopotential height were computed at each 10 mb interval:

m_s = saturation mixing ratio (gm kg^{-1}) — Defn. 7.3.1

$= 0.622\ (e_s/p - e_s)$

Where

e_s = saturation vapor pressure (mb)

$= 6.11 \times 10^{(at/t+b)}$ (Tetens formula)

$a = 7.5$

$b = 237.3$ (deg C)

t = temperature (deg C)

p = pressure (mb)

T_v = virtual temperature (deg A) — Defn. 7.3.2

$= T(1 - 0.61\ m\ )$

Where

T = temperature (deg A)

$= t + 273.16$

m = mixing ratio (gm kg^{-1})

$= rm_s$

r = relative humidity (%)

Z_p = geopotential height at pressure level p (m) — Defn. 7.3.3

$$= \sum_{p = p_{sfc}}^{p} \Delta Z$$

Where

p_{sfc} = pressure at surface

ΔZ = geopotential height increment over a 10 mb pressure interval

$$= \frac{R_d}{g}\int_{p_1}^{p_2} T_v \, d\ln p \quad = \quad \frac{R_d}{g}\, \overline{T}_v \ln \frac{p_1}{p_2}$$

p_1 = pressure at level 1 (mb)

p_2 = pressure at level 2 (mb) $\quad p_1 > p_2$

$\overline{T}_v$ = mean virtual temperature between levels p_1 and p_2

g = 980 (cm sec^{-2})

R_d = gas constant for dry air

= 2.8704×10^6 (ergs gm^{-1} deg A^{-1})

As the final output was desired at 50 m intervals, the temperature, pressure, relative humidity, mixing ratio and virtual temperature were then interpolated for these levels. The resulting data were then in a form which could be readily used in a 50 m step vertical velocity model.

7.3.2 Cloud Base Conditions

As was outlined for the Squires-Turner model and the Weinstein-Davis model, the conditions at cloud base are a very important part of the vertical velocity calculation. The parameters required are:

T_o - cloud base temperature (deg C)

P_o - cloud base pressure (mb)

W_o - cloud base updraft (m sec^{-1})

Unlike the models outlined in Section 7.2, it is not necessary to know the cloud base radius (R_o) since the LMA model does not consider the effect of entrainment.

Ideally, one wishes to have direct measurements of the above three parameters at cloud base. However, in lieu of direct cloud base observations, the temperature (T_o) and pressure (P_o) at cloud base were obtained by determining the lifting condensation level (LCL) from observations of the surface temperature (T_{sfc}) and surface dewpoint (T_d). Hourly surface observations were available from weather stations located at Penhold, Rocky Mountain House, Edmonton, Calgary and Coronation. These were utilized to determine an estimate of the surface temperature and dewpoint of the inflow air in the immediate vicinity of the particular storm in question. In most instances, surface observations were available within 50 km (30 st mi) and 30 min of the location and time of the maximum storm height.

The third parameter required is a measure of the vertical velocity (W_o) at cloud base. Auer and Sand (1966) have reported aircraft-observed average cloud base updrafts of 3.8 m sec^{-1} for heavily precipitating thunderstorms. More recently, Auer and Marwitz (1968) reported similar measurements for hailstorms which indicate that average cloud base updrafts associated with hailstorms range between 4 and 5 m sec^{-1}. In the absence of measured cloud base updraft information, a standard updraft of 5 m sec^{-1} at cloud base was assumed. Except in extreme cases, it is likely that this estimate is within ±2 m sec^{-1} of the actual updraft at cloud base. As becomes evident in the following section, the initial cloud base updraft has but a small effect on the maximum vertical velocity achieved, unless the cloud base updraft is substantially more than one-third of the updraft maximum. For example, a storm having sufficient energy available to produce a vertical velocity maximum of 20 m sec^{-1} beginning with $W_o = 0$, would have a vertical velocity maximum of approximately 20.6 m sec^{-1} if instead W_o were 5 m sec^{-1}.

7.3.3 Cloud Parcel Temperature

As becomes evident in Section 7.3.4, a prime requirement for numerical computations in the LMA model is the temperature along a moist adiabat (trajectory of a moist air parcel under adiabatic conditions, all condensed moisture being dropped). A moist adiabat is defined by a constant value of the pseudo-wet-bulb potential temperature (θ_{sw}) or by a constant value of the pseudo-equivalent temperature (θ_{se}).

Although there are a number of methods of computing the trajectory of a moist adiabat, the method used here is essentially that used by Stackpole (1967). The moist adiabats are defined by the Rossby definition of the pseudo-equivalent potential temperature (θ_{se}):

$$\theta_{se} = \theta_d \exp(L_v m_s / C_p T) \qquad \text{Defn. 7.3.4}$$

Where

t = temperature (deg C)

T = absolute temperature (deg A)

$= t + 273.16$

C_p = specific heat of air at constant pressure

$= 0.24$ (cal gm^{-1} deg C^{-1})

L_v = latent heat of vaporization (cal gm^{-1})

$= 596.73 - 0.601t$

e_s = saturation vapor pressure (mb)

$= 6.11 \times 10^{(at/t+b)}$ (Teten's formula)

$a = 7.5$

$b = 273.3$ (deg C)

m_s = saturation mixing ratio

$= 0.622\ (e_s/p - e_s)$

p = pressure (mb)

θ_d = partial potential temperature (deg A)

$= T\ (1000/(p - e_s))^{2/7}$

The initial value of θ_{se} is calculated using the input values of temperature (T_o) and pressure (P_o) at cloud base. An iterative method is then utilized to compute the parcel temperature (T_p) which will yield the same θ_{se} value as computed at cloud base. The procedure is as follows:

(i) Compute θ_{se} at cloud base.

(ii) Advance to next grid point (at 50 m intervals) and compute a guess value of the parcel temperature (T_p) at this pressure level.

(iii) Using the guess temperature, pressure and mixing ratio at this pressure level, compute a value of θ_{se} and label it θ_{se}'.

(iv) Compare θ_{se} and θ_{se}'. If $|\theta_{se} - \theta_{se}'| < 0.05C$, retain the value of T as the parcel temperature.

(v) If $|\theta_{se} - \theta_{se}'| > 0.05C$, adjust the guess value of the parcel temperature and return to step (iii). Continue until an appropriate parcel temperature (T_p) has been reached.

The resulting series of parcel temperatures thus define the trajectory of a moist adiabat.

As Stackpole indicated, the Goff-Gratch expression, as used to calculate the saturation vapor pressure (e_s) for Table no. 94 of the Smithsonian Meteorological Tables (List; 1958), could have been used instead of the much simpler Teten formula. However, tests performed by Stackpole indicated that the computational sophistication and the additional time required by the Goff-Gratch formula were not justified.

As a test of the accuracy of the computation of θ_{sw}, comparisons were made with Table no. 78 of the Smithsonian Meteorological Tables. Computations were made using the LMA program for θ_{sw} values of 16C, 20C and 24C, as the majority of the vertical velocity computations were made at θ_{sw} values between 16C and 20C, with θ_{sw} = 23.7C being a maximum. The differences between the Smithsonian Tables and the program results are zero at cloud base and increase with height. At 250 mb, the Smithsonian value minus the LMA program value was:

(i)	$\theta_{sw} = 16C$	Difference = −0.15C
(ii)	$\theta_{sw} = 20C$	Difference = −0.10C
(iii)	$\theta_{sw} = 24C$	Difference = +0.40C

The majority of all moist adiabatic temperature calculations are therefore within ±0.10C of the values quoted by the Smithsonian Meteorological Tables; a sufficient degree of accuracy.

7.3.4 Vertical Velocity Calculations

Sections 7.3.1 to 7.3.3 have been devoted to outlining the procedures used to establish the environmental and cloud base conditions and the manner in which cloud parcel temperatures were calculated. The model, which will be outlined in this section, is in essence the classical moist adiabatic parcel theory with adiabatic water loading added. Entrainment and freezing are not included. As explained in Section 7.3, it is reasonable to neglect entrainment in computing cloud parameters along the updraft axis, particularly in the lower and middle portions of the storm updraft. Since the axially directed penetration of entrained air is greatest at high levels, it may not be a reasonable approximation to neglect entrainment there. But, it is in these upper portions that freezing of the supercooled cloud droplets occurs, adding energy (approximately 10% if all liquid freezes) while entrainment expends it. It would be desirable to incorporate both freezing and entrainment in the model. However, lacking a simple, realistic entrainment scheme, and taking account of the compensating effect of entrainment and freezing, neither entrainment nor freezing has been incorporated.

Consider a parcel of air which is not in hydrostatic equilibrium. It is acted upon by two forces:

(i) gravitational force $\quad -(mg)$

(ii) pressure force $\quad -\left\{\frac{m}{\rho_p}\frac{dp}{dz}\right\}$

Applying Newton's second law, and writing the forces in terms of unit mass, one obtains:

$$\frac{dw}{dt} = -g - \frac{1}{\rho_p}\frac{dp}{dz} \qquad \text{(Eqn. 7.3.1)}$$

Where

m = mass

p = pressure

z = height

w = vertical velocity

ρ_p = density of a parcel of moist air

t = time

g = gravitational force

Utilizing $\frac{dp}{dz} = -\rho_e g$ (ρ_e = density of the environmental air) and rearranging the terms, it is found that:

$$\frac{dw}{dt} = g\left[\frac{\rho_e - \rho_p}{\rho_p}\right] \qquad \text{(Eqn. 7.3.2)}$$

Equation 7.3.2 gives the acceleration due to buoyant forces acting on a parcel of moist air and could be calculated using the environmental temperature and the cloud parcel temperature obtained in Section 7.3.3. However, the moist adiabatic cloud parcel temperature is calculated using the assumption that all condensed water falls out immediately. Since the cloud water is in the form of micron size cloud droplets, it will instead be carried with the parcel. Adding the effect of m_ℓ gm of liquid water, Eqn. 7.3.2 becomes:

$$\frac{dw}{dt} = g\left[\frac{\rho_e - \rho_p}{\rho_p}\right] - gm_\ell \qquad \text{(Eqn. 7.3.3)}$$

Using $p = \rho_p R_d T_{vp}$ and $p = \rho_e R_d T_{ve}$ (assuming pressure in cloud parcel and environment are equal)

Where

R_d = gas constant for dry air

T_{vp} = virtual temperature of the moist parcel

T_{ve} = virtual temperature of the environment

it is found that:

$$\frac{dw}{dt} = g\left[\frac{T_{vp} - T_{ve}}{T_{ve}}\right] - gm_{\ell} \qquad \text{(Eqn. 7.3.4)}$$

Multiplying both sides of Eqn. 7.3.4 by dz, and using $dz = -dp/\rho_e g$, $p = \rho_p R_d T_{vp}$ and $p = \rho_e R_d T_{ve}$, Eqn. 7.3.4 becomes:

$$wdw = -R_d(T_{vp} - T_{ve} - m_{\ell} T_{ve}) \frac{dp}{p} \qquad \text{(Eqn. 7.3.5)}$$

Integrating Eqn. 7.3.5 between pressures p_1 and p_2, yields:

$$w_2 = \left(w_1^2 + 2R_d(\overline{T}_{vp} - \overline{T}_{ve} - m_{\ell}\overline{T}_{ve}) \ln \frac{p_1}{p_2} \right)^{1/2} \qquad \text{(Eqn. 7.3.6)}$$

Where

$\overline{T}_{vp}$ = mean virtual temperature between p_1 and p_2 (in the parcel)
$\overline{T}_{ve}$ = mean virtual temperature between p_1 and p_2 (in the environment)
w_1 = vertical velocity at p_1
w_2 = vertical velocity at p_2

Since the vertical velocity (w_z) is required at p_z, starting with w_o at p_o, Eqn. 7.3.6 may be re-written in the following fashion:

$$w_z = \left(w_o^2 + 2R_d \sum_{p_i = p_o,\, 1}^{p_i = p_{z-1}} (\overline{T}_{vp} - \overline{T}_{ve} - m_{\ell}\overline{T}_{ve})_i \ln \frac{p_i}{p_i} \right)^{1/2} \qquad \text{(Eqn. 7.3.7)}$$

where p_i and p_{i+1} are 50 m apart and $(\overline{T}_{vp} - \overline{T}_{ve} - m_{\ell}\overline{T}_{ve})_i$ represents the contribution due to the mean virtual temperatures in a 50 m layer between p_i and p_{i+1}.

In the preceding equations the term $-m_{\ell}\overline{T}_{ve}$ is the "buoyant temperature correction" or the decrease in temperature which would account for

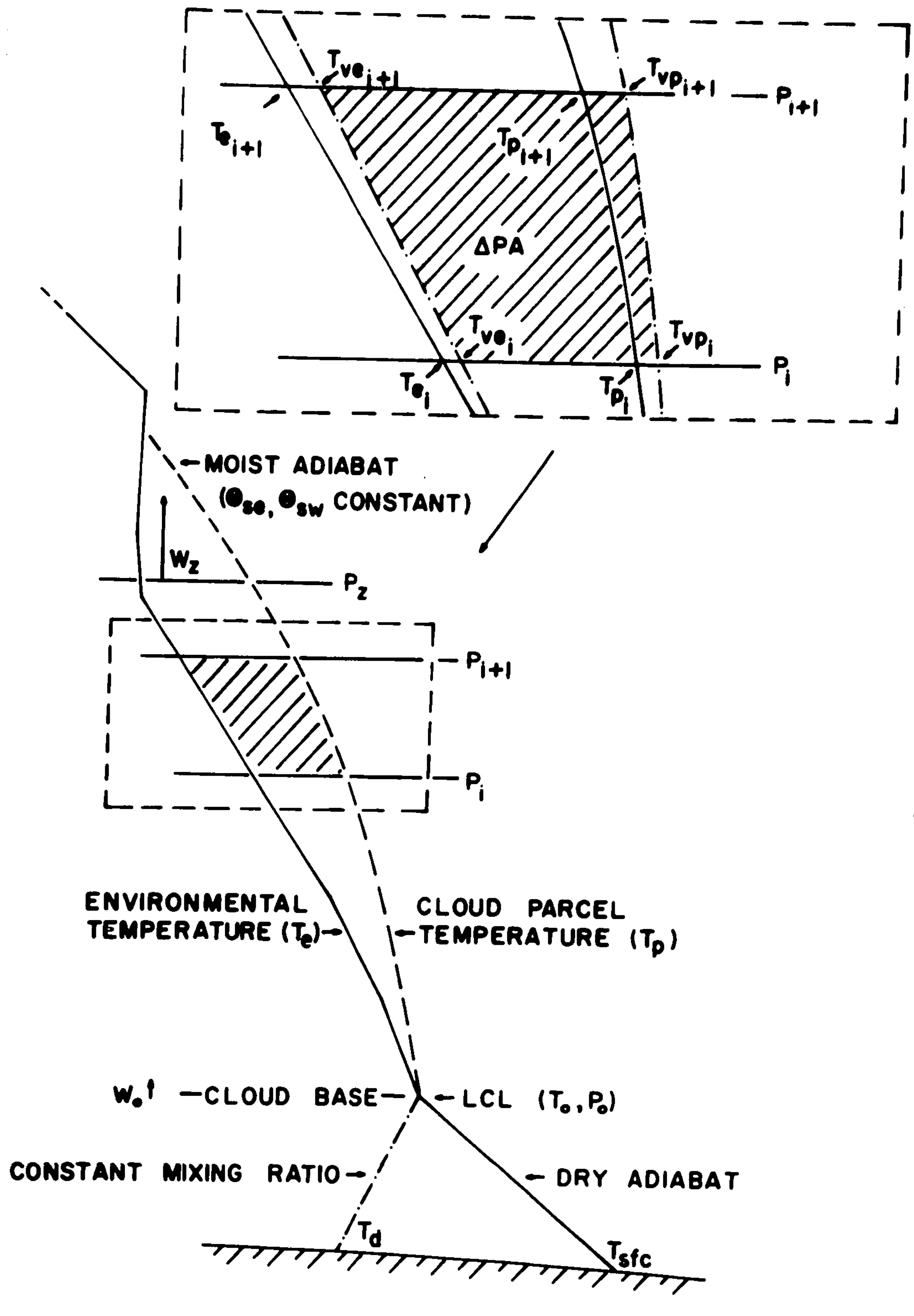

Fig. 7.3.3 Schematic Tephigram Illustrating the Variables Used in the LMA Model. A tephigram is shown with the variables and parameters used in the LMA model computations. The insert in the upper right corner displays the "positive area" increment.

the loading due to the liquid water content. The term:

$$\sum_{p_o}^{p_z} \Delta PA = \sum_{p_i = p_{o,1}}^{p_i = p_{z-1}} (\overline{T}_{vp} - \overline{T}_{ve})_i \ \ln \frac{p_i}{p_{i+1}}$$

represents the "positive area" on a tephigram which lies between the environmental curve and a moist adiabat (with the virtual temperature correction being used) as shown in Fig. 7.3.3. With the addition of the water loading term ($-m_\ell \overline{T}_{ve}$) the "loaded positive area" becomes:

$$\sum_{p_o}^{p_z} \Delta PA_1 = \sum_{p_i = p_{o,1}}^{p_i = p_{z-1}} (\overline{T}_{vp} - \overline{T}_{ve} - m_\ell \overline{T}_{ve})_i \ \ln \frac{p_i}{p_{i+1}}$$

which represents the loaded area on a tephigram (ie. the energy available when water loading is added).

7.4 Observations and LMA Model Results for Alberta Hailstorms

The availablility of comprehensive radar observations (with 3 min time resolution, 1.15 deg radar beamwidth) for hailstorms in the ALHAS project area during the summers of 1967 and 1968 prompted a study of 29 hailstorm days. The days chosen for this study were days on which 20 or more hail reports (both mail and survey reports) were received by ALHAS for hailfall within the project area. Although this criterion is arbitrary, it was adopted to ensure that the storms chosen were of substantial dimension and duration, and thus reasonably represented by the LMA model.

The radar study consisted of a determination of the radar-observed

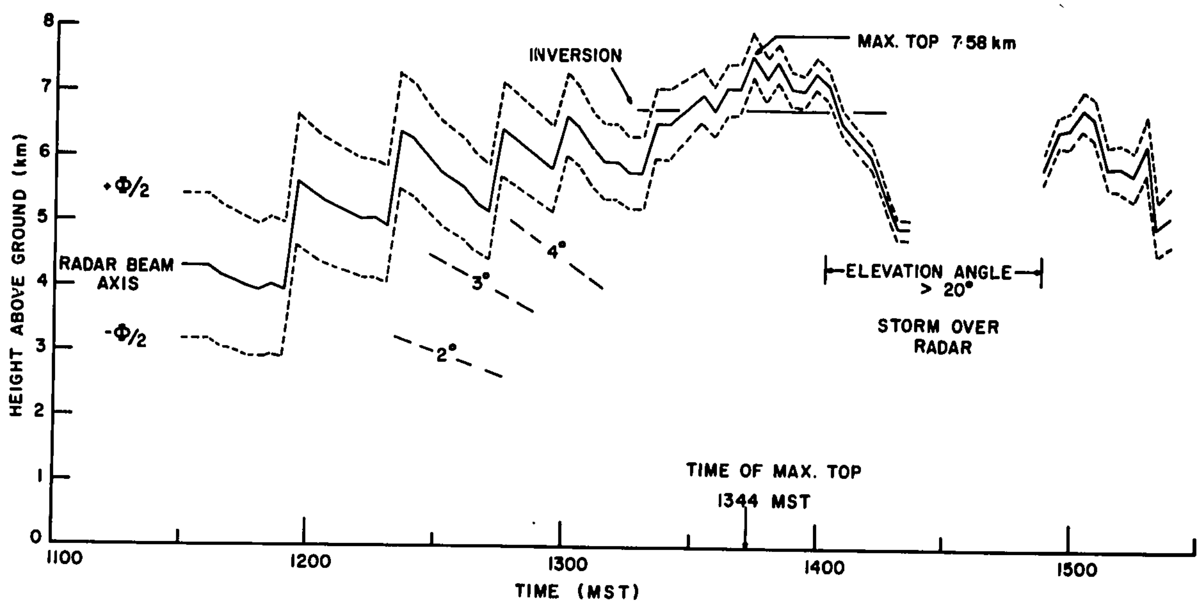

Fig. 7.4.1 Height of Radar-Observed Storm Top vs. Time - 29 June 1967. The height of the radar beam axis at 3 min intervals is indicated by the solid line. In addition, the upper and lower half-power beam points (Ø/2, -Ø/2) are delineated by dashed lines. Note the maximum radar-observed storm top (7.58 km) at 1344 MST. The sawtooth pattern is due to the discrete (1 deg) increases in the radar-observed elevation angle.

storm top history for the highest storm on any given day. From projected 35 mm radar film, the slant range (±0.8 km), maximum elevation angle (recorded in integral degrees), and azimuth angle (±5 deg, to correct elevation angle for spiral antenna program) were obtained at 3 min intervals. Radar-observed storm tops were then computed to be at the height of the radar beam axis ± one-half of the vertical component of the vertical half-power beamwidth. Corrections were made for the spiral antenna program, the curvature of the earth and the refractive index of the atmosphere[1]. An example of the resulting height vs. time graph is shown in Fig. 7.4.1.

[1]Correction for the refractive index was made using R´= 6/5R (instead of the standard R´= 4/3R) based on an analysis of the water vapor distribution calculated from a median Alberta hail sounding quoted by Henry (1964).

The time of the maximum radar-observed storm top (shown in Fig. 7.4.1) was used to determine an estimate of the cloud base conditions (as described in Section 7.3.2) and the particular radiosonde sounding which was most appropriate for use with the LMA model. These data were then utilized with the LMA model to yield the storm parameters at the time of maximum storm height. This is a limiting case; in fact it is an estimate of the maximum height, maximum liquid water content and maximum vertical velocity which the storm could have attained.

As discussed in Section 7.2, the radar-observed storm top will underestimate the height of the cloud top due to the fact that weather radars detect precipitation size particles with a finite fallspeed. Since the fallspeed of these particles is approximately 10 m sec^{-1}, for purposes of comparison with radar-observed storm tops in this study, the height at which the vertical velocity (computed from the LMA model) decreases to 10 m sec^{-1} will be utilized and referred to as the computed storm top (or model storm top). This computed storm top is distinct from the computed cloud top at which point the vertical velocity decreases to zero.

Figure 7.4.2 illustrates the radar-observed storm tops vs. the computed storm tops (at the time of maximum storm height) for the 29 hailstorms studied. Additional data regarding the maximum vertical velocity, maximum liquid water content, maximum energy (the maximum value of the energy given by the loaded "positive area") and surface hail observations are summarized in Table 7.4.1 for these 29 hailstorms.

The radar-observed storm tops plotted in Fig. 7.4.2 are accompanied by an error bar which is equal to the vertical component of the vertical half-power beamwidth. It is more difficult to assess the limits of error associated with the computed storm top. Temperature errors at cloud base would

Table 7.4.1 Updraft Parameters for 29 Alberta Hailstorm Days

Date	Observed Radar Top km		Computed Model Top km	W_{max} m sec^{-1}	LWC_{max} gm m^{-3}	Maximum Energy J gm^{-1}	Observed Maximum Hail Size	Total Hail Reports
27 June 67	7.11	±.70	7.08	16.44	3.19	0.1227	walnut	61
29 June 67	7.58	±.35	7.53	23.09	3.22	0.2665	golfball	265
06 July 67	6.42	±.86	5.70	15.33	3.19	0.1049	grape	58
08 July 67	5.39	±.40	5.20	14.17	4.53	0.0879	grape	21
09 July 67	6.18	±.88	6.47	20.34	3.42	0.1943	walnut	111
14 July 67	12.74	±.94	12.30	45.82	4.63	1.0371	larger	55
18 July 67	10.00	±.43	11.17	34.82	3.45	0.5935	larger	153
19 July 67	8.56	±.35	8.33	23.98	3.44	0.2750	grape	40
27 July 67	12.26	±.49	12.81	43.36	4.51	0.9276	walnut	118
28 July 67	10.86	±.47	11.55	31.21	3.74	0.4746	larger	278
29 July 67	10.53	±.77	11.15	28.94	3.87	0.4062	golfball	27
30 July 67	12.34	±.87	11.52	34.23	3.85	0.5734	walnut	28
31 July 67	8.18	±1.18	8.35	24.92	3.15	0.2979	walnut	27
06 Aug 67	11.21	±.48	11.40	39.21	5.07	0.7562	larger	382
12 Aug 67	11.42	±.91	12.20	43.27	5.09	0.9238	walnut	43
21 Aug 67	11.26	±1.46	10.85	35.43	4.36	0.6153	golfball	35
17 June 68	6.32	±.45	6.60	17.36	2.72	0.1383	pea	21
20 June 68	7.20	±.81	7.10	17.64	3.33	0.1431	golfball	128
27 June 68	9.13	±.65	9.45	27.38	3.15	0.3624	grape	157
05 July 68	10.21	±.37	11.55	28.98	3.04	0.4075	grape	51
09 July 68	11.43	±.76	11.10	22.12	2.87	0.2320	golfball	159
10 July 68	11.01	±1.12	10.04	21.25	4.09	0.3729	walnut	80
15 July 68	8.49	±.79	8.94	21.76	2.58	0.2244	walnut	118
17 July 68	8.93	±.33	10.05	26.98	2.98	0.3386	walnut	30
25 July 68	10.54	±.34	10.05	19.09	4.01	0.1642	walnut	116
28 July 68	13.58	±.66	14.40	68.64	5.62	2.3431	larger	108
04 Aug 68	10.51	±.45	11.55	35.51	5.22	0.6180	golfball	100
05 Aug 68	9.42	±1.26	9.91	24.74	4.90	0.2935	golfball	20
11 Aug 68	9.88	±.31	10.00	21.14	3.70	0.2109	larger	116

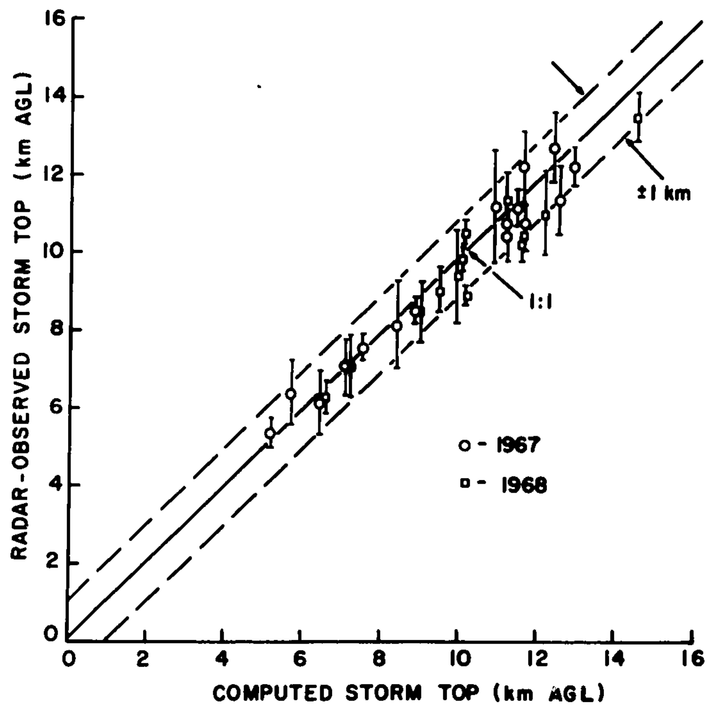

Fig. 7.4.2 Radar-Observed Storm Tops vs. Computed Storm Tops (LMA Model) for 1967 and 1968. Radar observations of the highest storm top for a given storm are compared with the height at which the vertical velocity computed from the LMA model decreases to 10 m sec^{-1}. The error bars denote the vertical component of the vertical half-power radar beamwidth.

be of the order of ±0.5 - 1.0C which would result in an error in the computed storm top of approximately ±0.5 - 0.75 km and an associated error in the maximum vertical velocity of ±3 - 5 m sec^{-1} for a Medium Energy storm ($H_{max} \simeq 10$ km, $W_{max} \simeq 25$ m sec^{-1}). A cloud base temperature error of this order would represent a substantial change in energy for a Low Energy storm ($H_{max} \simeq 7$ km, $W_{max} \simeq 16$ m sec^{-1}) and would, therefore, have a more serious effect on the computed storm top and vertical velocity. However, for High Energy storms a cloud base error of ±0.5 - 1.0C would result in only a small percentage error in the computed storm top and vertical velocity. On the average, it is estimated that the computed storm tops are reliable to within ±0.5 km.

From Fig. 7.4.2 it is clear that the LMA model is capable of estimating the storm top with reasonable accuracy. In 79% of the cases studied, the radar-observed storm top and computed storm top agreed within the limits of observational error. This agreement indicates that the cloud temperature, liquid water content and vertical velocity estimates are also of reasonable accuracy. As such, the estimates obtained for 29 major hailstorms represent a consistent and useful description of Alberta severe storm parameters, which are of considerable value in studying the microphysics of hail growth. English (1969) and Warner, English, Chisholm and Hitschfeld (1969) have used vertical velocity estimates from the LMA model to compute hailstone growth for an Alberta hailstorm (29 June 1967) with considerable success. Computed parameters for specific Alberta storms will be used in Chapter IX to describe the growth environment for graupel and hailstones. However, it is also of interest to consider the basic updraft characteristics of different types of Alberta severe storms.

7.4.1 Updraft Characteristics of Alberta Hailstorms

During the study of the 29 hailstorm days, it became evident that there are a number of striking relationships between storm energy, storm height, liquid water content and vertical velocity. Figure 7.4.3 is a graph of the maximum radar-observed storm top (± one-half of the radar half-power beamwidth) vs. the computed maximum vertical velocity. It is apparent from this figure that the greater the vertical velocity (and therefore the greater the storm energy) the higher the maximum storm top. Two items in particular contribute to the scatter in this figure; observational error and the fact that each storm existed in an environment with different characteristics. Nevertheless, there still is a striking relationship between maximum observed storm top and maximum computed vertical velocity.

Behaviour of the updraft upon penetrating the tropopause is sub-

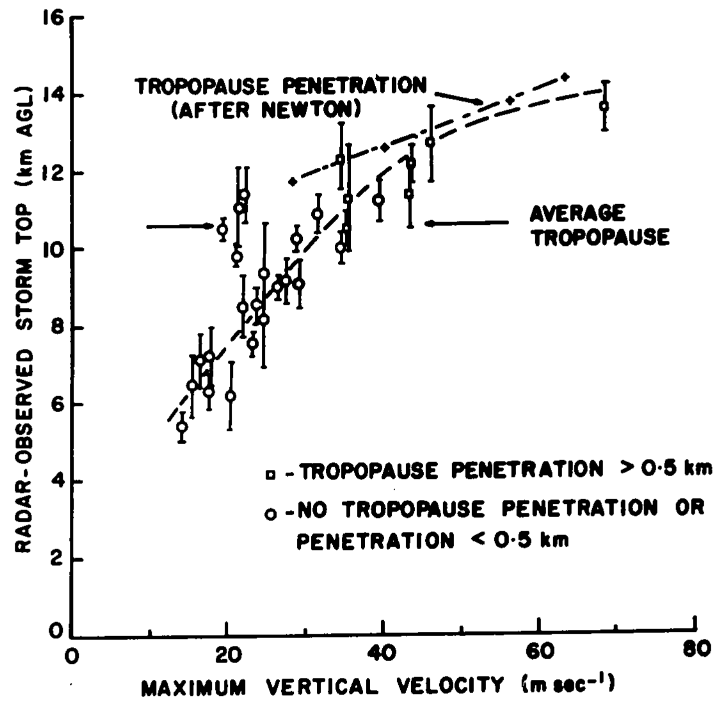

Fig. 7.4.3 Radar-Observed Storm Tops vs. Maximum Vertical Velocity (LMA Model) for 29 Hailstorms in 1967 and 1968. Circles denote storm tops which did not penetrate the tropopause or penetrated the tropopause by less than 0.5 km. Squares indicate storms which penetrated the tropopause by more than 0.5 km; the average tropopause height for these 7 storms is indicated.

stantially different to its behaviour beneath the tropopause. The updraft decelerates rapidly after penetrating the tropopause to come to rest not far above the tropopause. Newton (1968) has computed the tropopause penetration for updrafts of varying speeds. An average tropopause height (for those 7 days on which the storms penetrated the tropopause by more than 0.5 km) has been added to Fig. 7.4.3 along with Newton's tropopause penetration curve. Much more data would be required to conclude that the observations follow Newton's tropopause penetration calculations. There is little doubt, however, that a much different relationship exists between height and vertical velocity above the tropopause than beneath it.

Although it must be recognized that the 29 hailstorms represented in this study are individual members from a very broad spectrum, it is convenient to classify them into groups which have certain similarities. It is evident from Fig. 7.4.3 that there is a definite relationship between storm height and vertical velocity. In the previous section, the vertical velocity was computed from the square root of the summation of the "loaded positive area". The "loaded positive area" reaches a maximum when the parcel temperature (with liquid water accounted for) equals the environmental temperature. This maximum "loaded positive area" or maximum storm energy is thus a convenient parameter to use in the classification of the 29 hailstorms. Three categories have been utilized: Low, Medium and High Energy hailstorms. The boundaries between these three groups have been assigned on the basis of cloud physical and dynamical considerations which are outlined below:

Low Energy Hailstorms (0.00 - 0.20 J gm^{-1})

(i) do not penetrate the tropopause
(ii) maximum storm top not colder than -40C

Medium Energy Hailstorms (0.20 - 0.45 J gm^{-1})

(i) do not significantly penetrate the tropopause
(ii) maximum storm top colder than -40C but not colder than -60C

High Energy Hailstorms (0.45 → J gm^{-1})

(i) penetrate the tropopause significantly
(ii) maximum storm top colder than -60C

Low Energy hailstorms generally occur in late June and early July in cool airmasses with low surface mixing ratios. The majority of these storms are characterized by the following range of parameters:

Parameter	Range
Maximum storm energy	0.00 - 0.20 J gm^{-1}
Maximum storm top	6 - 7 km (AGL)
Maximum vertical velocity	15 - 18 m sec^{-1}
Maximum liquid water content	3.1 - 3.3 gm m^{-3}

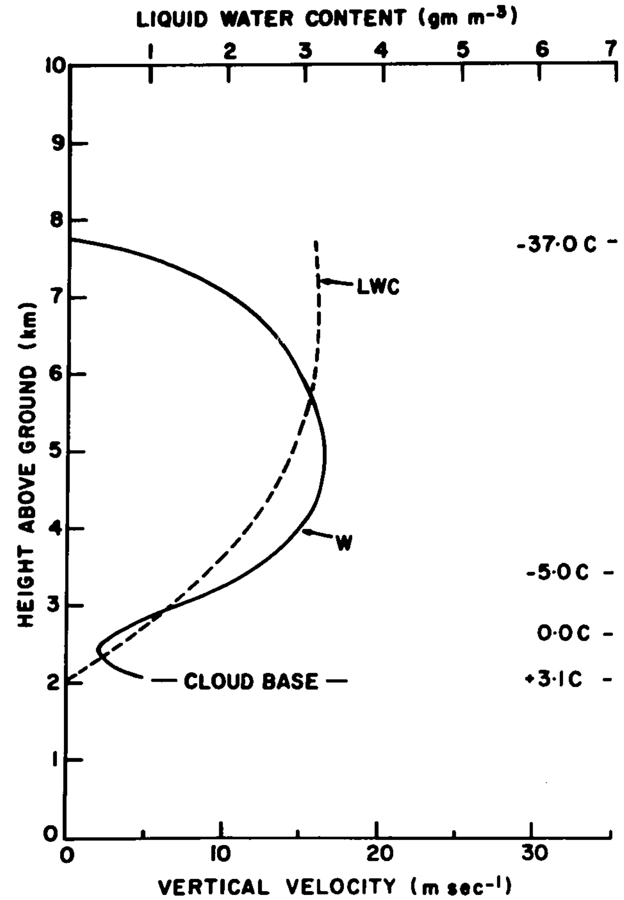

Fig. 7.4.4 A Typical Example of a Low Energy Storm Updraft - 27 June 1967. Vertical velocity and liquid water content values for a specific Low Energy storm are shown as a function of height above ground. Note the relatively warm (-37C) cloud top.

Cloud base temperature	3 → 5 deg C
Storm top temperature	-25 → -35 deg C
Tropopause penetration	Nil
Maximum observed hailstone size	grape - walnut

Table 7.4.2 lists the storm and updraft parameters for 7 hailstorms which are classified in the Low Energy category. A specific example of this type of hailstorm is that of 27 June 1967. Figure 7.4.4 illustrates the vertical velocity and liquid water content profiles for this particular storm (which will be examined in more detail in Chapter IX).

Medium Energy storms are the most common summer hailstorms, occur-

Table 7.4.2 Updraft Parameters of Low Energy Hailstorms

Storm Date	Model Top km	Maximum Vertical Velocity m sec^{-1}	Maximum Liquid Water gm m^{-3}	Cloud Base Height km	Cloud Base Temp. deg C	Storm Top Temp. deg C	Tropopause (or Inv.) Height km	Height of Storm Top Above Trop. km	Maximum Energy J gm^{-1}	Maximum Observed Hail Size	Total Hail Reports
27 June 67	7.08	16.44	3.19	2.05	3.1	-31.5	8.65	-1.57	0.1227	walnut	61
06 July 67	5.70	15.33	3.19	1.80	3.0	-24.0	10.40	-4.70	0.1049	grape	58
08 July 67	5.20	14.17	4.53	0.62	9.4	-18.5	10.10	-4.90	0.0879	grape	21
09 July 67	6.47	20.34	3.42	1.11	4.0	-34.3	8.85	-2.38	0.1943	walnut	111
17 June 68	6.60	17.36	2.72	1.94	0.1	-33.8	6.85 I	-0.25	0.1383	pea	21
20 June 68	7.10	17.64	3.33	0.95	3.4	-42.8	6.25 I	0.85	0.1431	golfball	128
25 July 68	10.05	19.09	4.01	1.53	7.3	-55.5	10.35	-0.30	0.1642	walnut	116

I = Inv = Inversion

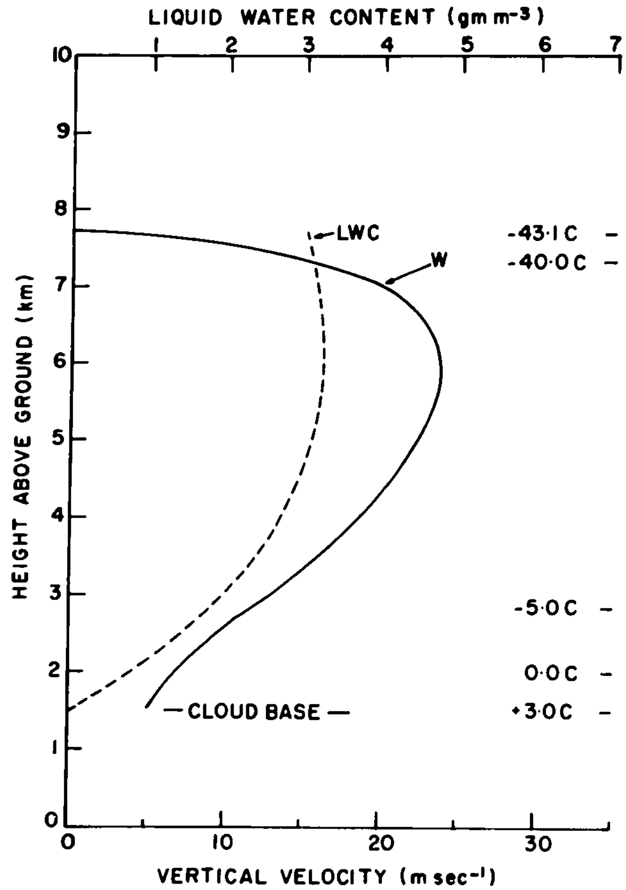

Fig. 7.4.5 A Typical Example of a Medium Energy Storm Updraft - 29 June 1967. Vertical velocity and liquid water content values for a specific Medium Energy storm are shown as a function of height above ground.

ring generally during July and early August. These important storms are usually characterized by the following parameters:

Parameter	Range
Maximum storm energy	0.20 - 0.45 J gm^{-1}
Maximum storm top	9 - 11 km (AGL)
Maximum vertical velocity	22 - 26 m sec^{-1}
Maximum liquid water content	3.2 - 3.8 gm m^{-1}
Cloud base temperature	3 → 8 deg C
Storm top temperature	-50 → -60 deg C
Tropopause penetration	0.25 → 0.75 km
Maximum observed hailstone size	walnut - golfball

Table 7.4.3 lists the specific storm and updraft parameter for 12

Table 7.4.3 Updraft Parameters of Medium Energy Hailstorms

Storm Date	Model Top km	Maximum Vertical Velocity m sec^{-1}	Maximum Liquid Water gm m^{-3}	Cloud Base Height km	Cloud Base Temp. deg C	Storm Top Temp. deg C	Tropopause (or Inv.) Height km	Height of Storm Top Above Trop. km	Maximum Energy J gm^{-1}	Maximum Observed Hail Size	Total Hail Reports
29 June 67	7.53	23.09	3.22	1.49	3.0	-41.7	7.15 I	0.38	0.2665	golfball	265
19 July 67	8.33	23.98	3.44	1.18	6.8	-49.0	10.35	-2.02	0.2750	grape	40
29 July 67	11.15	28.94	3.87	1.83	6.8	-64.3	10.25	0.90	0.4062	golfball	27
31 July 67	8.35	24.92	3.15	1.72	2.7	-48.2	8.70	-0.35	0.2979	walnut	27
27 June 68	9.45	27.38	3.15	1.60	2.7	-58.9	8.70	0.75	0.3624	grape	157
05 July 68	11.55	28.98	3.04	2.79	2.5	-66.2	11.00	0.55	0.4075	grape	51
09 July 68	11.10	22.12	2.87	3.15	1.6	-59.5	11.20	0.10	0.2320	golfball	159
10 July 68	10.04	21.25	4.09	1.90	8.0	-54.8	11.50	-1.46	0.3729	walnut	80
15 July 68	8.94	21.76	2.58	2.19	-0.7	-54.0	8.30	0.64	0.2244	walnut	118
17 July 68	10.05	26.50	2.98	1.93	1.7	-63.3	9.70	0.35	0.3386	walnut	30
05 Aug 68	9.91	24.74	4.90	0.76	11.2	-54.5	9.70	0.21	0.2935	golfball	20
11 Aug 68	10.00	21.14	3.70	1.49	5.7	-59.5	9.85	0.15	0.2109	larger	116

I = Inv. = Inversion

Table 7.4.4 Updraft Parameters of High Energy Hailstorms

Storm Date	Model Top km	Maximum Vertical Velocity m sec^{-1}	Maximum Liquid Water gm m^{-3}	Cloud Base Height km	Cloud Base Temp. deg C	Storm Top Temp. deg C	Tropopause (or Inv.) Height km	Height of Storm Top Above Trop. km	Maximum Energy J gm^{-1}	Maximum Observed Hail Size	Total Hail Reports
14 July 67	12.30	45.82	4.63	1.38	10.3	-72.3	10.85	1.45	1.0371	larger	55
18 July 67	11.17	34.82	3.45	2.14	4.6	-65.7	10.30	0.87	0.5935	larger	153
27 July 67	12.81	43.36	4.51	1.69	10.0	-74.0	11.15	1.66	0.9276	walnut	118
28 July 67	11.55	31.21	3.74	2.19	6.3	-65.0	11.30	0.25	0.4746	larger	278
30 July 67	11.52	34.23	3.85	1.89	6.7	-67.0	10.85	0.67	0.5734	walnut	28
06 Aug 67	11.40	39.21	5.07	0.77	12.0	-66.6	10.20	1.20	0.7562	larger	382
12 Aug 67	12.20	43.27	5.09	1.22	12.4	-67.9	11.50	0.70	0.9238	walnut	45
21 Aug 67	10.85	35.43	4.36	1.32	9.0	-62.0	9.95	0.90	0.6153	golfball	35
28 July 68	14.40	68.64	5.62	1.32	15.0	-80.4	10.95	3.45	2.3431	larger	108
04 Aug 68	11.55	35.51	5.22	0.71	12.6	-67.5	10.25	1.30	0.6180	golfball	100

I = Inv. = Inversion

medium energy hailstorms. Figure 7.4.5 illustrates the vertical velocity and liquid water content profiles for a specific example - 29 June 1967.

High Energy hailstorms normally occur between mid-July and mid-August. They require a very moist warm airmass near the surface as a source of energy. These storms are characterized by the following range of parameters:

Parameter	Range
Maximum storm energy	0.45 → J gm^{-1}
Maximum storm top	11 - 13 km
Maximum vertical velocity	35 - 45 m sec^{-1}
Maximum liquid water content	4.0 - 5.0 gm m^{-3}
Cloud base temperature	7 → 12 deg C
Storm top temperature	-65 → -72 deg C
Tropopause penetration	0.50 → 1.25 km
Maximum observed hailstone size	golfball - larger than golfball

Table 7.4.4 lists the specific storm and updraft parameters for 10 High Energy hailstorms. A specific example is illustrated in Fig. 7.4.6. - 28 July 1967.

In summary, a loaded moist adiabatic vertical velocity model has been presented and tested against radar observations of 29 hailstorms in Alberta. The agreement between maximum radar-observed storm tops and computed storm tops leads to considerable confidence in the computed values of the temperature, liquid water content and vertical velocity. A distinct relationship also appears between the maximum radar-observed storm top and the computed maximum vertical velocity. Classified on the basis of energy, the 29 hailstorms assigned to these three groups show similar characteristics. The computed updraft core parameters for specific storms will be utilized

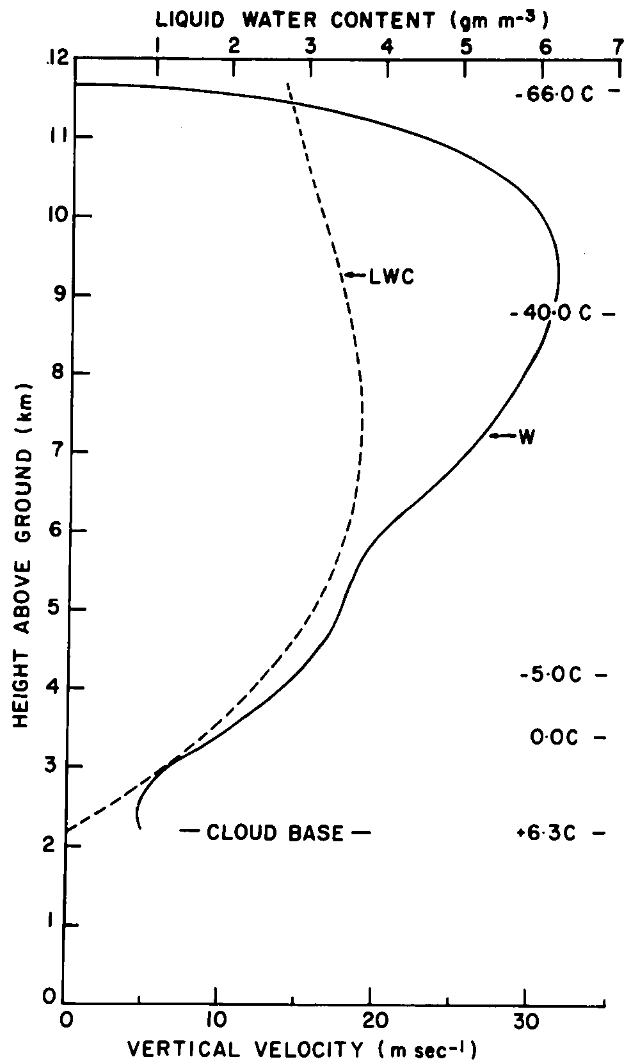

Fig. 7.4.6 A Typical Example of a High Energy Storm - 28 July 1967. Vertical velocity and liquid water content values for a specific High Energy storm are shown as a function of height above ground. Note the relatively cold (-66C) cloud top.

in Chapter IX to calculate the growth of graupel particles in the updraft core.

CHAPTER VIII

THE PRECIPITATION GROWTH ENVIRONMENT IN THE CORE OF A SEVERE STORM UPDRAFT

8.1 Introduction

In the previous Chapter, a simple loaded moist adiabatic (LMA) updraft model was devised and used to compute estimates of the temperature, vertical velocity and liquid water content along the axial core of a steady state updraft. These estimates will be utilized in this Chapter to describe a precipitation growth environment, which in turn, will be used in Chapter IX with a graupel growth model to compute the growth of initial graupel embryos as small as 100 μ diameter.

The liquid water content estimate which results from the LMA model is a bulk property; it does not specify how the water is distributed with respect to droplet size or number. This section deals with that problem, that is determining how the liquid water is distributed with respect to droplet size and number and how this distribution changes with height inside the updraft core.

8.2 Cloud Condensation Nuclei (CCN) and Cloud Droplet Concentrations at Cloud Base

In the previous Chapters, it has been established that hailstorms in Alberta are characterized by a broad, persistent updraft which originates in the sub-cloud layer. Let us consider a parcel of air with positive vertical velocity ($W \approx 5$ m sec^{-1}) in the updraft region beneath the cloud base of a hailstorm. As this parcel reaches cloud base and commences to cool below the dewpoint, cloud condensation nuclei (CCN) are activated. Each nucleus begins to grow when the supersaturation reaches a critical value typical of that particular nucleus. For a given nucleus this value will depend upon the size and composition of the nucleus. As the air parcel rises further inside the cloud, the supersaturation increases, causing more nuclei to be activated; those already activated continue to grow, removing water vapor at a steadily increasing rate. The removal of water vapor, by condensation onto activated nuclei, retards the increase of supersaturation until the two effects balance. This balance point determines the value of the maximum supersaturation (S_{max}). Proceeding further, the existing droplets continue to grow but the supersaturation decreases and no further nuclei are activated. Calculations performed by Fletcher (1962) illustrate that the maximum supersaturation is reached in 2 - 8 seconds (within 10 - 80 m of cloud base) in conditions representative of hailstorms. The maximum supersaturation attained is generally less than 1.5%.

It is clear that the number of cloud droplets formed is given by the number of nuclei activated at the time of maximum supersaturation. The maximum supersaturation (S_{max}) will depend upon:

(i) the properties of the moist air (T, p, e_s)
(ii) the rate of cooling (determined by the updraft velocity)
(iii) the cloud condensation nuclei (CCN) spectrum[1]

A formula for the total number of nuclei activated at maximum supersaturation has been derived by Twomey (1959) and is as follows:

[1] A cloud condensation nuclei spectrum consists of the total number of cloud condensation nuclei (CCN) activated at a given supersaturation plotted as a function of the supersaturation value.

$$N = cS_{max}^{k} = c^{\frac{2}{k+2}} \left[\frac{68.7 \times 10^{-3}\ U^{3/2}}{kB(3/2,\ k/2)} \right]^{\frac{k}{k+2}} \qquad \text{(Eqn. 8.2.1)}$$

Where

N = number concentration of cloud droplets (cm^{-3})

c = intercept value of the CCN spectrum (at S = 1.0%)

S = supersaturation with respect to a plane water surface (%)

k = slope of the CCN spectrum

U = cloud base updraft (cm sec^{-1})

B = Beta function

The validity of this equation has been established by several investigators. A recent paper by Warner (1969b) verifies particularly well the relation between the CCN spectrum, vertical velocity and cloud droplet concentration.

From the CCN spectrum it is thus possible to determine the number concentration of cloud droplets activated at cloud base. It is not possible to determine, however, how these cloud droplets are distributed with respect to size from the CCN spectrum. Observed cloud droplet spectra at cloud base and upward through the core of the updraft would be highly desirable for this purpose. Such data are not available for Alberta hailstorms at this time. However, CCN spectra were measured on 8 occasions during the summer of 1968. These data are tabulated (with permission from A.H. Auer) in Table 8.2.1.

From these data an average Alberta CCN spectrum has been constructed and is shown in Fig. 8.2.1. Utilizing Eqn. 8.2.1, it is thus possible to determine the number of cloud droplets formed at cloud base for a range of updrafts. The resulting cloud droplet concentrations, as a function of cloud

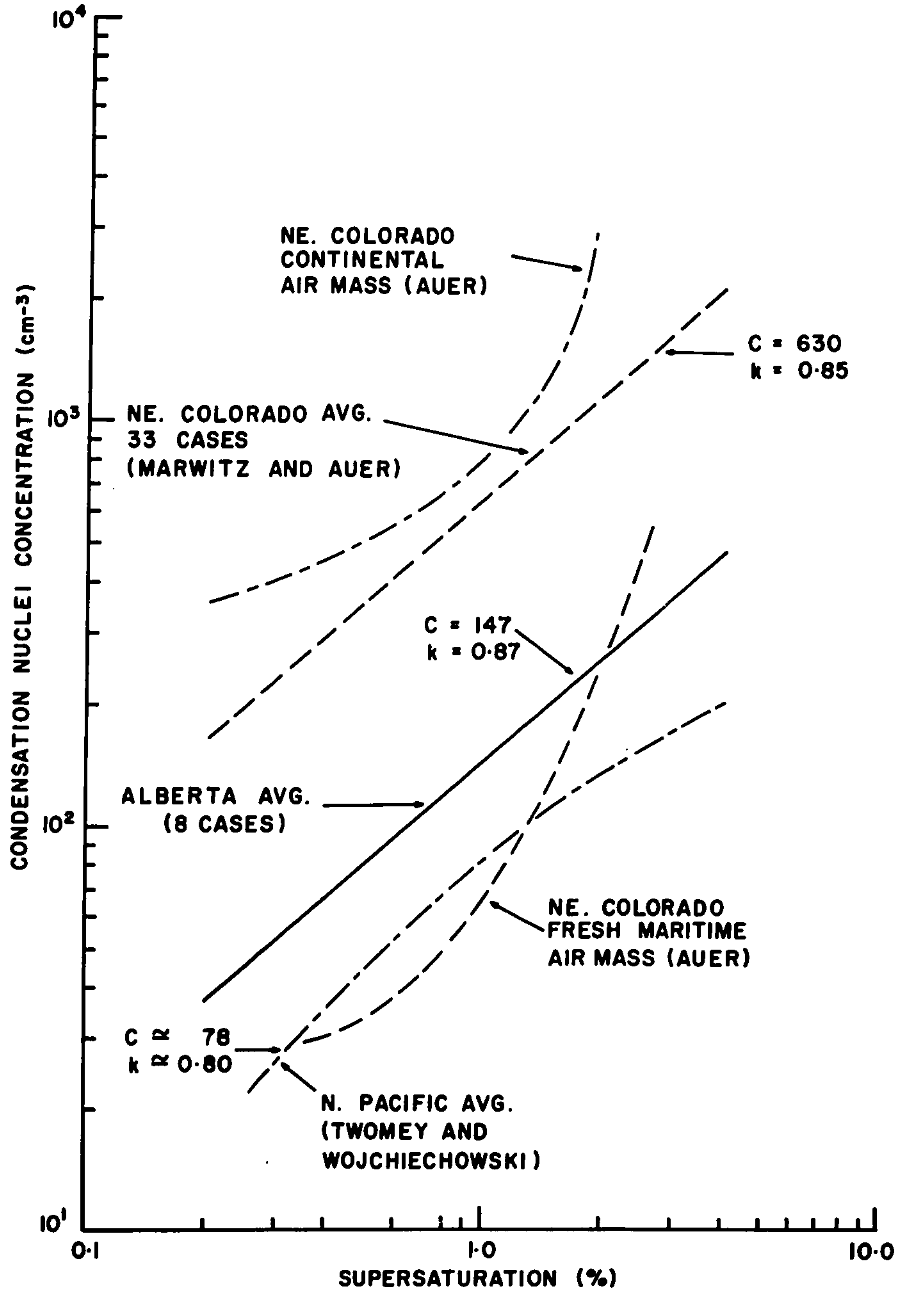

Fig. 8.2.1 Average Cloud Condensation Nuclei (CCN) Spectra for Alberta, Northeastern Colorado and the North Pacific. Average CCN spectra are shown for the North Pacific (maritime regime), Northeastern Colorado (continental regime) and Alberta. Also shown are individual CCN spectra for continental and maritime airmass regimes in Northeastern Colorado. Note the similarities in the CCN spectra for the North Pacific, Alberta and the fresh maritime airmass in Northeastern Colorado. Also note the substantially higher CCN concentrations exhibited by the average Northeastern Colorado spectrum and the Northeastern Colorado continental airmass spectrum.

Table 8.2.1 Cloud Condensation Nuclei (CCN) Spectra Data for Alberta

Date	Time MST	U m sec^{-1}	S_{max} %	c at 1%	k	N cm^{-3}	Cloud Type
17 July 68	1445	2.5	1.10	162	0.85	175	Cu
	1535	5.0	1.36	240	0.78	305	TRW
	1645	5.0	1.30	264	0.96	340	TRWA
24 July 68	1747	2.0	1.09	115	0.98	125	Cu
	1810	1.0	0.80	154	0.44	140	Cu
25 July 68	1848	6.0	1.68	152	1.15	275	TRWA
	1944	6.0	2.31	63	0.92	135	TRWA
29 July 68	1704	2.5	1.95	28	0.85	50	TRW
Average				147	0.87		

Cu = Cumulus cloud TRW = Thunderstorm TRWA = Hailstorm

base vertical velocity, are illustrated in Fig. 8.2.2. It is apparent that the cloud droplet number concentration is not a highly sensitive function of the cloud base updraft. Marwitz and Auer (1968) quote typical cloud base updrafts for hailstorms between 4 and 8 m sec^{-1}. Using the average Alberta CCN spectrum, corresponding cloud droplet concentrations would be 200 cm^{-3} (at 4 m sec^{-1}) and 270 cm^{-3} (at 8 m sec^{-1}). In this study, a representative cloud base updraft of 5 m sec^{-1} has been used which yields a corresponding cloud base concentration of 220 cm^{-3}.

Observations of cloud droplet spectra and cloud condensation nuclei (CCN) spectra have shown marked variations between maritime convective and continental convective clouds. For updrafts of 1 m sec^{-1}, Twomey (1959) quotes activated CCN concentrations of 61 cm^{-3} for maritime convective clouds and 554 cm^{-3} for continental convective clouds in Australia. The Alberta CCN spectra parameters tabulated in Table 8.2.1 were obtained in relatively fresh maritime airmasses. As a consequence, the average Alberta CCN spectrum and the deduced cloud droplet concentrations are probably not representative

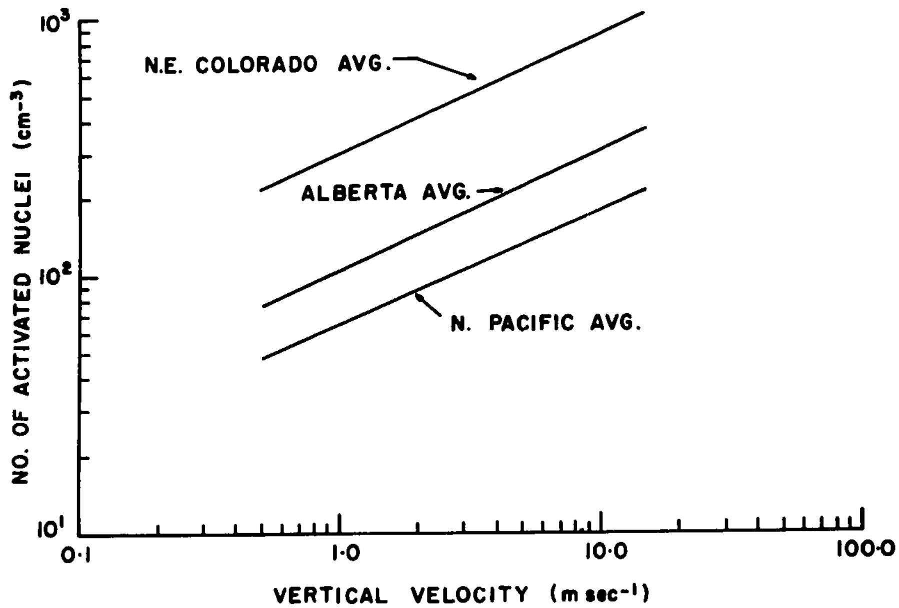

Fig. 8.2.2 Number of Activated CCN vs. Vertical Velocity Based on Average CCN Data. The number of cloud condensation nuclei (CCN) which would be activated just above cloud base (as computed from Eqn. 8.2.1; based on average CCN spectra for the N. Pacific, Alberta and NE Colorado) is shown as a function of the vertical velocity at cloud base. Note the higher concentrations of activated CCN in Alberta and NE Colorado airmasses than in N. Pacific airmasses for a given vertical velocity.

of airmasses of continental origin; they are instead typical of slightly aged maritime airmasses. Auer (1967), in an investigation of continental cumulus clouds, illustrates a CCN spectrum in air following a maritime frontal passage, and also in a stagnant continental airmass in Northeastern Colorado. These spectra are displayed in Fig. 8.2.1 for comparison with the average Alberta CCN spectrum. Auer's fresh maritime airmass spectrum is not unlike the average Alberta spectrum, but the stagnant continental airmass is substantially different. Utilizing CCN spectra data quoted by Marwitz and Auer (1968) for 33 convective cloud situations in Northeastern Colorado, an average CCN spectrum has been computed and is also displayed in Fig. 8.2.1. This average Northeastern Colorado spectrum is quite similar to the individual stagnant continental airmass case quoted by Auer (1967). It is apparent that CCN spectra in Northeastern Colorado are essentially continental in nature, although the influx of fresh maritime airmasses does indeed cause a substantial decrease in the CCN concentrations.

Recent CCN observations reported by Twomey and Wojchiechowski (1969) substantiate the concept of separate continental and maritime regimes. Observations of CCN spectra over the North Atlantic, South Atlantic and Caribbean show remarkably similar median spectra. It is interesting to note that the lowest CCN concentrations were found over the North Pacific. The North Pacific average spectrum is illustrated in Fig. 8.2.1. It is quite similar to the average Alberta CCN spectrum but displaced to slightly lower values, as might be expected for a maritime regime. Continental CCN spectra measured over the continental U.S.A. by Twomey and Wojchiechowski are not substantially different to the average Northeastern Colorado spectrum displayed in Fig. 8.2.1. In addition, observations by Radke and Hobbs (1969) of CCN concentrations in the Olympic Mountains in Washington, made with an automatic CCN counter, show CCN spectra in onshore flow very similar to the North Pacific average reported by Twomey and Wojchiechowski.

Alberta hailstorms frequently form in fresh maritime airmasses, so it is reasonable to anticipate that the CCN spectrum would be similar to, although with higher concentrations than, the average North Pacific CCN spectrum quoted by Twomey and Wojchiechowski. On the other hand, warm continental airmasses arriving in Alberta from the south would likely have CCN spectra similar to the Northeastern Colorado average. These two cases serve as approximate bounding values; for this reason activated CCN number concentrations (as a function of vertical velocity) for the average North Pacific spectrum and the average Northeastern Colorado spectrum have been added to Fig. 8.2.2. The resulting data are thus estimates of the average lower and upper bounds of the cloud droplet concentration at cloud base in Alberta. For example, at cloud base updraft values of 5 m sec^{-1}, the droplet concentration is probably not less than 130 cm^{-3} (North Pacific data) nor more than 600 cm^{-3} (Northeastern Colorado data). In this study the average Alberta droplet concentration (220 cm^{-3}) has been utilized except for storms in continental airmasses where a concentration of 600 cm^{-3} has been used.

For a given liquid water content, the cloud droplet concentration determines the cloud droplet diameters. Since D (diameter) is proportional to $N^{1/3}$ a decrease in N (number concentration) from 220 to 130 cm^{-3} would yield a corresponding increase in D by a factor of 1.19. Similarly, an increase in N from 220 to 600 cm^{-3} would result in a decrease in D by a factor of 0.72. Cloud droplet diameters are a determining factor in the microphysical stability of clouds and the density of ice which accretes onto hailstones. These effects will become evident in Chapter IX.

Having established an estimate and approximate bounds for the number concentration of cloud droplets at cloud base, it is necessary to consider how these cloud droplets are distributed with respect to diameter. Cloud droplet spectra at cloud base are not available for Alberta convective clouds. Auer (1967), however, has reported on cloud droplet observations taken approximately 250 m above cloud base in cumulus clouds in Northeastern Colorado. A summary of the important average cloud droplet parameters is given in Table 8.2.2. Figure 8.2.3 illustrates the cloud droplet distribution with respect to size revealing a relatively narrow droplet distribution centered around the average droplet diameter of 8 μ. The distribution of liquid water among the droplet population is also narrow as shown in Fig. 8.2.4. A total of 79.3% of the liquid water is contained in droplets between 6.75 and 11.0 μ diameter. The average cloud droplet concentrations quoted by Auer are higher than would be anticipated for Alberta hailstorms. At concentrations of 220

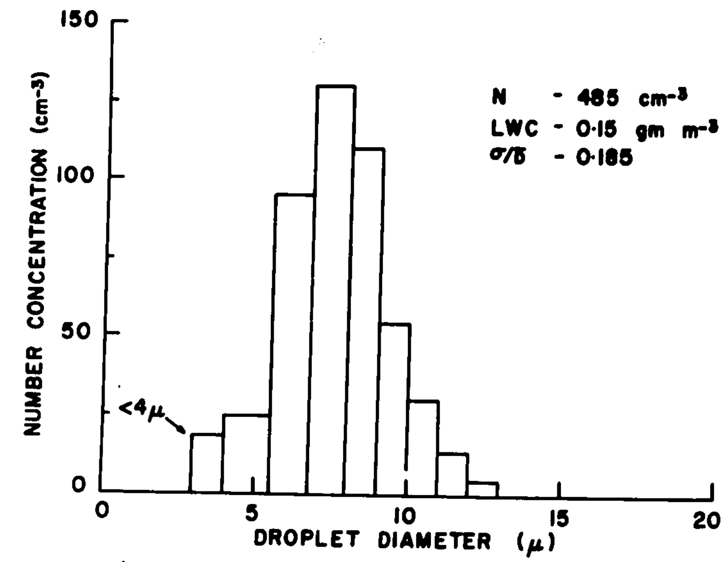

Fig. 8.2.3 Average Cumulus Cloud Droplet Spectrum for NE. Colorado (after Auer). Average cloud droplet concentrations as a function of diameter are shown for measurements taken approximately 250 m inside the cloud base of NE. Colorado cumulus clouds. Note the narrow spectrum.

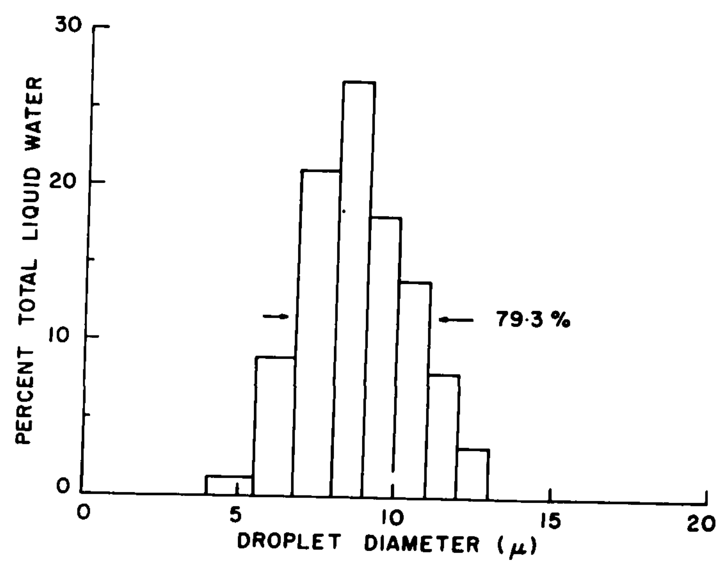

Fig. 8.2.4 Liquid Water Content vs. Droplet Diameter for NE. Colorado Cumulus Cloud Droplet Spectrum. The liquid water content distribution for the average NE. Colorado cumulus cloud droplet spectrum in Fig. 8.2.3 is illustrated. Note that 79.3% of the liquid water is concentrated in droplets between 6.75 and 11.0 μ diameter.

Table 8.2.2 Average Cloud Droplet Parameters for Northeastern Colorado Cumulus Clouds (after Auer)

Parameter	Average	Range
Updraft	2.0 m sec^{-1}	0.5 - 3.0
Cloud Depth	2.0 km	
Droplet Concentrations	485 cm^{-3}	175 - 800
Droplet Diameter	8.0 μ	6.3 - 10.4
Coefficient of Dispersion ($\sigma/\overline{D}$)	0.185	0.103 - 0.286
Liquid Water Content	0.15 gm m^{-3}	0.05 - 0.22

cm^{-3}, the average diameter would instead be shifted to 10.9 μ, but the major features of the spectrum would not likely be changed.

8.3 Cloud Droplet Growth by Condensation and Coalescence

Having examined the cloud droplet formation process at cloud base and the resulting spectrum, it is essential to consider the two growth processes which affect the cloud droplet population in the updraft region. These are:

(i) Growth by condensation of water vapor onto existing cloud droplets
(ii) Growth of cloud droplets by coalescence

Since growth by condensation (in a rising air parcel) must occur independent of whether coalescence does or does not occur, it will be considered first. Neglecting curvature and solute effects (small for droplets greater than 5 μ diameter), the condensation growth equation may be written:

$$\frac{dr}{dt} \propto \frac{S}{r} \qquad \text{(Eqn. 8.3.1)}$$

Where
r = droplet radius
S = supersaturation

t = time

It is evident that radial growth proceeds more rapidly for small droplets than for large droplets. In an updraft of the order of 5 m sec^{-1} just within cloud base, the growth of cloud droplets is very rapid. Within 10 sec of reaching cloud base, the average cloud droplet diameter is greater than 5 μ, and the supersaturation within the cloud is typically 0.2 - 0.4%. Supersaturations of this order would result in the evaporation of droplets smaller than 0.8 μ diameter, but the 5 μ droplets would not evaporate unless the supersaturation became less than 0.05%. In an accelerating updraft, it is thus clear that only very small droplets (comprising only a few percent of the total) could evaporate after maximum supersaturation is reached. Thus, neglecting coalescence, the total number of cloud droplets is effectively determined at cloud base.

After the initial formation of a cloud droplet population near cloud base, one would anticipate (on the basis of the selective radial growth) that a narrow droplet distribution would form rapidly and be maintained during droplet growth. East (1956) subjected a cumulus cloud droplet distribution to growth by condensation alone. His results are shown in Fig. 8.3.1 proceeding from liquid water contents of 1 gm kg^{-1} to 2, 4 and 10 gm kg^{-1}. For conditions typical of Alberta hailstorm cloud bases (790 mb, 5C), these liquid water contents would be equal to 1, 2, 4 and 10 gm m^{-3}. However, at a height comparable to maximum adiabatic liquid water content (350 mb, -30C), the liquid water contents would be equivalent to 0.5, 1, 2 and 5 gm m^{-3}. From Fig. 8.3.1, showing East's results, it is evident that cloud droplet growth by condensation alone does indeed maintain a very narrow droplet distribution.

The cloud droplet spectrum utilized by East was a relatively broad spectrum considered (at that time) to be representative of a cumulus cloud.

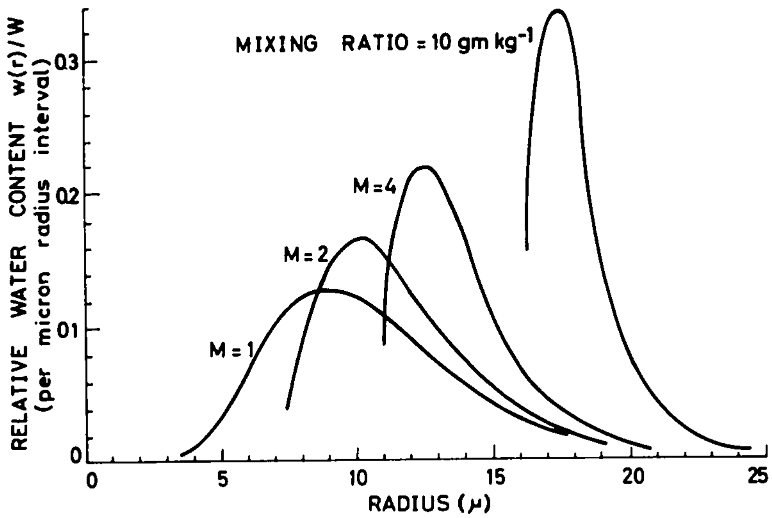

Fig. 8.3.1 The Modification of a Cumulus Cloud Water Content Distribution by Condensation. The liquid water content in a given class interval is given by w(r), and the total liquid water content for the droplet distribution is given by W. Curve M = 1 is for fair-weather cumulus cloud: the other curves show the distribution after water is condensed onto it rapidly. All are normalized to have equal area: the peak water content $w(r)_{max}$ actually increased 26 times from M = 1 to 10 gm kg^{-1}.

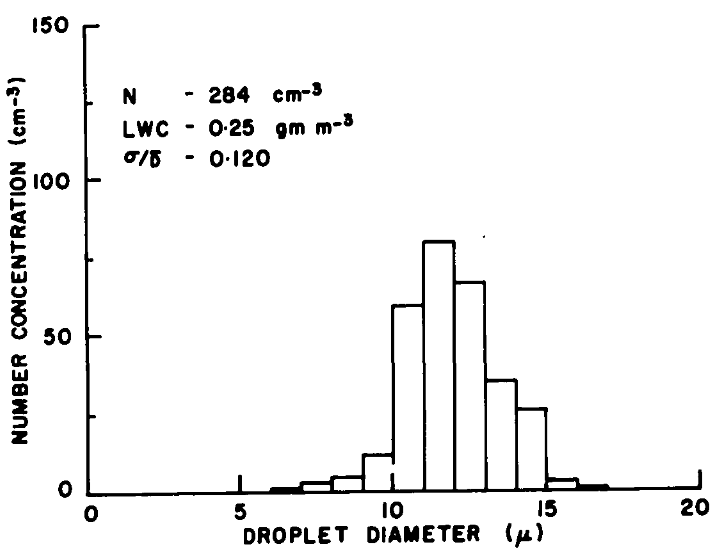

Fig. 8.3.2 Alberta Hailstorm Cloud Droplet Spectrum - 23 June 1967. A cloud droplet spectrum obtained in a developing cumulonimbus cloud (3.7 km AGL) using an MRI Continous Particle Collector is shown. Note the concentration of droplets between 10 and 13 μ diameter.

More recent observations, however, indicate that cloud droplet spectra at cloud base are quite narrow. A measure of the width of the spectrum which is commonly used is the coefficient of dispersion ($\sigma/\overline{D}$). Auer (1967) quotes an average $\sigma/\overline{D}$ value for Northeastern Colorado cumulus clouds of 0.185 and a range of 0.103 - 0.286. Recent work published by Warner (1969a) indicates an average value of $\sigma/\overline{D}$ of 0.21 for cumulus clouds in Australia. Similar values of $\sigma/\overline{D}$ have been reported by MacCready and Takeuchi (1968) for cumuliform clouds in Arizona.

The $\sigma/\overline{D}$ value of East's initial 1 gm kg^{-1} cloud droplet spectrum was 0.346, considerably higher than the recently observed values quoted. As East's initial distribution cannot be considered representative of conditions at the base of a hailstorm, an Alberta hailstorm cloud droplet spectrum (see Fig. 8.3.2) has been subjected to growth by condensation alone using the technique outlined by East. Beginning with an initial $\sigma/\overline{D}$ value of 0.120 at a liquid water content of 0.325 gm kg^{-1} (0.249 gm m^{-3}), the $\sigma/\overline{D}$ value dropped rapidly to become 0.026 with a liquid water content of 4.00 gm kg^{-1} (see Fig. 8.3.3). Similar calculations reported by Warner (1969b) show a comparable decrease in $\sigma/\overline{D}$ from 0.20 to 0.03 due to growth by condensation within a cumulus cloud. It is thus clear that the condensation growth process does indeed produce and maintain a very narrow cloud droplet spectrum. This narrow spectrum is of particular consequence when considering the growth of cloud droplets by coalescence processes.

The growth of cloud droplets by coalescence is by its very nature a time-dependent process. Figures 8.3.4 and 8.3.5 illustrate vertical velocity profiles which have been computed with the LMA updraft model for storms on 29 June 1967 (Medium Energy storm) and 28 July 1967 (High Energy storm). The transit times for an air parcel starting at cloud base indicate that the parcel traverses the updraft core in 450 - 550 sec and reaches the -40C level

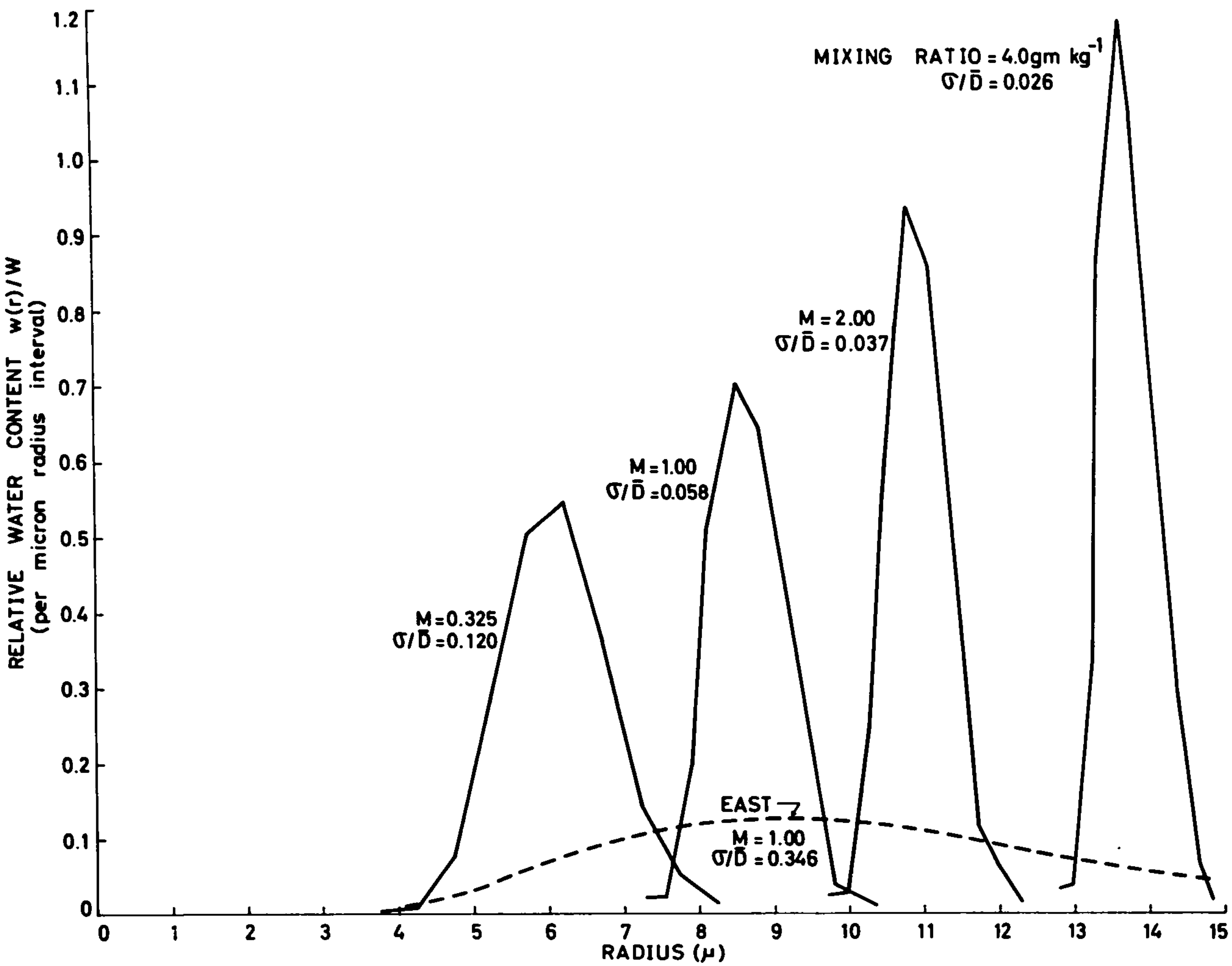

Fig. 8.3.3 The Modification of an Alberta Hailstorm Cloud Water Content Distribution by Condensation. Using East's computational technique, the cloud droplet distribution shown in Fig. 8.3.2 was subjected to growth by condensation. The water content in a given droplet class interval is given by w(r), and the total water content by W. All curves are normalized to have equal area. Note how the water content distribution becomes increasingly narrow as the total water content is increased. East's M = 1 curve (see Fig. 8.3.1) is shown for comparison; note the difference in the width of the two water content distributions.

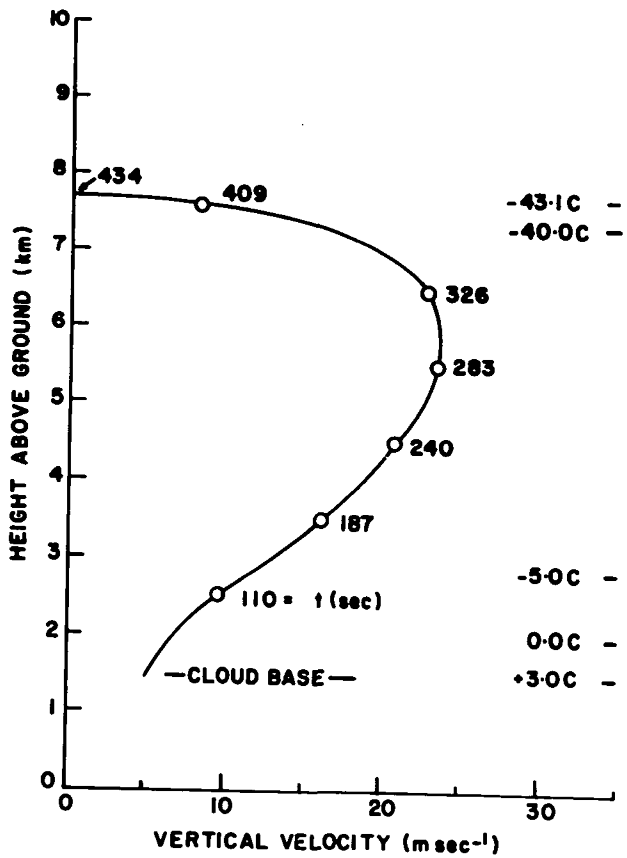

Fig. 8.3.4 Transit Times for an Air Parcel in the Up-Draft Core of a Medium Energy Storm - 29 June 1967. Transit times from cloud base to -40C are given in seconds. Note that the air parcel completes the traverse to -40C in less than 400 sec.

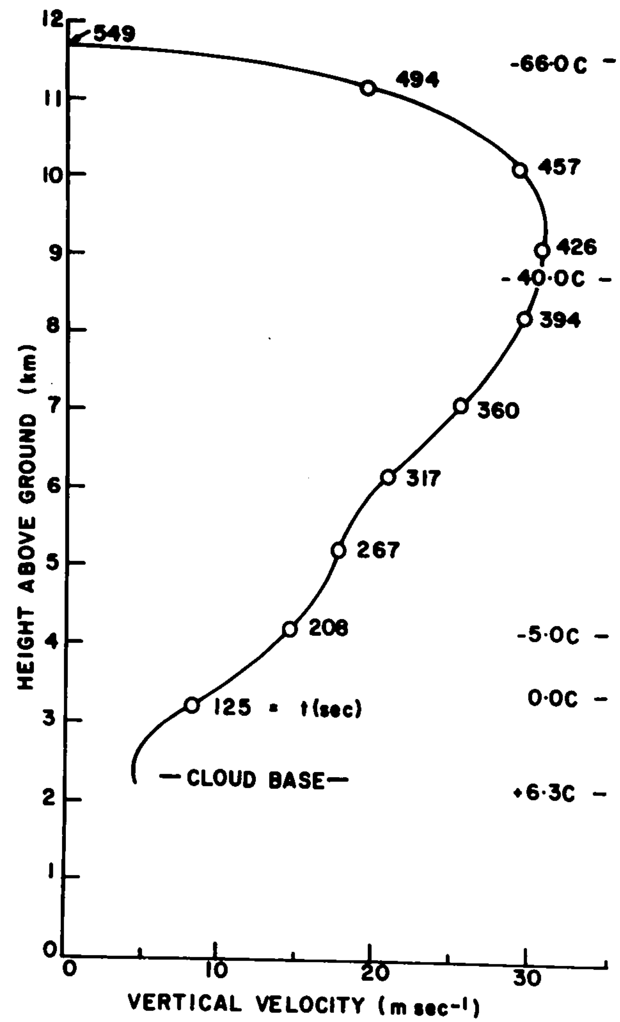

Fig. 8.3.5 Transit Times for an Air Parcel in the Up-Draft Core of a High Energy Storm - 28 July 1967. Transit times from cloud base to -40C are given in seconds. Note that the air parcel completes the traverse to -40C in less than 420 sec.

in ≈ 400 sec. If a population of cloud droplets is to grow to radar-detectable size by coalescence within the updraft core, then it must do so in less than 600 sec.

Recent work by Berry (1967) shows that the growth of cloud droplets by coalescence is not rapid. Figure 8.3.6 depicts the growth of a droplet population having an initial liquid water content of 1 gm m^{-3} and a droplet concentration of 240 cm^{-3}. A stochastic growth equation was used to compute the growth by coalescence and the liquid water content was held constant with time. The first appearance of a 200 μ diameter droplet occurred in 1600 sec; much longer than the transit time of an air parcel in the updraft core of a severe storm. It must be noted that Berry utilized the Shafrir-Neiburger collection efficiencies and the Hocking 36 μ diameter (18 μ radius) cutoff limit in his computations. The more recent Davis-Sartor collection efficiencies indicate that the Hocking limit does not exist and droplets smaller than 18 μ radius can coalesce, although their collection efficiencies are small. In addition, the situation in an updraft is such that the liquid water content increases from 0.0 to approximately 3.5 gm m^{-3}, so that initially coalescence growth would be less rapid than Berry's computations indicate. However, toward the latter portion of its traverse, the situation would reverse with coalescence proceeding more rapidly than Fig. 8.3.6 indicates. The final outcome is difficult to assess since the processes at work are nonlinear. A factor of considerable importance is the breadth of the initial droplet spectrum, narrow droplet spectra yielding droplets with very similar fallspeeds and therefore few collisions. The $\sigma/\overline{D}$ value for Berry's initial droplet spectrum was 0.364, considerably greater than is believed to exist within Alberta hailstorm updraft cores. A narrower initial spectrum would undoubtedly reduce the efficiency of the coalescence process. As a consequence, it is difficult to envisage the coalescence growth process providing

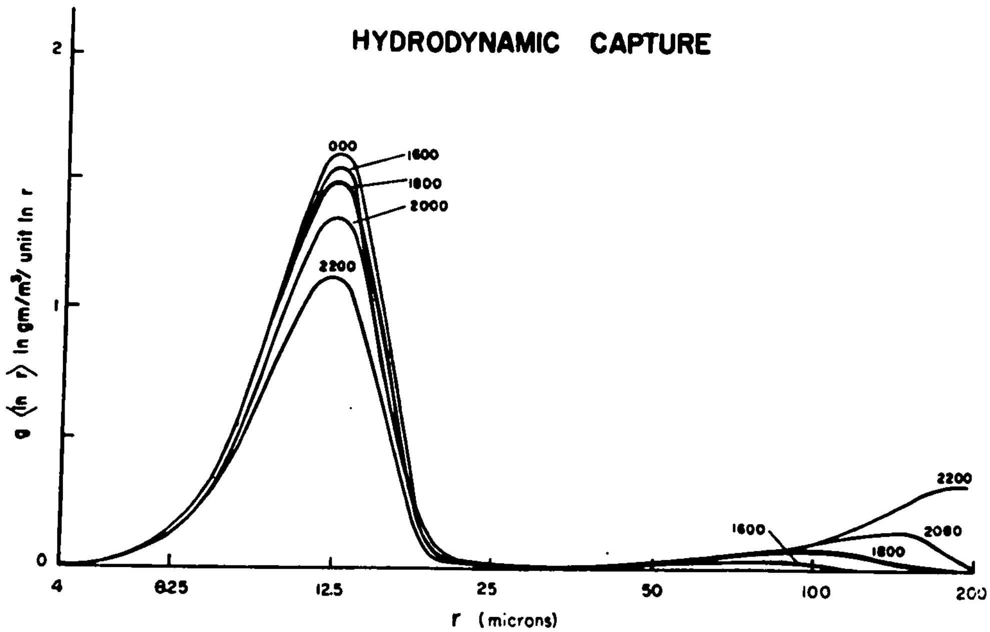

Fig. 8.3.6 Computed Droplet Growth for Hydrodynamic Capture (after Berry). The droplet mass density function, designated g<ℓnr>, is plotted as a function of ℓnr. The area under the curve between any two values of the radius will be equal to the liquid water mass (gm m^{-3}) contained by droplets having radii between these same two values. Coalescence growth times in seconds are indicated. Note the small change in the first 1600 sec.

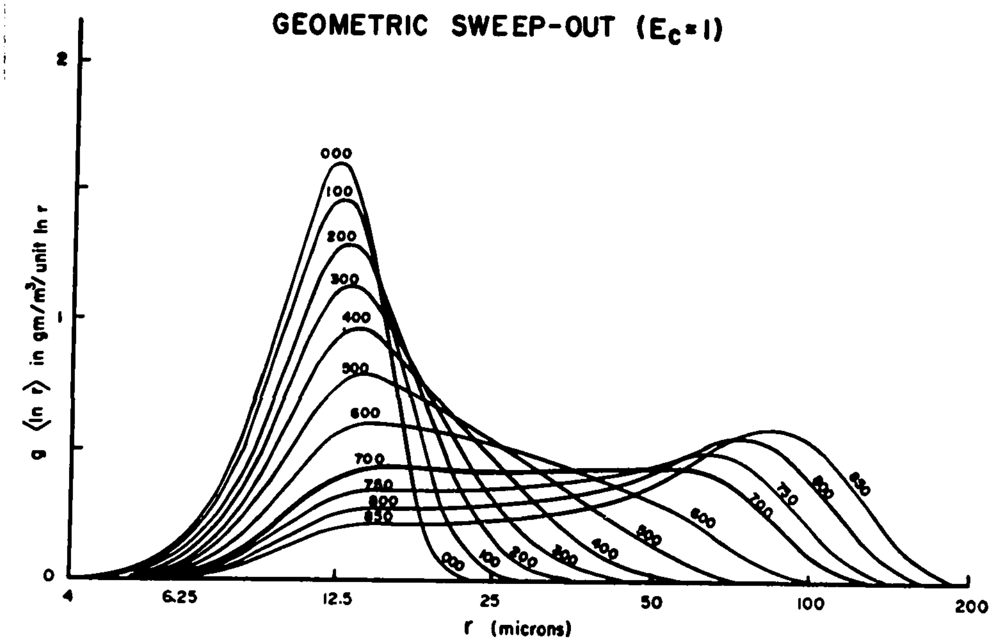

Fig. 8.3.7 Computed Droplet Growth Due to Geometric Sweep-Out (after Berry). A collection efficiency of 1.0 has been used instead of the Shafrir-Neiburger collection efficiencies used for Fig. 8.3.6. Note the shift of the water mass after 400-500 sec to include droplets with r>50 μ.

any number of large droplets in 400 sec.

An extreme example is the geometric sweepout case (collection efficiency = 1.0) computed by Berry and displayed in Fig. 8.3.7. In 400 - 500 sec a small portion of the liquid water content is found in 100 μ diameter droplets. However, the coalescence process does not gain control until 700 - 800 sec have passed.

Recent laboratory experiments by Phillips and Allee (1968) with an 18.3 m spherical cloud chamber indicate that the coalescence growth process does not significantly modify the droplet population in the first 450 - 600 sec. The cloud chamber was subjected to an initial expansion resulting in the formation of a cloud droplet population with a given liquid water content. This droplet population was sampled at 150 sec intervals, the results being shown for a liquid water content of 3.18 gm m^{-3} in Fig. 8.3.8. The results indicate that the initial narrow distribution ($\sigma/\overline{D}$ = 0.10) was preserved for at least 450 sec. Thereafter, the distribution was modified rapidly by coalescence processes. Since the liquid water content remained constant with time, the coalescence within the cloud chamber would proceed much more rapidly than in severe storm updrafts where the liquid water content increases from 0.0 to $\approx$ 3.5 gm m^{-3} in 400 sec. Similar experiments for a liquid water content of 2.28 gm m^{-3} showed little change until 750 sec had passed. <u>In conclusion, it is clear from both computational evidence and experimental evidence that the coalescence growth process does not significantly modify the cloud droplet population in the first 600 sec</u>.

8.4 A Simple Cloud Droplet Model

In the two previous sections an examination has been made of the cloud droplet formation process, the initial droplet spectrum and the two

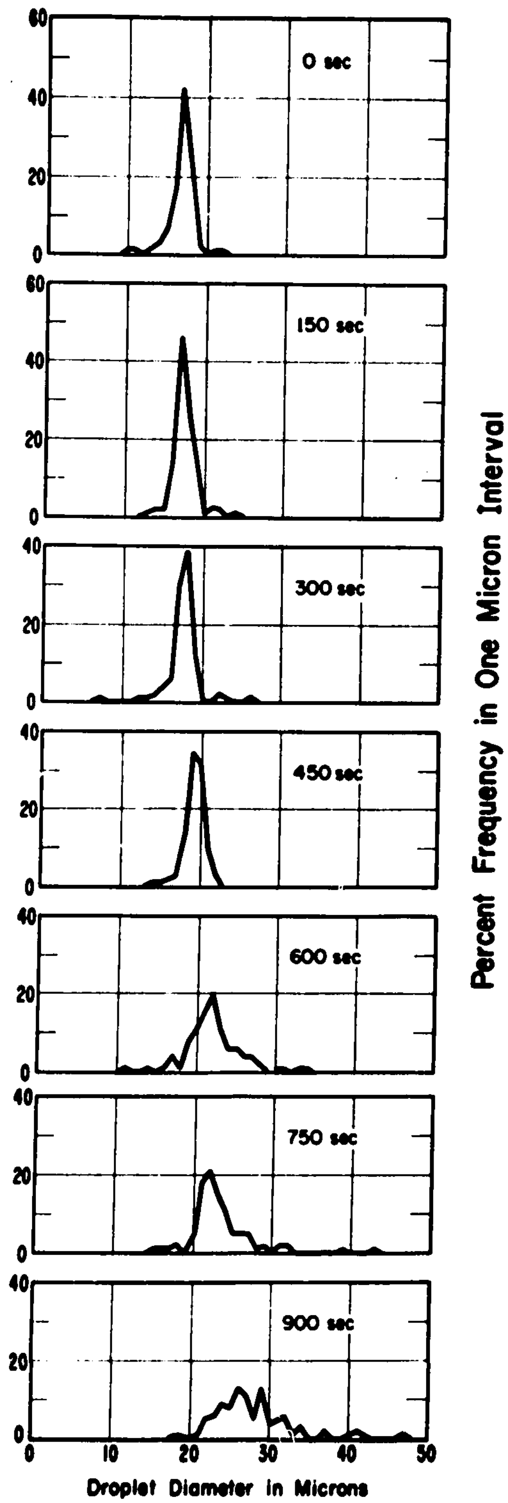

Fig. 8.3.8 Experimentally Determined Cloud Droplet Growth by Coalescence (after Phillips and Allee). Sequential cloud droplet spectra obtained experimentally in an 18.3 m spherical cloud chamber are plotted as percent frequency per micron interval vs. droplet diameter. Initial N = 1145 droplets cm^{-3}, LWC = 3.19 gm m^{-3}. Note the small change in the droplet spectrum during the first 450 sec.

growth processes which occur in the core of a severe storm updraft. Several important conclusions can be made from these investigations:

(i) The cloud droplet number concentration is effectively determined at at cloud base

(ii) The condensation growth process forms and maintains a narrow cloud droplet distribution

(iii) The coalescence growth process does not significantly affect the cloud droplet distribution in the first 450 - 600 sec.

The last item is of prime importance since an air parcel traverses the entire depth of a severe storm updraft core in less than 600 sec. To a reasonable degree of approximation, therefore, the coalescence growth process may be neglected in the core region of a severe storm updraft. This is an important simplifying assumption; it means that the cloud droplet number concentration (per unit volume) is modified only by expansion as no new droplets are formed and none destroyed. In addition, growth by condensation is the dominant process resulting in a very narrow cloud droplet spectrum. As the $\sigma/\overline{D}$ values are typically less than 0.20, the cloud droplet distribution may be approximated by a monodisperse distribution. Thus by using estimates of the cloud number concentrations for expansion of an air parcel, the droplet concentration may be determined at any height in the updraft. Utilizing this number concentration as well as the computed adiabatic liquid water content and the monodisperse approximation a droplet diameter may be computed.

Observations made in the unmixed core region of cumulonimbus clouds at Flagstaff, Arizona, by MacCready and Takeuchi (1968) indicate that cloud droplet number concentrations do decrease with height at approximately the rate predicted by expansion. Concurrently, with an increasing liquid water content the average droplet diameter also increases with height.

Using this simple cloud droplet model to describe how the liquid water content is distributed within the updraft region, the information required for a precipitation growth environment is complete. It must be recognized that the growth environment outlined here is an estimate, based on many simplifying assumptions. Observations of radar storm tops indicate that the LMA model yields a reasonable estimate of the severe storm updraft. Inclusion of entrainment and freezing would probably not change the liquid water content, temperature excess or maximum storm height by more than 10% or the vertical velocity by more than 20%. The estimated droplet concentrations are not likely to be in error by more than a factor of 1.5 which would result in a droplet diameter correction factor of not more than 1.14. In summary, the estimates of the precipitation growth environment for the core of a severe storm updraft, deduced in this chapter, are considered to be reasonable first approximations to the precipitation growth environment.

CHAPTER IX

THE GROWTH OF PRECIPITATION IN THE CORE OF A SEVERE STORM UPDRAFT

9.1 Introduction

The results of the two previous chapters provide a description of the precipitation growth environment in the core of a severe storm updraft. It is the purpose of this chapter to examine the possible precipitation growth modes, with particular emphasis on whether or not the resulting particles could be detected by radar. The following possibilities will be considered:

(i) The growth of a raindrop,

(ii) The growth of a graupel or small hail particle which has re-entered the updraft,

(iii) The growth of cloud droplets.

In regard to (i), it was concluded in Chap. VIII, on the basis of theoretical and experimental evidence, that the growth of cloud droplets to raindrop size by coalescence processes could not occur in the updraft core, due to the strong updraft and therefore short residence time. As a consequence, the updraft core would be composed of cloud droplets having a Z value typically less than -5 dBz - that is a weak echo region.

Possibility (ii) has been invoked by Browning (1963) as a means of explaining the growth of large hailstones by a "cycle" mechanism. The embryo particle reaches the strong updraft by cycling through it once and re-entering or by being drawn in from a neighbouring updraft. Both exist as possibilities but would be most likely to occur on the periphery of the updraft. Since severe storm updrafts are typically 5 - 10 km in diameter, it is highly improbable that a millimetric graupel particle could penetrate across the updraft to reach the inner core. Additionally, the existence of a substantial updraft maximum near the top of the storm would prevent the entry of graupel particles into the updraft core from above. Consequently, it is very unlikely that the updraft core would contain millimetric graupel particles which had entered it by re-cycling. This too, would result in the updraft core appearing as a weak echo region consisting of cloud droplets.

The final possibility to consider is the growth of a cloud droplet. Growth by diffusion and coalescence, considered in Chapter VIII, indicates that growth to a diameter greater than 40 μ would be highly improbable. However, observations reported by MacCready and Takeuchi (1968) indicate the existence of giant cloud droplets beneath cloud base and within the "unmixed core" of the updraft. Particles of 100 μ diameter and possibly as large as 300 μ diameter (at the -5C level) were found in the updraft core. These giant cloud droplets froze in rapid succession after reaching 0C and the majority were detected as frozen particles at -5C.

It is the growth of such particles in the ice phase within the updraft core which will be examined in this chapter. These frozen giant cloud droplets will be referred to as graupel embryos. For ease of reference, a graupel particle, during its growth, will be designated by its initial diameter; that is a 100 μ diameter graupel embryo which has grown to 420 μ will be referred to as the 100 μ graupel.

9.2 The Graupel Growth Model

This section describes the graupel growth model which has been formulated and programmed specifically to compute the growth of graupel from small embryos (as small as 100 μ diameter) within the updraft core. It has been inspired by the work of Browning, Ludlam and Macklin (1963). However, it permits the calculation of graupel growth in an environment having variable temperature, vertical velocity, liquid water content and cloud droplet size; all these being the results from specific storms as calculated by the LMA model described in Chap. VII. In addition, the supercooled liquid water fraction, drag coefficients and wet growth modes are treated in a more sophisticated fashion.

9.2.1 The Cloud Environment

The LMA model results for specific days were subjected to a polynomial curve fitting routine, reducing the pressure, temperature, vertical velocity and liquid water content data to several polynomial coefficients for convenience and ease of operation. The resulting equations become:

$$\text{Pressure (mb)} = CP(1) + CP(2)Z + CP(3)Z^2 + \ldots \qquad \text{Eqn. 9.2.1}$$

$$\text{Temperature (deg A)} = CT(1) + CT(2)Z + CT(3)Z^2 + \ldots \qquad \text{Eqn. 9.2.2}$$

$$\text{Vertical Velocity (m sec}^{-1}) = CW(1) + CW(2)Z + CW(3)Z^2 + \ldots \qquad \text{Eqn. 9.2.3}$$

$$\text{Liquid Water Content (gm m}^{-3}) = CL(1) + CL(2)Z + CL(3)Z^2 + \ldots \qquad \text{Eqn. 9.2.4}$$

Where

C(P)J = pressure coefficient
C(T)J = temperature coefficient
C(W)J = vertical velocity coefficient
C(L)J = liquid water coefficient
Z = height above ground in meters

These equations enable one to compute pressure, temperature, vertical velocity and liquid water content at any point within the cloud, given the height above ground. The curve fitting technique does smooth minor fluctuations in each parameter. The discrepancies are small, however, and normally do not exceed ±0.1 mb for pressure, ±0.1C for temperature, ±0.01 gm m^{-3} for liquid water and ±0.5 m sec^{-1} for vertical velocity.

9.2.2 The Cloud Droplet Number Concentration and Droplet Diameter

Based on the concept that droplet number concentrations are determined at cloud base and that droplet sizes are narrowly dispersed, computations of number concentrations and diameter are possible. The number of cloud droplets at any height Z in the cloud is given by:

$$N_z = N_{cb} \times \frac{T_{cb}}{P_{cb}} \times \frac{P_z}{T_z} \qquad \text{Eqn. 9.2.5}$$

Where

N_z = droplet number concentration at height Z
N_{cb} = droplet number concentration at cloud base
T_{cb} = temperature at cloud base
P_{cb} = pressure at cloud base
P_z = pressure at height Z
T_z = temperature at height Z

And the diameter at any height Z is thus given by:

$$D_z = \left(\frac{6 \times LWC_z \times 10^{-6}}{\pi \times N_z} \right)^{1/3} \qquad \text{Eqn. 9.2.6}$$

Where

D_z = droplet diameter at height Z
LWC_z = liquid water content at height Z
N_z = droplet number concentration at height Z

9.2.3 The Supercooled Cloud Droplet Fraction

At temperatures colder than 0C, the cloud droplets in the updraft freeze or become supercooled. For purposes of calculating graupel growth, it is necessary to estimate what fraction of the cloud droplet population will remain supercooled at various temperatures. Experiments by Vali (1968) have shown that ice nuclei in Alberta hail and rain samples are smaller than 0.01 μ diameter. Particles of this size diffuse very rapidly into cloud droplets of 20 - 40 μ diameter. As a consequence, it has been assumed (as suggested by Vali) that there is a one-to-one correspondence between the number of ice nuclei and the number of frozen cloud droplets. The freezing behaviour of the cloud droplets is then only a function of temperature. Figure 9.2.1 illustrates the ice nuclei spectrum (cm^{-3} deg C^{-1}) which has been used in this study. It is based on typical ice nuclei spectra for Alberta convective precipitation (after Vali) between -5C and -20C and extrapolated to -40C, where it is assumed that all cloud droplets freeze. This ice nuclei spectrum may be expressed as:

$$\ell n \left\{ \frac{dN}{dT} \right\} = -(C_1 + C_2 T)$$

$$\frac{dN}{dT} = e^{-(C_1 + C_2 T)} \qquad \text{Eqn. 9.2.7}$$

$$N = -\int_0^{-40} \frac{dN}{dT}$$

$$N = \left[\frac{e^{-(C_1 + C_2 T)}}{C_2} - \frac{e^{-C_1}}{C_2} \right]_0^{-40} \qquad \text{Eqn. 9.2.8}$$

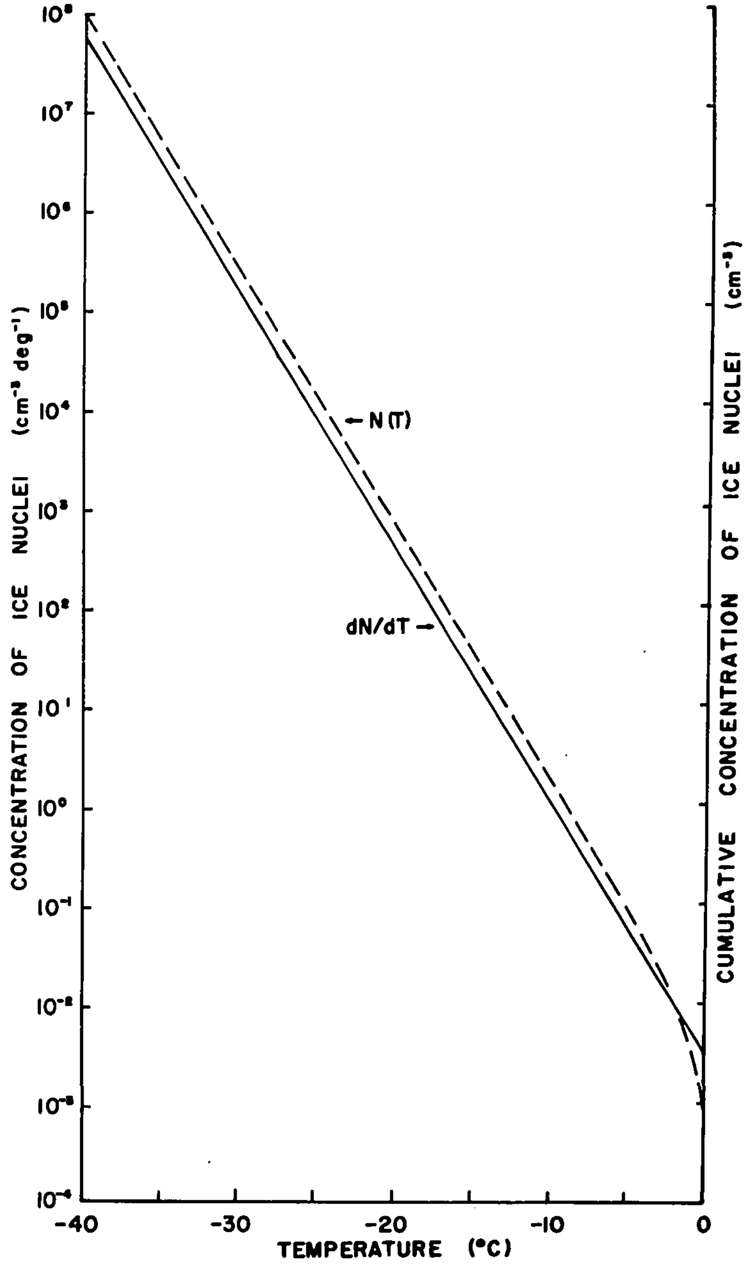

Fig. 9.2.1 Ice Nuclei Spectrum for Alberta Hailstorms Used in Graupel Growth Model. The above ice nuclei spectrum has been constructed using values (from -5C to -20C) typical of Alberta convective precipitation. Values between 0C and -5C and between -20C and -40C are extrapolated.

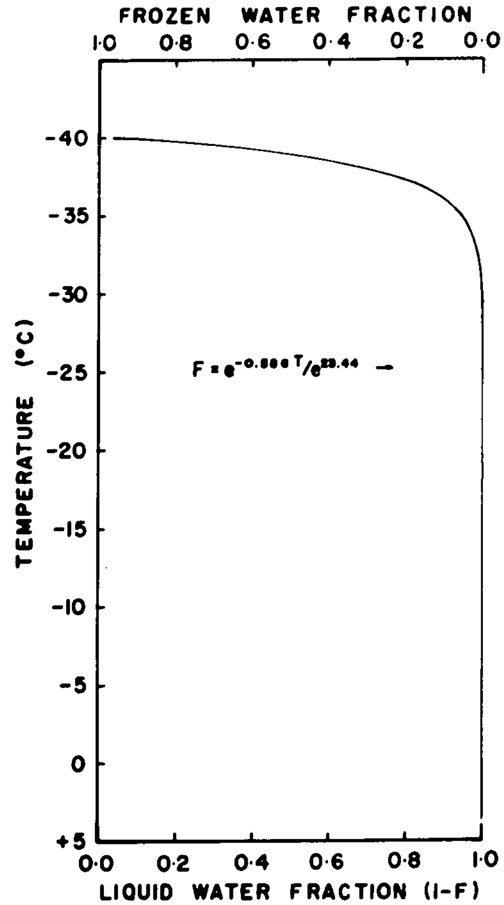

Fig. 9.2.2 Supercooled Liquid Water Fraction as a Function of Temperature. The fraction of cloud droplets which exist at various temperatures in supercooled form is shown. Note the rapid decrease of supercooled droplets at temperatures colder than -35C.

Where

N = ice nuclei concentration per cm^3 of liquid water

T = temperature (deg C)

C_1 = 5.860

C_2 = 0.586 (deg C^{-1})

The fraction of cloud droplets frozen at temperature T will then be given by:

$$F = \frac{-\int_0^T \frac{dN}{dT}\, dT}{-\int_0^{-40} \frac{dN}{dT}\, dT} \simeq \frac{e^{-C_2 T}}{e^{40C_2}} = \frac{e^{-.586T}}{e^{23.44}} \qquad \text{Eqn. 9.2.9}$$

And the fraction of the adiabatic liquid water content which is then supercooled and available for graupel growth is given by:

$$1 - F = 1 - \frac{e^{-.586T}}{e^{23.44}} \qquad \text{Eqn. 9.2.10}$$

Figure 9.2.2 illustrates the liquid water fraction as a function of temperature. It is apparent that the major portion of the adiabatic liquid water remains supercooled until -30C, then proceeds to freeze rapidly between -35 and -40C. All liquid is assumed frozen at -40C, so that all graupel growth ceases at this temperature.

9.2.4 The Graupel Embryo

The graupel embryo, which is initially assumed to be in the "cloud", can be of any size, density and surface temperature. The initial conditions which have been utilized in this study are:

Diameter	$= D = 100, 300, 600\ \mu$
Density	$= \rho = 0.917$ gm cm^{-3}
Cloud Temperature	$= T_e = -5C$
Graupel Surface Temperature	$= T_s = -5C$

9.2.5 Graupel Fallspeeds and Collection Efficiencies

Other workers calculating hailgrowth have assumed a constant drag coefficient and computed hailstone fallspeeds using:

$$V = \left(8gR\rho_h \,/\, 3\rho_a C_d\right)^{\frac{1}{2}} \qquad \text{Eqn. 9.2.11}$$

Where

V = fallspeed

g = acceleration of gravity

ρ_a = air density
R = hailstone radius
ρ_h = hailstone density (range 0.80 - 0.90 gm cm^{-3})
C_d = drag coefficient (range 0.50 - 0.60)

As the fallspeed is a square root function of the drag coefficient, an error or change of 50% in the drag coefficient incurs an error or change of 25% in the fallspeed. For hailgrowth from sizes of several millimeters to several centimeters, this is not serious. For the smaller sizes which are to be considered here, this is not satisfactory. At 100 μ the drag coefficient of a smooth sphere is ≈ 20, at 1.0 mm ≈ 1.0 and 2.0 cm ≈ 0.45.

Following Mason (1957) and Goldstein (1938), a scheme has been designed to compute the drag coefficient of a smooth sphere. Goldstein gives the empirical equation for smooth spheres:

$$C_d R_e / 24 = \left\{ 1 + 0.197 R_e^{0.63} + 2.6 \times 10^{-4} R_e^{1.38} \right\} \qquad \text{Eqn. 9.2.12}$$

and

$$C_d R_e^2 / 24 = \left\{ R_e + 0.197 R_e^{1.63} + 2.6 \times 10^{-4} R_e^{2.38} \right\} \qquad \text{Eqn. 9.2.13}$$

Where

$$R_e = 2VR\rho_a / \eta = \text{Reynolds Number} \qquad \text{Eqn. 9.2.14}$$

$$C_d R_e^2 / 24 = 4R^3 \rho_a \rho_h g / 9\eta^2 \qquad \text{Eqn. 9.2.15}$$

V = fallspeed
R = radius
η = dynamic viscosity of air
g = acceleration of gravity
ρ_a = air density
ρ_h = hail or graupel density

An initial calculation is made of $C_d R_e^2/24$ from Eqn. 9.2.15 and

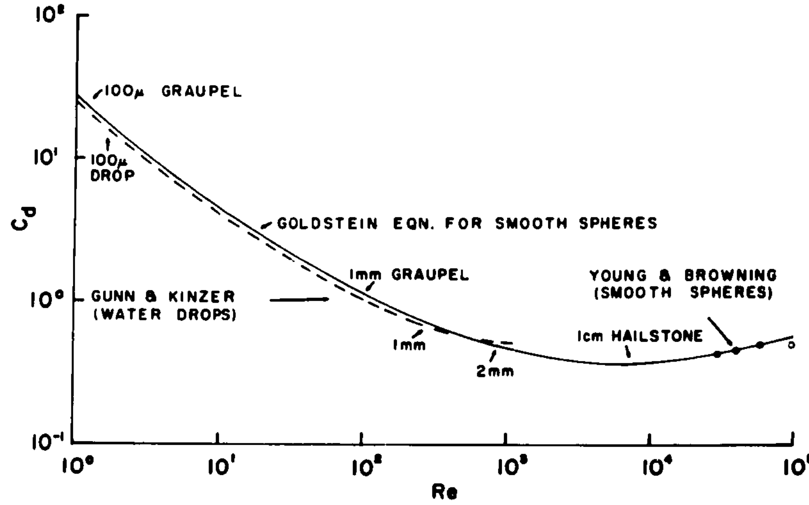

Fig. 9.2.3 Drag Coefficient vs. Reynolds Number for Smooth Spheres. The drag coefficient for smooth spheres as a function of the Reynolds number is shown, with drag coefficients appropriate to 100 μ, 1 mm, and 1 cm graupel and hail particles indicated. Experimentally determined drag coefficients for water drops and for larger (several cm) smooth spheres are also shown.

used as an initial guess value for R_e. Then, $C_d R_e^2/24$ is computed from Eqn. 9.2.13 using the guess value of R_e and the result is compared with Eqn. 9.2.15. If the value of $C_d R_e^2/24$ computed from Eqn. 9.2.13 does not agree with Eqn. 9.2.15, adjustments are made in the guess value of R_e and the procedure iterated to solve for the appropriate Reynolds number from which C_d and V may also be calculated. Figure 9.2.3 illustrates the resulting drag coefficient as a function of the Reynolds number. Also shown are experimental values from wind tunnel tests on smooth spheres by Young and Browning (1967). A distinct lack of experimentally determined data on densities and fallspeeds of spherical graupel and hailstones from 100 μ - 2 cm has made it difficult to determine the validity of the fallspeed computations. Experimentally determined water drop fallspeeds, measured by Gunn and Kinzer (1949), are also shown in Fig. 9.2.3. These values compare quite reasonably with the calculated results from Goldstein's empirical equation. It may be noted that the fallspeed computations used here are valid only for smooth spherical graupel particles and hailstones. Over a wide range of graupel and hailstone diameters, this computational scheme yields a better estimate of V, C_d and R_e than the assumption of a constant drag coefficient.

9.2.6 Graupel Growth Equations

The growth of a graupel particle is determined by two factors: accretion and sublimation (or evaporation). Thus:

$$\frac{dM}{dt} = \left\{\frac{dM}{dt}\right\}_a + \left\{\frac{dM}{dt}\right\}_{es} \qquad \text{Eqn. 9.2.16}$$

Where

$\left\{\frac{dM}{dt}\right\}_a$ = rate of mass increase due to accretion

$\left\{\frac{dM}{dt}\right\}_{es}$ = rate of mass increase due to evaporation and sublimation

Dealing first with growth by accretion, one finds:

$$\left\{\frac{dM}{dt}\right\}_a = \pi R^2 \int_0^{\infty} E_r \, (V_R - V_r) \, M_r dr \qquad \text{Eqn. 9.2.17}$$

Where

R = radius of the graupel particle

E_r = collection efficiency for droplets of radius r (coalescence efficiency assumed = 1.0)

V_R = fallspeed of graupel particle of radius R

V_r = fallspeed of droplet of radius r

M_r = mass of water substance contained in droplets of radius r

Since we have assumed a monodisperse droplet distribution, the equation above may be re-written in simplified form as:

$$\Delta M_a = \pi R^2 \times E_r \times V_R \times M_r \times \Delta t$$ Eqn. 9.2.17

This assumes, additionally, that $V_r << V_R$. This is valid except for very small graupels (100 μ) where the terminal fallspeed of a 20 μ droplet is 6% of that for a 100 μ particle. The errors incurred due to this simplification are very small.

The mass growth due to evaporation and sublimation is given by:

$$\left\{\frac{dM}{dt}\right\}_{es} = 4\pi R^2 \, \{(2.00 + 0.60 S_c^{1/3} R_e^{\frac{1}{2}}) \, D \, (\rho_s - \rho_e)\} \, / \, 2R$$ Eqn. 9.2.18

$$\Delta M_{es} = 2\pi R \, (2.00 + 0.60 S_c^{1/3} R_e^{\frac{1}{2}}) \, D \, (\rho_s - \rho_e) \, \Delta t$$ Eqn. 9.2.19

Where
ΔM_{es} = mass acquired by sublimation or evaporation
R = graupel or hailstone radius
S_c = Schmidt number
R_e = Reynolds number
D = diffusivity of water vapor in air
ρ_s = vapor density over the graupel or hailstone surface
ρ_e = vapor density in the cloud
Δt = time interval

A collection efficiency E is required in order to complete the computation of mass growth by accretion. The Langmuir collection efficiency (E) is used:

$$K = 2\rho r^2 V \, / \, 9\eta R$$ Eqn. 9.2.20

$$E_v = \{1 + (3/4 \ln 2K) \, / \, (K - 1.214)\}^{-2}$$ Eqn. 9.2.21

$$E_p = K^2/(K + \tfrac{1}{2})^2$$ Eqn. 9.2.22

$$E_L = (E_v + E_p R_e/60) \, / \, (1 + R_e/60)$$ Eqn. 9.2.23

Where

ρ = density of the graupel or hailstone

r = radius of collected droplet

η = dynamic viscosity of air

R = radius of collector

V = fallspeed of collector

E_p = collection efficiency in potential flow

E_v = collection efficiency in viscous flow

E_L = interpolated collection efficiency (valid for $20 < R_e < 100$)

For R_e values greater than 100, the collection efficiency for potential flow (E_p) has been utilized. However, for $R_e < 100$ the Langmuir interpolation formula (E_L) has been used instead. Thus calculations for graupel with diameters greater than 300 μ should not be in error. Calculations at 100 μ will overestimate the collection efficiency slightly.

9.2.7 Graupel Density

Experiments performed by Macklin (1962) have shown that the density of the ice formed by the accretion of supercooled water droplets varies and is a function of the droplet radius (r), the impact velocity (V), and the graupel or hailstone surface temperature (T_s). Figure 9.2.4 illustrates the ice density (ρ_i) as a function of rV/T_s. In order to utilize this data, a curve was fitted to the data resulting in the equation:

$$\rho_i = e^{(c_1 + c_2\sigma + c_3\sigma^2)} \qquad \text{Eqn. 9.2.24}$$

Where

c_1 = -2.10

c_2 = -0.88 (μ^{-1} m^{-1} sec deg C)

c_3 = -0.10 (μ^{-2} m^{-2} sec^2 deg C^2)

σ = rV/T_s (μ m sec^{-1} deg C^{-1})

Due to fluctuations and limitations in the original data, the program was

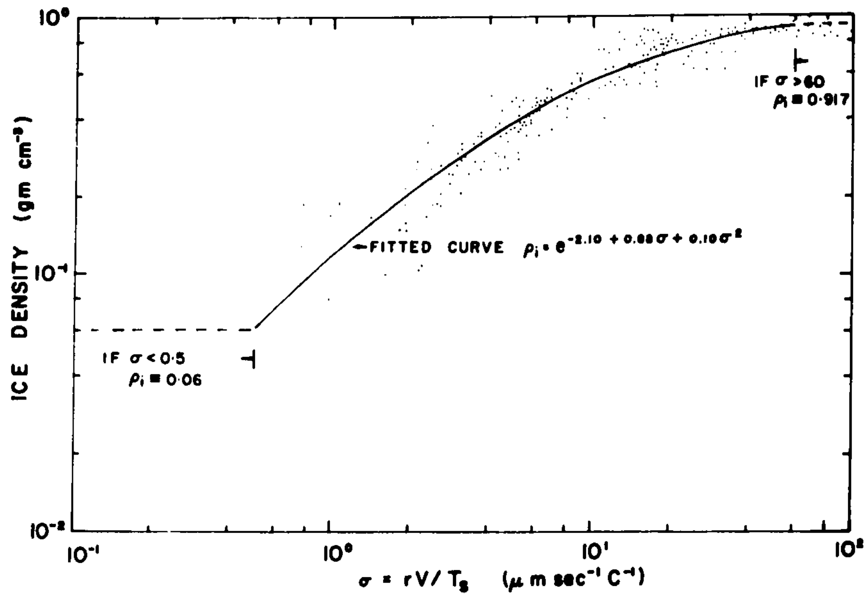

Fig. 9.2.4 Accreting Ice Density as a Function of rV/T_s. A curve, fitted to Macklin's experimental data, is shown. Note that limiting values of ice density have been assigned for large and small values of rV/T_s.

designed so that $\rho_i \equiv 0.06$ if $\sigma < 0.5$ and $\rho_i \equiv 0.917$ (limiting value of ice density) if $\sigma > 60.0$.

9.2.8 The Graupel Heat Balance

The heat balance for spherical hailstones has been investigated extensively by List (1963) and Macklin (1963). Macklin's heat balance has been utilized with the heat transfer coefficients due to Ranz and Marshall (1953). Neglecting the finite heat capacity of the graupel particle, a heat balance may be written as:

$$Q_f + Q_{cp} + Q_{cc} + Q_{es} = 0 \qquad \text{Eqn. 9.2.25}$$

Where

Q_f = heat released by accreted supercooled water during freezing

Q_{cp} = heat absorbed by supercooled cloud particles being warmed to 0C

Q_{cc} = heat lost due to conduction and convection

Q_{es} = heat lost or gained due to evaporation or sublimation

In terms of heat increments over a time Δt, these become:

$$\Delta Q_f = \Delta M \times L_f \qquad \text{Eqn. 9.2.26}$$

$$\Delta Q_{cp} = \Delta M \times (C_w \times T - C_i \times T_s) \qquad \text{Eqn. 9.2.27}$$

$$\Delta Q_{cc} = 2\pi R\ (2.00 + 0.60 P_r^{1/3} R_e^{\frac{1}{2}})\ \kappa\ (T - T_s)\ \Delta t \qquad \text{Eqn. 9.2.28}$$

$$\Delta Q_{es} = 2\pi R\ (2.00 + 0.60 S_c^{1/3} R_e^{\frac{1}{2}})\ L_v D\ (\sigma_e - \sigma_s)\ \Delta t \qquad \text{Eqn. 9.2.29}$$

Where

ΔM = water mass accreted onto graupel or hailstone in time Δt
C_w = specific heat of water
C_i = specific heat of ice
T = cloud temperature
T_s = graupel or hailstone surface temperature
R = graupel or hailstone radius
P_r = Prandtl number
S_c = Schmidt number
R_e = Reynolds number
κ = thermal conductivity of air
L_v = latent heat of vaporization of water
D = diffusivity of water vapor in air
σ_e = vapor density of water in the environment
σ_s = vapor density of water over the hailstone surface.

During dry growth conditions ($T_s < 0C$), the graupel particle or hailstone will not accrete ice particles and so we need only consider the growth by supercooled liquid water. The heat balance is then as in Eqn. 9.2.25 and the hailstone surface temperature may be computed by:

$$T_s = (B - E) / C \qquad \text{Eqn. 9.2.30}$$

Where

$B = 2\pi R\ \{(2.00 + 0.60 P_r^{1/3} R_e^{\frac{1}{2}}) \kappa T + (2.00 + 0.60 S_c^{1/3} R_e^{\frac{1}{2}})\ L_v D\ (\sigma_e - \sigma_s)\}\ \Delta t$

$E = \Delta M (C_i T + L_f)$

$$C = 2\pi R\ (2.00 + 0.60P_r^{1/3}R_e^{\frac{1}{2}})\ \kappa\Delta t + \Delta MC_i$$

It is possible that during hailstone growth, however, the heat balance outlined above will require that $T_s > 0C$. This is the case of "wet growth", which means that the hailstone surface acquires a water coat which must be at 0C. In this instance, the heat balance outlined in Eqn. 9.2.25 does not hold, and instead we have the conditions:

$T_s = 0.0C$

and $FQ_f + Q_{cp} + Q_{cc} + Q_{es} = 0$ Eqn. 9.2.31

Where

F = fraction of water accreted which freezes

Strictly speaking, it is conceivable that during the wet growth stage (T_s = 0C), ice crystals may be accreted onto the liquid water surface. However, the wet growth phase does not normally occur until the cloud temperature is -20C or warmer and thus the number of ice crystals which might accrete onto the liquid water surface is insignificantly small.

9.2.9 The Reflectivity of Cloud Droplets and Graupel Particles

A major purpose in calculating the growth of graupel and hail particles within the updraft region is to compare the computed radar reflectivity factor (Z) values with observed equivalent radar reflectivity factor (Z_e) values. One component of the radar reflectivity factor in the weak echo region is the contribution from cloud droplets. Using the monodisperse approximation discussed in Sections 8.2.2 and 8.2.3, to compute Z values for a broad droplet spectrum would lead to poor estimates of the actual Z_e value. However, in the case of a narrow droplet spectrum (as has been deduced to exist within the updraft), the assumption of a monodisperse spectrum does not result in a significant error in the estimated Z value. For example, the Z value computed from Auer's cumulus cloud droplet distribution (see Fig. 8.2.3) is 1.92×10^{-4} mm^6 m^{-3} (-37.2 dBz). Using a monodisperse approximation, the computed Z value is 1.69×10^{-4} mm^6 m^{-3} (-37.7 dBz) - an underestimate of 12%. Similarly, for the ALHAS cloud droplet spectrum (see Fig. 8.3.2), the Z value computed from the distribution is 1.04×10^{-3} mm^6 m^{-3} (-29.8 dBz) and from the monodisperse approximation 0.81×10^{-3} mm^{6}m^{-3} (-30.9 dBz) - a difference of 22%. It is unlikely that a monodisperse approximation would introduce errors in excess of 25% (≃ 1 dBz). Therefore, it is considered acceptable to compute Z values for cloud droplets in the updraft core using the following equation:

$$Z_{cloud} = N_d D_d^6 \times 10^6 \qquad \text{Eqn. 9.2.32}$$

Where

N_d = number concentration of cloud droplets

D_d = monodisperse droplet diameter

The Z values of the graupel particles were also calculated. Estimates of the number concentration of graupel particles are difficult to obtain (as will be discussed in the following section). Calculations here were performed using a constant number concentration of 1 m^{-3}; adjustments to other concentrations are then easily performed. For dry graupel particles (T_s < 0C), the reflectivity was calculated by:

$$Z_{graupel} = 0.21\,(\bar{\rho})^2\, N_g D_g^6 \qquad \text{Eqn. 9.2.33}$$

Where

$\bar{\rho}$ = mean density of the graupel or hailstone particle

N_g = graupel or hailstone number concentration (assumed = 1 m^{-3})

D_g = graupel or hailstone diameter

For wet growth T_s = OC, the Z value was calculated using:

$$Z_{graupel} = N_g D_g^6 \qquad \text{Eqn. 9.2.34}$$

9.2.10 <u>The Number Concentration of Graupel Particles and Hailstones</u>

As was mentioned in Section 9.2.9, it is necessary to have an estimate of the graupel number concentration (per cubic meter) in order to compute the radar reflectivity factor. MacCready and Takeuchi (1968) observed giant droplets (D = 100 - 300 μ) and ice pellets formed from frozen giant droplets, in number concentrations of 1 - 3 x 10^4 particles m^{-3}, on four out of five days of observation. The fifth day yielded no giant droplets. From this small amount of data, it appears that giant droplets may exist in concentrations from 0 - 3 x 10^4 m^{-3}.

By utilizing the surface hail reports, it is possible to estimate the concentration of hail particles as they reach the surface. The estimated number concentration of hailstones arriving at the surface (on 29 June 1967), in the area of maximum hailfall, was N ≈ 0.05 m^{-3}. This estimate represents hailstones of all sizes, determined by counting the number on the ground at the end of hailfall. The maximum size was approximately 2.5 cm and sizes smaller than 1.0 cm would melt rapidly. It is therefore reasonable to assume that:

$$N_{1.0cm}^{2.5cm} \simeq 0.05 \ m^{-3}$$

Hailstone size distributions from Alberta have been found by Douglas (1963, 1965) to follow a distribution of the form:

$$N = N_o e^{-\lambda D} \qquad \text{Eqn. 9.2.35}$$

Where

λ = 3.09 (cm^{-1})

D = hailstone diameter (cm)

N_o = intercept at D = 0 (m^{-3})

Using a Douglas hail distribution and the fact that $N_{1.0}^{2.5} \simeq 0.05\ m^{-3}$, one finds that N_o = 3.43 m^{-3} and that the total number of hailstones (from 0 - 2.5 cm diameter) is 1.1 m^{-3}. This yields an ice mass of 0.106 gm m^{-3} and a Z value (assuming Rayleigh scattering for wet spheres) of 6.1 x 10^6 mm^6 m^{-3} (68 dBz). Observed equivalent radar reflectivity factor values, in this region were found to be $10^6 < Z_e < 10^7$ mm^6 m^{-3} (60 dBz < Z_e < 70 dBz).

Strictly speaking, it is not correct to assume that the number concentration of graupel particles and hailstones is constant with height in the updraft. Thus far, the majority of investigators have assumed a constant flux through a given layer which yields:

$$N\ |W - V|\ R^2 = N_o\ |W_o - V_o|\ R_o^2 \qquad \text{Eqn. 9.2.36}$$

$$\text{and} \quad N = N_o \frac{|W_o - V_o|}{|W - V|} \left(\frac{R_o}{R} \right)^2 \qquad \text{Eqn. 9.2.37}$$

Where

N_o = number concentration of particles at cloud base or injection point

N = number concentration of particles at a given height above cloud base

W_o = updraft speed at cloud base or injection point

W = updraft speed at a given height above cloud base

V_o = terminal fallspeed of particles at cloud base or injection point

V = terminal fallspeed of particles at a given height above cloud base

R_o = radius of updraft at cloud base or injection point

R = radius of updraft at a given height above cloud base

When V = W (maximum height of particle trajectory), the denominator becomes zero and the number concentration approaches infinity. This is clearly unsatisfactory for computing radar reflectivity factors.

Srivastava and Atlas (1969) have pointed out that this infinitely large number concentration is a mathematical artifact and not a physical reality. They have proposed a somewhat different scheme, dealing with a continuous distribution of particle sizes:

$$N \Delta V (W - V) R^2 = N_o \Delta V_o (W_o - V_o) R_o^2 \qquad \text{Eqn. 9.2.38}$$

which becomes $$N = N_o \frac{(W_o - V_o)}{(W - V)} \frac{dV_o}{dV} \left(\frac{R_o}{R} \right)^2 \qquad \text{Eqn. 9.2.39}$$

Where

$N\Delta V$ = number of particles in unit volume having fallspeeds between V and $V - \Delta V$.

By using analytic forms for updrafts, fallspeeds and particle growth, Srivastava and Atlas have obtained solutions for the variations of particle concentration with height. The results obtained show that particle number concentrations decrease monotonically during both the upward and downward traverse of the particle in the updraft system. The updraft, fallspeed and particle growth schemes used in the present study are not suitable for use with the Srivastava-Atlas computational scheme.

Srivastava and Atlas, using an updraft with 20 m sec^{-1} maximum (similar to the 29 June 1967 case), find that particles with V = 1 m sec^{-1} (D ≃ 300 μ) introduced into the updraft at V = 8 m sec^{-1} and with an initial number concentration of 1 m^{-3} descend through cloud base with a number concentration of 0.035 m^{-3}. For the 29 June 1967 storm, with $N_{1.0}^{2.5} = 0.05\ m^{-3}$ at the ground, one would estimate number concentrations at -5C of 1.0 - 1.5 m^{-3}. In addition, the Srivastava-Atlas computations show that, during the upward traverse, number concentrations would decrease from approximately 1 m^{-3} to 0.35 m^{-3}. As was indicated in Section 9.2.9, all computations in this study have assumed N = 1 m^{-3}. It will be useful to use the approximate number variations with height computed by Srivastava and Atlas when interpreting the results which follow.

Particle number concentrations (and diameters) determine the rate at which the liquid water within the cloud is depleted. This in turn determines the final size of the particles, and whether they are affected by competition among one another for the available liquid water. List et al (1968) have performed hailgrowth computations starting with 5 mm (5000 μ) diameter particles at 0C while taking account of liquid water content depletion. The results show only small depletion effects for number concentrations of 1 m^{-3}, but significant depletion effects occur at concentrations in excess of 5 m^{-3}. The initial diameter of particles used in this present study is much less (10 - 50 times smaller) than that used by List et al, resulting in a cross-section 100 - 2500 times smaller. For this reason, liquid water depletion has been neglected in this study.

9.3 The Growth of Graupel Particles in the Core of a Severe Storm Updraft

In this section, the results of the graupel growth program will be examined and discussed. During the course of these studies, it has become apparent that the graupel growth which results in a given storm is dependent largely on the magnitude of the updraft. For this reason, results will be discussed in detail for a typical Low Energy storm - 27 June 1967 (see Chap. V), a typical Medium Energy storm - 29 June 1967 (see Chap IV) and a typical High Energy storm - 28 July 1967. The results of graupel growth in the storms of 25 July 1968 - a Medium Energy storm (see Chap. II) and of 28 July 1968 - a very High Energy storm (see Chap III) are presented in the summary in Chap. X. The graupel growth in these two storms exhibits behaviour similar to the Medium and High Energy storms discussed in this chapter.

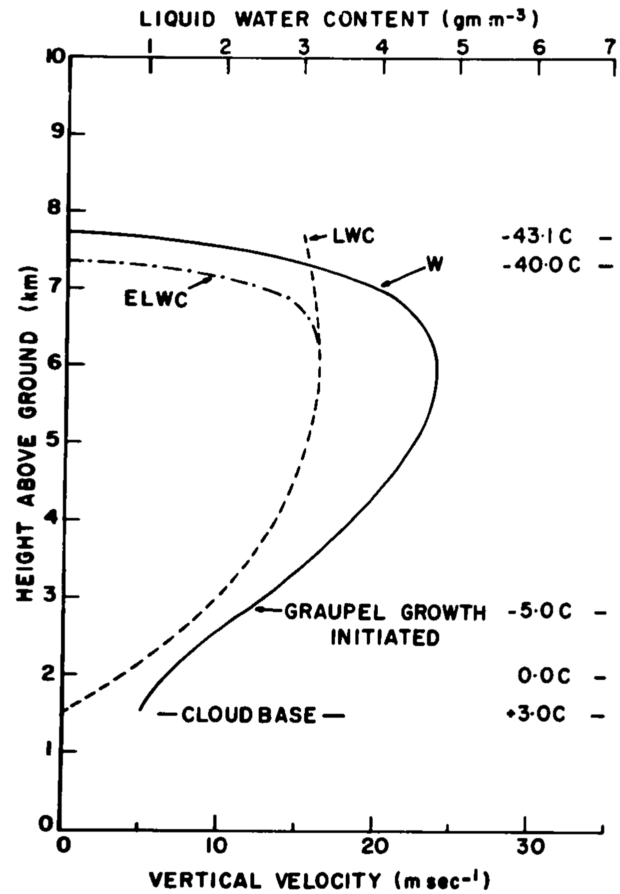

Fig. 9.3.1 Vertical Velocity and Liquid Water Content for a Medium Energy Storm - 29 June 1967. Vertical velocity (W) and liquid water content (LWC) are illustrated as a function of height. The curve labelled ELWC depicts the water available in supercooled form.

9.3.1 Graupel Growth in the Updraft Core of a Medium Energy Storm 29 June 1967

The vertical velocity and liquid water content for the storm of 29 June 1967 (at approximately 1330 - 1400 MST) is illustrated in Fig. 9.3.1. This storm was relatively shallow (maximum top 7.7 km AGL); in fact the temperature at the top of the storm was not much colder than -40C. Thus, graupel growth was possible throughout a considerable portion of the total storm depth. The total water content (liquid and solid phases), which has been referred to in this study as the liquid water content, is labelled LWC in Fig. 9.3.1. The supercooled portion of the liquid water content, which

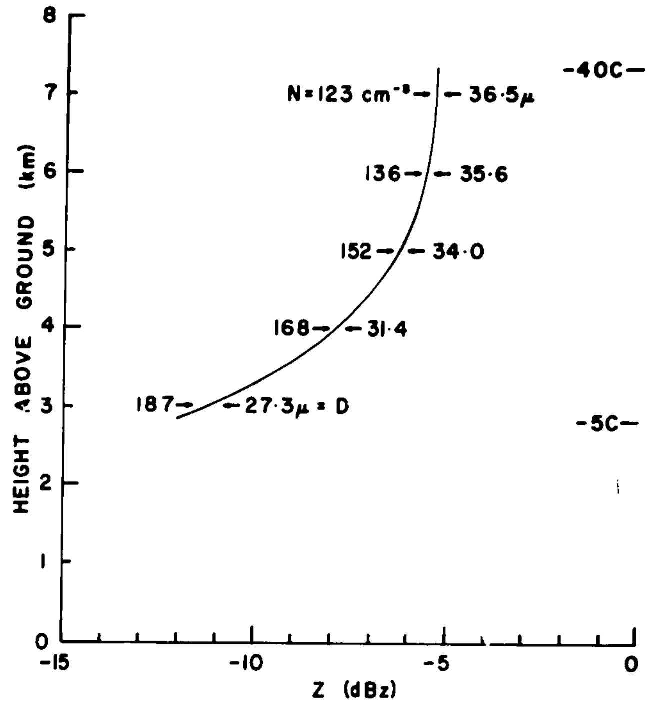

Fig. 9.3.2 Cloud Droplet Concentrations, Diameters and Z Values - 29 June 1967. The number concentrations, diameters and Z values (dBz), calculated using a monodisperse distribution, are shown as a function of height.

will be referred to as the effective liquid water content, is labelled ELWC in Fig. 9.3.1.

As was indicated in Chap. IV, the 29 June 1967 storm occurred in a fresh maritime Arctic airmass. In accordance with Section 8.2.2, the cloud droplet concentration at cloud base has been assumed to be 220 cm^{-3}. The variation of the cloud droplet concentration with height and the resulting monodisperse droplet diameter is illustrated in Fig. 9.3.2. By 3 km, the cloud droplet concentration has decreased to 187 cm^{-3} and the droplet diameter is 27.3 μ. At the -40C level (where graupel growth ceases), the diameter has increased to 36.5 μ and the cloud droplet concentration has decreased to 123 cm^{-3}. The Z_e value of this cloud, within the updraft core, is sufficiently low so that it could not be detected by the ALHAS 10 cm radar. At 16 km (10

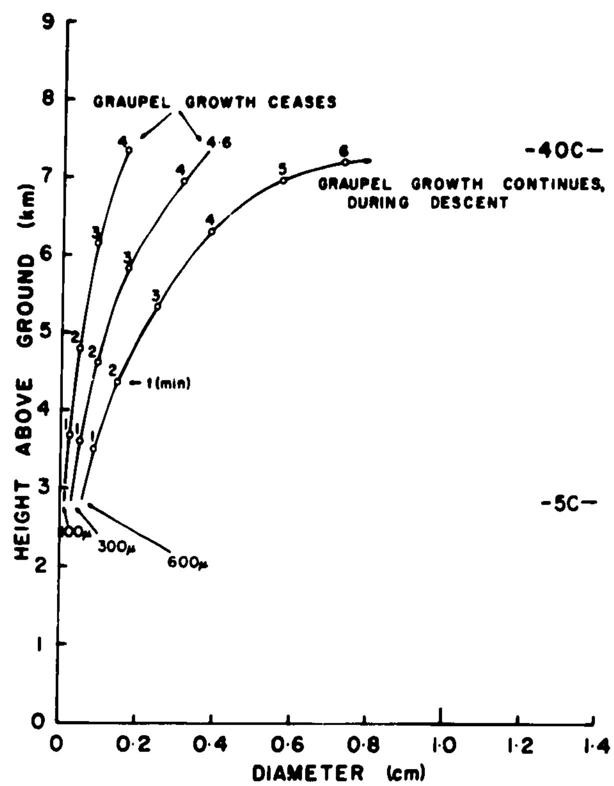

Fig. 9.3.3 Graupel Growth - 29 June 1967. The diameter of growing graupel particles is shown as a function of height. Small circles are located at 1 min intervals. Note that the 100 and 300 μ graupels cease to grow at -40C.

st mi) range, the nominal minimum detectable Z_e value of the radar is ≃ 0 dBz; specifically, on 29 June 1967, due to technical problems, the minimum detectable Z_e value was 25 dBz at 16 km (10 st mi). It is apparent that cloud in the updraft core having a maximum Z value of -5 dBz (see Fig. 9.3.2) would escape detection and appear instead as a WER.

In the computations, graupel embryos in the form of frozen giant water droplets (D = 100, 300, 600 μ, $\rho = 0.917$, T_s = -5C), were introduced into the updraft core at -5C level and permitted to grow according to the graupel growth model outlined in Section 9.2. The growth of these graupel[1]

[1]List (1965) has defined graupel as "white, opaque, conical (sometimes mainly dendritic, rounded or irregular) pellets of diameters up to about 5 mm, densities up to 0.8 gm cm^{-3}!" However, for ease of reference in this study, the growing particles will be designated "graupel" during dry growth and "hail" during wet growth.

particles is illustrated as a function of height in Fig. 9.3.3. The 100 μ and 300 μ graupel embryos ascend and grow in the updraft core, reaching the -40C level in approximately 4 min. At this point graupel growth ceases and the graupel particle must continue to ascend to a point in the updraft where the graupel fallspeed equals the vertical velocity of the updraft. It is impossible for these graupel particles (1.7 and 3.7 mm diameter) to re-enter the updraft core region from above and continue to grow while descending. This is not the case for the 600 μ embryo; after 6.5 min it has reached the highest point in its trajectory. Since it is below the -40C level, it is able to continue growing while completing its descent back through the updraft core. The observations of MacCready and Takeuchi (1968) indicate that frozen giant droplets of 100 - 300 μ diameter can and do exist in convective clouds at -5C. Droplets as large as 600 μ diameter were not observed. Thus the 100 μ and 300 μ particle trajectories can be considered realistic; the 600 μ trajectory is not.

It has been established that the cloud particles within the updraft could not be detected by the ALHAS radar at 16 km (10 st mi) range. The Z values for the graupel particles, with a number concentration of 1 m^{-3}, are shown in Fig. 9.3.4. It is apparent that the 100 μ and 300 μ graupel particles reach a maximum Z value of -15 and 18 dBz respectively, both well below the minimum detectable Z_e value of 25 dBz. Thus the concept of a weak echo region is upheld, in spite of having a concentration of graupel particles of 1 m^{-3} within the updraft core. Increasing particle concentration to 10^4 m^{-3}, would make the 100 μ graupel particles detectable only above 7 km and the 300 μ particles detectable only above 5 km. Even in such an extreme case, a WER would be found throughout a substantial depth of the storm as, indeed, was found in the storm of 29 June 1967.

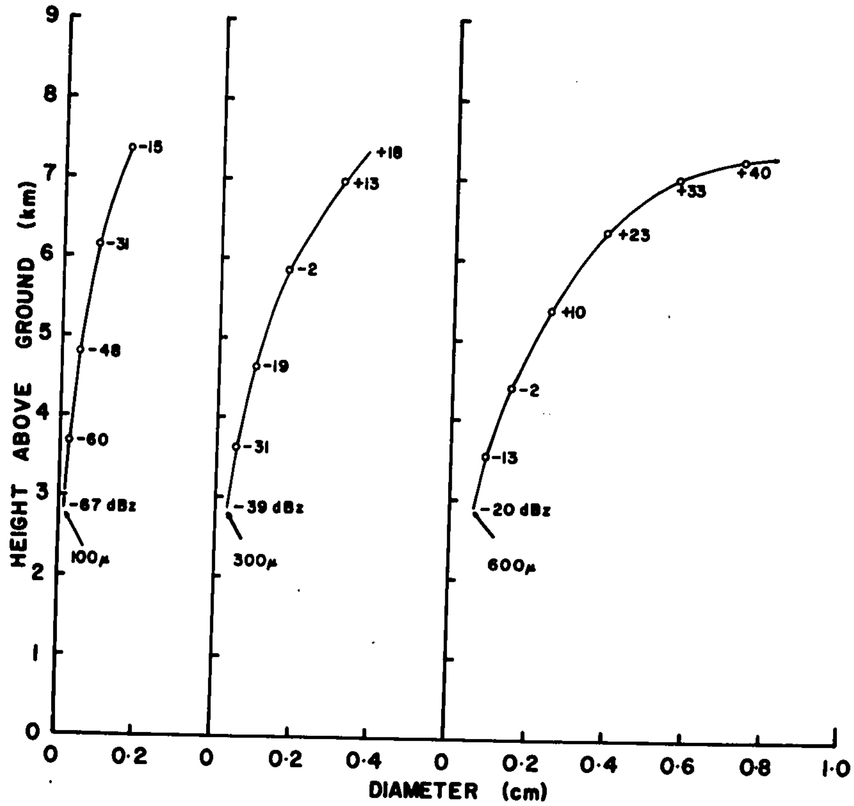

Fig. 9.3.4 Graupel Z Values - 29 June 1967. The Z values (dBz) of graupel particles growing in the updraft core are shown as a function of height (at 1 min intervals), calculated for a number concentration of 1 m^{-3}. Note that the 100 μ and 300 μ Z values do not exceed the minimum detectable Z_e value of 25 dBz.

It is clear that by using estimates of the precipitation growth environment and the initial graupel embryo, it is possible to explain the growth of millimetric graupel particles during an upward traverse through a severe storm updraft core without reaching radar detectability. The updraft velocity is sufficiently great to prevent these particles from falling back through the updraft from the top. These millimetric graupel particles will be carried radially outward at the top of the updraft system to descend through regions of lower vertical velocity. The one-dimensional vertical velocity model presented here does not enable one to study the three-dimensional precipitation growth trajectories which must exist. At least one bounding case is of interest; that is to re-introduce the 100 μ graupel particle into a stagnant cloud (W = 0) having the same liquid water content as

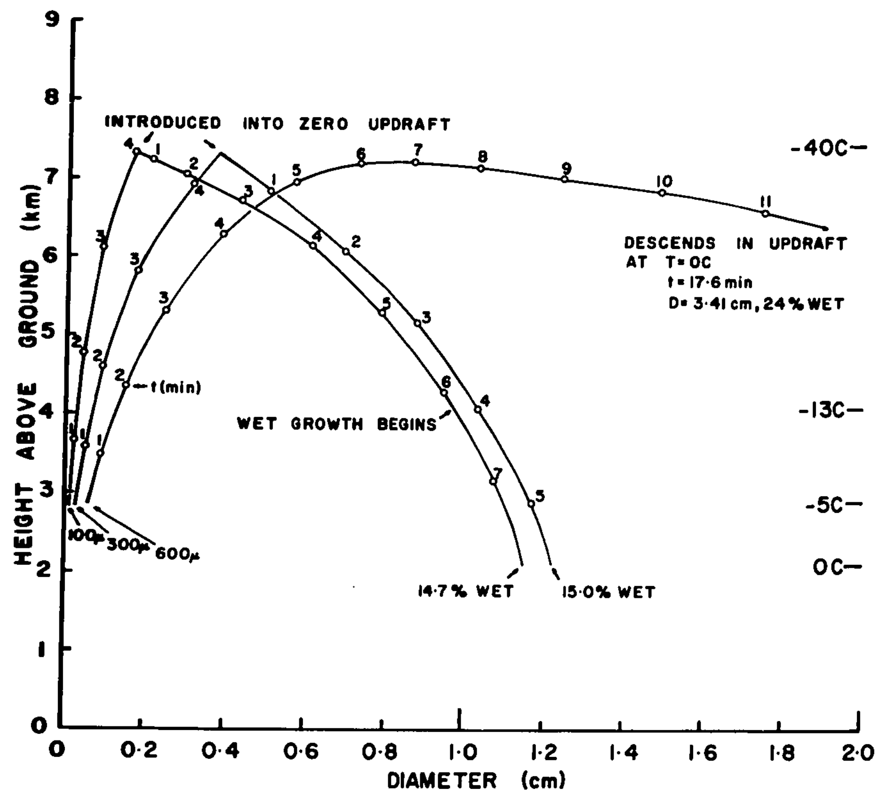

Fig. 9.3.5 Graupel and Hail Growth - 29 June 1967. The diameters of growing graupel and hail particles are shown as a function of height. Small circles are located at 1 min intervals. The 100 and 300 μ graupel particles are re-introduced into stagnant cloud (W = 0) having the same LWC and T as in the previous case. This represents a minimum growth path, and yet hail of 1.2 cm diameter results at the freezing level.

has been used during the upward traverse. The 100 μ particle grows rapidly during descent and begins wet growth (T_s = 0C) at 4 km (T = -13.0C). In 8 min (see Fig. 9.3.5), it reaches the 0C level with a diameter of 1.14 cm (14% wet, assuming no water shedding). A hailstone of this size at the freezing level is sufficiently large to reach the surface (2 km below) without melting completely. Excepting downdraft regions, the path followed by this 100 μ graupel is the path along which minimum growth would occur. It is conceivable that paths (just outside the inner updraft core) might exist which have a positive vertical velocity permitting the hailstone to reach substantially larger sizes. English (1969) has performed a study of this type with similar hailgrowth models and a tilted two-dimensional updraft for the 29 June 1967 storm. Hailstones in excess of 2 cm diameter resulted from the computations, in reasonable agreement with the grape and walnut size hail commonly observed on the ground during the 29 June 1967 storm.

A picture emerges of a severe storm having a powerful updraft in its central region. Due to short residence times, graupel particles are unable to grow to large sizes in this central core; instead the graupel particles descend in lesser updraft zones, close to this core, to become large hail. This is consistent with the high reflectivity gradients which exist around weak echo regions and also with surface precipitation observations which show a sharp hail - no precipitation boundary on the right flank of the storm.

Since the graupel growth program permits a determination of the density of the accreting material, it is also possible to compute the bulk density of the graupel particle. The bulk density (as a function of diameter) of the 100, 300, and 600 μ graupel particles is displayed in Fig. 9.3.6. Starting as a frozen giant droplet ($\rho = 0.917$ gm cm^{-3}), the bulk density falls rapidly to values as low as 0.07 gm cm^{-3} for the 100 μ particle and 0.23 gm cm^{-3} for the 300 μ particle. This trend reverses when the graupel reaches a diameter of 1 - 2 mm and the bulk density increases to approach the density of pure ice. As has been pointed out by Douglas (1957), the bulk density of the graupel particle reflects quite rapidly the density of the accreting ice. Listed in Table 9.3.1 are the diameters and densities for the hailstones at OC level. This table indicates the trend which was found for all the case studies performed; the larger the final hailstone diameter at the OC level, the greater the bulk density. Unless low density particles are ejected out of the cloud to fall into clear air, their downward trajectory will result in a hard, high density outer shell yielding a bulk density of

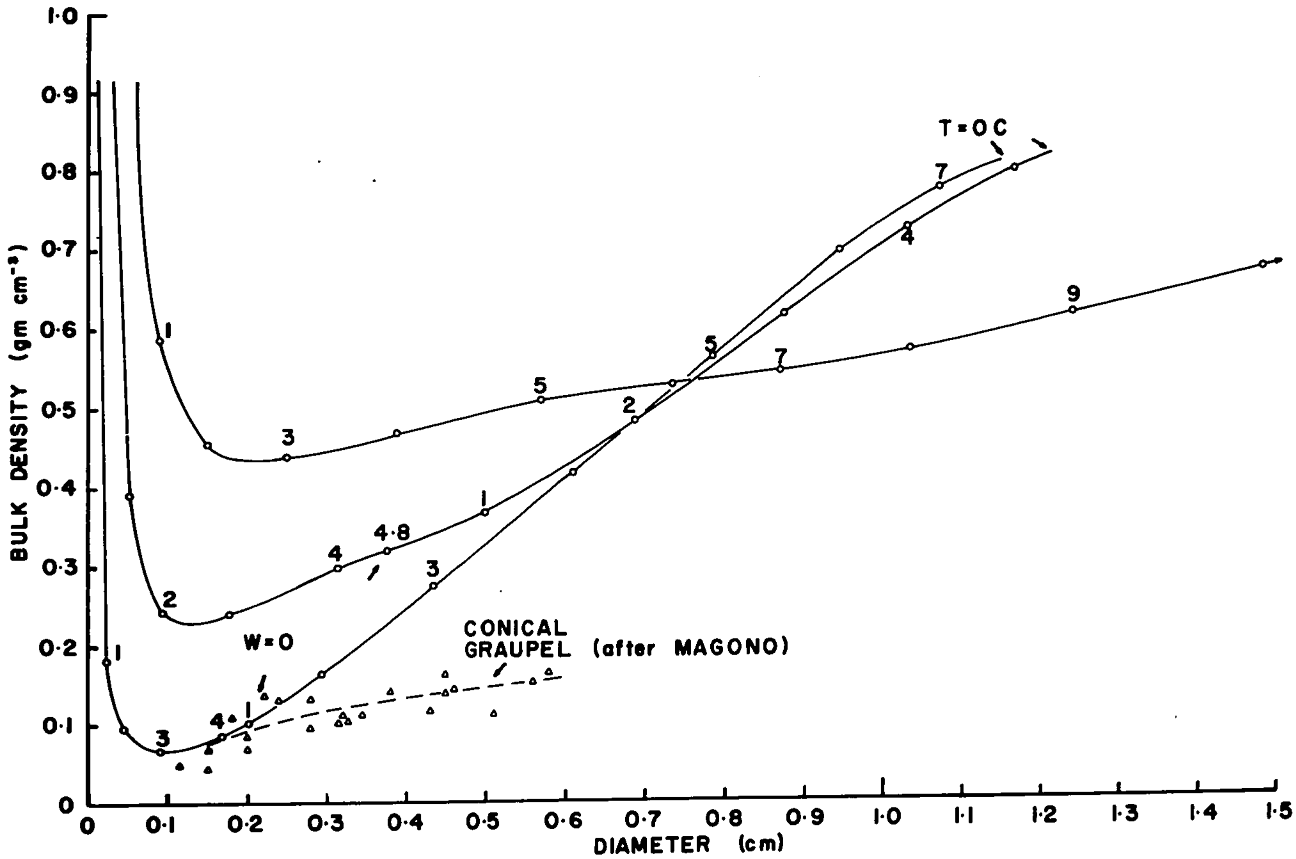

Fig. 9.3.6 Bulk Density vs. Graupel Diameter - 29 June 1967. The bulk density of the growing graupel is shown as a function of diameter with 1 min intervals indicated by small circles. Note the correspondence between the minimum bulk density achieved by the 100 μ graupel and graupel bulk densities observed by Magono.

approximately 0.8 - 0.9 gm cm^{-3}. Densities of centimetric size hailstones, observed at the ground, commonly lie between 0.875 and 0.915 gm cm^{-3} (see Macklin, Strauch and Ludlam; 1963). Measurements of small graupel particles have been performed by Nakaya, Takahashi and Magono on mountain slopes in Japan. The density of these graupel particles, reported by Magono (1954), is as low as 0.04 gm cm^{-3}, with a distinct dependence on the diameter of the graupel. Magono's data are plotted in Fig. 9.3.6 and are seen to be similar to the density curve for the 100 μ graupel. Since information regarding the conditions which existed during Magono's observations is not available, it is not possible to make direct comparisons. Nevertheless, it is an established fact that graupel particles, of the size and density calculated here, do exist in the atmosphere.

Table 9.3.1 Hailstone Parameters at the 0C Level - 29 June 1967

Diameter at -40C cm	Density at -40C gm cm^{-3}	Diameter at 0C cm	Density at 0C gm cm^{-3}	Traverse time (-40C to 0C) min	Water Fraction at 0C %
0.168	0.085	1.15	0.807	7.9	14.7
0.375	0.320	1.21	0.814	5.7	15.0
T = -38.8C	T = -38.8C				
0.803	0.534	3.41	0.911	11.1	24.0

9.3.2 Graupel Growth in the Updraft Core of a High Energy Storm 28 July 1967

The storm of 28 July 1967 was an intense mid-Summer hailstorm which yielded hail larger than golfball size. It was first observed by radar at 1340 MST at a range of 87 km (54 st mi) almost due west of the radar site. This storm progressed east-northeastward with the precipitation area passing 20 km (12.5 st mi) north of the radar site at 1640 MST. The storm existed, as a radar detectable feature, for over 4½ hr, during which time a bounded weak echo region (BWER) was continuously visible between 1511 and 1716 MST. During this two hour period, the storm was in its most intense stage, reaching its maximum height and yielding its largest hail.

There are a number of striking similarities between the storm of 29 June 1967 and the storm of 28 July 1967. As was indicated in Chapters IV and VI, the 29 June 1967 storm existed in a highly sheared environment with strong westerly winds at upper levels and winds from the south and southeast below cloud level. This pattern is also evident in the wind structure on

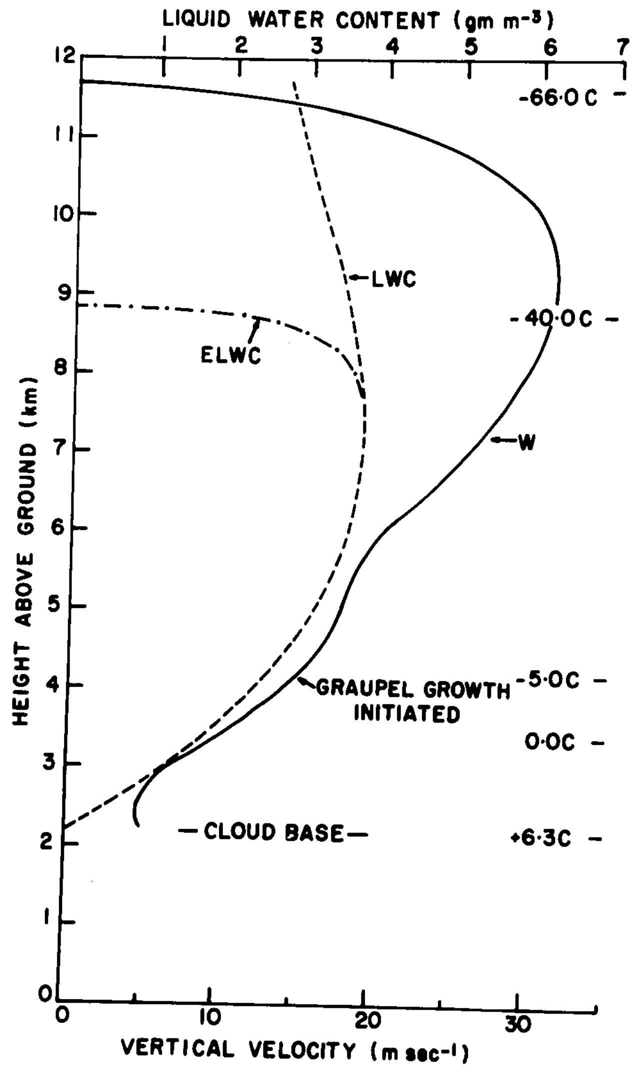

Fig. 9.3.7 Vertical Velocity and Liquid Water Content for a High Energy Storm - 28 July 1967. Vertical velocity (W) and liquid water content (LWC) are illustrated as a function of height. The curve labelled ELWC depicts the water available in supercooled form. Note that the maximum vertical velocity occurs above the -40C level and the storm extends some 3 km higher than the -40C level.

28 July 1967: winds at 2 km were from 180 deg/10 m sec^{-1} and at 9 km from 265 deg/40 m sec^{-1}. The radar structure of the 28 July 1967 storm was also similar with a UWER at low levels (opening on the RH flank of the storm) and a BWER aloft.

The two storms differed in the fact that the storm of 28 July 1967 existed in a much warmer airmass and penetrated the troposphere to a greater

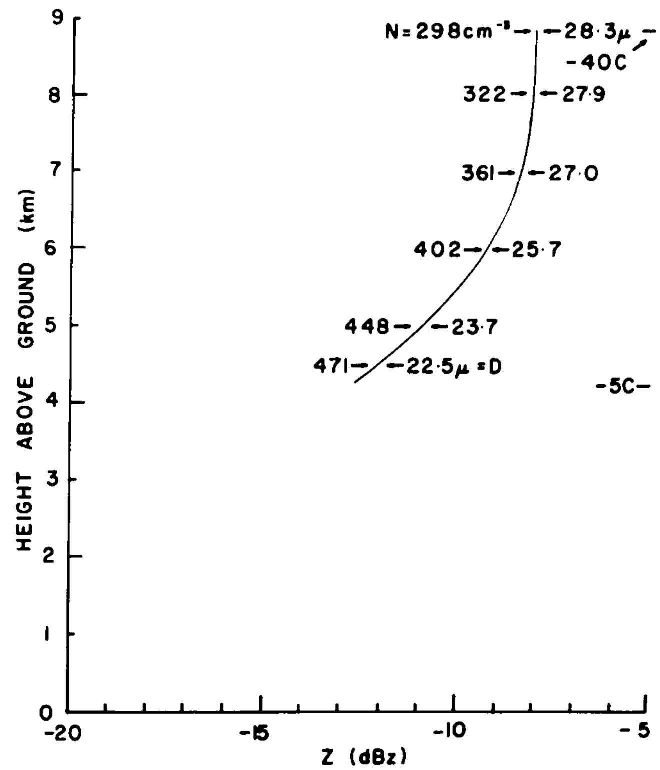

Fig. 9.3.8 Cloud Droplet Concentrations, Diameters and Z Values - 28 July 1967. The number concentrations, diameters and Z values (dBz), calculated using a monodisperse distribution, are shown as a function of height.

degree than did the storm of 29 June 1967. Vertical velocity and liquid water content profiles for the storm of 28 July 1967 (at approximately 1530 MST) are displayed in Fig. 9.3.7. Characteristic of High Energy storms, it was deep (11.7 km) with a powerful updraft (W_{max} > 30 m sec^{-1}). One of the most significant features is that the storm had its top approximately 3 km above the -40C level. Contrasted with the storm of 29 June 1967, hailgrowth could occur in a much smaller portion of the total storm depth.

Since this storm occurred in a relatively warm, moist (T_{sfc} = 28C, ie 82F, T_d = 12C, ie 54F), maritime Pacific airmass, the cloud base droplet concentration has been assumed to be 600 cm^{-3}, based on the estimates quoted in Section 8.2.2. Figure 9.3.8 illustrates that the droplet concentration

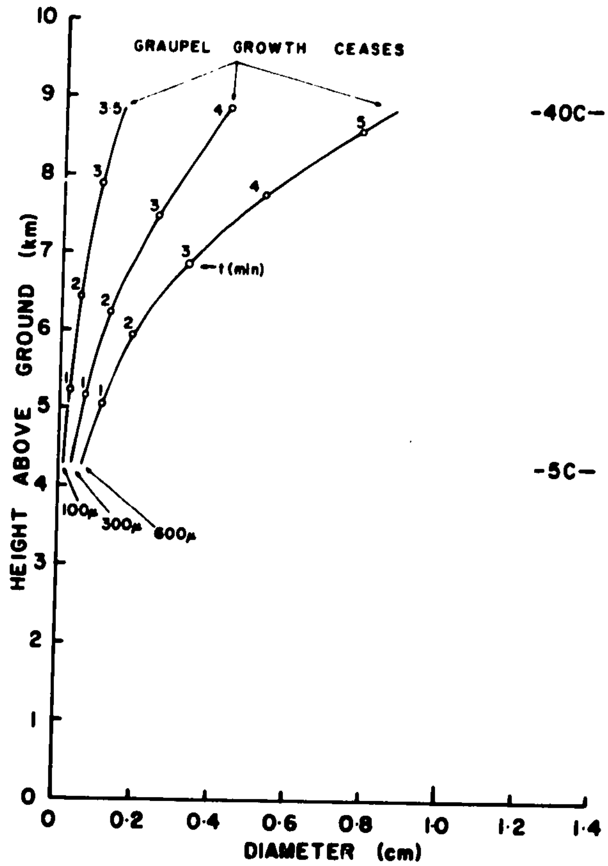

Fig. 9.3.9 Graupel Growth - 28 July 1967. The diameters of growing graupel particles are shown as a function of height. Small circles are located at 1 min intervals. All particles cease to grow while ascending through the -40C level.

decreases from 471 cm^{-3} to 298 cm^{-3} between -5C and -40C. Correspondingly, the monodisperse cloud droplet diameter increases from 22.5 μ to 28.3 μ. Also illustrated in Fig. 9.3.8 is the Z value of the cloud in the updraft core. It is apparent that with a minimum detectable Z_e value of 10 dBz at 16 km (10 st mi) on 28 July 1967, cloud with a calculated Z value of -8 would not be detected and would appear instead as a WER.

Graupel embryos of 100, 300 and 600 μ diameter, introduced into the updraft at -5C, ascend very rapidly to the -40C level. As seen in Fig. 9.3.9, they are unable to grow beyond millimetric size (1.5, 4.3 and 8.6 mm diameter). Even the 600 μ particle (which is unrealistically large) is unable

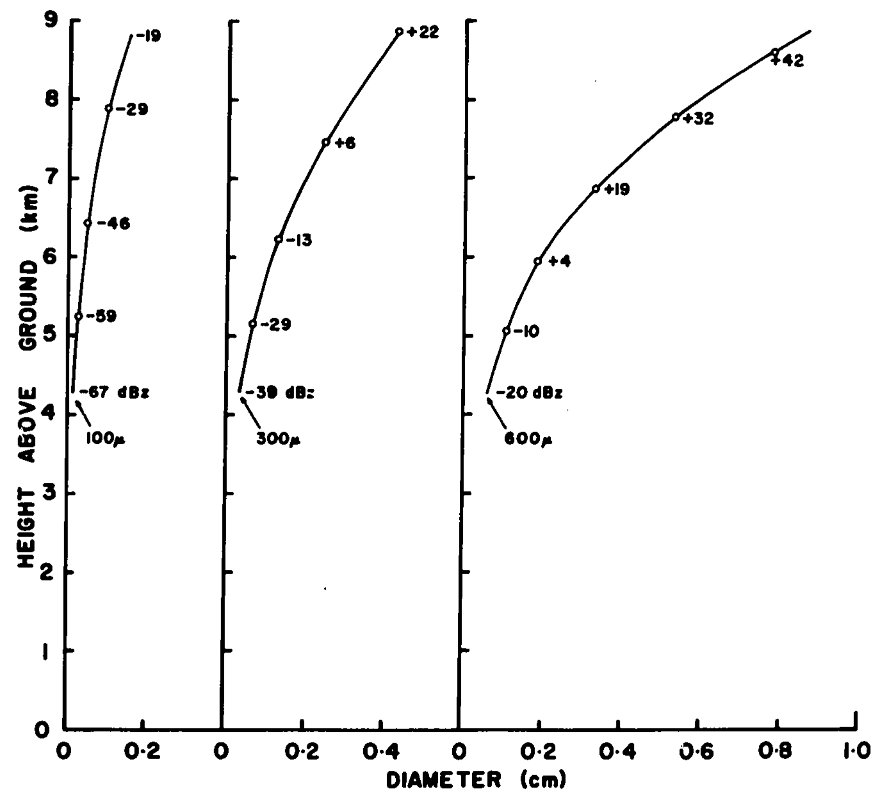

Fig. 9.3.10 Graupel Z values - 28 July 1967. The Z values (dBz) of graupel particles, growing in the updraft core, are shown as a function of height (at 1 min intervals), calculated for a number concentration of 1 m^{-3}.

to grow sufficiently large to descend back through the updraft core. In fact, it would take a hailstone greater than 2.1 cm diameter ($\rho = 0.9$, $C_d = 0.6$) to descend directly back through the updraft core. Thus, graupel particles which grow in the updraft core must be carried into regions of lesser vertical velocity to descend. This also means that the updraft core must be free of hailstones and any increase in the Z_e value over the contribution due to cloud must come from graupel particles.

The Z values, calculated for the graupel particles (assuming N = 1 m^{-3}), are illustrated in Fig. 9.3.10. At 1636 MST, the core of the BWER was at minimum range, 10 km (6 st mi) north of the radar site, resulting in a minimum detectable Z_e value of 6 dBz at this range. Thus, 100 μ graupel

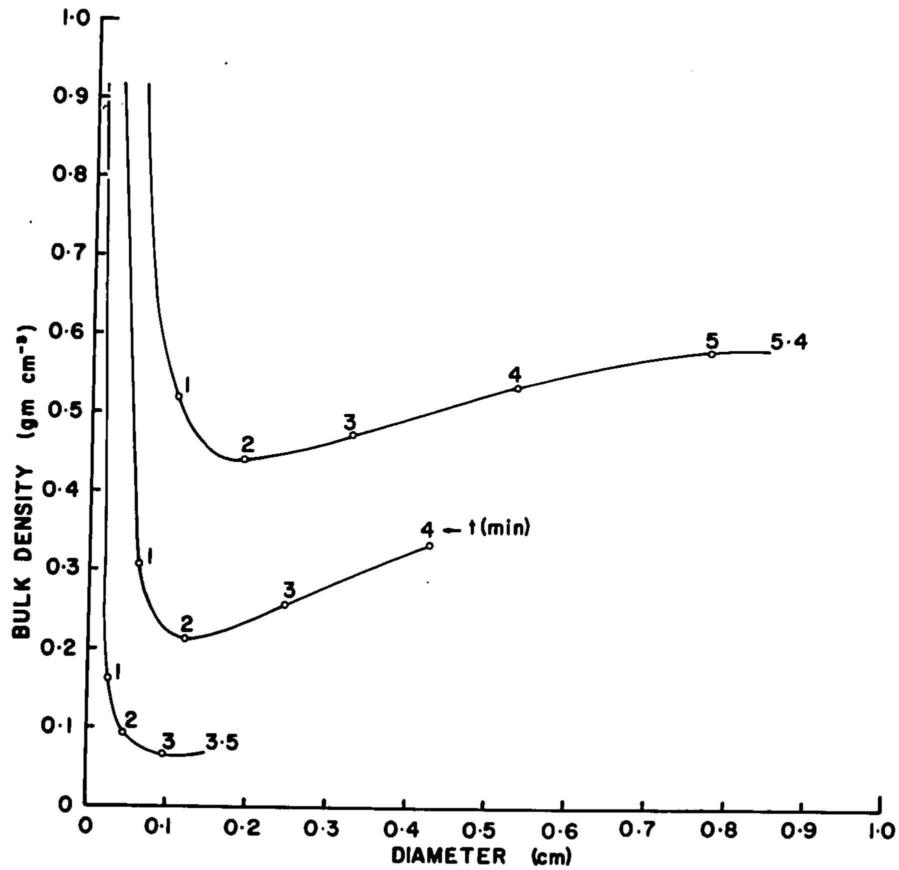

Fig. 9.3.11 Bulk Density vs. Graupel Diameter - 28 July 1967. The bulk density of the growing graupel particles is shown as a function of diameter with 1 min intervals indicated by small circles. Note the similarity with Fig. 9.3.6.

particles could not be detected and the 300 μ particles would only be detected at points higher than 7.5 km. Due to the close range, the maximum height of the radar beam (at 20 deg) was 3.3 km, far below the height at which graupel particles might be detected. At 1702 MST, the core of the BWER was located 29 km (18 st mi) east of the radar site (minimum detectable Z_e = 13 dBz). The BWER closed in above 18 deg elevation or at approximately 8.3 km. Referring to Fig. 9.3.10, the 100 μ graupel particles could not have been detected but the 300 μ graupel particles (with $N = 1\ m^{-3}$) would be detected above 8 km. If 600 μ particles existed (with $N = 1\ m^{-3}$), they would have been detected some 2 km lower. Not knowing the size distribution, it is difficult to make any definite conclusions. However, it may be stated that the Z_e values detected would indicate that 600 μ particles could not exceed approximately 10^{-3} - 10^{-2}, 300 μ particles could not exceed 1 m^{-3} and 100 μ particles could not exceed 10^3 m^{-3} at this point (≈ 8 km AGL) in the updraft core.

The density variation of the graupel particles with diameter (as illustrated in Fig. 9.3.11) is strikingly similar to the previous case. Graupel densities at the -40C level vary between 0.065 and 0.583 gm cm^{-3} for the 100, 300 and 600 μ graupel particles.

Since the graupel particles cannot descend back through the updraft core, a computation was performed assuming their entry into a stagnant cloud (W = 0) with the same liquid water content as the core region. The resulting hailstone diameters, traverse times (from -40C to 0C), and densities are given in Table 9.3.2.

Table 9.3.2 Hailstone Parameters at the 0C Level - 28 July 1967

Diameter at -40C	Density at -40C	Diameter at 0C	Density at 0C	Traverse time (-40C to 0C)	Water Fraction at 0C
cm	gm cm^{-3}	cm	gm cm^{-3}	min	%
0.149	0.065	1.33	0.886	6.7	29.4
0.429	0.334	1.41	0.845	4.9	29.8
0.860	0.583	1.72	0.853	3.8	28.4

It is obvious that these hailstones are substantially smaller than the largest hailstone observed on the ground. A similar computation was made for the 300 μ graupel embryo (0.429 cm diameter at -40C) introducing it into a constane updraft of 8 m sec^{-1}. After 6.85 min, it reached the 0C level with a diameter of 1.95 cm, a density of 0.884 and a liquid water fraction of 34%. It is quite conceivable that trajectories close to the inner core could result in hailstones of 3 - 4 cm diameter, similar to maximum hailstone sizes observed at the surface on 28 July 1967.

9.3.3 Graupel Growth in the Updraft Core of a Low Energy Storm - 27 June 1967

As was shown by the radar study in Chap. V, the storm of 27 June 1967 was quite different from the other storms studied. It existed in an environment with very little wind shear. As a consequence, it stood essentially vertical. This appeared to have a profound effect on the storm behaviour. The storm consisted of a succession of relatively small cells which lasted approximately 25 - 35 min as radar identifiable features. For this reason, it cannot be considered a long-lived steady state storm. The development of precipitation size particles in this storm occurred in 12 - 15 min (as will be seen later in computations in this section) so for the purpose of computing precipitation the updraft may be treated, to a reasonable degree of approximation, as a steady state system.

Figure 9.3.12 illustrates the steady state values of the vertical velocity and liquid water content at approximately 1700 MST. Typical of Low Energy storms, the maximum vertical velocity reached only 16.4 m sec^{-1}. In addition, the maximum storm top was not high, reaching only 7.8 km. This is of considerable significance; the coldest temperature in the computed storm updraft was -37C, permitting hail growth to occur everywhere within the updraft system at temperatures colder than 0C.

Cloud base droplet concentrations have been assumed to be 220 cm^{-3}, resulting (as shown in Fig. 9.1.13) in N = 189 cm^{-3}, D = 26.7 μ at -5C and N = 127 cm^{-3}, D = 36.3 μ at -33.3C. At 1700 MST, the storm was 68 km (42 st mi) southwest of the radar site, resulting in a minimum detectable Z_e value of 35 dBz. It is clear that cloud in the updraft core (Z = -5 dBz) would appear as a weak echo region. Although this storm did not exhibit a

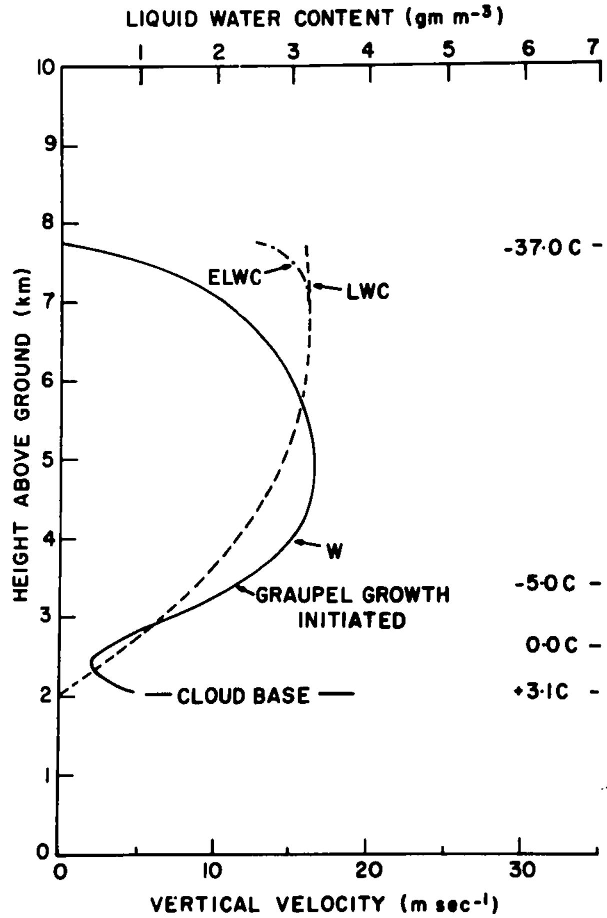

Fig. 9.3.12 Vertical Velocity and Liquid Water Content for a Low Energy Storm - 27 June 1967. Vertical velocity (W) and liquid water content (LWC) are illustrated as a function of height. The curve labelled ELWC depicts the water available in supercooled form. Note that the storm top temperature is only -37C, permitting graupel and hail to grow throughout the entire depth of the storm above the freezing level.

BWER as did the storms of 29 June 1967 and 28 July 1967, a definite UWER was found in the lower portions of the storm during the development of each cell.

Growth curves for particles of 100, 300 and 600 μ diameter are shown in Fig. 9.3.14. The growth pattern exhibited is quite different to the two previous cases. All graupel particles are shown to be able to grow sufficiently large to descend back through the core of the updraft. In 12 - 15 min, hailstones of 1.84 - 2.05 cm diameter reach the freezing level.

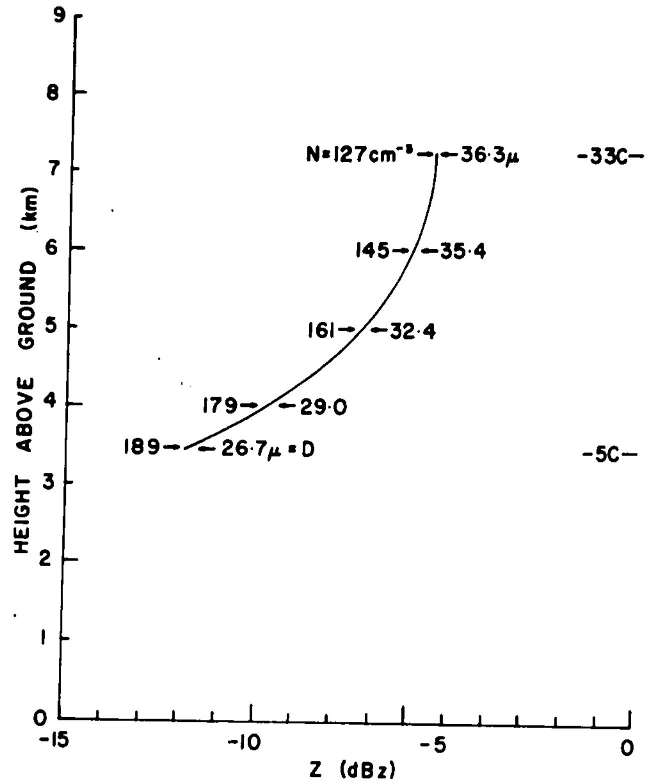

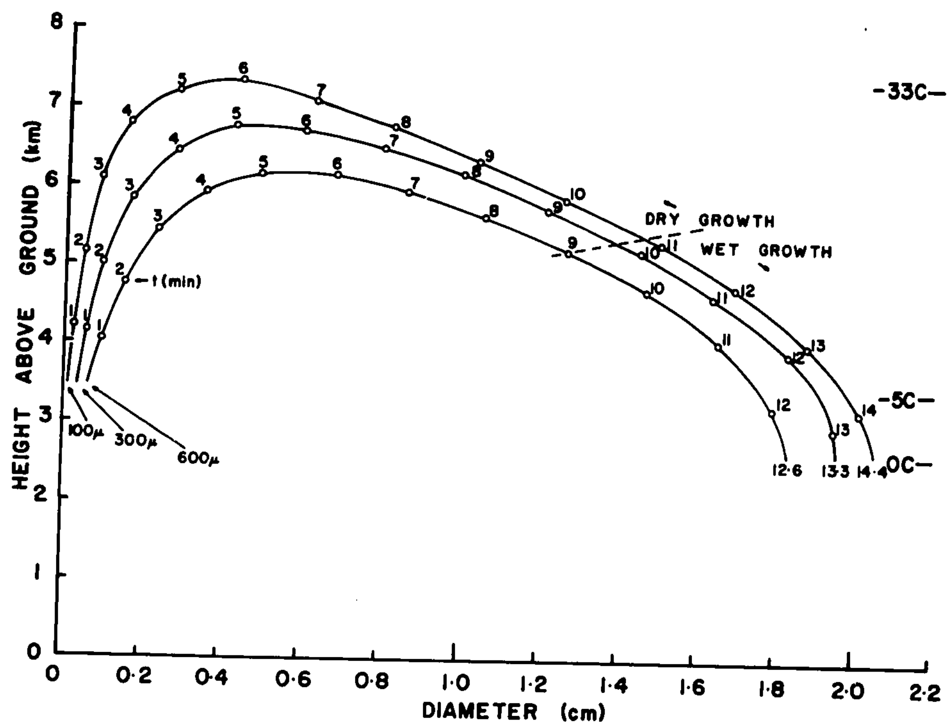

Fig. 9.3.13 (Top) Cloud Droplet Concentrations, Diameters and Z values - 27 June 1967.

Fig. 9.3.14 (Bottom) Graupel and Hail Growth - 27 June 1967. Small circles indicate 1 min intervals. Note that the graupel ascends and descends to reach hailstone size in the updraft.

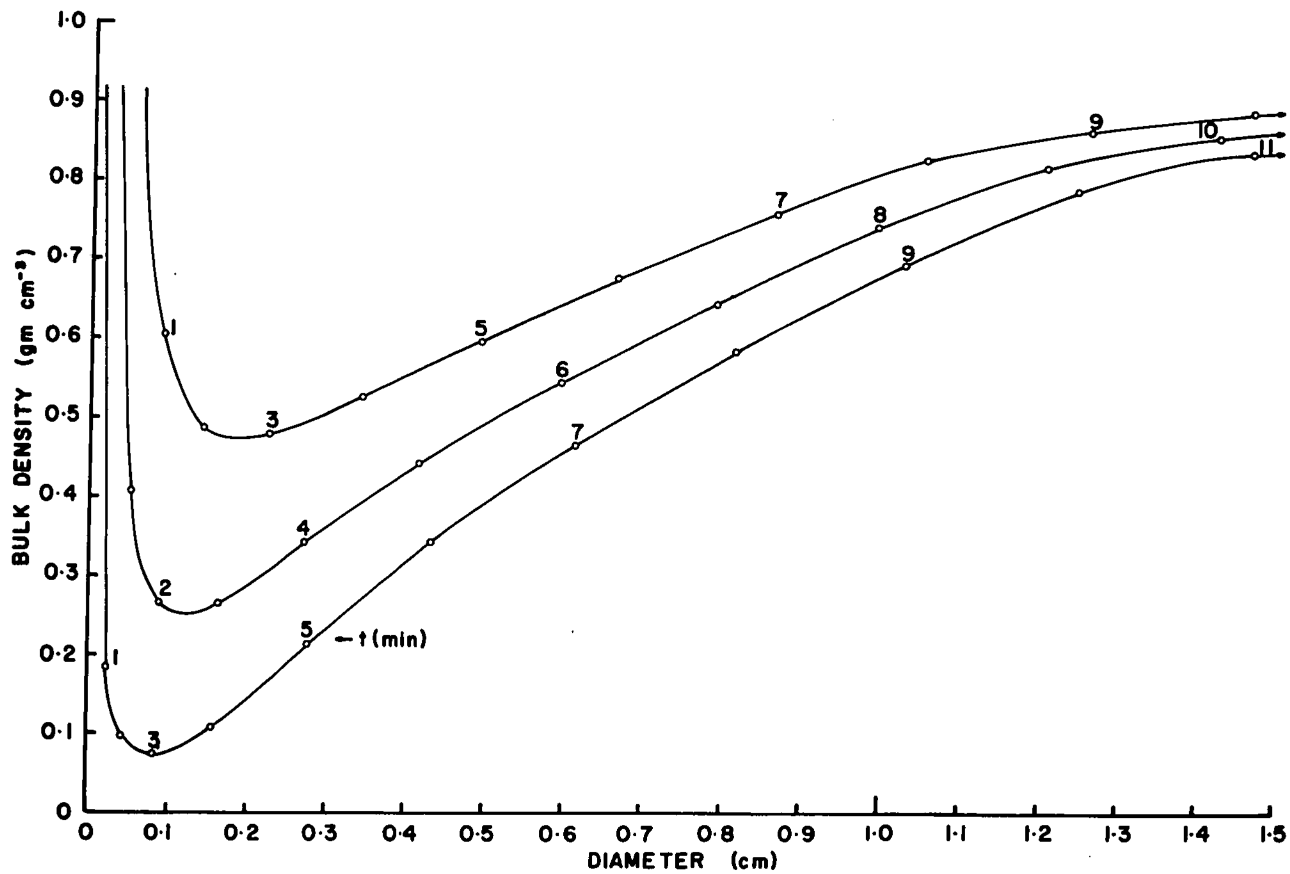

Fig. 9.3.15 Bulk Density vs. Graupel Diameter - 27 June 1967. The bulk density of the growing graupel particles is shown as a function of diameter with 1 min intervals indicated by small circles. Note the similarity to Figs. 9.3.6 and 9.3.11.

This is in reasonable agreement with the pea and grape size hail which was observed at the surface at this stage of the hailstorm. It might be pointed out that the smallest starting particle (100 μ) resulted in the largest hailstone at 0C by virtue of the longer traverse time.

The simple step integration technique employed in this program was tested using data for this case, since the lengthy, uninterrupted traverse is an extreme example and should yield errors as large as might be expected with this computational scheme. Normally, a 5 sec time step was utilized; this was reduced to 1 sec and calculations were performed for the 300 μ graupel particle. The resulting diameter was different by 1.7%, the density by

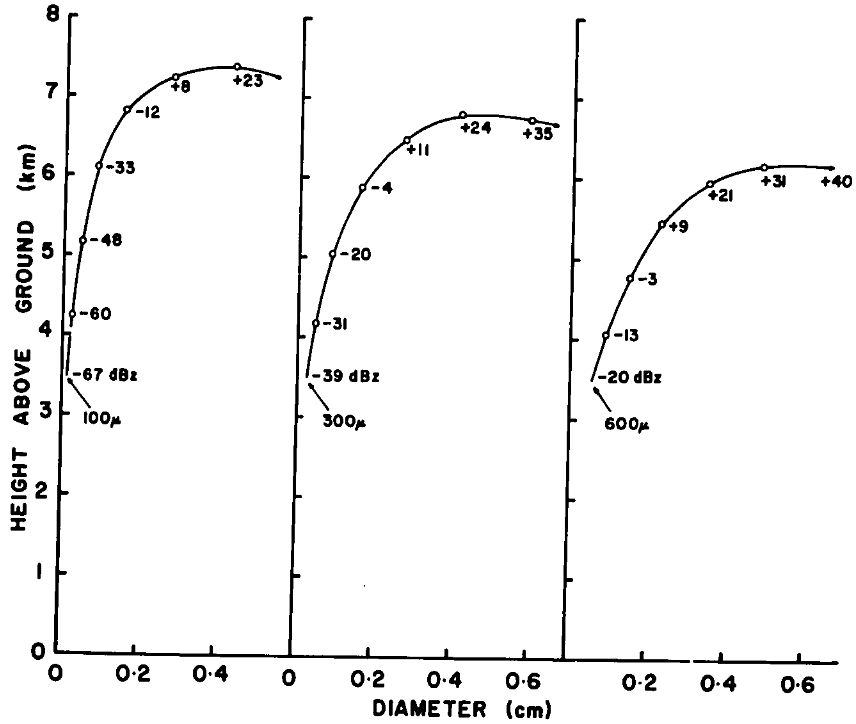

Fig. 9.3.16 Graupel Z values - 27 June 1967. The Z_e values (dBz) of growing graupel and hail particles are shown as a function of height (at 1 min intervals), calculated for a number concentration of 1 m^{-3}.

0.5% and the maximum height by 1.5%, indicating that the computational technique utilized was of sufficient accuracy for the purposes of this study.

With regards to hailstone density, the same pattern was followed as for the previous two cases; initially decreasing, as is illustrated in Fig. 9.3.15, and then increasing to approach (and in one case exceed) the density of pure ice. This is due to the liquid water fraction acquired by the hailstone. Table 9.3.3 gives the resulting diameters, densities and water fraction at 0C.

It is apparent from the computations performed here that graupel particles could grow large enough to descend back through the updraft core. Consequently, a BWER, containing only cloud droplets and small graupel particles, could not exist or could exist only briefly. The radar observations in Chap. V confirm this. It is also difficult to compare steady state Z values shown in Fig. 9.3.16 with observations. With a minimum detectable Z_e value of 35 dBz, it is apparent from Fig. 9.3.16 that echo could not be detected above 6.7 km. Z values computed at 0C (assuming $N = 1\ m^{-3}$), for the three hailstone sizes, ranged from 76 to 79 dBz. Observed values at the surface were 65 dBz < Z_e < 79 dBz, indicating that (as was discussed in Section 9.2.10) the hailstone concentrations at the surface were probably of the order of $10^{-1}\ m^{-3}$.

Table 9.3.3 Hailstone Parameters at the 0C Level - 27 June 1967

Diameter at max. height cm	Density at max. height gm cm^{-3}	Diameter at 0C cm	Density at 0C gm cm^{-3}	Traverse time Max. ht. to 0C min	Water Fraction at 0C %
0.38	0.297	2.05	0.909	8.8	26.4
0.49	0.484	1.96	0.915	7.9	26.3
0.58	0.639	1.84	0.922	7.3	26.7

The picture which emerges for the storm of 27 June 1967 is not unlike the Byers-Braham model. For reasons of simplicity, it has been treated here as a steady state system. Radar observations indicate that the cells were relatively short-lived. The precipitation growth computations reveal that graupel particles could descend back through the updraft core. This would add an additional load to the relatively weak updraft, bringing about its collapse. The radar observations are in accord with this concept.

In summary, it is clear from the computations performed and presented here, that it is possible for giant cloud droplets (100 - 300 μ diameter at -5C) to grow to millimetric size graupel within the updraft core. Based on the estimates of their number concentration ($N = 1\ m^{-3}$), deduced from hailstone observations at the surface, these graupel particles would escape detection by radar to result in a weak echo region. Number concentrations, even several orders of magnitude larger, would still result in a weak echo region in the lower portion of the storm. The existence of a weak echo region is most likely in a High Energy storm, where the strong updraft carries small particles from 0C to -40C in approximately 4 min. This results in very little graupel growth and the graupel particles are prevented from descending back through the updraft by virtue of their low fallspeed. A similar situation exists for Medium Energy storms - although to a lesser degree. Low Energy storms, however, due to their weak updraft and storm top below -40C, permit the ascent and descent of graupel particles within the updraft core. Weak echo regions would be shallow and short-lived unless the updraft were tilted, permitting separate ascent and descent paths.

CHAPTER X

SUMMARY AND CONCLUSIONS

10.1 Summary

Following a brief review of recent and relevant storm studies in Chap. I, Chapters II - V (Part I) consider analyses of the configuration and behaviour of six different storms. Narrow-beam 10 cm radar observations are supplemented by aircraft measurements of updrafts at cloud base, temperature and wind soundings in the vertical and surface observations of the resulting precipitation. Based on these observations and the hypothesis that weak echo regions consist primarily of freshly-formed micron-size cloud droplets in the core of an updraft, a qualitative airflow model has been deduced in Chap. VI (Part II) for each of the storms analyzed.

The radar structures characteristic of these storms (both in plan view and in the vertical) are summarized, with their deduced airflow, in Figs. 10.1.1 - 10.1.3. The items of major importance which are revealed by Fig. 10.1.1 are:

(i) Inflow air originating in the sub-cloud layer has a wind component, relative to the storm, such that it enters the storm through a broad cloud base updraft region.

(ii) Aircraft measurements indicate that the cloud base updraft is smooth and persistent with vertical velocities averaging 4 - 6 m sec^{-1}.

(iii) These cloud base updrafts are found directly beneath weak echo regions which extend upward into the storm.

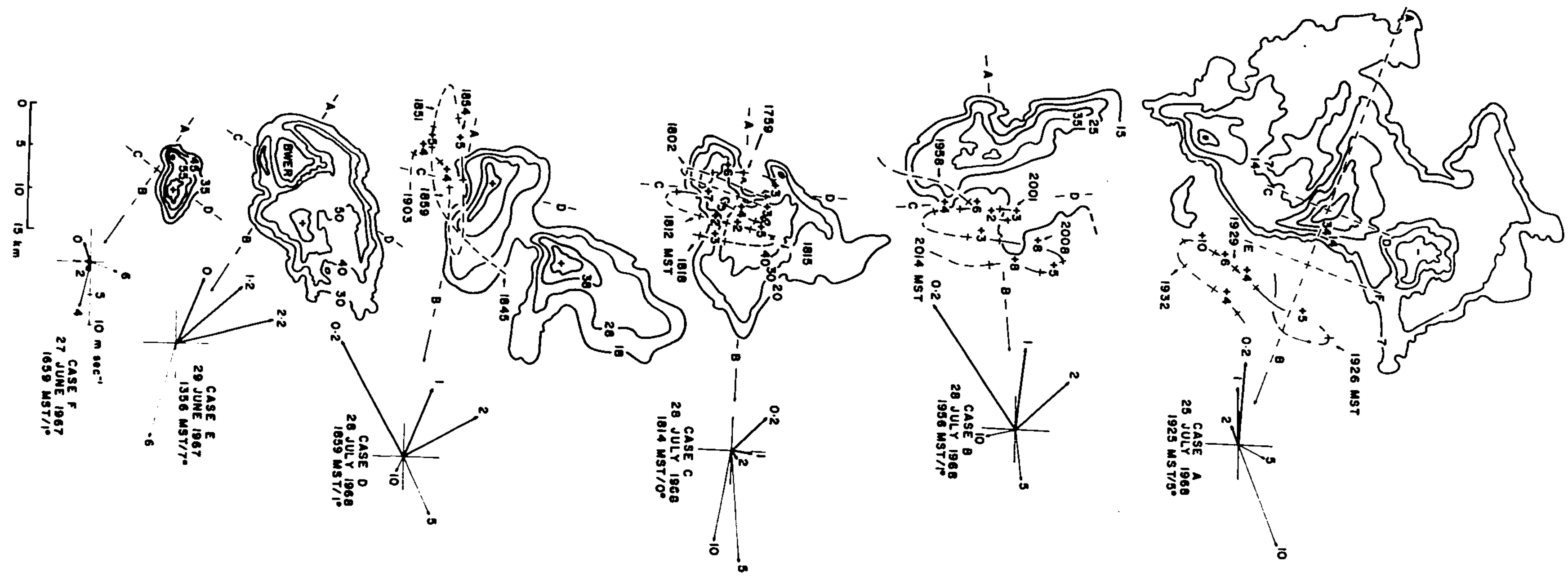

Fig. 10.1.1 PPI Sections, Cloud Base Vertical Velocities and Sub-Cloud Relative Winds for Six Severe Storms. Shown are PPI sections, cloud base vertical velocities and sub-cloud relative winds for the storms analyzed in Chaps. II - V. Z_e contours are labelled in dBz, vertical velocities in m sec^{-1} and heights for winds (shown at end of wind vector) in km AGL. Note that the sub-cloud winds (heavy arrows) relative to the storm are directed toward the WER and cloud base updraft.

Fig. 10.1.2 Schematic Airflow in the Plane of Storm Motion for Six Severe Storms. The airflow in the plane of storm motion is illustrated schematically for six severe storms, each superimposed on the appropriate vertical radar cross-section. Dashed Z_e contours are labelled in dBz. Wind components relative to the storm (in the plane of storm motion) are shown on the left hand side of each figure. Note the different airflow structures in relation to the relative wind.

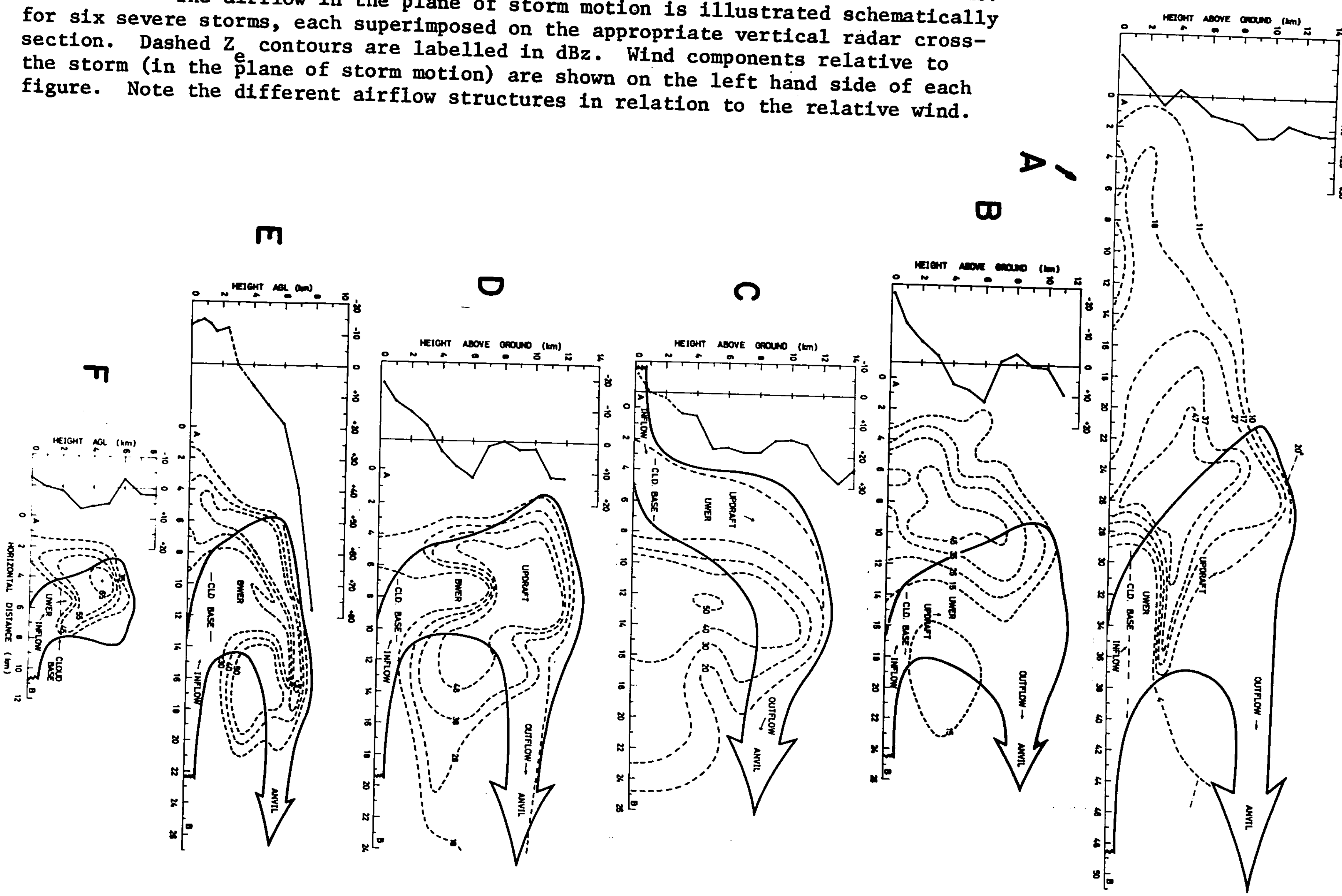

D

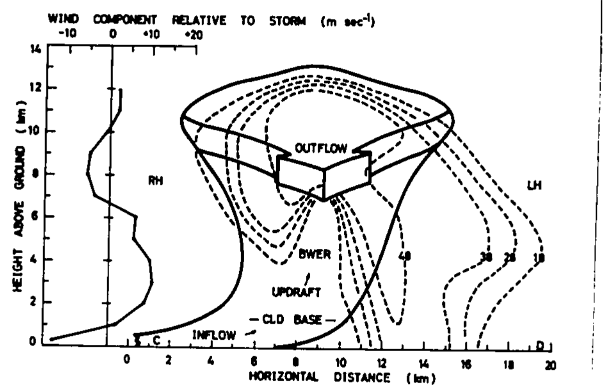

E

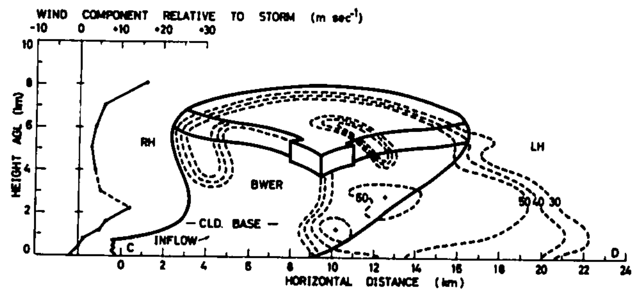

F

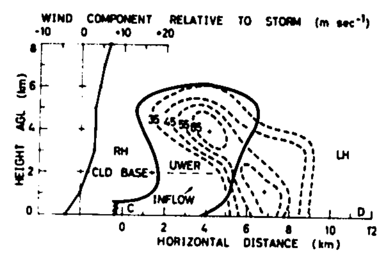

Fig. 10.1.3 Schematic Airflow Normal to the Plane of Storm Motion for Three Storms. The airflow normal to the plane of storm motion is illustrated schematically, for the three storms with significant airflow in this plane, superimposed on the appropriate vertical radar cross-section. The storms are viewed looking upstream. Dashed Z_e contours are labelled in dBz. Wind components relative to the storms (normal to the plane of storm motion) are shown on the left hand side of each figure.

(iv) Z_e maxima (with associated heavy rain and hail at the surface) are found in close proximity to cloud base updrafts and weak echo regions, resulting in strong gradients of reflectivity bordering the weak echo regions.

Based on radar reflectivity structures, qualitative horizontal momentum considerations, the weak echo region hypothesis, calculated vertical velocities within the updraft core and the environmental wind structure relative to the storm, schematic airflow patterns, in the plane and normal to the plane of storm motion, have been deduced as shown in Figs. 10.1.2 and 10.1.3. These two figures display the following concepts:

(i) The inflow air above cloud base penetrates upward through the weak echo region toward the radar storm top.

(ii) The radar storm top is the highest point in the storm to which radar-detectable precipitation particles are carried.

(iii) The updraft path is influenced by the initial horizontal momentum of the inflow air, the environmental wind relative to the storm, and the vertical velocity of the updraft.

(iv) Upon decelerating near the storm top, the updraft acquires the horizontal velocity of the environment and typically flows away from the storm in the downstream direction.

(v) Z_e maxima and strong reflectivity gradients, mentioned in conjunction with Fig. 10.1.1, appear to originate from the growth of large precipitation particles in the upper reaches of the updraft in close proximity to the weak echo region.

The resulting airflow structures, exhibited in Figs. 10.1.2 and 10.1.3, are consistent with one another in that weak echo regions (suggested to be due to updrafts) are found in close proximity to Z_e maxima (suggested to be due to the growth of large precipitation particles on the updraft periphery) in each storm. These two features are found in association with one another in a variety of different configurations. However, in each instance, the deduced airflow agrees with the location of updraft origin and with the forces exerted on the airflow by the relative environmental wind. Both two and three-dimensional airflow structures have been found, and inflow regions have been detected (in separate storms) on the downwind, right hand and upwind sides of the storms considered.

The existence of a broad, continuous flow updraft and associated weak echo regions in the storms studied here has lead to the formulation of a loaded moist adiabatic (LMA) vertical velocity model in Part III (Chap. VII) of this thesis. This model yields cloud temperatures, liquid water contents, vertical velocities and storm tops which represent conditions within the updraft core. The resulting calculated maximum storm tops have been compared with maximum radar storm tops for 29 hailstorms and found to agree within the limits of observational error in 79% of the cases studied. Vertical velocities, liquid water contents and cloud temperatures for storm cases A - F (see Figs. 10.1.1 - 10.1.3), computed with the LMA model, are illustrated in Fig. 10.1.4. These data are particularly useful in describing a growth environment for graupel and hail particles within the updraft core. However, they have also been useful in deducing storm airflow structures. In addition, the characteristic updraft parameters constitute a unique means of classifying severe storms. A distinct pattern of relationships between maximum storm energy, maximum vertical velocity, maximum storm top and maximum observed hail size has been revealed by the study of 29 hailstorms. In essence, the greater the maximum storm energy, the higher are the computed values of maximum vertical velocity, maximum liquid water content and maximum storm top and the larger

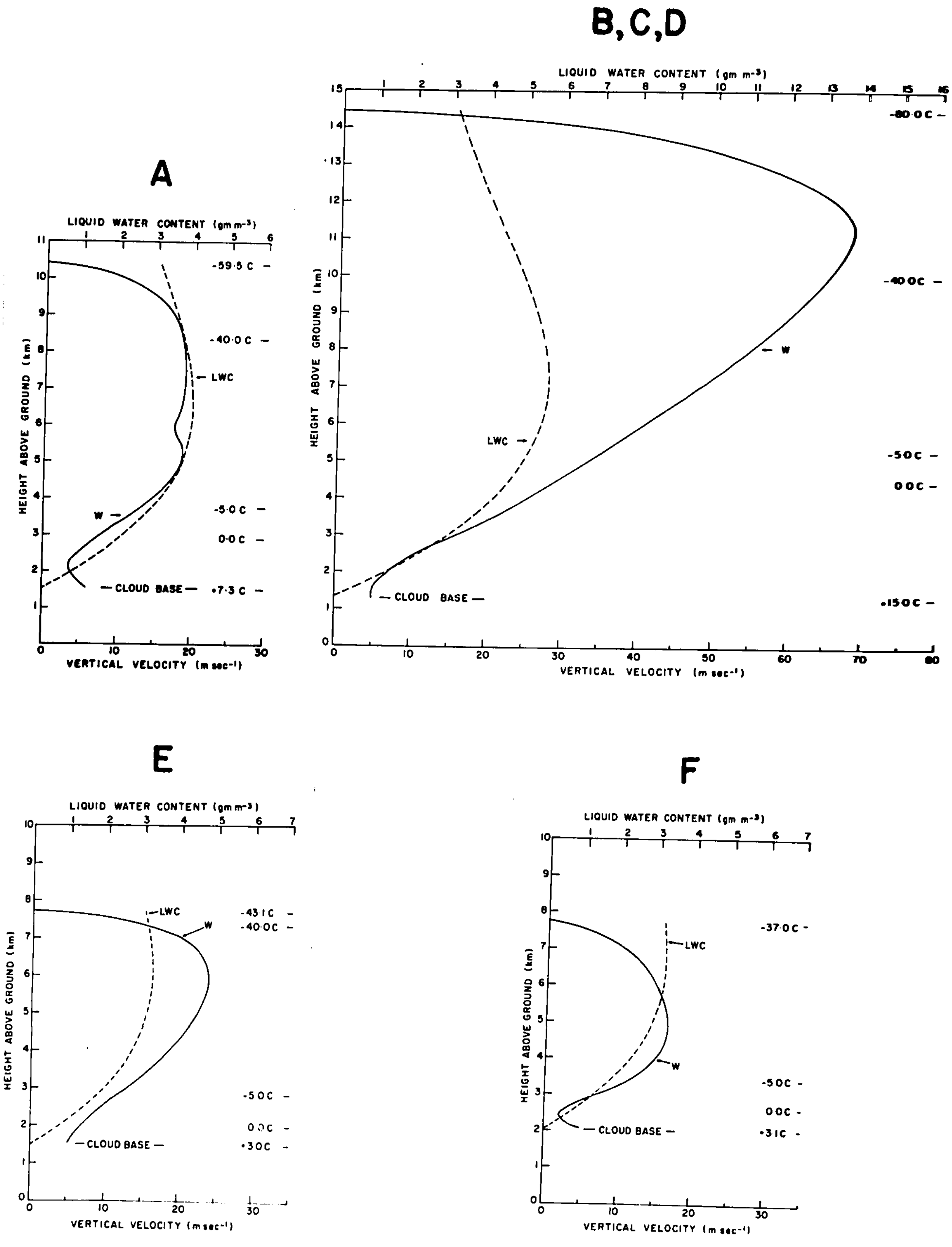

Fig. 10.1.4 Vertical Velocities, Liquid Water Contents and Cloud Temperatures for Six Severe Storms. The LMA model results for severe storm cases A - F are shown above. Note the very high vertical velocity associated with cases B, C and D. Also note that case F (Low Energy storm) is the only storm whose updraft exists entirely below the -40C level.

the maximum observed hail size at the surface.

In Chaps. VIII and IX (Part IV), a review of observed cloud condensation nuclei spectra, cloud droplet spectra, updraft velocities and cloud droplet growth processes in convective clouds, with accompanying calculations and arguments, has resulted in the following items of importance:

(i) Cloud droplet number concentrations are determined within a few hundred meters of cloud base.

(ii) Cloud droplet number concentrations for Alberta convective clouds (cloud base updraft assumed 5 m sec^{-1}) are estimated to average 220 cm^{-3} with lower and upper bounds of 130 cm^{-3} and 600 cm^{-3}. These estimates are relatively insensitive to changes in cloud base vertical velocities.

(iii) Cloud droplet spectra observed just above cloud base are narrow ($\sigma/\overline{D}$ typically 0.10 - 0.20). Considering growth by condensation alone (within a rising air parcel), it is evident that radial growth proceeds most rapidly for small droplets, resulting in a cloud droplet spectrum which becomes increasingly narrow with height above cloud base.

(iv) Traverse times (between cloud base and -40C) for an air parcel in an updraft core are of the order of 400 sec. Recent theoretical and experimental studies of cloud droplet growth by coalescence processes indicate that coalescence growth processes do not significantly affect the cloud droplet population in the first 600 sec.

Taking these factors into consideration, a monodisperse cloud droplet model has been formulated to describe how the liquid water content within the updraft core is distributed among the cloud droplet population. After specifying the total number of cloud droplets at cloud base, the droplet number per unit volume is modified by taking account of changes in air parcel density with height. Knowing the liquid water content, droplet diameters and Z values can be readily obtained.

The results of the LMA vertical velocity model and the cloud droplet model describe a growth environment within the updraft core. Growth of cloud droplets to raindrop size by coalescence within the updraft core, between cloud base and the freezing level, is highly improbable, as is the penetration inward to the updraft axis by small hail or graupel particles during a recycling stage. Consequently, the most rapid growth process which might occur within this central updraft region is the growth of giant cloud droplets by an ice accretion process above the 0C level. The growth of such particles has been calculated using a graupel growth model formulated specifically for this purpose. In brief, the major features of this model are as follows:

(i) The drag coefficient appropriate to a smooth sphere, of the same diameter and density as the graupel particle, is computed and from it a corresponding fallspeed is derived.

(ii) The Langmuir collection efficiency is computed appropriate to the collector and droplet diameters.

(iii) The fraction of liquid water available in supercooled form is computed using a freezing law derived from ice nuclei measurements for Alberta hailstorm precipitation.

(iv) Graupel growth due to both accretion and sublimation processes is calculated using the information outlined above.

(v) A heat balance (neglecting the finite heat capacity of the graupel) is maintained and from it a graupel surface temperature is determined. Both dry and wet growth modes are permitted.

(vi) Utilizing the fallspeed, droplet size and graupel surface temperature, the density of the accreting ice is determined and the resulting bulk density of the graupel is calculated.

(vii) During wet growth, all liquid water accreted is assumed to remain attached to the hailstone and the resulting liquid water fraction is calculated.

Based on hailstone number concentrations at the surface, graupel growth calculations have been performed using a number concentration of 1 m^{-3} for starting particles of 100, 300 and 600 μ diameter using data for specific storms. An analysis of the results for typical Low, Medium and High Energy storms has been performed in Chapter IX. Summarizing these results, it is clear that:

(i) Frozen giant cloud droplets can grow from 0.1 mm (100 μ) to ≈ 2 - 4 mm diameter while ascending from the -5C to -40C level in the updraft core. During this ascent stage, the low graupel fallspeed and low graupel surface temperature result in accreted ice of low density.

(ii) The descent path of the millimetric graupel particle is determined to a great extent by the graupel fallspeed attained beneath the -40C level. In the case of the High Energy storm, it is virtually impossible for the graupel particle to grow sufficiently rapidly to attain a fallspeed greater than the updraft prior to reaching the -40C level. Consequently, the updraft core of a quasi-steady state, High Energy storm is devoid of precipitation larger than millimetric graupel particles. Computations have shown that the radar reflectivity within this updraft core is typically lower than the minimum

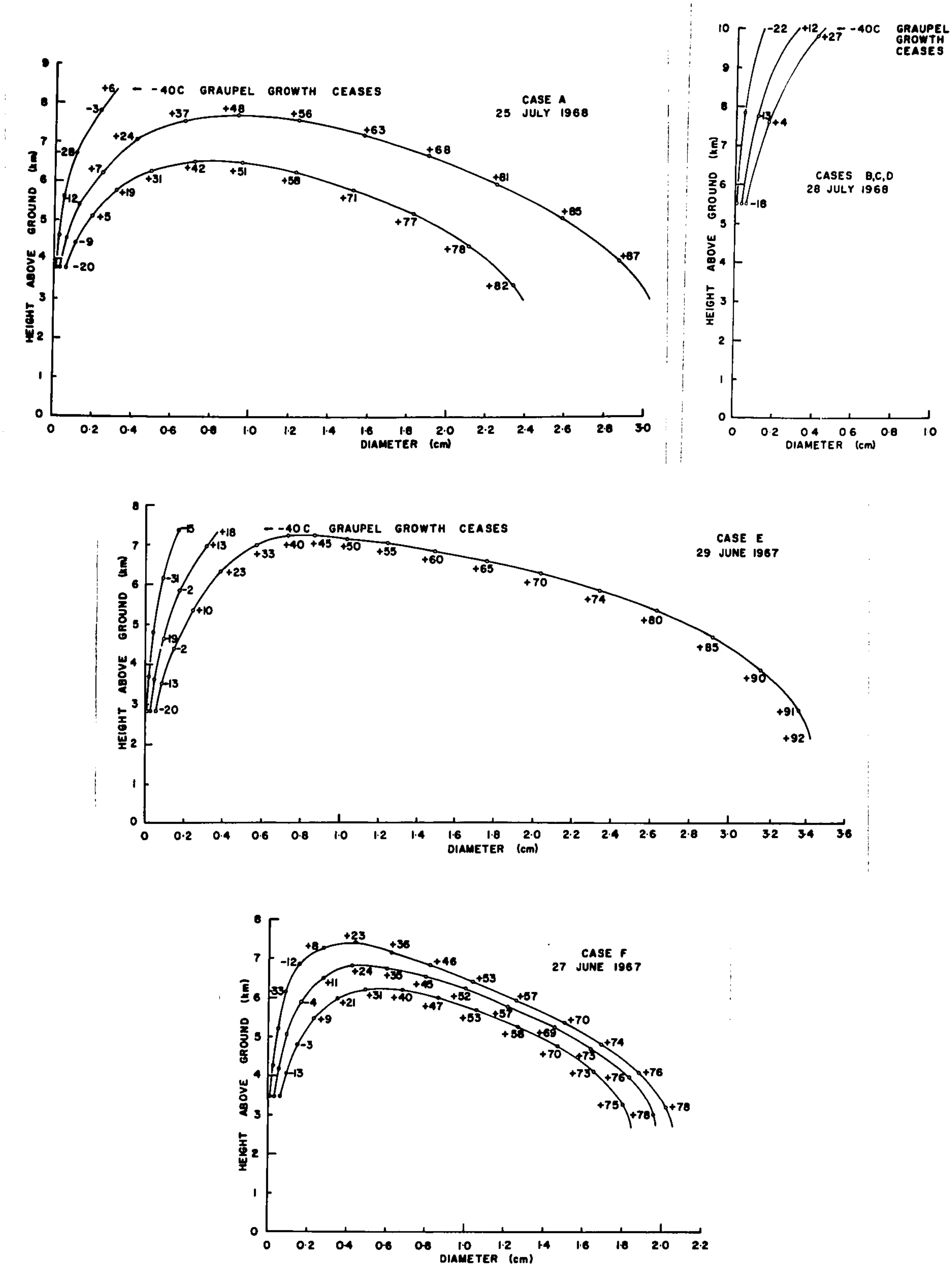

Fig. 10.1.5 Graupel Growth and Radar Reflectivity for Six Severe Storms. The diameter of the graupel or hailstone is shown as a function of time and height within the updraft. Each small circle is placed at a one minute time interval. Figures plotted alongside these minute marks are Z values calculated for a particle concentration of 1 m^{-3}. Note the rapid ascent and restricted growth of the 100 μ starting particles in all cases but Case F.

detectable reflectivity of a 10 cm radar; that is - a weak echo region.

(iii) On the other hand, Low Energy storms have tops lower than -40C so that it is possible for graupel particles to attain a fallspeed of sufficient magnitude to descend back through the updraft. In doing so, the radar reflectivity of these particles is sufficiently high that they can be detected by radar. Weak echo regions in Low Energy storms would be expected only during early developing stages unless a tilted airflow structure prevented graupel particles from descending back through the updraft core.

(iv) Medium Energy storms behave in a fashion not unlike High Energy storms. Unless particles larger than 300 μ exist at -5C, the behaviour of graupel particles in the updraft core would be similar to that of the High Energy storm. Observational evidence indicates that giant cloud droplets larger than 300 μ do not exist at -5C. Consequently, Medium Energy storm updraft cores would appear as weak echo regions.

Specifically, the graupel growth and reflectivity data, illustrated in Fig. 10.1.5, show that storm cases A, B, C, D and E would exhibit well-developed weak echo regions unless giant cloud droplets 300 μ and larger were available at -5C. As Figs. 10.1.1 - 10.1.3 illustrate, weak echo regions were indeed observed in these storms. Conversely, Case F (Fig. 10.1.5) shows that a weak echo region could exist only for a short period during the developing stages of the storm. The radar analysis in Chap. V and Figs. 10.1.1 - 10.1.3 confirm this behaviour.

Sample calculations, performed external to the updraft core, suggest that the millimetric particles found near the storm top can descend through an updraft region, in close proximity to the weak echo region while growing to hailstone sizes comparable to those observed at the surface. This finding is in excellent agreement with the radar-observed Z_e maxima found bordering weak echo regions.

10.2 Conclusion

An analysis of radar and supplementary observations for six severe storm structures has revealed three-dimensional radar configurations which differ vastly. Nevertheless, these storms were characterized by a common element - a region of low equivalent radar reflectivity factor, designated a weak echo region. Utilizing aircraft-measured vertical velocities at cloud base in conjunction with radar observations, it has been established that these weak echo regions are found in association with, and extending aloft above, the broad, smooth, persistent cloud base updraft. Using the hypothesis that these weak echo regions consist primarily of freshly-formed micron-size cloud droplets in the core of an updraft, the weak echo region structure has been used, with various other pieces of evidence, to deduce an airflow model for each of the storms studied. In view of the consistency, both individually and collectively, among the resulting six storm models, there is good reason for confidence in their validity. Although it is unlikely that these models encompass all modes of severe storm operation in Alberta, they are indeed representative of a large portion of Alberta severe storms. As such it is concluded that these storm models and the principles used to derive them, will be of considerable value in the study, interpretation and understanding of similar severe storms.

The existence of a smooth, persistent updraft at the cloud base of a severe storm, sufficiently broad that it precludes the effects of entrainment at its inner core, has led to the formulation of a loaded moist adiabatic (LMA) updraft model. As a result of the consistent capability of this model to compute a maximum storm top which is in close agreement with maximum radar observed storm tops, it is concluded that there exists an unmixed inner core within the severe storm updraft with adiabatic properties. The resulting cloud temperatures, vertical velocities and liquid water contents are, therefore, considered to be reliable estimates of the properties within the updraft core. It has also been shown that characteristic values of these properties can be used in a unique manner to typify and thus compare individual severe storms.

However, of equal importance to this study is the fact that the results of the LMA model essentially describe a precipitation growth environment within the updraft core of a severe storm. Based on observational evidence and theoretical computations, it has been concluded that, within the updraft core, the growth by coalescence processes is of secondary importance. Since the condensation growth process dominates, the resulting cloud droplet spectrum must be narrow and is approximated to a reasonable degree of accuracy by a monodisperse cloud droplet model.

It has been deduced that the only particles within this updraft core which can grow to precipitation size are giant cloud droplets. Using a graupel growth model formulated for this task, giant cloud droplets were grown within the updraft core of specific storms. From the results, it is concluded that weak echo regions would be found to exist in quasi-steady state High and Medium Energy storms, and would be found for brief periods during the development of Low Energy storms. This is in excellent agreement with the observed radar structure and behaviour of the storms studied in this thesis, which further verifies the validity of the Weak Echo Region Hypothesis. In conjunction with the updraft core, the growth of graupel particles to substantial hailstone size computed external to, but in close proximity with the updraft core, is in agreement with the Z_e maxima observed close to the weak echo region in the storms studied.

From observational and computational evidence, there has emerged a consistent model of the Alberta hailstorm. Being capable of operating in numerous different configurations, it is nevertheless dominated by an updraft whose inner core gives rise to a weak echo region composed of micron-size cloud droplets and millimetric graupel particles. Bounding this updraft, on one or more sides, exists a Z_e maximum, the result of graupel particles growing to hailstone size during descent, in close proximity to the updraft core. In total, this is a model which should be of considerable assistance in future studies designed to bring about greater understanding of the Alberta hailstorm.

REFERENCES

Auer, A.H., 1967: A cumulus cloud design for continental airmass regimes. J. des Rech. Atmos., 3, 91-100.

_____, and W. Sand, 1966: Updraft measurements beneath the base of cumulus and cumulonimbus clouds. J. Appl. Meteor., 5, 461-466.

_____, and J.D. Marwitz, 1968: Estimates of air and moisture flux into hailstorms on the high plains. J. Appl. Meteor., 7, 196-198.

_____, D.L. Veal and J.D. Marwitz, 1969: Updraft deterioration below cloud base. Proc. Sixth Conf. on Severe Local Storms, Amer. Meteor. Soc., Chicago, 16-19.

Bates, F.C. and C.W. Newton, 1965: The forms of updrafts and downdrafts in cumulonimbus in a sheared environment. Address to National Meeting on Cloud Physics and Severe Local Storms, Reno, mimeographed, 9pp. plus figs.

Battan, L.J., 1963: A survey of recent cloud physics research in the Soviet Union. Bull. Amer. Meteor. Soc., 44, 757-758.

Berry, E.X., 1967: Cloud droplet growth by collection. J. Atmos. Sci., 24 688-701.

Booker, D.R., D.C. Hall, H.E. Hart and L.W. Cooper, 1969: Evidence of severe storm rotational characteristics from super-pressure balloon trajectories. Proc. Sixth Conf. on Severe Local Storms, Amer. Meteor. Soc., Chicago, 32-37.

Browning, K.A., 1963: The growth of large hail within a steady updraft. Quart. J. Roy. Meteor. Soc., 89, 490-507.

_____, 1965: A family outbreak of severe local storms - a comprehensive study of the storms in Oklahoma on 26 May 1963. Part I, AFCRL -65-695(1) Special Report No. 32, 346pp.

_____, and F.H. Ludlam, 1960: Radar analysis of a hailstorm. Tech. Note No. 5, Contract AF61(052)-254, Dept. of Meteor., Imperial College, London, 109pp.

_____, and _____, 1962: Airflow in convective storms. Quart. J. Roy. Meteor. Soc., 88, 117-135.

_____, and R.J. Donaldson, 1963: Airflow and structure of a tornadic storm. J. Atmos. Sci., 20, 535-545.

_____, F.H. Ludlam and W.C. Macklin, 1963: The density and structure of hailstones. Quart. J. Roy. Meteor. Soc., 89, 75-85.

Byers, H.R. and R.R. Braham, 1949: The Thunderstorm, U.S. Govt. Printing Office, Washington, 287pp.

Chisholm, A.J., 1966a: Small-Scale Radar Structure of Alberta Hailstorms. M.Sc. thesis, Dept. of Meteor., McGill University, Montreal, 73pp.

_____, 1966b: Small-scale radar structure of Alberta hailstorms. Proc. Twelfth Conf. on Radar Meteor., Amer. Meteor. Soc., Norman, 339-341.

_____, 1967: Small-scale radar structure of Alberta hailstorms. Sci. Report MW-49, Stormy Weather Group, McGill University, Montreal, 81pp.

_____, 1968: Observations by 10 cm radar of an Alberta hailstorm in a sheared environment. Proc. Thirteenth Radar Meteor. Conf., Montreal, 82-87.

_____, and C. Warner, 1969: Radar and stereo cloud photo measurements. Part II - The hailstorm of 29 June 1967. Sci. Report MW-59, Stormy Weather Group, McGill University, Montreal, 8-16.

Cunningham, R.M., 1959: Hailstorm structure viewed from 32,000 feet. Physics of Precipitation, Amer. Geophys. Union Monograph No. 5, 325-332.

Donaldson, R.J., 1962: Radar observations of a tornado thunderstorm in vertical section. National Severe Storms Project, Report No. 8, U.S. Weather Bureau, Washington, 21pp.

Douglas, R.H., 1957: Snow Cells and Showers. Ph.D. thesis, Dept. of Meteor., McGill University, Montreal, 161pp.

_____, 1963: Size distribution of Alberta hail samples. Sci. Report MW-36, Stormy Weather Group, McGill University, Montreal, 55-70.

_____, 1965: Size distributions of Alberta hail samples. Sci. Report MW-42, Stormy Weather Group, McGill University, Montreal, 43-48

East, T.W.R., 1956: Precipitation mechanisms in convective clouds. Sci. Report MW-22, Stormy Weather Group, McGill University, Montreal, 74pp.

English, M., 1969: Hailgrowth in the storm of 29 June 1967. Sci. Report MW -59, Stormy Weather Group, McGill University, Montreal, 28-37.

Fankhauser, J.C., 1967: Some physical and dynamical aspects of a severe right moving cumulonimbus. National Severe Storms Lab., Tech. Memo. No. 32, Norman, 11-32.

Fletcher, N., 1962: The Physics of Rainclouds. Cambridge University Press, Cambridge, 133-134.

Fujita, T. and H.R. Byers, 1962: Model of a hail cloud as revealed by photogrammetric analysis. Nubila, 1, 85-106.

_____, and H. Grandoso, 1968: Split of a thunderstorm into anticyclonic and cyclonic storms and their motion as determined from model experiments. J. Atmos. Sci., 3, 416-439.

Goldstein, S., 1938: Modern Developments in Fluid Dynamics. Clarendon Press, Oxford, p. 15.

Gunn, R. and G.D. Kinzer, 1949: The terminal velocity of fall for water drops in air. J. Meteor., 6, p. 243.

Haglund, G.T., 1969: A study of a severe local storm of 16 April 1967. National Severe Storms Lab., Tech. Memo. No. 44, Norman, 54pp.

Hammond, G.R., 1967: Study of a left-moving thunderstorm of 23 April 1964. National Severe Storms Lab., Tech. Memo. No. 31, Norman.

Hart, H.E. and L.W. Cooper, 1968: Thunderstorm airflow studies using radar transponders and super-pressure balloons. Proc. Thirteenth Weather Radar Conf., Amer. Meteor. Soc., Montreal, 196-201.

Henry, C.D., 1964: High radar echoes from Alberta thunderstorms. Sci. Report MW-38, Stormy Weather Group, McGill University, Montreal, 105-126.

Hitschfeld, W., 1959: The motion and erosion of convective storms in severe vertical wind shear. Sci. Report MW-29, Stormy Weather Group, McGill University, Montreal, 48pp.

List, R., 1963: General heat and mass exchange of spherical hailstones. J. Atmos. Sci., 20, 189-197.

_____, 1965: The mechanism of hail formation. Proc. Intn'l. Conf. on Cloud Physics, Tokyo, 481-491.

_____, R.B. Charlton and P.I. Buttulus, 1968: A numerical experiment on the growth and feedback mechanisms of hailstones in a one-dimensional steady-state model cloud. J. Atmos. Sci., 25, 1061-1074.

List, R.J., 1958: Smithsonian Meteorological Tables. Sixth Revised Edition, Smithsonian Institution, Washington, 318-322.

Ludlam, F.H., 1963: Severe local storms: a review. Meteor. Monograph No. 5, Amer. Meteor. Soc., Boston, 1-30.

MacCready, P.D. and D.H. Takeuchi, 1968: Precipitation initiation mechanisms and droplet characteristics of some convective cloud core. J. Appl. Meteor., 7, 591-602.

Macklin, W.C., 1962: The density and structure of ice formed by accretion. Quart. J. Roy. Meteor. Soc., 88, 30-53.

_____, 1963: Heat transfer from hailstones. Quart. J. Roy. Meteor. Soc., 89, 360-370.

_____, E. Strauch and F.H. Ludlam, 1963: The density of hailstones collected from a summer storm. Tech. Note No. 7, Dept. of Meteor., Imperial College, London, 9pp.

Magono, C., 1954: On the falling velocity of solid precipitation elements. Sci. Report Sec. 1, No. 3, Yokohama National University, Yokohama, 33-40.

Marwitz, J.D. and A.H. Auer, 1968: Cloud nuclei spectra and updrafts beneath convective cloud bases in the high plains. J. Appl. Meteor., 7, 449-451.

_____, A.J. Chisholm and A.H. Auer, 1969: The kinematics of severe thunderstorms sheared in the direction of motion. Proc. Sixth Conf. on Severe Local Storms, Amer. Meteor. Soc., Chicago, 6-12.

_____, J.R. Middleton, A.H. Auer and D.L. Veal, 1969: The dynamics of updraft vaults as inferred from the entraining jet model. Proc. Sixth Conf. on Severe Local Storms, Amer. Meteor. Soc., Chicago, 310-313.

Mason, B.J., 1957: The Physics of Clouds. Clarendon Press, Oxford, p. 420.

Newton, C.W., 1966: Circulations in large sheared cumulonimbus. Tellus, XVIII, 699-713.

_____, 1968: Convective cloud dynamics - a synopsis. Proc. Intn'l. Conf. on Cloud Physics, Toronto, 487-498.

Phillips, B.B. and P.A. Allee, 1968: Experimental study of rain formation by coalescence. Proc. Intn'l. Conf. on Cloud Physics, Toronto, 102-106.

Radke, L.F. and P.V. Hobbs, 1969: Measurement of cloud condensation nuclei, light scattering coefficient, sodium containing particles and Aitken nuclei in the Olympic Mountains of Washington. J. Atmos. Sci., 26, 281-288.

Ranz, W.E. and W.R. Marshall, 1952: Evaporation from drops, Part I and II, Chem. Eng. Prog., 48, 141-146 and 173-180.

Smith, P., 1970: Fundamentals of Weather Radar. Unpublished manuscript, Stormy Weather Group, McGill University, Montreal.

Stackpole, J.D., 1967: Numerical analysis of atmospheric soundings. J. Appl. Meteor., 6, 461-466.

Squires, P. and J.S. Turner, 1962: An entraining jet model for cumulonimbus updraughts. Tellus, XIV, 4, 422-434.

Srivastava, R.C. and D. Atlas, 1969: Growth, motion and concentration of precipitation particles in convective storms. J. Atmos. Sci., 26, 535-544.

Takeda, T., 1970: Numerical simulation of large convective clouds. Sci. Report MW-64, Stormy Weather Group, McGill University, Montreal, 65pp. plus figs.

Twomey, S., 1959: The nuclei of natural cloud formation - part II: The supersaturation in natural clouds and the variation of cloud droplet concentration. Geofisica Pura E Applicata - Milano, 43, 243-249.

_____, and T.A. Wojchiechowski, 1969: Observations of the geographical variation of cloud nuclei. J. Atmos. Sci., 26, 684-688.

Vali, G., 1968: Ice nucleation relevant to formation of hail. Sci. Report MW-58, Stormy Weather Group, McGill University, Montreal, 51pp.

Warner, C.W., 1969: Photographic, surface and pilot balloon observations of low altitude phenomena of the hailstorm. Part III - the hailstorm of 29 June 1967. Sci. Report MW-59, Stormy Weather Group McGill University, Montreal, 17-27.

_____, M. English, A.J. Chisholm and W. Hitschfeld, 1969: The pattern of an Alberta hailstorm. Proc. Sixth Conf. on Severe Local Storms, Amer. Meteor. Soc., Chicago, 290-295.

Warner, J., 1969a: The microstructure of cumulus cloud - part I. General features of the droplet spectrum. J. Atmos. Sci., 26, 1049-1059.

_____, 1969b: The microstructure of cumulus cloud - part II. Effect on droplet size distribution of the cloud nucleus spectrum and updraft velocity. J. Atmos. Sci., 26, 1272-1282.

Weinstein, A.J. and L.G. Davis, 1967: A parameterized numerical model of cumulus convection. Report No. 11, NSF Grant No. GA-777, University Park, 43pp.

Wichmann, H., 1951: Über das vorkommen und verhalten das hagels in gewitterwokken. Ann. Meteor., 4, 218-225.

Young, R.G.E. and K.A. Browning, 1967: Wind tunnel tests of simulated spherical hailstones with variable roughness. J. Atmos. Sci., 24, 58-62.